UNIVERSITY OF SOUTHAMPTON

FACULTY OF MEDICINE

Human Development & Health,

Endocrinology & Metabolism

Volume 1 of 1

Flow Cytometer Optimisation & Standardisation for the study of Extracellular Vesicles as Translational Biomarkers

By

Joshua A. Welsh

Thesis for the degree of Doctor of Philosophy

September 2016

UNIVERSITY OF SOUTHAMPTON

ABSTRACT

FACULTY OF MEDICINE, HUMAN DEVELOPMENT AND HEALTH, ENDOCRINGOLOGY & METABOLISM

Doctor of Philosophy

Flow Cytometer Optimisation & Standardisation for the study of Extracellular Vesicles as Translational Biomarkers

Joshua A. Welsh

Background: The term 'extracellular vesicles' (EVs) encompasses a range of vesicles. These include apoptotic vesicles (1000-300nm), microvesicles (30-1000nm), exosomes (~30-120nm) and retrovirus-like vesicles (90-100nm). EVs have been linked to promising diagnostic, and therapeutic potentials. Their characterisation is poorly understood due to the lack of resolution and standardisation in detection equipment currently used.

Aims & Methods: In this thesis, I have developed methods for flow cytometer (FCM) resolution quantification, improvement, and standardisation. This involved building, testing and validating FCM optical models for EV analysis standardisation, and optimising FCM settings and protocols to increase resolution and decreasing variation in results. I then tested the benefits of these optimisations on EV analysis, which involved comparing optimised to non-optimised EV analysis protocols utilising clinical samples. Finally, EVs potential as translational biomarkers in non-alcoholic fatty liver disease (NAFLD) was investigated, employing the previously developed protocols in this thesis.

Results: FCM optimisations combined with a novel fluorescent assay resulted in a validated modelling technique, that allows diameter of EVs in plasma samples to be approximated using their scatter power, and separation of microvesicles, apoptotic vesicles, and residual platelets. Comparison of EV optimised to non-optimised protocols showed the FCM optimisation protocol to have increased EV absolute count reliability, and lower variation between results, when compared to a non-optimised FCM analysis protocol. Upon applying these methods to a biobank of clinical samples from individuals with NAFLD, novel insights were gained between the association of platelet-, endothelial-, and leukocyte-derived EVs in the progression of the disease. A clinically relevant finding being leukocyte EVs showing potential as a diagnostic marker of liver fibrosis severity.

Table of Contents

List of Tables

List of Figures

List of Accompanying Material

NO ACCOMPANYING MATERIALS ATTACHED

Declaration of Authorship

I, **Joshua A. Welsh**, declare that this thesis and the work presented in it are my own and has been generated by me as the result of my own original research.

'Flow Cytometer Optimisation & Standardisation for the study of Extracellular Vesicles as Translational Biomarkers'

I confirm that:

- This work was done wholly or mainly while in candidature for a research degree at this University;
- Where any part of this thesis has previously been submitted for a degree or any other qualification at this University or any other institution, this has been clearly stated;
- Where I have consulted the published work of others, this is always clearly attributed;
- Where I have quoted from the work of others, the source is always given. With the exception of such quotations, this thesis is entirely my own work;
- I have acknowledged all main sources of help;
- Where the thesis is based on work done by myself jointly with others, I have made clear exactly what was done by others and what I have contributed myself;
- Parts of this work **have** been published as:

***Welsh J.A.**, Englyst N.A., Holloway, J. A. Microvesicles as Biomarkers in Diabetes, Obesity and Non-Alcoholic Fatty Liver Disease: Current Knowledge and Future Directions. Intern Med 2014, S6:009*

Signed: _____ Date: _____

Acknowledgments

I would firstly like to thank Prof. Martyn Mahaut-Smith who introduced me to the topic of extracellular vesicles in my undergraduate degree and inspired me to undertake a PhD researching them. I would like to express my sincere gratitude to all my supervisors Dr. Nicola Englyst, Dr. Judith Holloway, Dr. David Smith and Prof. James Wilkinson for their continuous support, patience and motivation throughout my project.

I would also like to thank Dr. Peter Horak, who has been patient, knowledgeable, and dedicated a great deal of time to explaining and helping construct the optical models within this thesis; Prof. Christopher Byrne, Prof. Philip Calder and Prof. Geraldine Clough who have given me access to their non-alcoholic fatty liver disease study biobank and database; Dr. Ruth Challis, Richard Jewel and Dr Carolann M^{c}Guire for their initial help with using flow cytometers, and allowing me to make alterations to communal flow cytometers. I would like to thank Dr. Michael Stadnisky for his support with obtaining and modifying FlowJo software. Dr. Kate Easten for making much of our sample analysis possible by giving considerable discounts on reagents throughout my PhD; Dr Lee Edwards for access to Beckman Coulter flow cytometers; project students Harriet McMillan and Matthew Duffield for their help obtaining some of the data within this thesis.

I would like to give special thanks to all the ThermoFisher Scientific team who I have either been in contact with directly or been were behind the scenes; they have been invaluable to my PhD. I have always been met with enthusiastic and helpful support in modifying equipment, obtaining consumables, supporting travel, and allowing me to visit and speak at their flow cytometry R&D facility. Members of this team I would particularly like to highlight are: Mrs. Beverly Goward and Dr. Kate Alford for help in obtaining consumables and putting me in contact with the ThermoFisher Scientific R&D team, leading to a collaboration; Dr. Michael Ward, Mr Wesley Smith, Mr Jason Malkin, and Mr Jace Akerlund for their technical support and patience making modifications to flow cytometers, as well as providing immense insight into the workings of flow cytometers. I would also like to thank Dr. Christoph Hergersberg, Mrs Gayle Buller, Mrs Jolene Bradford, and Mr Michael Quick for financial support and helping to instigate our collaboration agreement, and I would also like to thank Dr Shane Oram and Ms Bonnie Bell for travel support.

Thank you to my parents and sister for their belief and encouragement; Alan, Hugh, Iain, Matt and Rachel for their humour, company and support through the highs and lows.

Finally, thank you Diabetes UK and the National Institute of Academic Anaesthesia (NIAA) for sponsoring the research in this thesis, and University of Southampton who also sponsored and hosted it. This work has culminated in a fruitful collaboration with ThermoFisher Scientific to

further develop their flow cytometers for small particle analysis, and I look forward to my future research with them and the journey beyond.

Definitions & Abbreviations

AFM – Atomic force microscopy.

CE - Cholesterol ester.

cFCM – Commerical flow cytometry.

dFCM – Dedicated flow cytometry.

CM – Chylomicron.

CRM – Ceramide.

DLS – Dynamic light scatter.

Elastic light scatter – the wavelength is not changed by the scattering process and therefore no loss of energy.

EM – Electron microscopy.

EMV – Endothelial microvesicle.

Extracellular Vesicle (EV) – describes vesicles that can be found outside of the cell.

Exosome – a type of extracellular vesicle released from multivesicular bodies, rather than directly from the plasma membrane. Classically defined as ~20-100nm.

FC - Free cholesterol.

Flow Cytometry (FCM) – a technique that passes cells through a laser, with the scattered light from the cell providing information.

Forward Scatter (FSC) – The light measurement collected around the obscuration bar, in line with the laser incidence angle.

Gaussian – alternative term for normal distribution.

Hydrodynamic Focusing – The thinning of an inner fluid stream using a surrounding fluid at higher pressure.

IDL - Intermediate Lipoprotein.

Inelastic light scatter – a photon is absorbed and re-emitted at a different energy.

ISTH – International Society of Thrombosis & Haemostasis

Laser waist – the smallest achievable diameter of laser geometry.

LDL - Low density lipoprotein.

LMV – Leukocyte microvesicle.

Microparticle (MP)– alternative term for microvesicle used in earlier literature.

Microvesicle (MV) – a type of extracellular vesicle shed directly from the plasma membrane of a cell. Classically defined as ~100-1000nm.

Molar Extinction Coefficient – The efficiency of a fluorescent molecule to absorb photons.

Multivesicular Body (MVB) – an organelle within the cell.

NMR – Nuclear magnetic resonance.

NTA – Nanoparticle tracking analysis.

PE – Phosphatidylethanolamine.

PI – Phosphatidylinositol.

Phosphatidylcholine (PC) – a type of lipid found in the cell plasma membrane, commonly found on the outer side.

Phosphatidylserine (PS) – a type of lipid found in the cell plasma membrane, commonly found on the inner side.

PL – Phospholipid.

PMV – Platelet Microvesicle.

Quantum Yield – The ratio of photons emitted to photons absorbed by a fluorophore.

Quasi-elastic light scatter – is a limiting case of elastic scatter whereby small fluctuations are seen in the scattered light occurs when a medium's concentration changes due to Brownian motion of particles within the medium.

Refractive Index (RI) – the ratio of the velocity of light in a vacuum to its velocity in a specified medium.

RPS – Resistive Pulse Sensing.

RS – Raman Spectroscopy.

SAXS – Small-angle x-ray scattering.

Side Scatter (SSC) – The light measurement collected at 90° to the incident laser beam.

SRM – Super-Resolution Microscopy.

SM – Syphingomyelin.

TG – Triacylglycerides.

VLDL - Very Low Density Lipoprotein.

Window Extension (WE) – The time period extension on either side of the window gate.

Window Gate (WG) – The amount of time an event is above threshold.

Chapter 1: Introduction to Extracellular Vesicles (EVs)

Extracellular Vesicles (EVs) have been linked to promising diagnostic, and therapeutic potentials, their characterisation however has been to date been poorly understood due to the lack of standardisation in detection equipment, and lack of resolution currently detection techniques hold. The term 'extracellular vesicles' encompasses a range of vesicles. These include apoptotic vesicles (AVs, apoptotic bodies and apoptotic blebs), microvesicles (MVs, microparticles, MPs, and ectosomes), exosomes and retrovirus-like vesicles (RLVs). Lipoproteins could also be considered within the umbrella term of EVs, due to being structurally similar (outer lipid membrane (monolayer), surface proteins, overlapping diameters) and possibly being mistaken for other EV types in current isolation and detection methods.

1.1 Discovery of EVs

The discovery of extracellular vesicle has spanned the 20th century. The first of this group to be discovered were lipoproteins, whose discovery spanned from the early 1920s to 1950. Apoptotic vesicles, RLVs, and MVs were identified in the 1960s, followed by exosomes in the 1980s, Figure 1.1. The vesicles contributing to this umbrella term are therefore not a recent discovery. The definitions of each of these different vesicles however remains problematic, due to the inconsistency in published data regarding the measurable criteria allowing their differentiation.

1.1.1 Lipoproteins

Lipoproteins are phospholipid structures expressing proteins and containing lipids. Lipoproteins are important in the regulation of metabolism and play a role in the transport of lipids around the body. There are five main types of lipoproteins: chylomicrons (CMs), very low-density lipoproteins (VLDLs), intermediate density lipoproteins (IDLs), low density lipoproteins (LDLs) and high density lipoproteins (HDLs). Although all consist of lipids and proteins, each have different compositions, diameters, and functions, as shown in Table 1.1.

1.1.2 Apoptotic vesicles

Apoptotic vesicles (AVs) are the result of programmed cell death. The term apoptosis was first coined in 1972, describing a morphologically distinct form of cell death, though aspects of apoptosis had been described several years before[7]. This process involves cell condensation and fragmentation into vesicles, before phagocytosis of the vesicles. These vesicles range in diameter from approximately one to three, and above, micrometres and are therefore in the approximate

diameter range of platelets[7-10]. These large vesicles contain genetic information and express cell surface proteins. They are usually differentiated from living cells using the phospholipid phosphatidylserine (PS), which is externalized upon cell apoptosis, or by staining intracellular genetic material using a dye, such as propidium iodide, which can only enter through the permeable lipid bilayer of apoptotic vesicles and not living cells.

1.1.3 Microvesicles

Microvesicle (MV) identification was a result of coagulation research spanning from the 1940s by Chargaff and West, until the late 1960s when Wolf reported visual evidence of platelet activation, using electron microscopy[11, 12]. The activated platelets appeared to be shedding small vesicles (20-50nm) directly from the plasma membrane, capable of thrombin generation. These vesicles were so minute in comparison to platelets that Wolf termed them 'platelet dust'. Wolf noted a linear correlation between the levels of platelet MVs (PMVs) and the original platelet count. He also noted that individuals with polycythaemia had a higher concentration of PMVs, with lower concentrations in individuals with thrombocytopenia.

1.1.4 Exosomes

Exosomes were first identified in 1987 by Johnstone, who was researching the transformation process of reticulocytes into mature erythrocytes. Using electron microscopy, Johnstone identified small vesicles (30-100nm) held within the cytoplasm in multivesicular bodies (MVBs). Transferrin was identified as an abundant protein on MVBs using immunogold labelling, with the MVBs eventually binding to the plasma membrane, releasing the enclosed exosomes[13, 14].

1.1.5 Retrovirus-like vesicles

Retrovirus-like Vesicles (RLVs) are thought to arise from human endogenous retrovirus (HERV) sequences, which contribute approximately 5-8% of the human genome, and were reported as early as 1965[15, 16]. RLVs are grouped into families denoted by a suffix letter i.e. HERV-A. HERV-K is the only one of these families that contains open reading frames for functional retroviral proteins, *gag*, *env*, *rec* and *pol*[17, 18]. Cells experiencing stress, such as radiation, chemical treatment, cytokine stimulation, hormone stimulation, or oncogenic transformation can cause the usually repressed expression HERV-K genes to be de-repressed[19-26]. RLVs bud directly from the plasma membrane and their mechanism of biogenesis is thought to differ from those of MVs or exosomes. Their diameter is currently being reported as fairly homogenous at 90-100nm[27].

1.1.6 Summary of EVs

Although each of these EVs differs, there is overlap in density, diameter, composition and derivation. Further study for more precise definitions and function, as well as development of better identification machinery and markers is therefore required. The main focus of the extracellular vesicle field is on the study of microvesicles and exosomes. Whilst lipoproteins, RLVs and apoptotic vesicles are not being highly studied in the EV field, they must be considered due to their overlapping properties, and for potentially causing contamination and inadvertent misinformation in publications to date due to their properties and the detection/isolation techniques used. From this point, AVs, MVs and exosomes shall be the main focus of this thesis.

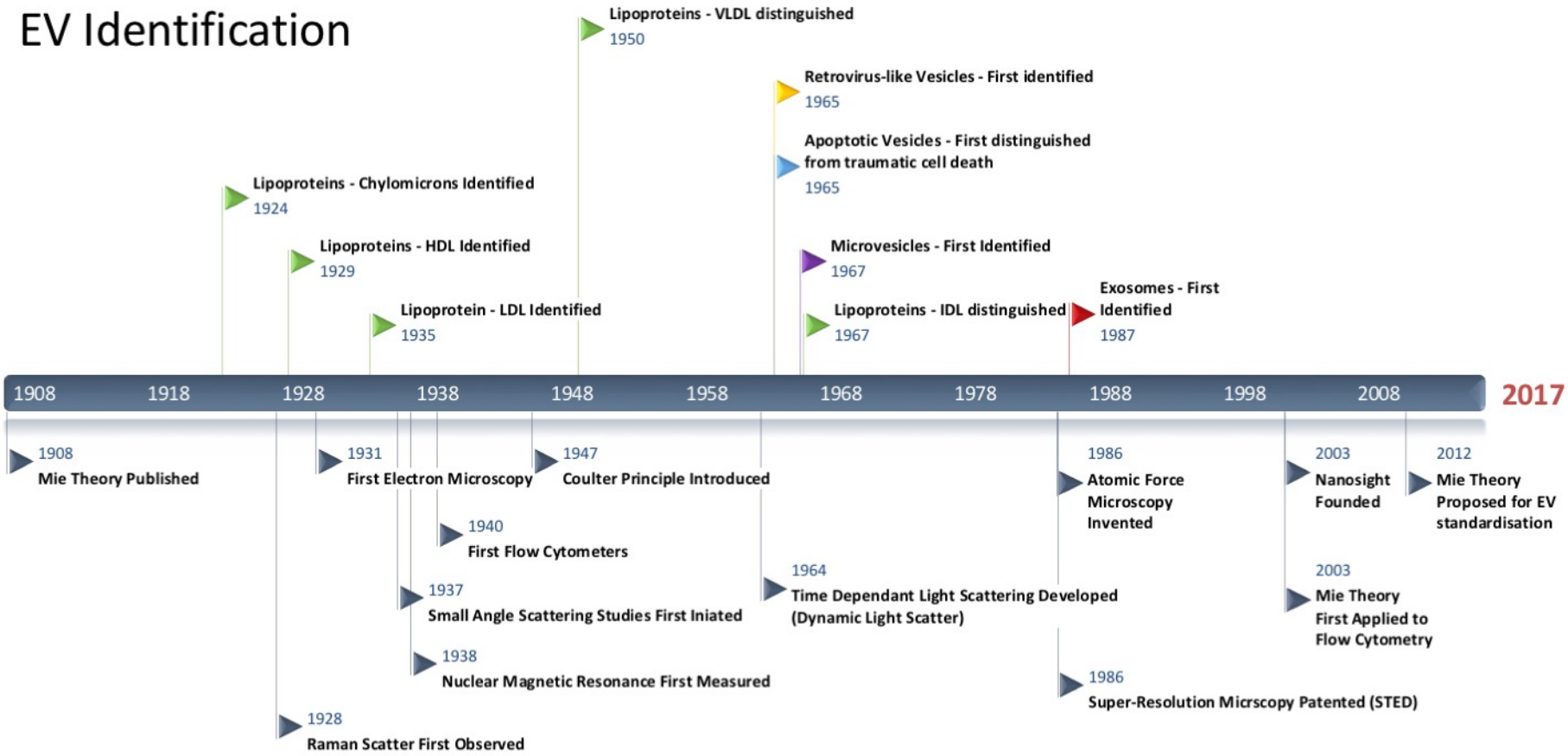

Figure 1.1 | EV Discovery and Detection Developments Timeline.

The top of the timeline shows the identification of individual lipoprotein populations (green), retrovirus-like vesicles (yellow), apoptotic vesicles (light blue), microvesicles (purple), and exosomes (red). The discoveries and development of theories and machinery are shown on the bottom half of the timeline (dark blue).

Table 1.1 | EV Lipidomic Comparisons.

Lipoprotein subpopulation (CM-Chylomicron, VLDL-Very Low Density Lipoprotein, IDL- Intermediate Lipoprotein, LDL-Low Density Lipoprotein), are compared in terms of separation density, lipidomics (TG=Triacylglyercides, CE=Cholesterol Ester, FC=Free Cholesterol, PL=Phospholipid, P=Protein, CRM=Ceramide, PC=Phosphatidylcholine, PS=Phosphatidylserine, PE=Phosphatidylethanolamine, PI+Phosphatidylinositol, SM=sphingomyelin, UD – Undetectable amount. Comparisons of lipoprotein subpopulations were made with MVs and exosomes from several cell derivations, along with RLV and APVs[1-6]. Highlighted areas correspond to data from the same source, and is therefore directly comparative.

Vesicle	Size Range (nm)	Mean Size (nm)	Density (g/mL)	TG (%)	CE (%)	FC (%)	PL (%)	P (%)	Apoliprotein	CRM (%)	PC (%)	PS (%)	PE (%)	PI (%)	SM (%)	PS+PI (%)
CM	75-1200	-	<0.95	86	3	1	8	2	A-I, II, B-48, C-I, II, III, E	-	1.55	UN	13.92	12.52	20.54	NA
VLDL	30-80	-	0.95-1.006	52	14	7	18	8	B-100, C-I, II, III, E	-	0.44	UN	5.43	4.05	4.94	NA
IDL	15-35	-	1.006-1.019	38	30	8	23	11	B-100, C-III, E	-	0.07	UN	0.51	1.1	2.06	NA
LDL	18-25	-	1.019-1.063	10	38	8	22	21	B-100	-	2.45	UN	16.04	17.86	35.93	NA
HDL	7.5-20	-	1.063-1.21	05-Oct	14-21	03-Jul	19-29	33-57	A-I, II, C-I, II, III, D, E	-	95.14	UN	0	61.88	32.5	NA
Platelets	1000-3000	-	1.040-1.080	-	-	-	-	-	NA	-	~40	~16	~9	~3	-	-
Platelet MVs		-		-	-	-	-	-	NA	-	~37	~14	~7	<1	-	-
		209	1.24-1.3	-	4.4	37.1	NA	-	NA	0.84	17.2	14.1	6	2.5	8	NA
		213	1.19-1.24	-	2.1	36.1	NA	-	NA	0.89	18	15.4	6.4	3.1	8	NA
		254	1.16-1.19	-	2.7	34	NA	-	NA	1.07	19.7	14.5	6.6	3.7	7.7	NA
		257	1.15-1.16	-	2.5	35	NA	-	NA	1.04	19.7	13.9	6.3	3.9	7.4	NA
		233	1.13-1.15	-	5	30.8	NA	-	NA	1.3	17.2	18.9	6.5	3.8	6	NA
Platelet Exosomes		184	1.1-1.13	-	4.1	42.5	NA	-	NA	0.4	15.9	10.5	3.1	5.2	12.5	NA
Erythrocyte Exosome		-	-	-	-	-	-	-	NA	-	44.4	NA	23.9	NA	15.9	15.8
Erythrocytes		-	-	-	-	-	-	-	NA	-	43.2	NA	28.3	NA	12.1	16.4
Mast Cell Exosomes		-	-	-	-	-	-	-	NA	-	33	NA	27	NA	14	18
Mast Cells		-	-	-	-	-	-	-	NA	-	50	NA	25	NA	5	5
Dendritic Cell Exosomes		-	-	-	-	-	-	-	NA	-	26	NA	26	NA	20	19
Dendritic Cells		-	-	-	-	-	-	-	NA	-	43	NA	23	NA	9	12
RLV	90-100	-	-	-	-	-	-	-	-	-	-	-	-	-	-	-
Apoptotic Vesicles	1000-5000	-	-	-	-	-	-	-	-	-	-	-	-	-	-	-

1.2 Formation of EVs

1.2.1 Eukaryotic Cell Membrane Structure and Regulation

Biological membranes are comprised of lipids and proteins, with carbohydrates linked to some of these. Membranes tend to have a thickness of 6-10nm, equivalent to two phospholipid molecules, forming a lipid bilayer. Lipids are structurally diverse, generally hydrophobic, and have three general functions: to store energy, to act as 1st or 2nd messengers, and to form cellular membranes from polar lipids[28].

Amphipathic lipids form the lipid bilayer, which has an asymmetric distribution of both proteins and phospholipids. This asymmetric distribution is maintained by multiple factors, including biophysical properties, retentive mechanisms trapping lipids in a specific leaflet, and transporters aiding lipid translocation[28]. Structural integral lipids in eukaryotic cells are glycerophospholipids, which include phosphatidylcholine (PC), phosphatidylethanolamine (PE), PS, phosphatidylinositol (PI) and phosphatidic acid (PA)[28]. The relative quantities of these phospholipids appear to differ between lipoproteins, cell types, and EVs, Table 1.1. PC however makes up the majority in all cells and EVs tested. The inclusion of PE within a PC bilayer asserts a curvature stress upon the membrane due to its shape, which is thought to be utilized in budding, fission and fusion [29].

The cell plasma membrane is enriched with sphingolipids and sterols. Sphingolipids contain a hydrophobic ceramide backbone, with the predominant mammalian sphingolipids being sphingomyelin (SM) and glycosphingolipids. Sterols are non-polar lipids, and are predominantly in the form of cholesterol in mammalian cells[28]. This high density of sphingolipids and sterols, in comparison to glycerolipids, makes the cell membrane resistant to curvature stress. The lipidome of EVs has shown them to be more concentrated in SM than their cells of derivation, Table 1.1, though lipidome studies in EVs do appear to yield varying results based on their isolation technique.

The asymmetric distribution of lipids is also a contributor to curvature stress, with PC, SM and sterols on the outer leaflet, while PS and PE are predominantly on the inner leaflet of inert cells. This distribution also plays a functional role. When membrane dysregulation occurs, causing a loss of phospholipid asymmetry and PS externalization, phagocytotic signalling, and a catalyst for thrombin generation is mediated. Transporters involved in maintaining lipid asymmetry include: flippases, floppases and scramblases. Flippases are responsible for the ‘flipping’ of PS and PE from the exterior surface to the interior surface, whilst floppases are responsible for the opposite. Scramblases are capable of bidirectional transbilayer transport, and can be activated through Ca^{2+} currents. It is also thought that some scramblases are activated through apoptosis.

Although steps have been made to elucidate the mechanisms in the biogenesis of EVs, much remains to be explained. This is predominantly due to detection and isolation methodology currently requiring development for smaller EVs.

1.2.2 Apoptotic Vesicle Formation

Apoptotic vesicles can be formed via a number of cell death pathways. Cellular death is generally discussed dichotomously, in terms of apoptosis or necrosis, with apoptosis being an active, programmed process, whilst necrosis has been presumed as passive, accidental cell death as a result of environmental factors. Understanding of the process of cell death has become increasingly complicated however, and is not a dichotomous divide as has been assumed.

Apoptosis is induced by three pathways, the extrinsic, intrinsic, and perforin/granzyme pathway, Figure 1.2. Each pathway ends in the activation of caspase-3 leading to cytomorphological changes such as cytoskeletal reorganisation, chromatin and cytoplasmic condensation, nuclear fragmentation, and more. This then results in the cell blebbing, forming apoptotic vesicles (For further details on pathway associated proteins see reviews[30-33]).

Figure 1.2 | Apoptotic Cell Death Pathways.

Shown are the main pathways that lead to apoptosis, these include the extrinsic, intrinsic and perforin/granzyme pathway. Each pathway has its own initiator, caspase-8/9/10, in turn activating caspase-3 leading to cytomorphological changes and apoptotic body formation.

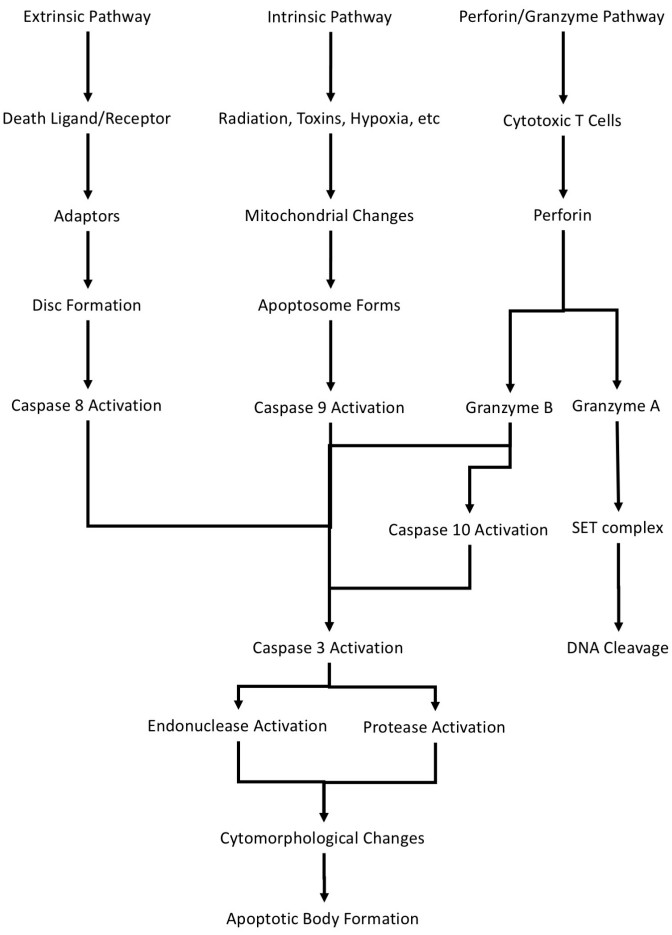

Contrary to the passive, accidental cell death it was perceived to be, in recent years necrosis has been shown to be caused by a number of regulated pathways, some of which overlap with apoptosis. Some of these regulated modes include PARP1 hyperactivation, mitochondrial complex 1, Cys/Glu antiporter, necrosome, NADPH oxidases, inflammasome[34].

Other forms of cell death also exist; oncosis is a form of cell death accompanied by cellular and organelle swelling, along with membrane blebbing and membrane permeability. Along with oncosis, pyroptosis is another form of cell death that has been characterised, and is induced by infection[32].

The crucial message is that large vesicles, resulting from regulated cell death, are not solely derived from apoptosis but rather from cell death as a whole. The difference between these vesicle characteristics is not something that has been investigated, and those vesicles that are in the circulation are likely to depend upon the circumstance of the individual cells releasing vesicles. This therefore could be important when characterising these types of vesicles in translational studies. Here, the different large vesicles resulting from cellular death are collectively referred to as AVs.

1.2.3 Exosomes Formation

Exosomes are formed within multivesicular bodies (MVBs). MVBs however are prone to fusion with lysosomes, within the lysosomal pathway, causing degradation of MVBs and their contents, Figure 1.3. There appears to be biochemical and morphological distinction between MVBs who will undergo degradation, and those secreted from cells. The composition of exosomes from studies to date show them to be formed of proteins from endosome, plasma membrane and cytosolic origin. This suggests that exosomes do not contain just random proteins, but infers that they represent a specific compartment of the cell[10]. Databases have since been created to compile the published data on the exosome proteome from different origins[35, 36]. Exosome formation within the MVB has been extensively studied at a molecular level, particularly in yeast[37]. The endosomal sorting complex required for transport (ESCRT) machinery is very important in the formation of exosomes within the MVB. The ESCRT proteins essentially allow invagination of the membrane in the opposite direction to the cytosol. ESCRT-0 is important for ubiquitin-dependant cargo clustering, with ESCRT-I (TSG101) and ESCRT-II inducing bud formation, with vesicle scission being driven by ESCRT-III. Accessory proteins also have roles to play, with VPS4 ATPase allowing dissociation and recycling of the ESCRT machinery itself. Further details of the role of each protein's role within exosome biogenesis can be found in reviews[38-41]. ESCRT independent mechanisms of exosome formation have also been proposed. Mammalian cells depleted of key ESCRT machinery components are still capable of producing MVBs[42]. These involve tetraspanins, lipids and heat shock proteins.

Once formed, MVBs fuse with the plasma membrane allowing release of their exosomal contents. The trafficking and fusion of the MVB with the plasma membrane is regulated by the RAB family of small GTPases proteins. The RAB family of proteins appear to have major intracellular

localizations according to their role. The RAB2B protein is localised to the endoplasmic reticulum and Golgi apparatus, while RAB5A, RAB7, RAB9A, RAB11, RAB27A, RAB27B and RAB35 are localised to the endosome depending on its stage within the pathway[43-47].

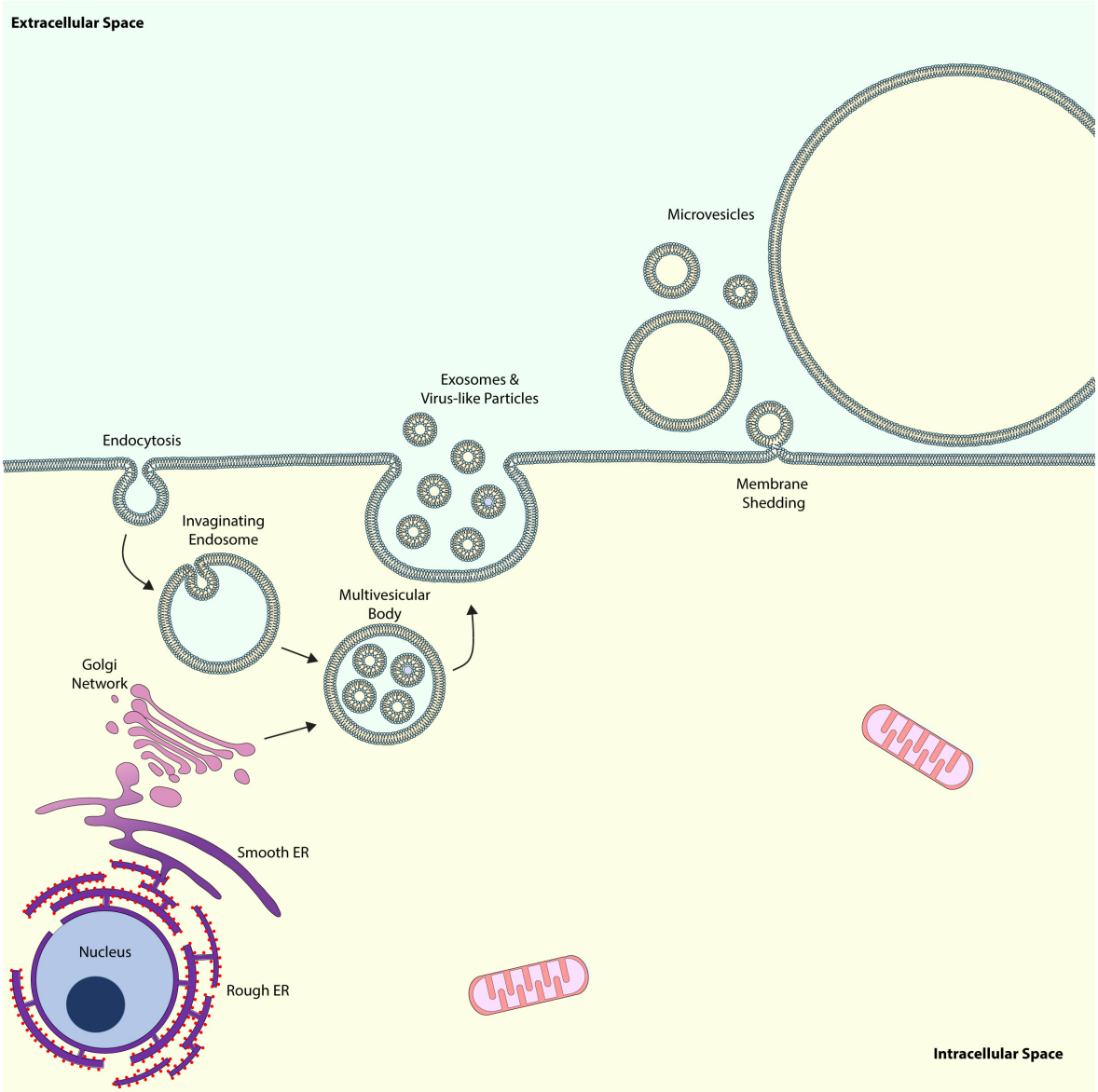

Figure 1.3 | Overview of Exosome and Microvesicle Release.

Illustration is depicts the simplified biogenesis of exosomes from endocytosis, to early endosome formation, multivesicular body formation, to exosome, as well as RLV release, and microvesicle release through budding directly from the plasma membrane.

1.2.4 Microvesicle Formation

MVs are formed upon cellular activation, death and even at rest, with diameters considered to vary from 20nm to above 1000nm. The majority of vesicles however are in the bottom half of this range[48]. MVs are the result of plasma membrane vesiculation, and were originally identified on the basis of phosphatidylserine (PS) exposure, due to dysregulation of the plasma membrane. A wide range of stimuli can induce MV vesiculation.

An initial clue to platelet MV formation came from the rare haemorrhagic disorder, Scott syndrome[49]. This syndrome is associated with a genetic mutation in a scramblase, transmembrane protein 16F (TMEM16F), also known as anoctamin 6. As a result of this mutation, platelets exposed to Ca^{2+} ionophore are unable to expose PS to their outer-membrane, and are also thought not to shed MVs[50, 51]. The inability to expose PS to outer-membrane is also true of erythrocytes, T-cells and B-cells derived from individuals with Scott Syndrome. These cells however all appear to display normal PS exposure and lipid scrambling rates when given an apoptotic trigger[52, 53]. It has since been confirmed that TMEM16F can be activated both via Ca^{2+} currents and apoptotic signals[53].

The exact mechanism of MV formation is unknown. The majority of agonists known to result in MV formation produce a Ca^{2+} current or flux, with many research groups inducing MV formation using Ca^{2+} ionophores such as A23187 or ionomycin[54-58]. Ca^{2+} activated K^{+} channels also aid MV release, likely providing a decreased cell volume which allows the reduction in surface area required for MV release; this has previously been observed in apoptotic cells[59, 60]. Further clues into MV budding have come from the study of the ESCRT machinery. The ESCRT proteins play an important role in the shedding of membrane vesicles, as well as the formation of MVBs, in response to small wounds that stimulate early signalling pathways such as Ca^{2+} influxes[61, 62]. MV morphology and mechanisms leading to budding may however differ between cell types, with evidence in some models showing budding regulation by ADP-ribosylation factor 6, phospholipase D and a variety of kinases[39].

1.2.5 Summary of EV Formation

In each case of EV formation there appear to be multiple pathways leading to vesiculation, but the end result of these pathways on the morphological and biochemical characteristics of the vesicles is ill defined. Making true distinction between subsets of EVs is an area requiring study, that translational studies may benefit from.

Due to the current limitations in distinction between EV subsets when analysing physiological fluids, density and diameter appear to be the best option for currently of allowing distinction between apoptotic vesicles and small vesicles (MVs & exosomes). However, due to some MVs overlapping in diameter with exosomes, it is debatable how effective density and diameter differentiation is in this case, and more likely protein markers and relative abundance also need to be factored in. It is questionable whether it is even possible to differentiate between exosomes and MVs (once they have been released) within their overlapping diameter ranges, at which both are at their most abundant.

1.3 Significance of EVs

1.3.1 Apoptotic Vesicle Significance

Apoptotic vesicles (AVs) tend to be investigated qualitatively using imaging techniques, or cumulatively using techniques such as ELISA that identify features of apoptosis, such as activated caspases, cytochrome C, PS exposure, nucleosomal DNA, to name a few[63]. Many cell studies include apoptotic assays within their protocols, specifically to gate apoptotic cells out of living cell analysis.

Studies investigating apoptotic cells and AVs have identified them as potential biomarkers in liver fibrinogenesis and enhancing endothelial progenitor cells [8, 64]. Tracking apoptotic tumour cells is a particularly targeted area of quantifying apoptotic cell biomarkers, in order to determine the efficacy of treatments[63]. Apoptotic neutrophils and T-cells have also been hypothesized to sequester chemokines, in turn promoting resolution of inflammation[65]. Having detection and detailed assays of apoptotic markers in large translational studies could therefore yield promising avenues for novel diagnostic and prognostic biomarkers.

1.3.2 Microvesicle & Exosome Significance

MVs are becoming of particular interest due to the modulation observed in a variety of diseases, when compared to healthy individuals. MVs vary between individuals with regard to numbers, ratios of subsets, phenotypic markers and intracellular cargo. This enables MVs to potentially have an important functional role in the homeostasis and pathology of individuals. MVs also hold a great deal of potential as clinical biomarkers due to the large amount of observable variation, particularly in cases where current definitive diagnostic biomarkers have not yet been identified, or are inaccessible and/or would require invasive procedures to test due to the diseased area.

The function of MVs are likely to be wide ranging, due to the pleiotropic nature of MV characteristics. It is thought all human cells can produce MVs, and almost all human media appear to contain MVs. These include: blood, urine, saliva, cerebrospinal fluid, amniotic fluid, and breast milk[66-70]. MV vesiculation is also a phenomenon conserved through three domains of life, Archaea, Bacteria and Eukarya[71-77]. It therefore seems likely that these minute vesicles have come to play important roles within these life forms, some of which we have only just started to understand. MV modulations are correlated with cancer, autoimmune diseases, haematological disorders, cardiovascular diseases, infectious diseases, kidney disorders, transplantation, metabolic disease, neurological disease and more (in depth review[78]). While this variety in MV subsets is exciting for the progression of the biomarker field, a number of techniques have been implemented to

quantify MV modulation in disease without addressing the necessary standardization. Many studies are therefore not comparable for validation purposes.

Broadly speaking platelet MVs (PMVs) remain one of the most studied MV both in terms of function and biomarker studies. Platelet MVs have been associated with a number of functions including coagulation, adhesion, inflammation, angiogenesis, cell proliferation[76, 79, 80]. Endothelial MVs (EMVs) are also relatively well studied, with evidence suggesting they can promote anti-inflammatory effects and cell survival, counter coagulation processes, or induce endothelial regeneration as well as having deleterious effects[81]. Leukocyte MVs (LMVs), are some of the least studied MVs. Leukocyte MVs have however been suggested to be mediators of the pro-resolution pathway; being capable of regulating gene expression as well as directly mediating pro-resolution effects[82].

Exosomes are of great interest for potential therapeutic intervention due to their intracellular genetic content, an example of which is research into using cultured cardiac explant-derived cell exosomes in myocardial infarction (MI). Research has shown these exosomes are capable of regenerating dead tissue post-MI by over 10% more than controls[83]. Other research avenues using exosomes have developed customisable vesicles in the hope of implementing them in high specificity therapeutic intervention[84].

1.3.3 Summary of EV Significance

EVs have continued to be an area of increasing interest, with the number of publications per year growing from 328 to 2,030 between 2000 and 2014. (PubMed - searching terms; extracellular vesicles, exosomes, microvesicles, microparticles, ectosomes). Their role in medicine as biomarkers and drug delivery vectors, and their roles in pathophysiology are slowly being identified. Whilst research continues to progress on extracellular vesicles at an increasing rate, it is limited by standardisation and detection methods.

As interest continues to grow, the International Society of Extracellular Vesicles (ISEV), the International Society of Thrombosis and Haemostasis (ISTH), and the International Society for Advancement of Cytometry (ISAC), have formed a partnership to address standardisation in the field due to the growing issues of reproducibility and reliability of published results. This work builds upon previous attempts set out by the ISTH to standardise the extracellular vesicle field[85, 86].

Whilst the prospects of EVs are exciting for a number of areas of study, in order for the functional roles and effects of EVs on the body to be truly elucidated, standardization of detection and isolation must first be implemented and replicated across studies. For standardization to occur,

detailed characterization of EVs must be carried out at a basic level utilizing high resolution multi-parametric analysis equipment, some of which does not yet exist.

Definitively identifying EVs remains a big challenge due to the relatively loose criteria used to identify them, and overlapping characteristics, Table 1.1. MVs are generally defined by having a diameter range of 30-1000nm and PS exposure. These two criteria overlap with other EV particles as previously stated.

1.4 EV Isolation

Centrifugation, sucrose density gradients, dialysis, filtering, size-exclusion chromatography, and immune-affinity separation have been used to isolate and concentrate EVs. These can be useful for improving the ratio of EV events to sample-derived noise, e.g. soluble proteins, for light scatter techniques such as flow cytometry. Each of these techniques uses different EV characteristics to increase their relative concentration to potential background contaminants. Extensive comparisons of EV yields using these techniques are yet to be performed, there are however limited reviews comparing some details of those tested[87-89].

All of these techniques, however, have their individual drawbacks, as well as potentially introducing inter-sample variation, and are not being likely to give comparative results if used interchangeably. Whilst differential centrifugation and ultracentrifugation have been popular methods for isolating MVs, they have an effect on MV concentration depending on speeds and types of rotors implemented[90, 91]. Different groups however continue to utilise their own methods that consist of different relative centrifugal forces lasting for differing periods of time[86].

1.4.1 EV Labelling

1.4.1.1 Phosphatidylserine Labelling

Annexin V is a molecule that binds to externalised PS and has been heavily used to enumerate phosphatidylserine (PS) positive MVs. Annexin V staining has been seen as a gold-standard, likely due to MV first being identified with flow cytometry using annexin V, along with many of the subsequent papers[92-96].

1.4.1.1.1 Annexin V

Annexin V was first isolated from chondrocytes and identified as a collagen-binding protein, initially named anchorin CII for its ability to bind to type II collagen. This protein also bound with a lower affinity to collagens I, IX, XI and V. Anchorin CII later became known as annexin V; it has a four 4 domain structure with five α-helices, with a pore in the centre of the molecule serving as a

Ca^{2+} channel. Domains I, II and IV each contain Ca^{2+} binding sites on the convex sides of the molecule. Annexin V has become a popular marker of PS exposure, and staining dead cells, apoptotic bodies, and EVs. However, the accuracy of annexin V in this role has been increasingly scrutinized as more studies have been conducted, as described below, with new markers of PS exposure subsequently being developed.

Annexin V also binds oxidised phospholipids, sulfatides and even incorporate itself into the phospholipid bilayer and act as a Ca^{2+} channel[97-99]. Annexin V binding is not only dependent on the amount of PS exposed, but also the amount of phosphatidylethanolamine (PE) exposure. It requires Ca^{2+} binding, with the best results at high concentrations, and has a lower affinity for PS than other markers such as milk fat globulin (MFG)- EGF8[100].

Relatively recent studies have shown that the percentage of annexin-V positive PMV events vary drastically depending on the platelet agonist, and that the majority of unstimulated plasma membrane-derived EVs are annexin V negative[56]. It has also been shown that far more ionophore induced EVs have PS exposure than those created by endogenous agonists, with respect to annexin V binding[56]. These findings suggest that previous studies may have overlooked a proportion, or majority, of EVs in their research. Many previous findings, such as EV half-life used ionophores to generate EVs, so absolute EV counts defined by annexin V positive events may have therefore been fundamentally flawed.

Some groups therefore choose to identify EVs by their staining for markers of interest alone. This however does not allow an accurate absolute count of all EVs, due to background noise, consisting of protein complexes staining positive for CD markers of interest[101]. To remove these protein complexes, Triton X-100 was added and the remaining positive events in the Triton X-100 tube were subtracted from the non-treated control tube for calculation of the final count[101, 102]. This is based on the theory that EVs are more susceptible to the detergent than proteins. Further research is needed to verify these statements, however, as the flow cytometry detection methods implemented were outdated. In summary, annexin V alternatives may provide more accurate detection capabilities for EVs.

1.4.1.1.2 Annexin V Alternatives

Alternative markers such as milk fat globulin EFG factor 8 (MFG-E8), also known as lactadherin, have started being implemented as MV markers[103-105]. MFG-E8 is an endogenous marker of PS exposure used by macrophages for phagocytosis of MVs[55, 106]. MFG-E8 appears to have a higher affinity for PS binding than annexin V, it does not require Ca^{2+} for binding, and is not dependent on the amount of phosphatidylethanolamine (PE) and PS exposure[100, 107]. Due to its endogenous function MFG-E8 does however bind to integrins αVβ3 and αVβ5, and therefore is not ideal[108].

Ideally the EV community requires a molecule that has a high sensitivity and specificity for PS that is independent of Ca^{2+} and other phospholipid exposure for binding. A potential avenue for this may be a molecule such as the relatively understudied evectin-2, also know has 'pleckstrin homology domain containing, family B, member 2' (PLEKHB2), which is involved in the trafficking of PS from the recycling endosome to the trans-Golgi network[109-111]. Another option is the range of PSVue dyes which are based on fluorescent Zn^{2+}-dipicolylamine (DPA) coordination complexes, and have been shown to be highly-selective for PS, without being Ca^{2+} dependent[112]. In vitro studies investigating the total number of MV showing PS exposure with alternative markers to annexin V are yet to be carried out.

Novel universal EV markers for accurate and dependable identification of EVs from other biological and non-biological noise, aiding their detection using flow cytometry, may already be available in different cellular applications and simply need validation using EVs.

1.4.1.2 Phospholipid Bilayer Labelling

The most effective EV staining method to date uses membrane-staining techniques with dyes such as PKH-67, and setting a threshold on fluorescence[113, 114]. Generally there is a higher signal to noise ratio when a fluorescence threshold rather than FSC/SSC thresholds are used, resulting in more accurate counting at lower diameters[115]. Results for this technique have been very promising. The disadvantage of current membrane dyes is that they require a large amount of preparation time, which for larger studies is not practical. To date therefore generalised MV labelling has been inefficient, either in efficacy or practicality. Solutions to these problems may be available by utilising markers used and being developed in the field of membrane phospholipid scrambling research[116].

One particular dye of interest, whose properties were intentionally engineered, is F2N12S, a violet-ratiometric dye designed to study cell scramblase activity. This dye integrates itself into the plasma membrane in one of two orientations. These two orientations cause the dye to emit light at one of two wavebands. Upon phospholipid reorganisation, such as PS exposure, F2N12S re-orientates itself, changing its fluorescence emission profile. This allows ratiometric discrimination of membrane phospholipid exposure using one excitation source, and potentially provides a particularly powerful tool in EV research, Figure 1.4.

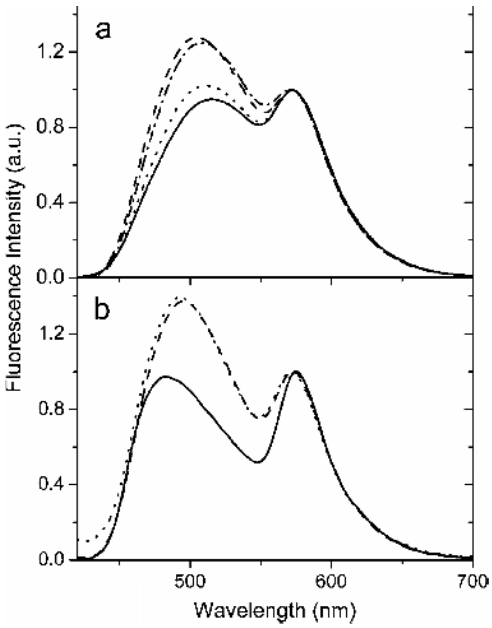

Figure 1.4 | Fluorescence Spectra of F2N12S in Lipid Vesicles (a) and in Cells (b).

In (a), lipid vesicles were composed of egg-yolk phosphatidylcholine (solid), egg-yolk phosphatidylethanolamine (dot), egg-yolk phosphatidylglycerol (dash dot), or PS (dash). In (b), the spectrum of F2N12S was recorded in normal (solid) or in apoptotic CEM cells either in the absence (dash) or in the presence of 2mM Ca^{2+} (dot). The excitation wavelength used was 400nm. The final probe concentration was 0.1 µM. Taken from Shynkar et al[117].

Utilising this dye could potentially give definitive answers to whether all EVs are PS positive or whether it is variable depending upon the protagonist to EV release, as suggested by work using annexin V. More importantly, as this dye allows EVs to be labelled, fluorescence thresholds could be utilised increasing the detection limits without the preparation time limits imposed by membrane stains such as PKH67. Washing steps can also be avoided, unlike PKH67 staining, as F2N12S has very low fluorescent properties when suspended in water. If PS exposure is variable with MV release, F2N12S provides a novel powerful phenotypic analysis tool for MV research, allowing the ratio of PS positive to negative MVs, along with CD markers of interest to be quantified.

1.4.1.3 Intracellular Labelling

BAPTA-1-AM is a Ca^{2+} sensitive dye that gains entry to the cell via its acetoxymethyl ester. This is cleaved upon hydrolysis via intracellular esterases once internalized, which stops the dye leaking easily from the particle. BAPTA-1AM has a high affinity for Ca^{2+} with a K_d value of 170nM and an F_{Ca}/F_{Free} of ~14. Due to its Oregon-Green tag, its excitation/emission wavelength of 493/523nm, closely resembles FITC and allows it to be excited to 93% of maximum excitation at a standard flow cytometer illuminating wavelength of 488nm. This dye has been previously described in applications staining 'microparticles'. These results however require validation, owing to their outdated analysis techniques[118].

1.4.1.4 Immunophenotyping

Immunophenotyping is a method of determining the protein expression of a surface. For analysis techniques such as flow cytometry immunoglobulins are labelled with fluorophores. These fluorescent-conjugated antibodies are mixed with cells and passed through a laser. If the fluorescence is seen to increase on the events that have passed through the laser, it can be deemed the particle is positive for the protein specific to the antibody used. Limitations arise from this method in two ways: the antibody specificity, and the fluorescence. While most

antibodies are screened for specificity to their protein target, non-specific binding can occur thereby giving false positives. Due to the detection of positive vs. negative particles depending on a fluorescence increase or decrease, the ability to determine whether a particle is positive or negative depends on the number of fluorescent molecules a flow cytometer can detect, and not solely on whether the antibody has bound to the particle or not. Resolution also depends on how many antibodies in the sample are left unbound, as this can increase background noise and decrease resolution. This method of investigating particles is versatile and allows mixtures of antibodies to be used to determine and differentiate the expression of multiple proteins simultaneously on particles, and has enabled the deduction of cell type. Using flow cytometry this published limit is the detection of 17 separate proteins, with many factors influencing the expansion of this number including: technology, fluorophore emission wavelengths, data analysis techniques[119, 120]. When applied to EV phenotyping limitations of Immunophenotyping are extended. Due to the small size range of EVs, the number of proteins expressed on their surface is far lower than cells, with small EVs expressing only single or tens of proteins with larger EVs capable of expressing several hundred. This is opposed to cells which express proteins in the tens to hundreds of thousands. Not only does this require high-sensitivity to the detection of individual fluorophores but the due to small EVs have a very small surface area steric hindrance is another likely problem limiting EV phenotyping due to a typical IgG molecule measuring ~15nm[121]. The limited surface protein expression of EVs also means determining the cell-type they are derived from needs to be done with only one or two antibodies. This is problematic due to very few cell-types expressing truly unique proteins. Many areas of EV immunophenotyping therefore require investigation and development for the progress of the field.

1.4.2 Summary of methods for identifying EVs

Not only are fluorescent differentiation assays required for flow cytometric analysis, but also improvement of the fluorophore panels themselves. Using very bright fluorophores will allow detection of phenotypes with few bound markers. Multicolour panels may also be used to increase the number of markers used in multicolour flow cytometry, with limited compensation.

1.5 Detection of EVs

Detection of EV poses a number of challenges including:

- a large diameter range 20-3000nm
- the majority are very small (<500nm) and not suitable for high throughput equipment
- limited surface area for traditional phenotyping tools
- overlapping lipid characteristics

- being in the same diameter range as a number of common non-EV structures e.g. immune complexes and calcium-phosphate micro-precipitates.

For these reasons a wide variety of equipment has been implemented to attempt EV analysis, with no gold-standard currently existing. An ideal piece of analysis equipment would be capable of analysing the full range of exosomes, and MVs, from 20-1000nm, as well as that of larger vesicles, such as those from an apoptotic derivation. The equipment would be able to determine the concentration of the analysed particles and distinguish between phenotypes of derivation or function. Currently no machine is capable of doing all three. The current EV detection equipment reported in the literature includes: electron microscopy (EM), super-resolution microscopy (SRM), atomic force microscopy (AFM), conventional flow cytometry (cFCM), nanoparticle tracking analysis (NTA), dynamic light scatter (DLS), Raman spectroscopy (RS), nuclear magnetic resonance (NMR), small angle X-ray scattering (SAXS), and resistive pulse sensing (RPS). An overview of when these different EV analysis techniques came about can be seen in Figure 1.1, with how they compare to one another in terms of detection characteristics and sample preparation characteristics in Figure 1.5.

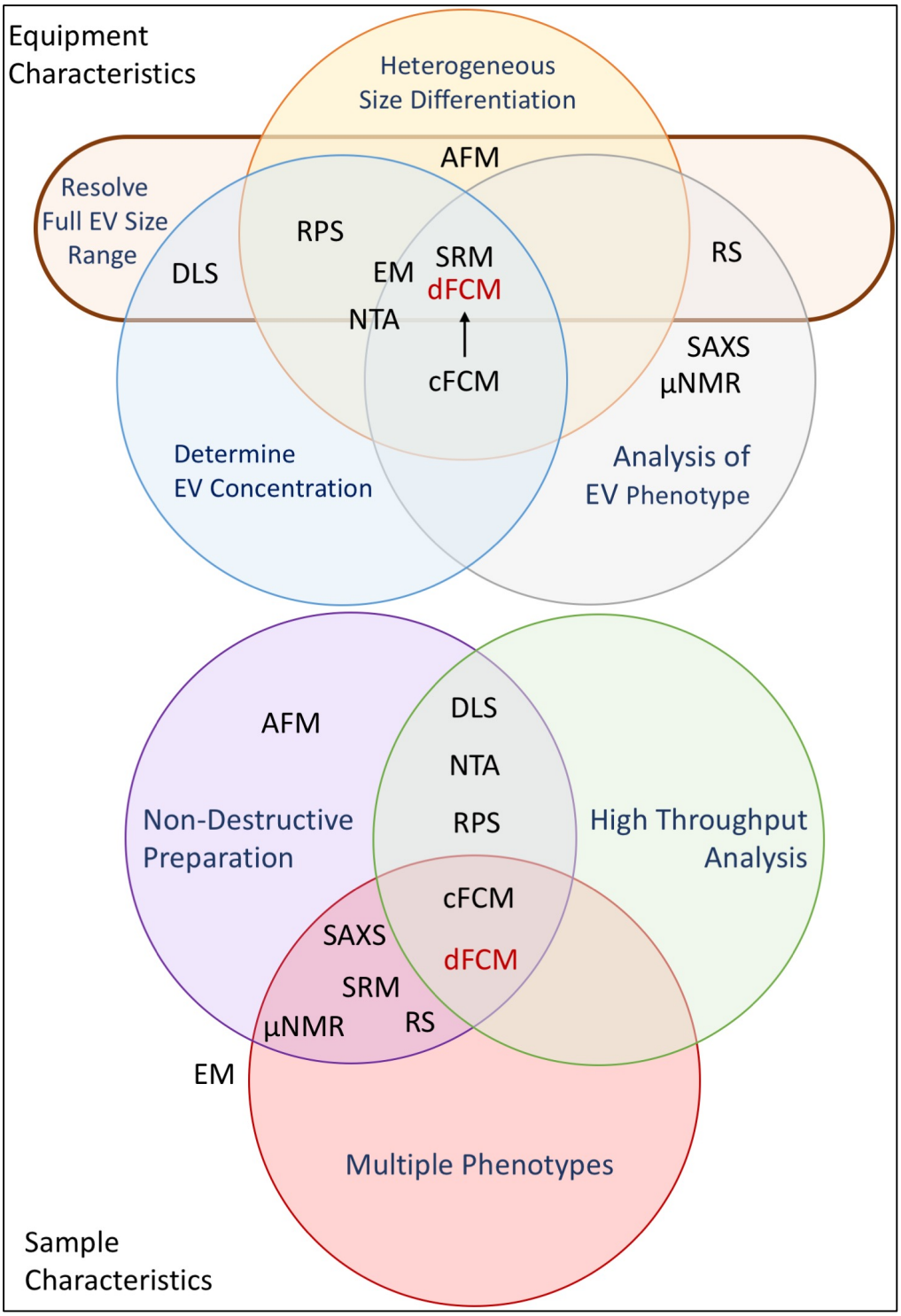

Figure 1.5 | Current EV Detection Equipment.

The top half of the figures shows a Venn diagram of the desired characteristics of ideal piece EV analysis equipment (resolution of full EV population, able to determine EV concentration, and able to analyse phenotypic characteristics). Plotted on the top Venn diagram are the current techniques available for EV analysis, and how they fit into each of the desired categories. The bottom half of the figure shows a Venn diagram of the sample characteristic of piece of the EV analysis equipment mentioned in the top of the figure, these include whether preparation techniques are destructive, whether multiple phenotypes can be gained simultaneously, and if the technique is high-throughput. (dFCM – dedicated flow cytometry, cFCM – conventional flow cytometry, EM – electron microscopy, SRM – super resolution microscopy, RPS – resistive pulse sensing, DLS – dynamic light scatter, NTA – nanoparticle tracking analysis, µNMR - µ-nuclear magnetic resonance, SAXS – small-angle x-ray scattering, RS – Raman spectroscopy.)

1.5.1 Current Detection Methods

1.5.1.1 Super-Resolution Microscopy (SRM)

Optical microscopy has been a cornerstone in the understanding of biology. Its resolution, however, is limited at the small scale (<200nm) by aberration and diffraction, both of which contribute towards the blurring of an image, making two adjacent points indistinguishable from one another. Aberration can be corrected for through expensive optics, however, diffraction is dependent upon the wavelength of light and the aperture of the objective according to Abbe's formula and the Rayleigh criterion. SRM is capable of circumventing these limitations and therefore increasing the resolution. SRM comes in a variety of forms, working in different ways. These include: saturated-structured illumination microscopy (SSIM), stimulated emission depletion (STED) microscopy, reversible saturable optical fluorescence transitions (RESOLFT) and stochastic optical reconstructive microscopy (STORM). These microscopes are capable of resolutions down to 10-30nm and capable of utilising 2-3 fluorescent colours for phenotyping. These microscopes are however expensive, not high throughput, and require relatively long preparation times for samples. While calculating concentrations is possible, it is slow when compared to equipment such as RPS, cFCM and NTA, Figure 1.5.

1.5.1.2 Electron Microscopy (EM)

EM allowed for the discovery of apoptotic vesicles, MV, exosomes and RLVs. Despite being developed in the early 1930s, the developments that have come over the following decades have ensured that the resolution of EM is a gold standard, currently capable of resolving 50pm[122]. Although EM is tough to match in terms of resolution, it does have drawbacks. These include lengthy sample preparation, lack of multi-parametric phenotyping, and low throughput analysis. These characteristics make large studies using EM impractical to run, with EV concentrations being a lengthy process to determine, and phenotypic analysis being very limited, Figure 1.5. Variations of EM exist such as Cryo-EM which allows the imaging of frozen-hydrated specimens at low temperatures, and therefore enables samples to retain their native structure without the need for dyes or fixatives. This high-resolution variation of EM has been useful in showing vesicles morphology, size, limited phenotyping, and concentration[123].

1.5.1.3 Atomic Force Microscopy (AFM)

AFM was invented in 1986, and has an extremely high resolution, at the atomic level[124, 125]. AFM works by measuring forces between a sharp probe (<10nm diameter) and the sample surface. This tip is located on a cantilever, allowing flexibility. AFM is therefore able to provide a three-dimensional surface profile, unlike EM, which provides two-dimensional projections. Sample

preparation for AFM does not require special techniques, unlike EM, therefore avoiding irreversible change or damage to samples. While the resolution of AFM is an advantage, disadvantages include slow scanning speeds, limited image diameters, and the images generated do not represent the true sample topography, but the interaction of the probe with the surface of the sample, Figure 1.5.

1.5.1.4 Dynamic Light Scatter (DLS)

DLS, also known as photon correlation spectroscopy or quasi-elastic light scattering, was developed in 1964[126]. The technique uses the mean diameter, concentration and refractive index (RI) of vesicles to calculate the differential diameter distribution of particles in the range of 1-6000nm[127]. DLS is capable of giving fairly accurate concentrations with a sample of relatively homogenous particle diameters. It is also a user-friendly technique. DLS however suffers from drawbacks due to the way it determines diameter and concentration. Brownian motion causes fluctuations in the scattered light intensity and this is used to determine diameter and concentration. This measurement is easily skewed by the presence of larger diameter particles in heterogeneously distributed samples, and does not have multi-parametric phenotyping capabilities, Figure 1.5.

1.5.1.5 Nanoparticle Tracking Analysis (NTA)

NTA is a light scattering technique also utilising the Brownian motion of individual particles, thus determining speed in a medium, of known temperature and viscosity, allowing the calculation of their diameter. NTA is relatively new to the EV detection field, with studies first utilising it from 2011. NTA is now a commonly used technique that is particularly popular in the EV field studying exosomes. This is because other high-throughput techniques do not have the appropriate resolution for single particle analysis. Whilst NTA allows relatively high throughput, has good resolution with small diameters, and can enable one fluorescent colour, its resolution appears to struggle with polydispersed samples, likely due to Brownian motion being harder to measure in larger particles. As only one fluorescent colour can be used at any one time, phenotyping is also limited, Figure 1.5. Future developments of NTA are working towards multiple fluorescent detection[128].

1.5.1.6 Nuclear Magnetic Resonance (NMR)

NMR measures the degree of sample magnetisation when a magnetic field is applied. Biological samples tend to be negligibly susceptible to magnetisation[129]. Therefore, using magnetic nanoparticles conjugated to antibodies, the presence of antigens of interest exposed on the vesicle can be detected. A form of NMR, known as μNMR is a microfluidic device capable of

measuring large magnetic contrasts between biological samples and magnetic nanoparticles, with the device currently having a detection diameter limited to 50-150nm due to the chamber diameter[130]. NMR is currently limited to the exosome diameter range, is not capable of determining concentration, and has a slow thoughput taking ~1hour per sample. It is however capable of multi-parametric phenotyping using non-destructive sample preparation, Figure 1.5.

Small-Angle X-ray Scattering (SAXS)

SAXS uses elastic scattering (see definitions) of X-ray photons collected at low angles, allowing deduction of structural information from nanomaterial such as plasma membrane thickness, within a diameter range of 1-100nm. Diameter determination can be performed, provided the sample is relatively monodispersed[131]. SAXS equipment powerful enough to detect biological material requires very intense monochromatic X-rays, limiting its use to specialised synchrotron facilities. Multi-parametric phenotyping using SAXS is not possible.

1.5.1.7 Resistive Pulse Sensing (RPS)

RPS utilises the Coulter principle to determine the absolute diameter distribution of particles in suspension in the range of ~50-10,000nm[132-134]. RPS utilised in the EV field, is generally carried out using the qNano (Izon Science Ltd, Christchurch, New Zealand). The qNano consists of two fluid cells separated by a non-conductive membrane. An electric current is passed through a single pore in the membrane. As particles pass through this pore, a transient attenuation of signal occurs that is approximately proportional to the particle volume. This system is calibrated using beads of a known diameter. Sample volumes in the qNano can be as low as 10µL. By applying pressure differences between the fluidic cells, pressure-driven flow overcomes the flow produced by diffusion, electrophoresis and electro-osmosis. The concentration is calculated using beads of a known concentration[135]. Disadvantages of this technique are: multiple pore sizes are required to measure the full EV size range, pores are prone to clogging, little phenotypic information regarding the EV's derivation is gained, and identifying EVs from similar sized contaminants is not possible.

1.5.1.8 Raman Spectroscopy (RS)

RS uses inelastic light scattering (see definitions) properties to study living cell structure and macromolecule chemical composition[136]. Samples are illuminated by a monochromatic laser beam. Energy loss or gains due to particle composition cause light to scatter at varying wavelengths to the illumination wavelength. This wavelength shift is molecule specific, and therefore RS allows label-free sample analysis. Raman micro-spectroscopy has a probe volume of $<1\mu m^3$ and is therefore suitable for EV analysis, with single vesicle analysis capable of being done

due to optical trapping. Though RS is capable of providing phenotypic information, it is not a high-throughput technique and does not allow concentration or diameter differentiation. These disadvantages might be overcome by pairing the technique with a complementary technique, such as RPS or flow cytometry (referred to as Raman cytometry), and these are currently being investigated, Figure 1.5[128, 137, 138].

1.5.1.9 Conventional Flow Cytometry (cFCM)

cFCM was first developed in the 1930s, and comprises three integral systems: fluidics, optics and electronics. Particles are suspended in a fluid stream that is passed through a series of laser beams. Upon illumination, the scattered light from the particles is collected perpendicular to the incident laser beam, as well as just off-centre to the laser beam incident angle. From here the light is fed to photon detectors and signals are further interpreted with a series of electronics. This machinery was, and predominantly still is, designed for cellular analysis (>1µm). FCM is currently one of the most popular techniques used to study extracellular vesicles, in particular microvesicles (MVs), Figure 1.5. The majority of flow cytometers used in studies are however working at their detection limits, as will be covered in depth later in this thesis.

1.5.1.10 Dedicated Flow Cytometry (dFCM)

Currently FCMs that have been developed for dedicated EV analysis, referred to as dedicated FCM (dFCM), have been shown to be capable of resolving particles consistent with biological vesicles to <30nm[139]. dFCM is usually found in the form of cFCMs that have been customised by a laboratory, with only one company (Apogee) advertising explicitly that they can cater for small particle work, and showing this in practice[140, 141]. Fluorescence resolution at the smaller range however remains somewhat of a hurdle.

1.5.2 Summary of Different Technologies for EV Investigation

Selection of the best detection equipment depends upon the EVs of interest and type of data to be collected. What is clear however is that all current detection methods require development in order for the field to develop and contain reliable, reproducible data within and between lab groups. Currently FCM appears to be at the forefront in terms of versatility regarding sample preparation and detection of the majority of EVs, with its main drawback being resolution in terms of sizing and phenotyping down to 20/30nm. Its use currently as a tool for translational EV studies is relatively unrivalled. For these reasons flow cytometry will be the platform for development and analysis of EVs studied in this thesis.

Chapter 2: Introduction to Flow Cytometry

FCM was first developed in the form of a microspectrophotometer in the 1930s, whilst the hydrodynamic focussing of cells to the centre of the stream was developed in the later 1940s[142, 143]. These machines were built to function as cell counters, and were not yet accurate enough to differentiate between cell types or make quantitative measurements. By the early 1960s a haemotology counter integrating fluorescence measurements with light scatter was proposed[144, 145]. By the mid-1960s cell sorters had been demonstrated to work. By the late 1960s fluorescence measurements were introduced into FCMs in order to improve quantitative and qualitative analysis. Cell-sorters working on selective fluorescent measurements, as they do today, were then commercialized in 1974 by Becton-Dickinson (BD). By 1979 BD, Coulter and a division of Johnson & Johnson (Ortho) were producing cFCMs capable of measuring light scatter in the forward and perpendicular direction to the laser, along with fluorescence of at least two different wavelengths, with a throughput of 1000s of events per second. High-throughput quantitative cellular analysis was born. While detection of cells was the main impetus to FCM development, niches of specialised FCM have developed and benefitted from the advancement in cellular analysis. One of these niches is small particle (<1μm) analysis, which is particularly applicable to EV analysis. Despite having been researched in the form of virus detection as early as 1979, it is only in the last decade the incentive for commercial small particle FCM has become apparent[146]. Although many companies are putting resources into developing FCMs for small particle detection, many instruments are compromised in order maintain their cellular analysis capabilities e.g. Gallios W2 (Beckman Coulter, High Wycombe, UK). Currently the only product solely designed for small particle detection is the Apogee series of FCMs. These were first developed in the 1990s by Bio-Rad, intended as bio-warfare agent detectors for the U.S. Army (the A20). The commercial version of this machine (the A30) was however made available to the public. In 2000, Apogee bought Bio-Rad small particle cytometers and has since released the A40 and A50 machines.

2.1 Principles of Conventional Flow Cytometry

Flow cytometry systems are comprised of three integral systems: fluidics, optics and electronics. Particles are suspended in a hydrodynamically focused fluidstream that is passed through a series of lasers beams. Upon illumination, the scattered light from the particles is collected perpendicular to the incident laser beam, as well as just off centre to the laser beam incident angle. From here the light is fed to photo-detectors and signals are further processed with a series of electronics. In detail from sample preparation to data being acquired this proceeds as follows.

Top Down View (Not to scale)

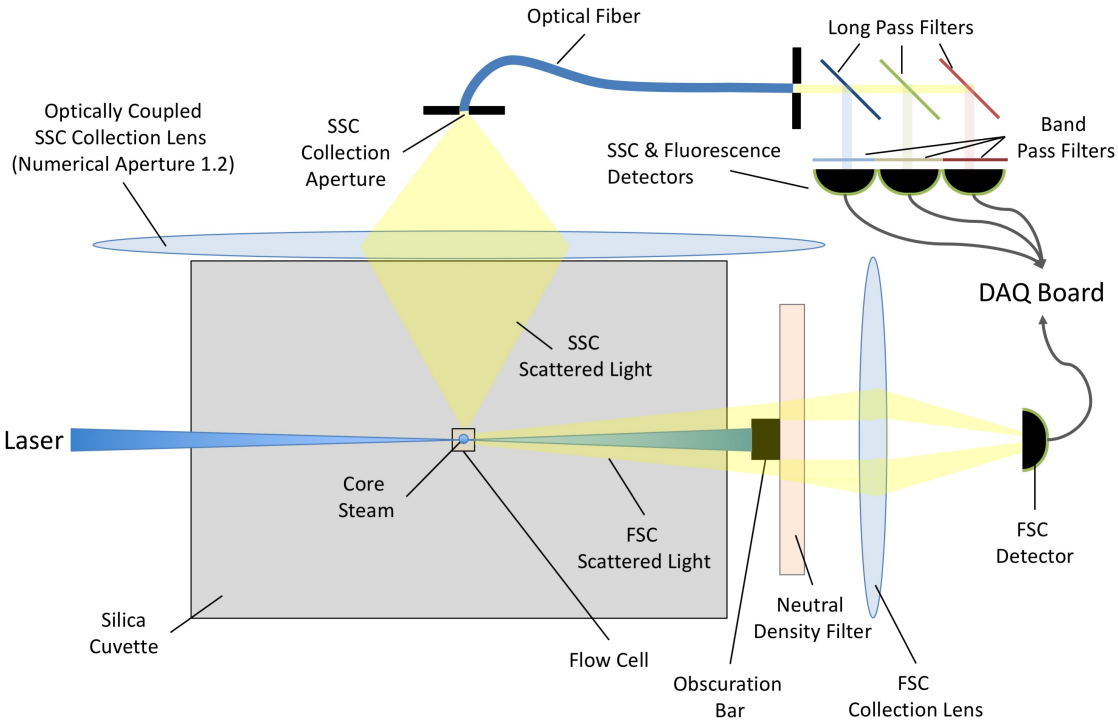

Figure 2.1 | Component Overview of Generic Conventional Flow Cytometer.

The top down view (not to scale) of the flow cytometry components depicts the monochromatic interrogation laser beam traversing through air before reaching the silica cuvette. From the silica cuvette the laser beam reaches the sheath filled flow cell, where the beam reaches its thinnest point at the core stream. The illuminated region of the core stream, where particles are passed through the beam, is known as the interrogation zone. Light scattered from the particles is sent in all directions. The light scattered perpendicular to the laser beam can be seen travelling through the silica cuvette before reaching an optically coupled collection lens. The collected light is then focussed onto a collection aperture, with a fibre optic cable attached. This light is carried to a PMT bank where it passed through a series of long pass filters, to the appropriate detector, which pass on the electrical signals to a digital acquisition (DAQ) board for further analysis. The forward scattered lights is passed through a neutral density filter, before being passed to a focusing lens where the light is focussed onto a FSC detector, in turn passing the electronic information onto the DAQ board. An obscuration bar is placed in front of the FSC collection lens in order to stop the laser beam light saturating the FSC detector, as well as differentiating particle scatter.

- Upon loading a sample tube into a cytometer, the sample enters the sample injection tube (SIT), usually being forced by the increased pressure in the FACS tube. In peristaltic or syringe pump machines, the sample enters the SIT under negative pressure.
- The sample will then pass into the flow cell. In cell sorters there is usually extended tubing between these two points.
- When the sample enters the flow cell, it forms the core stream (Figure 3). The core stream in the majority of flow cytometers is hydrodynamically focused, meaning the core stream's column shape and diameter is a result of its interaction with the high-pressured sheath fluid surrounding it. The relative pressure of the core stream to the sheath fluid will determine the diameter of both. In many cell analysers only the core stream pressure

can be manipulated, typically having pre-sets of low, medium and high, with the sheath fluid pressure being fixed. By having a low core stream pressure, the sheath is able to 'push' against it more, focusing the stream into a thinner column. If the core stream pressure is higher however, it will be more resistant to the sheath pressure and have a wider diameter.

- Upon the sample entering the flow cell, forming the core stream, it passes through a series of focussed laser beams. Cytometers tend to have elliptically focused Gaussian laser beam profiles directed onto the flow cell, with the centre aligned to the centre of the core stream. Gaussian optics are cheaply implemented, when compared to top-hat laser beam profiles which have a consistent laser beam intensity distribution, rather than a Gaussian distribution.
- Detectors are positioned around the flow cell to capture the light scattered from the particles suspended in the core stream. This light travels from the particle, through the suspending sheath, through the silica/quartz flow cell, before being focussed by a collection lens.
    - One of the detectors, located in line with the laser, is called the forward scatter (FS/FSC/FALS) detector. So as not to saturate the detector with the beam of light directly from the laser and to differentiate particle-scattered light, a laser obscuration bar is placed between the flow cell and FSC detector, which the laser is aligned to. The light scattered by a particle, around the obscuration bar, is collected by the FSC detector. To further prevent saturation, the scattered light passes through a neutral density filter (NDF) before hitting the FSC detector. The NDF is not selective of the wavelength of light, and acts purely to decrease light intensity.
    - Placed at 90° to the flow cell is the side scatter (SS, SSC, SALS) detector. The FSC measurement has been related to diameter, whilst the SSC measurement has been related to the granularity/complexity of the particles being detected. While this remains the case for large particles, such as cells, this is not the case for sub-micron particles. In order to observe the evidence for this, modelling must be done of particles of different diameters and refractive indices, as described in Chapter 5:.
- Upon reaching the FSC and SSC detectors, light is carried to a photodiode or photomultiplier tube (PMT) via fibre optic cables, where light scatter signals are then converted into electronic signals. After the sample has passed through the focussed laser beam, the core stream will proceed to the waste tank in a cell analyser, or pushed through a nozzle for cell sorting in a sorter. A basic overview can be seen in Figure 2.1.

2.2 Using Conventional Flow Cytometry for EV Analysis

EV concentrations differ by as much as 300,000 fold between healthy and diseased patients[147]. It is therefore important when undertaking large patient cohort studies to dilute appropriately, in order to reduce errors due to a phenomenon known as swarm detection where several particles, separated in space, are illuminated simultaneously and therefore have their fluorescent characteristics merged into one data point[148]. Although nanoparticle tracking analysis and resistive pulse sensing would seem appropriate methods of determining EV concentration prior to flow cytometric analysis, these techniques have limitations where polydispersed samples are concerned, and particularly struggle with large diameter particles. Currently, dedicated flow cytometry appears to obtain results not too dissimilar from these techniques where concentration is concerned, as well as offering more power in terms of phenotypic analysis and not struggling with the polydispersity of samples[147].

EV phenotyping is a field of emerging interest. As flow cytometry technology has progressed, so too has its application, with labs now starting to use multiple markers in order to characterize cell function. Some labs have been able to characterise 17 fluorescent markers simultaneously[119]. In the case of EVs, this could provide an insight into the phenotype of the parent cell at its generation – acting as a biomarker. Using larger numbers of fluorophores, however, means introducing more rigorous controls and having accurate compensation. Due to the limited surface area of EVs, and therefore limited numbers of each membrane protein bound by antibody-fluorophore conjugate, the staining efficiency of multiple fluorophores is debated. This means that only a portion, if any, of the MV population is detected depending on the FCM used, with diameter and density discrimination at the smaller diameters being inaccurate or impossible. The standards of EV detection also appear to differ. While some labs have stringent gating analysis for multiple events and electronic noise, others have more relaxed protocols and gating. This is particularly important in the case of detecting doublet EVs that are either separated in space or have adhered to one another. These differences result in contradictions within the field and hinder its progress.

MV research tends to utilise flow cytometry, as it is a readily available technique within research institutions, often provided as communal machines. However, this makes permanent alterations to machine settings difficult. Flow cytometry is also capable of providing powerful high throughput, multi-parameter, quantitative analysis, which alternative techniques such as nanoparticle tracking analysis are not yet capable of. The majority of flow cytometers being used, however, are optimised for cell detection rather than submicron particle analysis. While this remains the case, the accuracy of MV analysis using cell-calibrated flow cytometers remains

questionable. There are, however, a number of steps that can be implemented to further improve the analysis of EVs using cell-optimised flow cytometers that shall be discussed.

2.3 Flow Cytometer Resolution

The ideal FCM used for detection of EVs will have a high resolution in order to detect these small particles. Understanding FCM resolution, and making attempts to quantify it, therefore aid in selecting the best FCM available. FCM measurements are based around the detection of light. There are two types of light quantified by flow cytometers: scatter, and fluorescence. When defining the resolution of scatter and fluorescence, scatter can be quantified by determining the smallest particle size capable of detection using FCM, while fluorescence can be quantified by the minimum number of fluorophores that are detectable by the FCM, and how well these can be distinguished from an unstained population.

Methods for quantifying fluorescence resolution, in order to determine the minimum number of fluorescent molecules detectable by a FCM, and the optimum detector settings, are complex. The underpinning methodology relies on utilising a measure of detector efficiency (Q) and background noise (B). This is a large complex topic that will not be reviewed here, but has been described previously[149-155].

Methods for quantifying scatter resolution in absolute terms are not currently available. This is likely due to size and scatter power not having a completely linear relationship to extrapolate from, and to the determination of an extrapolation curve requiring collection angles and geometry to be taken into account. To date, quantifications of the ability of a flow cytometer to distinguish small particles from one another has predominantly been tested by whether it can, or cannot, detect polystyrene beads of increasingly smaller size. Determining the separation between differently sized bead populations has also been used as measure of scatter resolution between instruments[156, 157]. Not only is this inaccurate due to the scatter difference of polystyrene beads compared to biologicals, due to refractive index (RI), but it also does not give any idea of resolution difference between platforms with differing collection optics which will affect the difference in separation of particles with different refractive indices due to possessing different collection geometries [148]. The simplest hypothetical method of determining the ability of a flow cytometer to detect EVs across platforms, is to analyse particles with fixed diameters resembling EV in RI A stable particle of fixed size with a RI resembling an EV across various size ranges has yet to be demonstrated. Novel methods must therefore be developed. While this would enable users to have a yes/no answer as to whether they are able to detect EVs of a specific RI it would not be possible to compare resolution across different FCMs unless there was a way of integrating the

collection optics criteria also, as this would affect how one would extrapolate from the detectable particles to undetectable particles.

A situation where it is appropriate to use polystyrene beads in order to determine and track changes in resolution, is during optimisation of a single flow cytometer. This is, however, restricted to cases where modifications do not alter the scatter collection angle e.g. fluidic optimisation. One would then go about tracking resolution alterations using the separation index (S.I.), Equation 1.

$$S.I. = \frac{\tilde{B} - \tilde{A}}{\sigma_A + \sigma_B}$$

Equation 1 |Separation Index Formula.

A and B denote population measurement in arbitrary units of two different diameters, and the median ($\tilde{A}$, $\tilde{B}$) and standard deviation(σ) refer to their recorded arbitrary units on the parameter of interest. A higher ratio ouput infers a better resolution.

2.4 Flow Cytometer Optimisation

Flow cytometers are complex and expensive pieces of equipment, ranging from ~£50,000-£500,000. Commercial flow cytometers give users very limited access to adjusting the machine parameters, or to technical information, with one being at risk of voiding the warranty if attempting to alter parameters not intended for user modification. The term 'optimizing' from here on shall refer to increasing the analysis accuracy of flow cytometers for:

- EV sizing – quantified in scatter,
- Phenotyping - quantified by fluorescence scatter
- Absolute counts – quantified by fluidic stability.

2.4.1 Optical Optimization

The optics system is arguably the most important component of the flow cytometer to optimize as it determines the amount of scatter by the particle as well as the signal to noise ratio of collected light scatter. The optics system has a large number of components to consider. These include:

1. Laser power, wavelength, beam geometry
2. Flow cell dimensions
3. Sheath noise
4. Cuvette dimensions, composition (RI)
5. Collection lens numerical aperture and placement

6. Collection optics apertures
7. Optical density filter presence
8. Obscuration bar dimensions
9. Collection optics composition
10. Optical filter placement (transmission/reflection)
11. Detector type

Altering any of the above should therefore be considered for the optimisation of the optical system for EV analysis, particularly in terms of resolution. Optimizing these components for EV detection requires quantifying the resolution with acquired data, discussed in section 2.3, as well as with theoretical and standardisation data, introduced in section 6.1.1.

Optimisations made for an EV dedicated FCM would ideally have a continuous increase in scatter power with increases in particle diameter, and no regions of levelling off, or periodic decreases. This would enable a less ambiguous approximation of diameter between particles of interest when comparing them to particles with different diameters and refractive indices. This type of calculation is dependent upon how light is scattered from the particle of interest and how this scattered light is collected. This is predominantly optimised therefore through the flow cell and cuvette dimensions, with some emphasis on the collection lens numerical aperture.

The optimum signal to noise ratio is vital in increasing the resolution to its maximum. This can be done by reducing noise in the system – particularly through filtration of the focussing sheath fluid, where micro precipitants occur, and implementing this filtering as close to the flow cell as possible. Removing optical density filters and deciding on the wavelength filter arrangement will ensure that the maximum number of photons are able to reach the detector. Once the photons have reached the detector, the selection of detector becomes important, so as to be optimally sensitive for the particular wavelength of light being measured.

2.4.2 Electronic Optimization

Flow cytometer detectors convert collected photons into electronic signals, which are in turn converted to digital data. A particle scatters photons when passing through the laser beam. This scattered light is focused by a lens onto a fibre optic cable. From the fibre optic cable, the light is separated in wavelength by optical filters, directing wavelengths of choice to different detectors. Light hitting the detector generating an electronic pulse, undergoes a series of amplifications before undergoing quantization at the analogue-to-digital (ADC) converter. The ADC resolution in bits defines the dynamic range of the system. Many current cytometers have a resolution of 18bits, this means the arbitrary scale will contain 2^{18} channels (262,144). The electronic signal

pulse represents the particle's scatter, be it fluorescence or not, in the form of a height (H), width (W) and area (A) parameter. These can be seen in Figure 2.2.

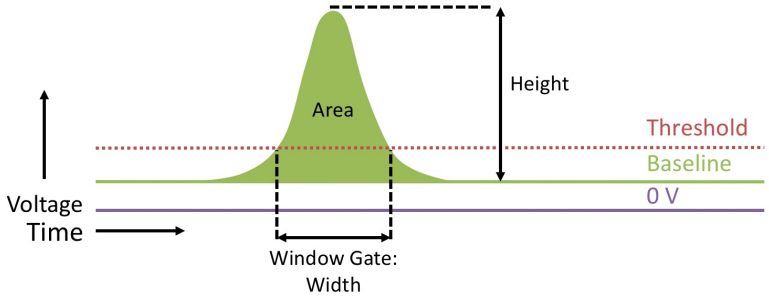

Figure 2.2 | Shows the electronic signal of one event in a flow cytometry system.

Pictured is a pulse from a single sample event, with the overall width representing the time spent in the laser, and the height being the intensity of light reaching the detector. The green baseline line represents no events at a set voltage, with the purple line representing the detector having a voltage of 0V. The red threshold line represents the arbitrary threshold unit setting, with the green pulse area event above this line being recorded. Events below the red line are not recorded.

The electronic aspect of the flow cytometer is one of the harder areas to adjust on both conventional and dedicated flow cytometers. Adjustments such as sampling rate and raw event rate analysis are often tied into complex software that is not easily altered without knock-on effects. Component aspects that should be considered for electronic optimisation include detector type and ADC. Software electronic optimisations to consider include window extensions, laser delays, sampling rates, and gating strategies.

2.4.2.1 Window Extension & Laser Delays

The time interval for which the pulse is above the set system threshold is referred to as the window gate (WG), Figure 2.3. However, to ensure that the pulse is properly integrated by the system, a set amount of time can be allocated on either side of the window gate, referred to as the window extension (WE). The WE is usually in the region of 3-5µs on either side of the window gate, depending on the core stream velocity, and ensures only single events are detected. When double peaks are detected in the WE the event will be aborted (not recorded). Having an inappropriate window extension setting can lead to incorrect data analysis.

Although accurate sample acquisition is a priority, accurate analysis of the results is equally important. Submicron particle analysis differs to that of conventional flow cytometry analysis in terms of parameters used for gating and scales used on certain parameters.

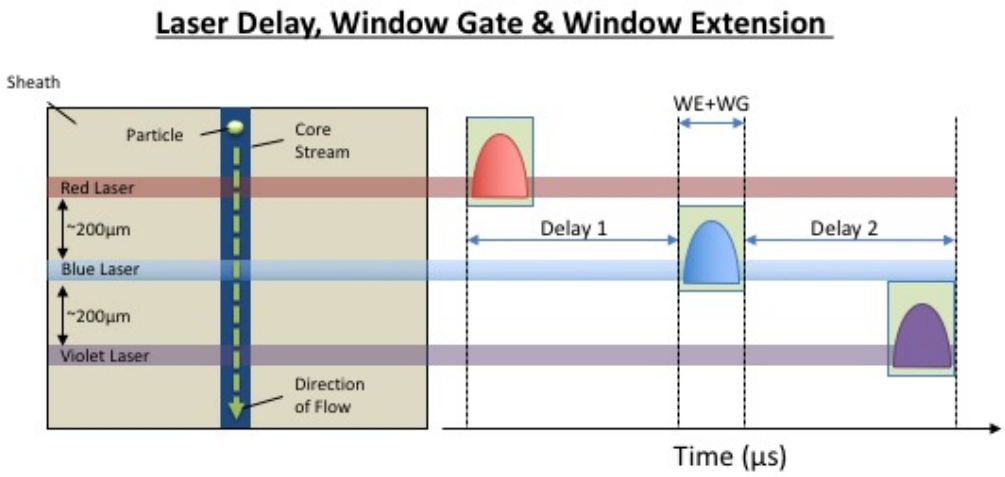

Figure 2.3 | Diagram outlining the laser delays as well as window gate (WG) and window extension (WE).

The left-hand side of the figure shows a particle travelling through the core stream, with its trajectory intercepting the lasers shown by the green dashed line.

2.4.2.2 Gating Strategies

Due to the large difference in diameter between the interrogation zone and EVs, multiple events entering this zone at the same time is to a certain extent unavoidable. However, its incidence can be significantly reduced through dilution, and by reducing the diameter of the interrogation zone through smaller laser beam spot diameters and smaller core stream diameters. It is therefore important that multiple events that do occur are excluded from data analysis. Singlet gates to a great extent are capable of doing this post analysis. This can be done by gating fluorescent events, ideally with a universal EV marker, then viewing them in SSC-H vs. SSC-A, Figure 2.4. A singlet gate that follows the area scaling linearly can then be drawn. This will exclude the doublet/swarm events, shown with an arrow in Figure 2.4. All subsequent gates would then be a subgates of the singlet gate.

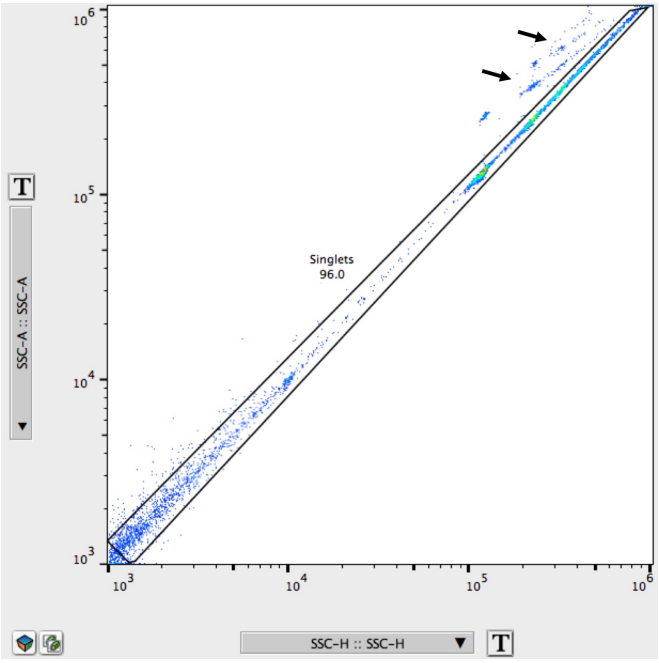

Figure 2.4 | Singlet gating using SSC-H to SSC-A plots.

The figure shows non-fluorescent sample of platelet poor plasma, acquired at a low flow rate on a Fortessa X-20. A singlet gate has been drawn using the SSC-H vs. SSC-A parameters, with a linear correlation show for events that fit inside the singlet gate. Aggregated, or swarm events appear outside of this gate, highlighted by blue arrows.

Gating on area takes diameter into account, since larger particles will spend slightly longer in the interrogation zone, generating a longer width and higher height, therefore biasing diameter, Figure 2.5. So as not to bias diameter only the height parameter (which is the strongest signal) should be used to gate scatter for submicron particles, unlike cellular analysis, which uses area.

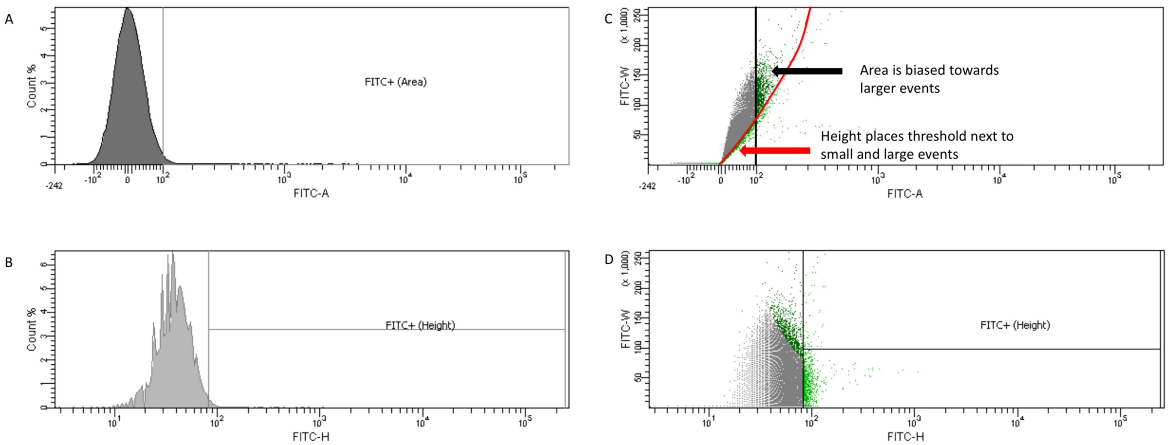

Figure 2.5 | Diagram outlining the difference between gating on a parameters area rather than height.

The figures show analysis of a non-fluorescent sample acquired at a low flow rate on a FACSAria. A) shows gating of non-fluorescent sample on FITC-A at 99.95% of the population. B) shows gating of non-fluorescent sample on FITC-H at 99.95% of the populations. C) shows a FITC pulse area to width dot-plot, with dark green events highlighting, 0.05% FITC-A positive events, while light green events highlight 0.05% FITC-H positive events. The height to area correlation with width is shown in red. D) shows a FITC pulse height to width dot-plot, with dark green events highlighting, 0.05% FITC-A positive events, while light green events highlight 0.05% FITC-H positive events.

2.4.3 Fluidic Optimization

The fluidic system is arguably the simplest system in terms of function. It is required to carry a sample from a receptacle to the interrogation zone, before being carried to a waste tank or sorted into another receptacle. An outer sheath fluid under pressure focuses an inner stream (core stream). This is known as hydrodynamic focussing. The illuminated region of the core stream is the interrogation zone of the flow cytometer. Its diameter determines how many particles are capable of fitting in this zone at once. Although reducing the laser beam waist can reduce the interrogation zone volume, one of the easiest ways is by reducing the core stream diameter. Despite its relative simplicity, the fluidic component of the flow cytometer is one of the most difficult to optimise for submicron particles. Its optimisation however, is vital for EV detection and accurate concentration determination.

2.4.3.1 Enumeration of Core Stream Flow Rate

Due to the role of EVs being poorly understood, translational medicine has focused on quantifying EVs in terms of counts. A relative count can be determined by recording markers of interest, providing the ratio of one phenotype to another. However, this does not provide an absolute count, due to issues such as whether a particular phenotype has increased or decreased relative to another. An absolute count requires flow rate measurement, which can be used to deduce sample concentrations.

Some flow cytometers are capable of determining particle concentration due to having syringe or peristaltic pumps. The accuracy of pumps for quantification is, however, limited by the tolerances of the components. Prior to pumps being integrated into flow cytometers, many counts were done using a known concentration of beads. These beads could be mixed with a sample to determine its concentration. These beads however are generally >4μm, and have a number of flaws, particularly when enumerating sub-micron particles, such as EVs.

When using a bead based enumeration method, one has to assume that the beads are homogenously dispersed within the sample, and that none have aggregated. When samples are run at too high a concentration, swarm detection, and event aborts become more frequent. All event aborts affect EV quantification; if bead events were electronically aborted, however, the absolute count is significantly more skewed than if a single sample event were aborted. It is not however possible to know what event was aborted. Aggregated populations of beads can occur either due to the beads sticking to one another, or through simultaneous detection of closely spaced beads. Even a few of these occurring can have large knock-on effects on the absolute count calculation, which also depends on how a research group chooses to interpret the data.

Along with their other flaws, calibration beads are also particularly expensive for studies with large sample numbers. A cheaper alternative is to determine the core stream flow rate at intervals throughout an experiment and then use an average to calculate the EV concentrations. This can be done with beads or spectroscopic dyes. When using beads to determine flow rate, even if beads were perfectly dispersed in the sample and no electronic aborts occurred, it would still have to be assumed that there were no fluctuations in the flow rate. There will always be fluctuations in flow rates however, and so the accuracy of this type of calculation will be dependent upon the tolerances of the flow rate.

The outer sheath and inner core stream should ideally be of matching constituents and RI, reducing noise and laser beam aberrations. The inner core stream should be kept at a consistent flow rate, allowing for accurate concentration calculation, with a fairly low velocity so as to extend particle duration in the interrogation zone, and of small diameter, so as to reduce the likelihood of multiple particles in the interrogation zone. As the largest EVs of interest (MVs) have an upper limit of 1000nm the core stream diameter need not be much higher than this, ideally ~1.5µm. The optimum velocity and tolerance of flow rate is something that must be established.

As well as establishing a core stream diameter that is both small and highly stable for quantification, the fluidics themselves ideally need to have a small surface area between the sample receptacle and the flow cell, with highly hydrophobic surfaces, so as to avoid sample particles sticking to the inner tubing, and skewing concentrations as well as contaminating other sample analysis.

In conclusion, it can be seen that a variety of factors need to be accounted for before attempting small particle FCM analysis. The detection efficiency of the system can also be improved using a number of methods.

Chapter 3: Thesis Objectives

It can be seen from the previous chapters that current technologies and methodologies cannot adequately count or phenotype EVs. The following chapters will describe improvements made to FCM in order to increase detection capabilities and data reliability, before validating and applying these methods to clinical sample analysis. The specific objectives for each chapter are as follows:

Chapter 4: Quantifying Flow Cytometer Resolution Using Separation Index

- To investigate how separation index varies across FCM platforms
- To investigate how separation index can be utilised in order to track resolution increases from FCM optimisation

Chapter 5: Understanding the Relationship between Small Particle Diameter and the Amplitude of Collected Light Scatter in Flow Cytometry Systems

- To understand how single EVs of varying size scatter light.
- To understand how collection geometry affects the relationship between total collected scatter amplitude and diameter.

Chapter 6: Implementing Mie Scatter Modelling as a Standardisation Technique for EV Analysis

- To investigate Mie theory as a standardisation technique for the EV field, with comparisons to previous standardisation attempts across multiple cFCM platforms.
- To develop Mie theory as a standardisation technique that is accessible without the need for proprietary information, geometric data and component refractive indices.
- To compare developed standardisation techniques.
- To validate Mie theory as a standardisation technique by using a staining assay that differentiates between EV subsets.

Chapter 7: Conventional Flow Cytometer Optimisation for EV Analysis

- To optimise optical, fluidic and electronics systems in cFCMs for EV analysis in order to produce higher optical resolution instruments, with increase counting accuracy.
- To develop method of enumerating vesicles using cell sorters, via core stream quantification

Chapter 8: Effect of Conventional Flow Cytometer Optimisation on Clinical EV Sample Acquisition

- To compare non-optimised EV analysis protocols, with an optimised protocol in order to understand the benefits of optimisation on analysis accuracy.

Chapter 9: Clinical EV Sample Analysis: Non-Alcoholic Fatty Liver Disease

- To investigate the potential of platelet, endothelial and leukocyte EVs as novel biomarkers in non-alcoholic liver disease, utilising modelling and optimisation steps developed previously, and a biobank of clinical samples.

Chapter 4: Quantifying Flow Cytometer Resolution Using Separation Index

4.1 Introduction

An ISTH initiative initially aiming to improve standardisation within the EV field resulted in a particular set of fluorescent polystyrene beads being produced, 'Megamix' beads. These beads have since become a source of contention as accumulating evidence suggests these beads relate to different biological sized populations on different flow cytometers (FCMs)[140, 158, 159].

Megamix beads have been used to determine resolution on flow cytometers using separation index. A high separation index score infers a better separation between the two different diameter ranges being compared, whilst a lower score infers worse separation between the two diameter ranges under comparison. For fluorescently labelled spheres the relationship between particle diameter and fluorescent intensity, assuming all particles are saturated with fluorophore, would be linear on a $\log_{10}$ scale as it is showing the relationship between particle surface area (how many fluorophores can fit on its surface) and diameter. This relationship is consistent across FCMs, and can therefore be used as a form of quantifying the fluorescent resolution of FCMs. For separation index to be used as a comparable quantitative method of determining the scatter signal resolution between FCMs, all particles must either scatter light isotropically, or the normalisation for FCM collection angle with each particle's angular scattering distribution must be taken into account.

Here we investigated how separation index compares across conventional FCM (cFCM) platforms, and how it can be implemented in a useful manner for EV research. Since normalisation is not used, and scatter is not isotropic across all diameters, I hypothesize separation index scores to be inconsistent with the lowest particle detectable.

4.2 Method & Results

4.2.1 Resolution Quantification of cFCMs Using Separation Index

System resolution of sub-micron particles using separation index shall be tested. Flow cytometer resolution has previously been quantified in terms of its ability to detect and resolve fluorescent polystyrene beads, and the separation index between these beads. This type of resolution

quantification was undertaken as a baseline on cytometers before more advanced resolution modelling was conducted (Chapter 5:Chapter 6:), acting as a comparison.

4.2.1.1 Bead Acquisition and Separation Index Calculation

SSC and FSC separation indices (see Section 2.3 for equation) were calculated in multiple cFCM systems by analysing fluorescent polystyrene beads of 100, 300, 500, 900nm (Megmix Plus FSC, Biocytex, France). Separation index was calculated between adjacent bead populations. All beads were acquired at the system's lowest attainable flow rate, with 10,000 bead events being acquired. FCM threshold settings differed between FSC and SSC depending upon the cFCM.

4.2.1.2 Result of Separation Index Calculation Across FCM Platforms

A comparison of obtained SSC separation indices can be seen in Figure 4.1, with a comparison of FSC separation indices seen in Figure 4.2. The acquisition of the same polystyrene bead populations in a variety of flow cytometers yielded very different results. Inter-comparisons of machines shows that having a low separation index with a larger diameter bead population i.e. 500-900nm, compared to another cytometer, does not diminish its ability to detect a smaller diameter bead populations i.e. 100-300nm, Figure 4.1. In the case of the Attune NxT, it has a separation index of <5 for the 500-900nm population, whereas the Aria and Gallios W2 have separation indices of >5 for this population. However, the Attune NxT has a separation index of 8.6 for the 100-300nm population, while Gallios W2 has a separation index of 2, and Aria was unable to detect the 100nm population at all, Figure 4.1. The separation index alone does not therefore appear to confer directly to cytometer resolution. It can be seen that generally cytometers with high separation index units for their SSC resolution, have a low FSC resolution, in terms of separation index units, and vice versa.

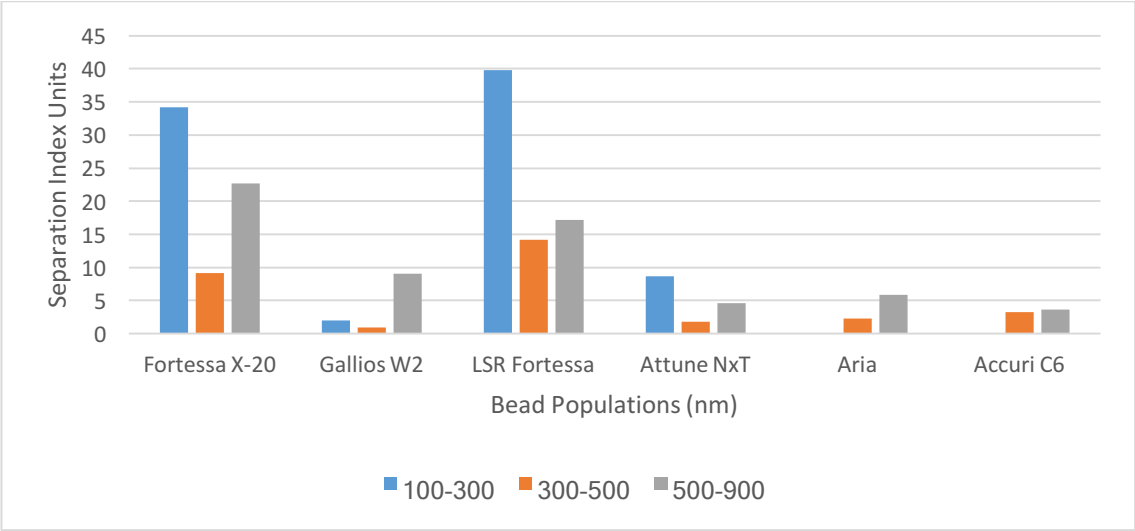

Figure 4.1 | SSC Resolution Quantification in Various Conventional Flow Cytometers using Separation Index and Sub-Micron Fluorescent Polystyrene Beads.

Shown are the calculated SSC separation index for Megamix Plus FSC beads acquired on the Fortessa X-20, Gallios W2, LSR Fortessa, Attune NxT, FACSAria, and Accuri C6.

It can be seen that flow cytometry platforms even with the same optical component geometries (Fortessa X-20 and LSR Fortessa) show different separation indices. This could be due to a number of factors including: variation in alignment of lasers and collection apertures, differing illumination intensities, quality of photomultiplier tubes, and more.

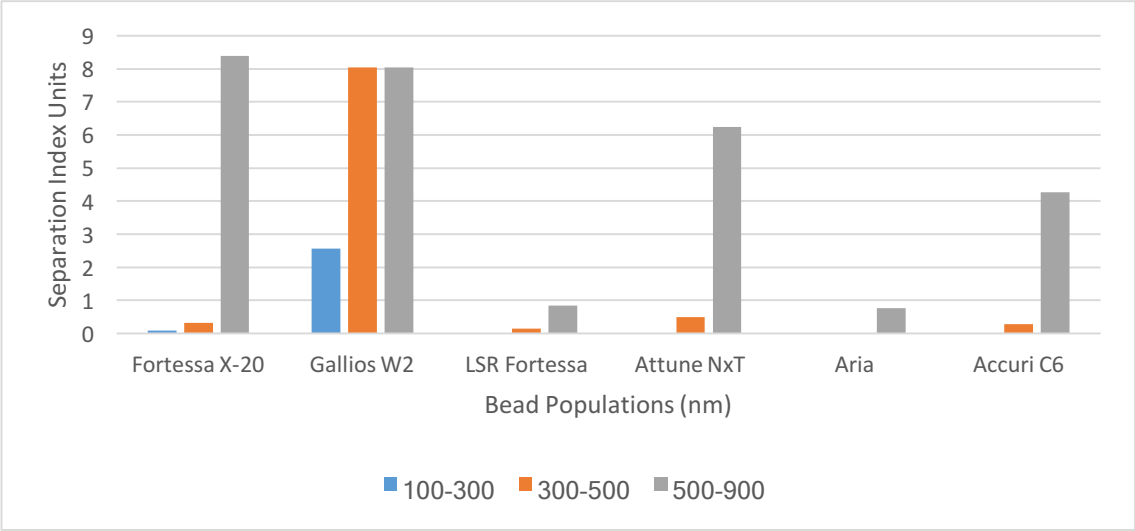

Figure 4.2 | FSC Resolution Quantification in Various Conventional Flow Cytometers using Separation Index and Submicron Fluorescent Beads.

Shown are the calculated SSC separation index for Megamix Plus FSC beads acquired on the Fortessa X-20, Gallios W2, LSR Fortessa, Attune NxT, FACSAria, and Accuri C6.

In conclusion, while it could be assumed at a glance the LSR Fortessa has the highest SSC resolution, and the Gallios W2 has the highest FSC, due to each having the highest separation indices when compared to other FCMs. When looking more closely it can be seen that a high separation index for one set of bead diameter populations does not confer to increasingly smaller

bead diameter separation indices. It is therefore reasonable to assume that these beads are not scattering light isotropically, and the collection angles across machines are not identical. Therefore, assumptions about comparative resolution cannot be made, a method taking into account angular scatter distribution for each particle along with the collection angle of each cytometer must be taken into account in order to have a comparable method of comparing cytometer resolution.

4.2.2 Tracking FCM Resolution Increases Using Separation Index

Flow cytometer collection fibres have oversized circular collection apertures when compared to the rectangular focal spot size of the focussed illuminated flow cell. This accounts for the multi-element lens correction not being perfect and therefore accommodating a higher average fluorescence resolution across a large wavelength range i.e. 405-800nm. Here we tested the effect of slit apertures on SSC (488nm) signal resolution of different sized fluorescent beads.

4.2.2.1 Effect of Optical Density (OD) Filter Removal on SSC Separation Index

Megamix Plus FSC and Megamix Plus SSC Beads were mixed in a 1:1 ratio, and acquired at a low flow rate on an 'Attune NxT Custom Modified for Small Particles'. Separation index units were calculated, and also converted to a percentage change compared to baseline, Figure 4.3. The SSC OD2 results were used as baseline, due to the filter being a standard setting in the Attune NxT.

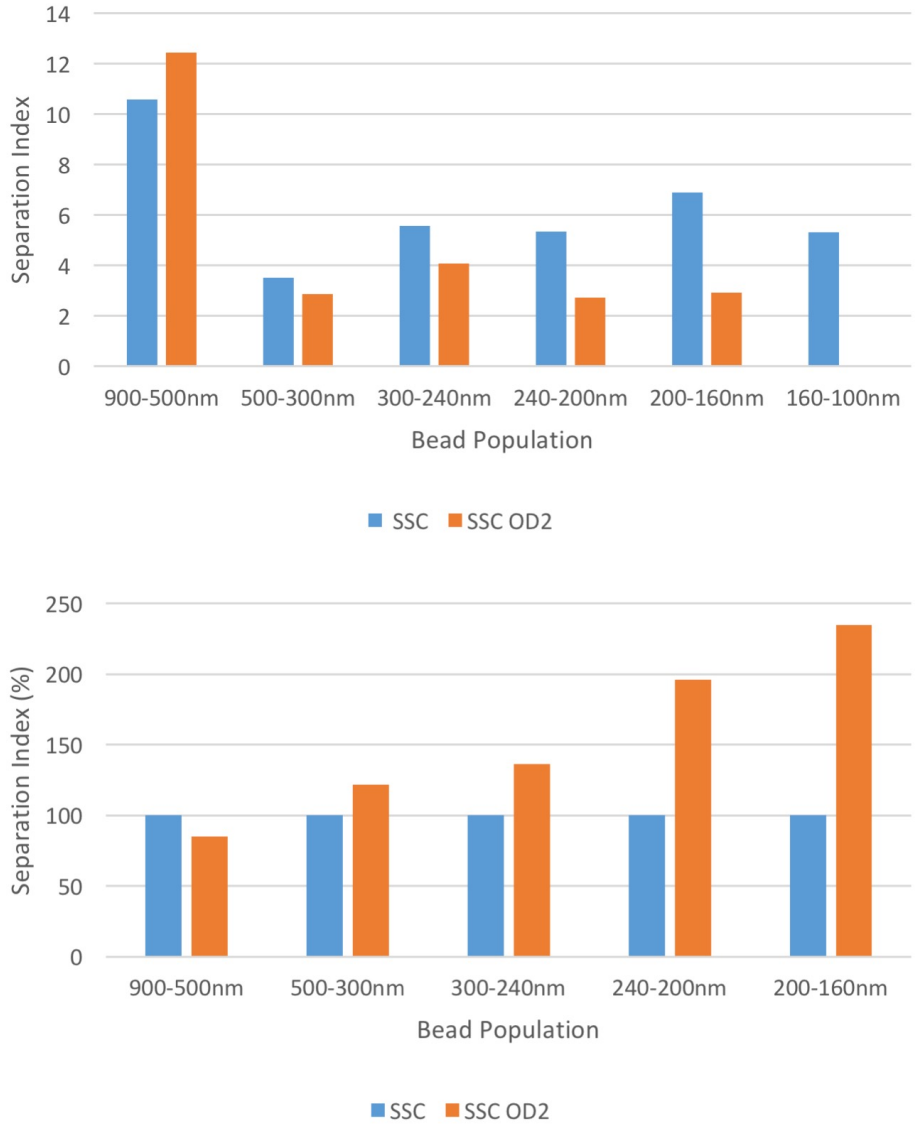

Figure 4.3 | Change in Separation Index Units (Top) and as a Percentage (Bottom) with and without OD2 SSC Filter.

Shown are the calculated SSC separation index for Megamix Plus FSC beads acquired on the Attune NxT with a SSC OD0 and SSC OD2 filter.

It can be seen that the removal of the OD2 SSC filter increases resolution for all bead populations, with the exception of the largest bead population 900-500nm, Figure 4.3. Furthermore, the separation index as a percentage change from baseline, shows that the smaller the bead population is, the greater benefit is gained from removing the OD2 filter. Its placement in cFCMs is due to a number of reasons: limiting saturation of the SSC detection, not requiring high scatter resolution for cells and therefore providing a higher dynamic range to cell types e.g. platelets, monocytes, and granulocytes analysis simultaneously.

4.2.2.2 Slit Modification, Bead Acquisition and Separation Index Calculation

FCM systems have oversized collection optical fibres in order to account for the differing focal points of different wavelengths of light, as well as making alignment easier. These however both

add noise, due to stray light being collected. This is less of an issue for cellular analysis which have much higher signals than EVs. We attempted to fine-tune a FCM system by using increasingly smaller slit apertures to block out background noise, and gain a better signal-to-noise ratio for the SSC parameter.

The naked optical fibres 950µm diameter along with slit apertures of 450µm and 200µm were tested on an 'Attune NxT Custom Modified for Small Particles'. The 200µm aperture was placed on first. The optimum position was found by running Megamix Plus FSC beads, gated on FSC and moving the collection optics forwards and backwards until the highest signal was achieved from the Megamix beads. When this position was found the collection optics were screwed into place. Megamix data was recorded and the other aperture diameters were then tested. Beads were all acquired at a low flow rate.

4.2.2.3 Effect of Slit Size on SSC Separation Index

The 450µm and 200µm apertures both result in higher separation indexes than the open 950µm collection aperture, for all 3 populations of polystyrene beads being compared, Figure 4.4.The 200µm aperture provides the highest separation index for the smallest bead populations (300-100nm), while the 450µm aperture provides the highest separation index for the largest of the 3 bead populations (900-500nm), though only by a small margin compared to the 200µm aperture. The 200µm aperture therefore appears to be optimal for small particle acquisition.

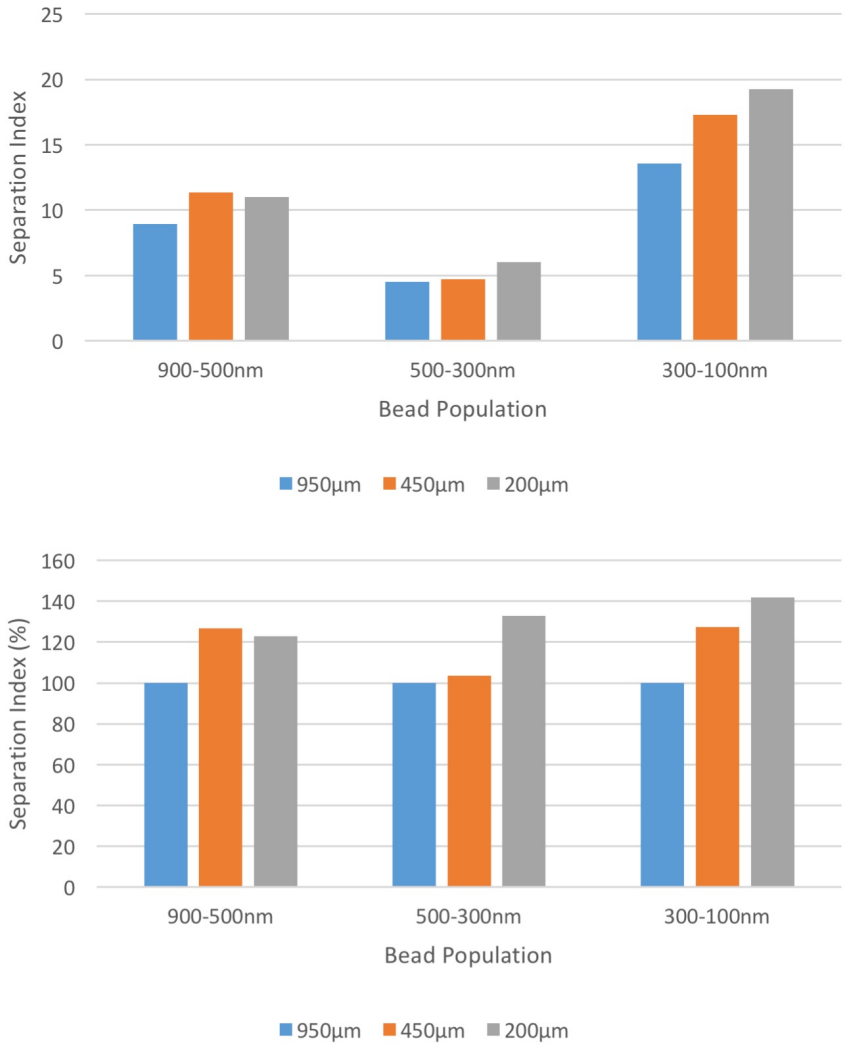

Figure 4.4 | Slit Aperture Testing of Attune NxT Optics using Separation Index Units (Top) and Percentage (Bottom) to show Resolution Changes.

Shown are the calculated SSC separation index for Megamix Plus FSC beads acquired on the Attune NxT with an open aperture (950µm), 450µm and 200µm slit apertures.

4.3 Conclusion

Testing of separation index across cFCM platforms shows that each has very different resolutions of the bead populations, whether it be FSC or SSC. Knowing how collection amplitude varies for small particles due to the collection geometry (refer to Chapter 4:) these values cannot be taken at face value, unless the relationship between diameter and scatter amplitude is taken into account in each system. This is because the collection geometry creates an intrinsic maximum separation distance between different sized populations, due to different scatter powers being collected for each particle depending on the collection angle (investigated in Chapter 5:). This is unlike fluorescence which has a linear correlation between surface area fluorescence intensity (assuming saturated) and particle diameter. It can be seen however that separation index can be a useful tool when collection geometry is fixed and modifications are made, as seen with the OD2 filter removal, and slit aperture placement.

Separation index calculation and detection of beads across platforms is therefore not a fair test and development of standardisation tools are required. A method of standardisation accounting for angular scatter distribution and collection geometry will therefore be investigated next.

Chapter 5: Understanding the Relationship between Small Particle Diameter and the Amplitude of Collected Light Scatter in Flow Cytometry Systems

5.1 Introduction

FCM systems are based around the detection of a particle's scattered light. As seen in the previous Chapter the collection angle and angular scattering distribution of particles must be taken into account in order to compare FCM scatter resolution.

Therefore, here I start by understanding the angular scattering distribution of particles with varying size and composition. Once this type of small particle scatter is understood, the collection of this scatter in a FCM – with particular regard to how the total collected scatter amplitude changes with size will be investigated. In order to accomplish both of these goals, a model of particle scatter must be constructed.

5.1.1 Parameters to Model

A model must be built in order to standardisation particle angular scattering distribution and the FCM scatter collection angle. This model would also enable the calculation of theoretic flow cytometer optimisations regarding scatter collection angles and therefore component geometries e.g. flow cells. Inputs and outputs of this model will include:

Inputs:

- Formation of sphere (coated/homogenous)
- Diameter of sphere
- RI of sphere
- Collection geometry (circular/rectangular)

Outputs

- Angular scattering distribution in horizontal plane of spheres
- Collected light scatter from homogenous and coated spheres in three dimensions for varying collection angles and geometries

These outputs will serve to allow visualisation of a coated sphere (a sphere with one RI surround by a layer with a second RI, such as the cytosol, and membrane), and homogenous sphere's angular light scatter distribution. This will provide an understanding of how particles in the EV diameter range which are below, around, and above the illuminating wavelength vary in the way they scatter light, Figure 5.1. From here, the FCM collection limiting angle based on its component geometry will be investigated, to see the effect it has on the relationship between diameter. From here, the basis for testing particles of a known diameter and RI, within a system of known dimensions can be investigated (see Chapter 6:). This will serve to see how well the theory relates to the reality, and whether RI can be accounted for within these systems. This in turn should be able act as a standardisation method for EV analysis, due to EVs having a lower, more complex RI that changes with size due to being a coated sphere (membrane shell, cytosolic interior) compared to the homogenous polystyrene and silica particles which to date have been used.

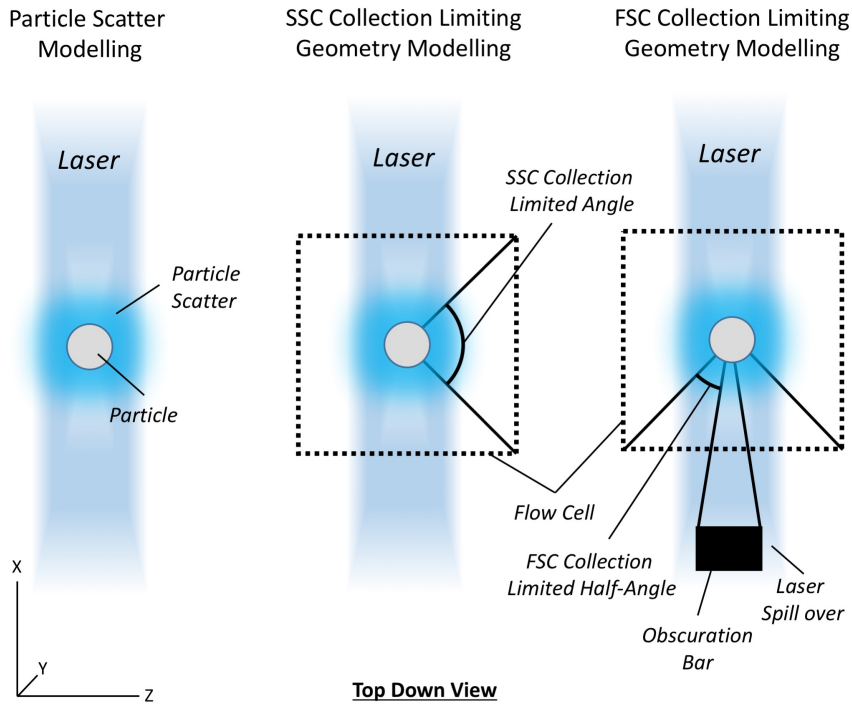

Figure 5.1 | Modelling Objectives.

Particle scatter modelling shows a particle illuminated by a laser beam, scattering light in all directions. SSC collection limited geometry modelling shows a particle being illuminated in a laser beam, with the outline of a flow cell, with the SSC collection limited angle highlighted. FSC collection limited geometry modelling shows a particle again being illuminated in a laser beam, with the outline of a flow cell, with the FSC collection limited angle highlighted as the angle between the obscuration bar and flow cell limit. Laser spill-over around the obscuration bar is also highlighted.

5.1.2 Selecting a Suitable Model

The model outputs listed in Section 5.1.1, require a model capable of predicting light scatter from spheres of different refractive indices, with total and limited collection angles, in both a rectangular and circular fashion.

5.1.2.1 Rayleigh Scatter

Rayleigh scattering theory was developed over a period of decades by Lord Rayleigh in the late 19th Century, and is an approximation of elastic light scatter for very small particles. This theory of light scatter requires the radius of particle to be significantly smaller than the wavelength. Flow cytometry uses monochromatic lasers with FSC and SSC generally collected at 488nm. Using a non-dimensional diameter parameter (x) of one, with a wavelength (λ) of 488nm, particles with a radius (r) of 75nm (x=1), and above, would therefore not be suitable for the total diameter range of EVs. The non-dimensional diameter parameter can be calculated using the equation: $\frac{2\pi r}{\lambda}$. When considering the microscopic density fluctuations in liquids however Rayleigh scatter is an ideal choice and could potentially be used to investigate system noise from sheath and combined with laser beam spill to calculate the ideal obscuration bar size in a particular FCM.

5.1.2.2 Mie Theory

Mie theory was first published in 1908 by Gustav Mie, and is based up on predicting the amount of light scatter derived from a spherical particle being illuminated[160]. This theory, based on the Maxwell equations, was first applied to relating particle diameter using flow cytometry in 2003; and translated to EV detection in 2012[148]. Using the Maxwell equations, it is possible to derive the incident, scatter, and internal fields. Rayleigh scatter as originally formulated applies to small spherical, non-absorbing particles, whereas Mie theory applies to both absorbing and non-absorbing particles, and does not have a cap on spherical diameter. This type of modelling is therefore suited to modelling the full range of EV.

5.1.3 Summary of Scatter Resolution Quantification Investigation

Before a novel modelling technique is approached, the current methodologies of using separation index will first be implemented to serve as a comparison with models[158] . Modelling of particle light scatter will then be done, giving an insight into how scatter varies with diameter. Understanding how changing the collection angle and geometry of scattered light will then be investigated to examine the correlation between diameter and light scatter.

5.2 Methods & Results

5.2.1 Model Selection Process of System and Small Particle Modelling

A model was built in MATLAB to quantify the collected light from a particle of known size and RI within a flow cytometry system with a known collection angle and geometry, Figure 5.2. Due to the extremes of collection being either, a rectangle due to slit apertures and/or component limitation geometry, or circular due to light being focussed onto a naked optical fibre, two variations of the same model were built. Scripts were based on those by Matzler[161], and further edited by Dr. Peter Horak to account for circular and rectangular collection geometries, Figure 5.2. Input parameters were modified by J. Welsh to account for the particular system/application being modelled. Input parameters needing consideration within these models included:

- Flow cell geometry & RI
- Cuvette geometry & RI
- Collection lens presence, distance, numerical aperture (N.A.)
- Obscuration bar geometry, distance
- Collection limiting angle determination
- Slit aperture presence
- Homogenous sphere, diameter, RI
- Coated sphere, diameters, RIs
- Laser illumination intensity, wavelength, divergence
- Suspending medium RI

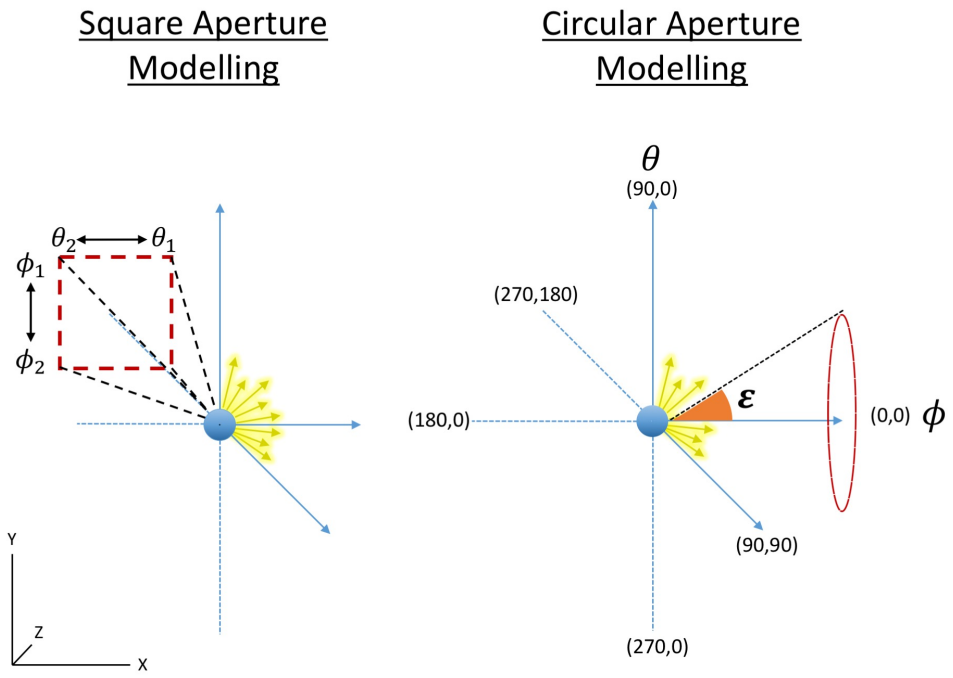

Figure 5.2 | Overview of Rectangular & Circular Aperture Model Inputs.

Rectangular aperture modelling (left) had 4 parameters. ϕ_1 & ϕ_2 increases/decreases particle collection angle range around the circumference of illumination input, whilst θ_1 & θ_2 increases/decreases the collection angle range around the cross-sectional plane of the particle. Circular aperture modelling (right) had 3 parameters. ϕ altered the direction of the collection geometry in line with the illumination source, whilst θ altered the collection direction around the circumference of the illumination source, ε increased/decreases the collection half-angle range of the circular aperture collection in the given direction of θ & ϕ. Apertures geometry is highlighted in red.

5.2.2 Mie Theory Modelling of Small Particle Scatter

The optimisation of FCM for small particles, particularly with regard to light scatter collection, requires an understanding of the relationship between small particles of varying diameters and refractive indices, and visualising how the light scatter they produce, with regard to relative amplitude and spatial distribution differs.

5.2.2.1 Model Design for Small Particle Scattering

Mie scatter was used to predict the light scatter cross-section, Figure 5.3, for 100, 250, 500, & 1000nm EV diameters, using the input parameters seen in Table 5.1, which resemble that of a conventional FCM. This model determined light scatter amplitude of each particle in 0.5° increments from 0° to 180° (0°=incoming laser direction), and assumed to be illuminated by a laser wavelength and intensity found within a conventional cytometer, Figure 5.4. This gave a relative amplitude of light scatter between different diameter particles. The same was repeated, however the maximum scatter amplitude reached for angles 0-180° was used as a denominator for all other angles. This normalised particle scatter amplitude irrespective of diameter, so that the direction of predominant light scatter could be visualised with ease, Figure 5.4.

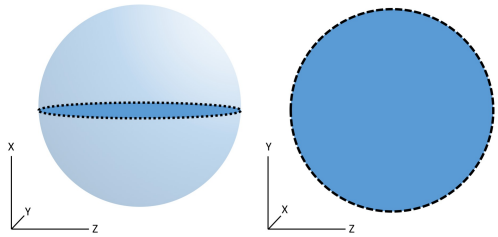

Figure 5.3 | Cross-Sectional Plane Through a Sphere and Top Down View of Cross-Section (right)

5.2.2.2 Model Output of Small Particle Scattering

Modelling of EV scatter through the cross-sectional plane of the particles (Figure 5.4 & Figure 5.5) gives an insight into the way in which light scatter varies with diameter variation.

Model Input Parameters	
Water RI	1.337
Cytosolic RI	1.38
Membrane RI	1.48
Vesicle Thickness (nm)	10
Illumination Wavelength (nm)	488
Illumination Intensity (Wm^{-2})	$1.09x10^{7}$

Table 5.1 | θ Scan Model Input Parameters.

Summaries are the Mie scatter θscan script Input parameters for modelling the scatter cross-section of EVs in a flow cytometry system. Refer to section 6.1.1 for details on selected RI values

When looking at the log scale of scatter amplitude and normalised scatter amplitude in Figure 5.4 and Figure 5.5, respectively, many peaks and troughs are seen. These are known as Mie resonances. As the particle becomes smaller than the illuminating wavelength the resonances disappear and light scatter becomes more isotropic. As particles decrease in RI the Mie resonance troughs become deeper with peaks appearing wider, Figure 5.5.

It can be seen in Figure 5.4 that polystyrene particles scatter more light than those of silica and EVs, across all angles. Silica particles also scatter more light than EVs over the majority of angles, though there are small regions where overlap is seen due to Mie resonance e.g. 500nm silica particles scatter less light than EVs of the same size at angles between 116° and 130°.

The peak amplitude for all particle sizes, regardless of composition, is at 0°. Interestingly there is one exception. 250nm EVs scatter the majority of their light at 61.5°. The peak scatter amplitude of a 1000nm EV compared to a 100nm EV is $1.86x10^8$ times greater, assuming the modelled refractive indices and illumination wavelength, Figure 5.4.

When considering collection of particle light scatter, detectors would ideally be placed where the highest quantity of light is being scattered. Looking at the cumulative light scatter across angles from 0-180° gives insight into the ideal collection range, Figure 5.6. For particles of 1000nm, regardless of composition, 90% light is scattered in the first 17°. This for 500nm particles however extends, with 90% of light not being collected until 33° is reached for polystyrene and silica particles, with EVs being ever further, at 40°. For 250nm particles, this extends further still with 90% of light scattered being collected at angle of 76.5° for polystyrene and silica particles, with EVs reaching 90% of total light scatter at 145°. At 100nm, the curves appear to be relatively linear for polystyrene and silica particles, and EVs reaching 90% of total light scattered at a smaller collection angle (137°) than those of silica and polystyrene (157.5°).

These results show that polystyrene and silica beads are not good representative markers for EV size based on scatter alone, as each scatters light at differing angles across each size range, when compared with EVs. Both polystyrene and silica also scatter far more light than EVs. These results also show that a single optimum collection angle for EVs does not exist, as particles of 1000nm scatter light very differently from those of 100nm. It is clear that a wide scatter angle for a FSC detector would be beneficial as all particles across the EV size range 30-99% of their total light scatter in the first 45°, Figure 5.6.

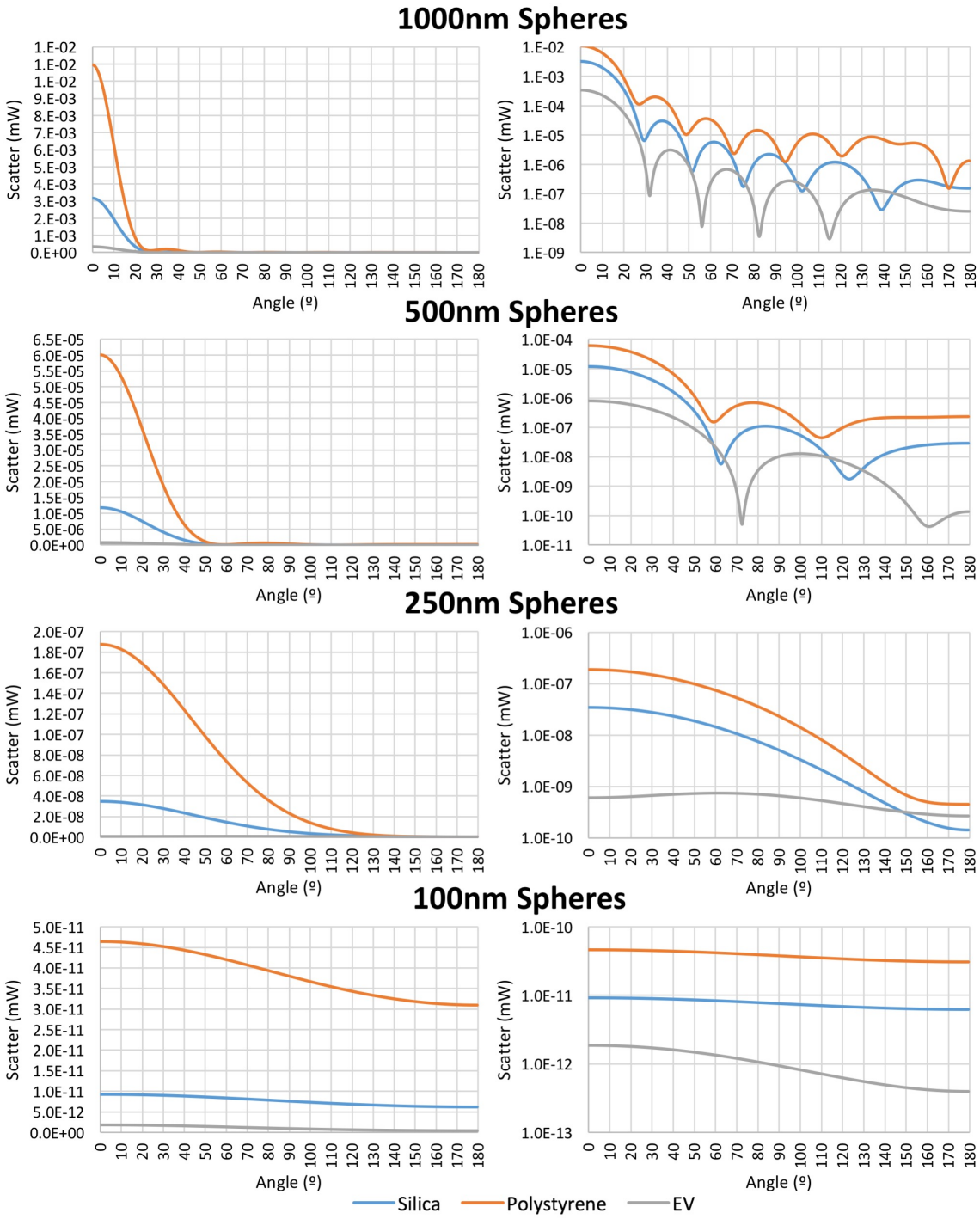

Figure 5.4 | Modelled Cross-Sectional Scatter Field Amplitudes of Small Particles.

Small particles of different diameters (1000, 500, 250, 100nm), and compositions (polystyrene – RI 1.59, silica – RI 1.45, EV - cytosolic RI – 1.38 and membrane RI – 1.48, with membrane thickness of 10nm) were modelled. All particles were assumed to be in water (RI – 1.337) and illuminated at 488nm with an illumination intensity of a conventional cytometer ($1.09x10^{8}$ W m^{-2}). Left graphs show scatter on a linear scale, with right hand graphs showing scatter on a log scale.

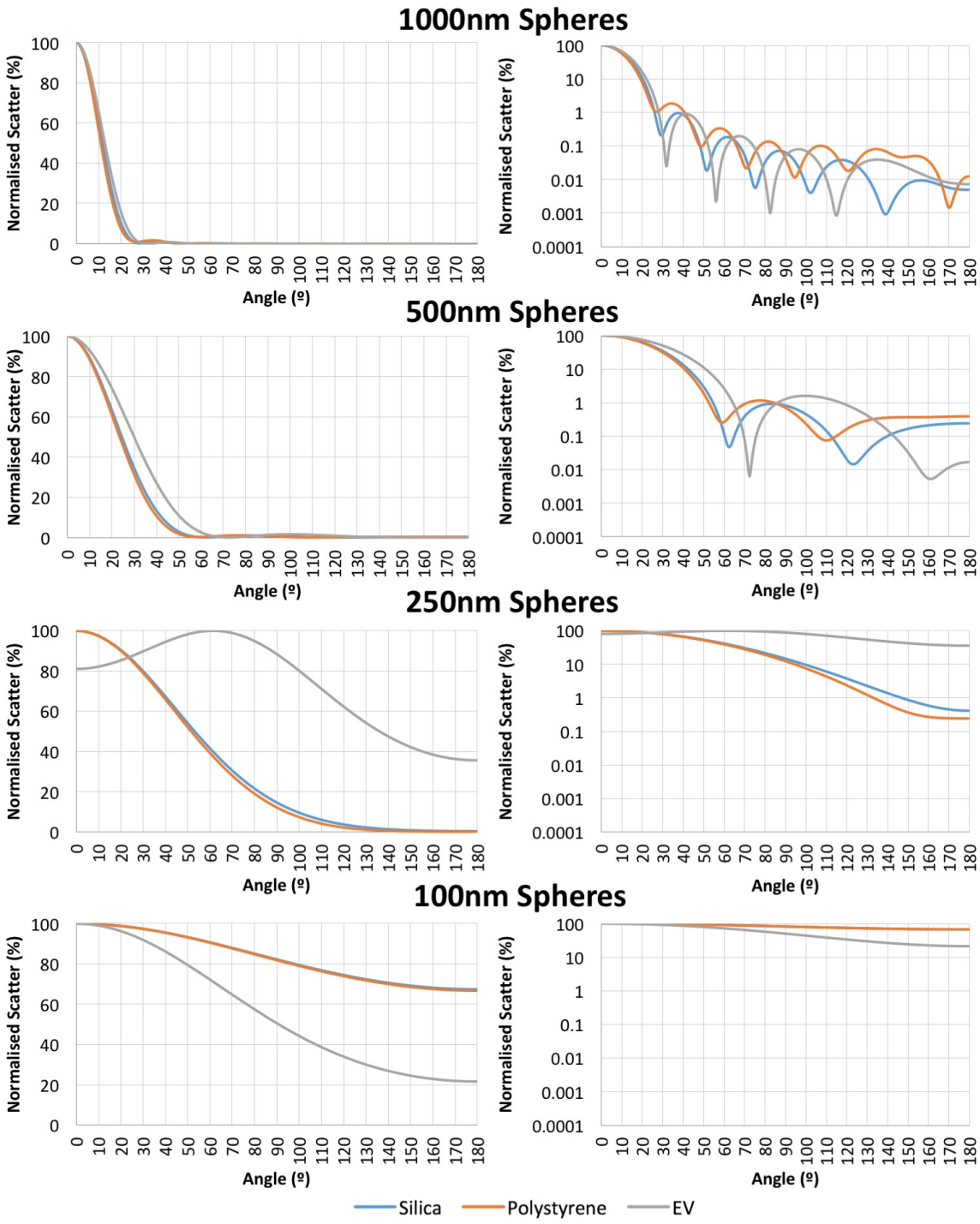

Figure 5.5 | Modelled Cross-Sectional Scatter Field Normalised Amplitudes of Small Particles.

Small particles of different diameters (1000, 500, 250, 100nm), and compositions (polystyrene – RI 1.59, silica – RI 1.45, EV - cytosolic RI – 1.38 and membrane RI – 1.48, with membrane thickness of 10nm) were modelled. All particles were assumed to be in water (RI – 1.337) and illuminated at 488nm with an illumination intensity of a conventional cytometer ($1.09x10^{8}$ W m^{-2}). Scatter amplitudes were normalised to a percentage, by dividing all angles by the angle with the highest scatter amplitude for a particular particle.

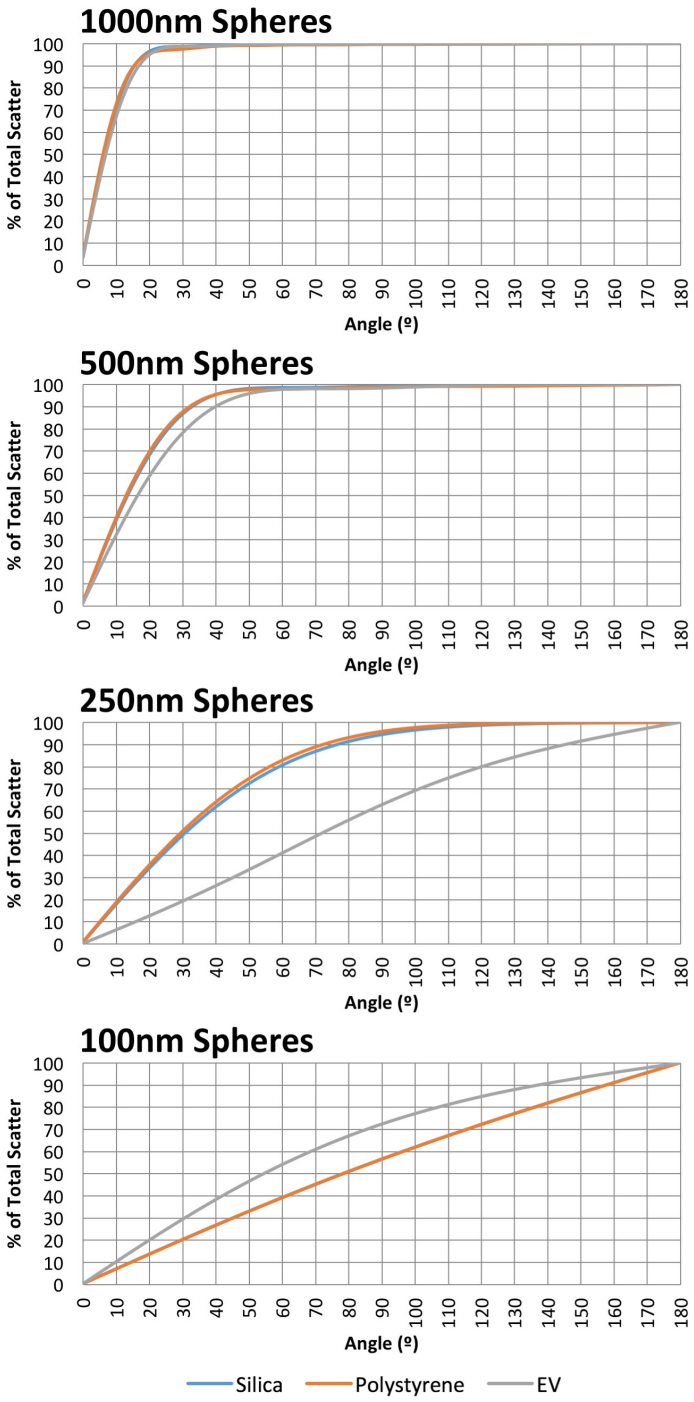

Figure 5.6 | Modelled Cross-Sectional Scatter Field Cumulative Amplitudes of Small Particles.

Small particles of different diameters (1000, 500, 250, 100nm), and compositions (polystyrene – RI 1.59, silica – RI 1.45, EV - cytosolic RI – 1.38 and membrane RI – 1.48, with membrane thickness of 10nm) were modelled. All particles were assumed to be in water (RI – 1.337) and illuminated at 488nm with an illumination intensity of a conventional cytometer ($1.09x10^{8}$ W m^{-2}). Scatter amplitudes were normalised to a percentage of total, by starting from 0° and adding each scatter amplitude to the previous angle before dividing the sum by the total scatter amplitude for a particular particle and multiplying by 100.

Now it is possible to determine the angular scattering distribution of spherical particles of varying diameter and RI, this can be applied to further building of models to determine the approximate scatter amplitude difference collected in flow cytometers with different optics. Based on these results is seems practical within a dedicated EV system to use a large angle collection in order to increase the number of photons reaching the detector increasing the signal, since EVs <500 are scattering light relatively isotropically. The relationship between the amplitude of collected light scatter perpendicularly (SSC) with varying collection angles and particle diameter, within a FCM system must next be investigated. It can be seen that the maximum SSC collection angle in several FCM systems, as determined by their flow cell dimensions differs, Figure 5.7. It can be seen that due to difference in scatter between EVs and polystyrene/silica, and the differing collection angles of the systems the relationship between particle size and scatter may differ between FCMs. This difference must therefore be investigated to understand the use of polystyrene/silica beads as size standards across multiple FCMs.

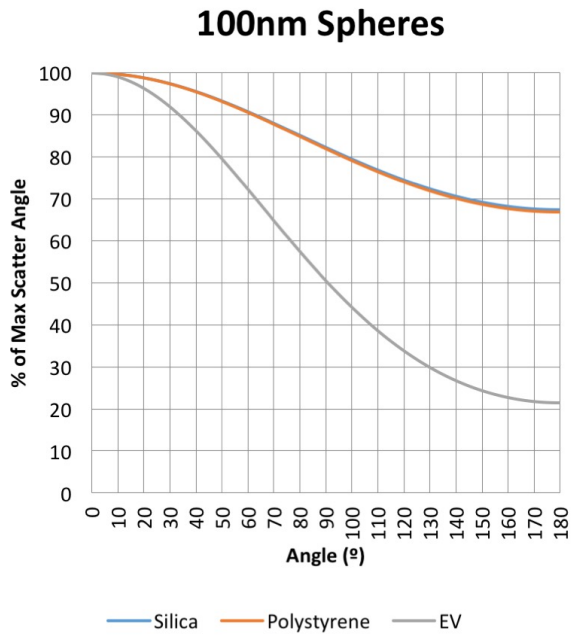

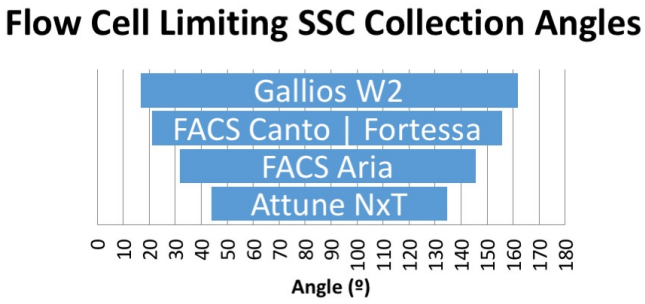

Figure 5.7 | Modelled Cross-Sectional Scatter Field Normalised Amplitudes of 100nm Particles with Flow Cytometer Flow Cell Limiting SSC Collection Angles

Top - Small particles of different diameters (1000, 500, 250, 100nm), and compositions (polystyrene – RI 1.59, silica – RI 1.45, EV - cytosolic RI – 1.38 and membrane RI – 1.48, with membrane thickness of 10nm) were modelled. All particles were assumed to be in water (RI – 1.337) and illuminated at 488nm with an illumination intensity of a conventional cytometer ($1.09x10^{8}$ W m^{-2}). Scatter amplitudes were normalised to a percentage, by dividing all angles by the angle with the highest scatter amplitude for a particular particle. Bottom - Flow cell limiting SSC collection angles from a variety of flow cytometers were calculated using the technical specifications provided by companies.

5.2.3 Effect of Limiting Small Particle Scatter Collection Angle on SSC Amplitude

cFCM systems collect light at varying angles depending upon the system application or manufacturer, Table 6.1. As seen in the previous results, light scatter amplitudes vary due to size, and composition, along with showing differing scatter amplitudes at different angles. These features, combined with differing FCM collection angles and geometries of light collection (rectangular/circular) likely introduces system differences between the separation of bead size standard beads. When considering EV analysis, a consistent increase in collected scatter amplitude with diameter would be ideal for determining the diameter of EVs, and therefore interpret the type of EV being analysed, and deduce the system limits with ease. Investigating the

effect of changing the collection geometry and angles is therefore required in order to understand the trend between collection angles, collection geometries, and particle diameter with the collected scatter amplitude of particles with different diameters.

5.2.3.1 Model Design Investigating SSC Collection Angle on Collected Amplitude of Submicron Particles

Models were based on circular and rectangular aperture collection geometries, Figure 5.2, for coated spheres, representing EVs, and solid spheres. The different geometries were to account for the two extremes of light collection within cFCMs. These were modelled using the input parameters in, Figure 5.2. Both geometries calculated the power of collected light scatter from between a range of 45-135° in 10° increments up to 0°-180° of collection, with 0° representing the incident illumination angle. Using rectangular modelling this involved 10° increases in $\theta$and ϕ ranges, for circular modelling this involved 5° increases in epsilon values. Modelling assumes cFCM illumination, with a wavelength of 488nm and an intensity of $4x10^6$ Wm^{-2}. Particles were assumed to be suspended in water (RI 1.337), with particle having refractive indices as highlighted in Figure 4.1.

The effect of altering the Phi angle alone in the rectangular aperture collection was done at a fixed θ collection angle range of 45-135°, whilst the ϕ collection angle range increased from 45-135° in 10° increments up to a 0-180° collection angle range. Modelling assumes cFCM illumination characteristics (488nm wavelength and an intensity of $4x10^6$ Wm^{-2}). Particles were assumed to be suspended in water (RI 1.337), with compositions of polystyrene, silica and EVs. Refractive indices as highlighted in Table 5.2.

Table 5.2 | Input Parameters for Rectangular and Circular Collection Apertures.

Rectangular & Circular Aperture Modelling Input Parameters	
Water RI	1.337
Cytosolic RI	1.38
Membrane RI	1.48
Vesicle Thickness (nm)	10
Polystyrene RI	1.605
Silica RI	1.45
Illumination Wavelength (nm)	488
Illumination Intensity (W m^{-2})	$4x10^6$

5.2.3.2 Model Output for Small Particle Collection Angle Variation on SSC Amplitude

Here I seek to understand how circular and rectangular collection apertures influence the relationship between particle diameter and scatter power collected. The scatter amplitude collected for varying ranges in both rectangular and circular aperture models are shown in Figure 5.8. It can be seen with a low range of θ collection angles (45-135°) in rectangular aperture modelling, and a low ε half-angle in circular aperture modelling, that the trend between diameter and scatter power begins to plateau more quickly than larger collection ranges (0-180°), Figure 5.8. In the case of all particles tested with rectangular aperture collection at the lowest collection

angle (45-135°), not only is there tailing off, but also a slight trough between 450 and 500nm, Figure 5.8. This does not appear to happen for the circular aperture modelling at the lowest collection angle however.

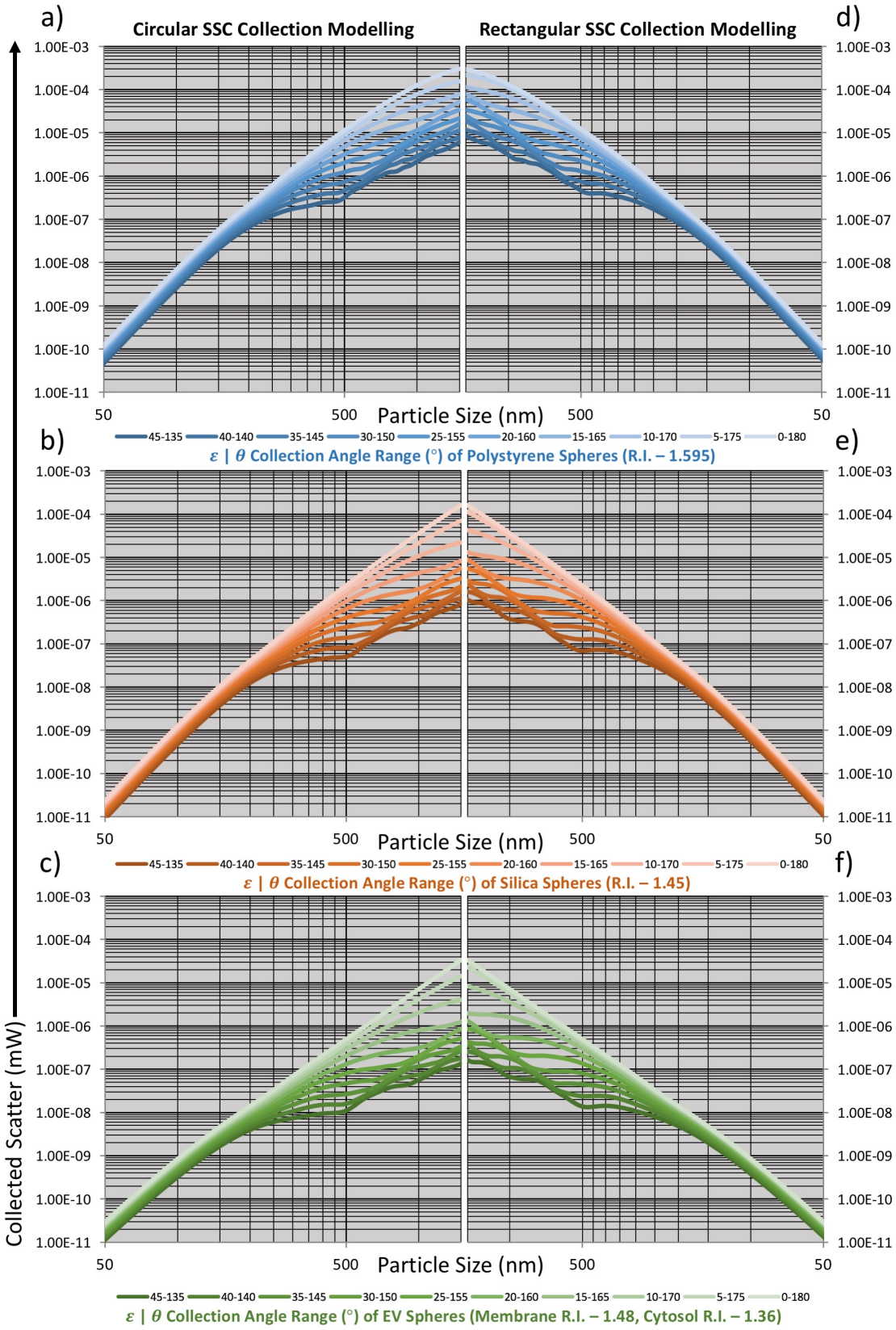

Figure 5.8 | SSC Collection Modelling of Polystyrene, Silica, and EV spheres.

Rectangular and circular geometries were modelled from 45-135° in 10° increments up to 0-180° of collection. Using rectangular modelling this involved 10° increases in θ and ϕ values, for circular modelling this involved 10° increases in epsilon values. Modelling assumes illumination at a wavelength of 488nm and an intensity of $4x10^6$ Wm^{-2}, particles being suspended in water (RI 1.337), and small particle having a RI as highlighted below each graph.

The lowest collection angle showing a clear continuous increase in diameter and scatter power, using rectangular aperture modelling, from 50-1000nm is between 10-170° and 15-165°, whilst for the circular aperture modelling it is between 20-160° and 25-155°.

The modelled rectangular aperture collection from particles of different RI look relatively similar in general trend from 0-180° collection to 45-135° collection, Figure 5.8. The same is true of circular modelling also. Though the trends are similar, the particles produce less scatter power in total i.e. a rectangular aperture collection 500nm polystyrene particle, with light being collected from 45-135°has an amplitude of ~$3x10^{-7}$ mW, while silica and EVs have an amplitude of ~$6x10^{-8}$ mW and ~$1.5x10^{-8}$ mW, respectively. These powers would likely be far lower in a system due to the transmission efficiency not being 100% through optical components.

When comparing rectangular and circular aperture modelling directly, each of the trends have subtle differences between corresponding collection angles and refractive indices. Rectangular aperture modelling however consistently provides higher amplitudes of collected light, due to collecting a larger relative surface area of scattered light for each set angle. This would therefore aid detection of smaller particles. Normalising on surface area alone however would not give equal collection powers due to light not being equally distribution on all axis.

It can be seen from changing the ϕ collection angle range in rectangular aperture modelling, that there is very little change in the correlation between collected light and particle diameter occurs, Figure 5.9. The features appear as they do for the same collection angle in Figure 5.8, but merely transpose up in amplitude, when the ϕ collection angle range increases, and down in the amplitude, as the ϕ collection angle decreases. Although very small, the difference between the largest collection and smallest collection angle is bigger at the smallest size, than at the largest size. The relationship between collected scatter power and diameter, regarding peaks, troughs, tailing off therefore appears to be predominantly dependent on the θ collect angle range, when symmetric collection is concerned. This also accounts for the larger spread of collected light scatter across the varying circular collection half-angles, when compared to rectangular aperture collection models.

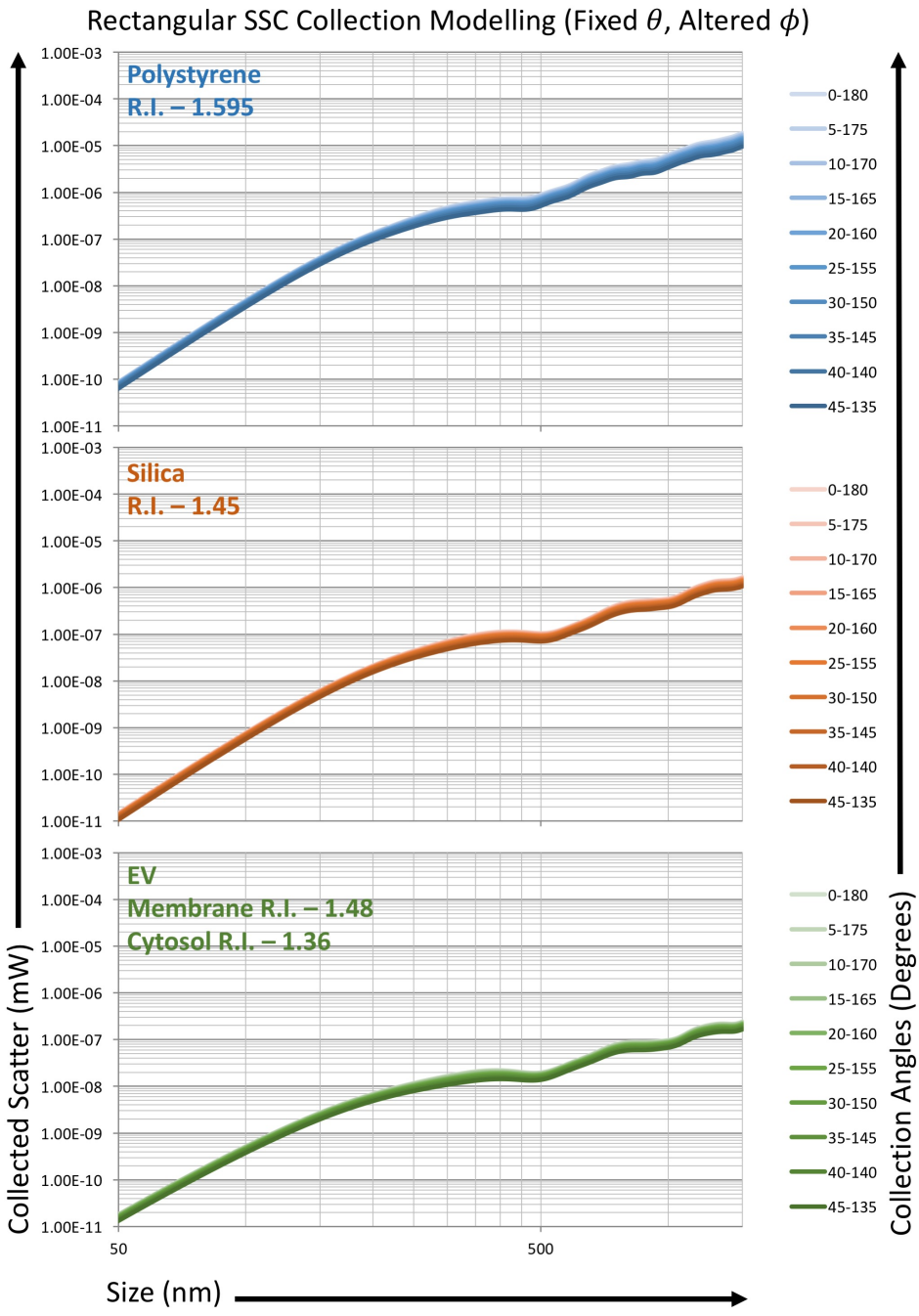

Figure 5.9 | Fixed θ, Altering ϕ Rectangular SSC Collection Modelling of Polystyrene, Silica, and EV spheres.

The effect of altering the ϕ collection range alone in the rectangular aperture collection was done at a fixed θ angle of 45-135°, whilst the ϕ collection range increased from 45-135° in 10° increments up to 0-180° of collection. Modelling assumes illumination at a wavelength of 488nm and an intensity of $4x10^{6}$ Wm^{-2}, particles being suspended in water (RI 1.337), and small particle having a RI as highlighted below each graph.

In summary, there appear to be trade-offs for circular and rectangular collection aperture geometries, with circular apertures offering better linearity between size and collected scatter power at lower angles, while rectangular collection apertures with collection ranges the same as circular apertures, will consistently provide a higher amplitude of collected scatter. It now needs to be determined whether acquired data in cFCMs correlates well with the predicted data within these models.

5.3 Conclusion

EV angular scattering distribution modelling has shown that as particles become smaller than the wavelength, light is more universally scattered in all directions around the particle, rather than with the majority in the forward direction, as particles above the illumination wavelength do. For this reason, SSC will in most cases will likely have a greater resolution than FSC due to the collection angles inherently being wider, and their signal likely having less noise due to not requiring blocking of the excitation laser.

Modelling collection of light at different angles has shown that larger angles of collection provide a more continuously increasing relationship between scatter amplitude and particle diameter, required for accurate EV sizing. If smaller angles (45-135°) are used, rectangular collection geometry provides an increased light scatter amplitude when compared to circular collection. At very small angles, however, circle collection is optimal due to rectangular collection having peaks and troughs in its diameter to collected scatter power relationship. An ideal system would therefore have a rectangular collection limiting geometry, but at an angle high enough to produce a continuously increasing relationship across diameter ranges up to 1000nm, with scatter amplitude.

Now that small particle scatter of various bead compositions has been investigated, along with how collection geometry affects the amplitude of collected scatter light from small particles, resolution and standardisation across flow cytometry platforms, accounting for RI and collection geometry, must be investigated.

Chapter 6: Implementing Mie Scatter Modelling as a Standardisation Technique for EV Analysis

6.1 Introduction

Standardisation, regardless of field, is required to enable reproducibility between research techniques, within or between laboratories. The EV field in particular requires a standardisation technique that allows researchers to know which population of EVs they are measuring, such as MVs and AVs, or whether they are in fact measuring small cells such as residual platelets. Due to cytometers having varying fluorescent and scatter resolutions, knowing the upper and lower diameters of detected EV will also enable reproducibility of experiments between laboratories using machinery with different collection optics.

Implementation of an easily applied method to allow standardisation between the size of sub-micron populations being analysed by FCMs with differing collection optics is currently required within this field. This chapter shall explore implementation of a model as a standardisation technique between FCMs to account for differences between the RI of EVs and calibration beads, building upon the concept by Van der Pol *et al*[148]. This method of standardisation will then be taken a step further by account for RI and deduce EV population size without the need for advanced physics, proprietary or unobtainable FCM information. Modelling as a standardisation technique shall then be validated using biological vesicles combined with a novel staining assay.

6.1.1 Modelling as a Standardisation Technique

Currently stable liposomes of fixed precise diameter are not commercially available and their similarity with endogenous biological vesicles has not been validated. The same problem stands with the development of beads with closer RIs to endogenous biological vesicles. Modelling of flow cytometers, in order to account for the differing RIs of beads when compared to measurement of EVs, is currently the most appealing method of producing a standardised protocol between pieces of equipment. Not only does modelling of a flow cytometer's light collection allow for sizing of EV in the current generation of flow cytometers, it can also be utilised to develop newer generations of flow cytometers, better suited to the detection of EVs.

A method of standardisation between FCMs, accounting for RI, for EV analysis is particularly required, owing to the complications in defining resolution within a FCM system, discussed in section 2.3. A method enabling this would allow for different collection geometries and alignments between FCM equipment. One method showing particular promise is implementation

of Mie scatter with beads of known diameter and RI, (discussed in Chapter 5:). This method then can deduce the upper and lower diameter of the analysed population to determine type and portion of EVs analysed, by using the light collection geometries within a given system. This method however requires an approximate RI for EVs, which is somewhat unknown, and likely to vary somewhat depending on composition, which is dependent on its derivation. The predicted RI of EVs is thought to resemble that of cells/bacteria, intracellularly (RI=~1.38±0.02 at 488nm) and, at the membrane (RI=~~1.48 at 488nm)[162-164]. Recently a research group has used nanoparticle-tracking analysis (NTA) to determine the difference in RIs of EVs, showing them to have a mean RI between 1.35 and 1.40 at 405nm[165, 166]. Whilst this research is useful in determining RI for computer modelling, the mean RI is diameter dependent and in the case of this experiment is biased to modal particle diameter, in this case ~200nm. NTA biases measurement of smaller EVs due to being dependant on Brownian motion, which is less effective towards the higher end of the EV diameter range. Even in the lower diameter range where Brownian motion is effective, large CVs can be seen in the obtained data[147]. The Mie scatter method of standardisation shall therefore be built upon, enabling cross-study and cross-platform standardisation of results.

6.2 Methods & Results

6.2.1 Validating SSC Modelling for EV Resolution Quantification Using FCM System Component Geometry

It can be seen from modelling different collection geometries and angles (Chapter 5:), that the amount of collected light over a range of submicron particle diameters and refractive indices shows considerable variation. How well data from acquired submicron particles of known diameter and RI fit with the predicted models of collection scatter power of those particles in different cFCMs is next investigated.

6.2.1.1 Model Design Investigating EV Resolution Quantification Using FCM System Component Geometry

For this work, geometries were obtained from company flow cytometer technical specifications and collated, shown in Table 6.1. The illuminating laser beam intensities were calculated for each cFCM system using the total power specified, and beam geometries. Collection angles of each of the influencing optical components (flow cell, cuvette, lens N.A.) were normalised to the limiting angle within the flow cell using Snell's law. The collection limiting angle for the system was then determined, and used to model the light scattered by illuminated particles in the flow cell. Depending on the collection limited angle on the pathway from the illuminated particle to the fibre optic cable, models would either need to simulate light collected in a circular geometry or a

rectangular geometry, therefore both scripts were run for all cytometers and compared. Particle refractive indices implemented for modelling can be found in Table 6.1

Testing of flow cytometer EV resolution involved acquiring NIST beads, shown in Table 6.2, at each cytometer's lowest flow rate, with the beads diluted until an acquisition rate of 500 events/sec was reached. The acquired flow cytometry output data in arbitrary units was then overlaid with the modelled data, based on the cytometer collection limited angle. This was calculated by dividing the median SSC -H value, for a specific bead population by the predicted light scatter power value for its diameter value. This was calculated for each population, giving a 'calibration factor' for each population. The median calibration factor value was taken for all bead populations, irrespective of RI. The product of outputted SSC-H median value, with the median calibration factor was then calculated for every population resulting in normalized data, .

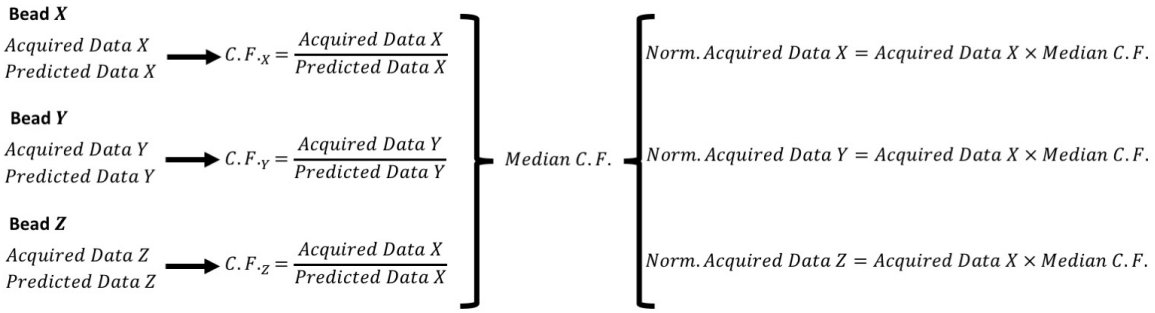

Figure 6.1 | Flow diagram of modelling data normalisation.

The flow diagram shows the normalisation process of acquired arbritrary data from flow cytometer, with predicted data with absolute units from modelling resulting in normalisation acquired data. C.F.=Calibration Factor, Norm=Normalised.

The rectangular and circular modelling data each had their gradient and variance between acquired bead data compared with predicted bead data calculated, and were compared across each cFCM platform. Plotted results are shown in Figure 6.2-Figure 6.5.

Table 6.1 | Collated Conventional Flow Cytometer Limiting Angles and Specifications.

Cytometer	FACS Canto	FACS Canto II	FACS Aria	Gallios W2	LSR Fortessa / FortessaX-20	Attune NxT
SSC Lens Numerical Aperture (N.A.)	1.2	1.2	1.2	1.2	1.2	1.2
N.A. Limited Collection SSC Angle (º)	63.8	63.8	63.8	63.8	63.8	63.8
Flow Cell Refractive Index	1.463	1.463	1.463	1.463	1.463	1.463
Refractive Index of Water	1.337	1.337	1.337	1.337	1.337	1.337
Cuvette Height (µm)	6500	6500	P.I.	P.I.	6500	4000
Cuvette Width (µm)	7000	7000	P.I.	P.I.	7000	6000
Cuvette Limited FSC Collection (º)	49.3	49.3	N.C.	N.C.	49.3	36.8
Cuvette Limited SSC Collection (º)	52.1	52.1	N.C.	N.C.	52.1	51.2
Flow Cell Height (µm)	180.0	180.0	160.0	150.0	180.0	200.0
Flow Cell Width (µm)	430.0	430.0	250.0	460.0	430.0	200.0
Flow Cell Limited FSC Collection (º)	22.7	22.7	32.6	18.1	22.7	45.0
Flow Cell Limited SSC Collection (º)	67.3	67.3	57.4	71.9	67.3	45.0
Blue Laser Power (mW)	20.00	20.00	20.00	20.00	50.00	50.00
Beam Width (µm) x axis	65.00	65.00	65.00	84.00	65.00	50.00
Beam Height (µm) y axis	9.00	9.00	9.00	10.00	9.00	10.00
Beam Profile	Gaussian	Gaussian	Gaussian	Gaussian	Gaussian	Top Hat
Beam Intensity (W/m^2)	1.09E+07	1.09E+07	1.09E+07	7.58E+06	2.72E+07	1.60E+08
Fluidic Pump Quantification	N/A	N/A	N/A	N/A	N/A	Syringe
Overall Adjustability	-	-	+++	-	++	+

Collection angles are assumed to have an illumination intensity of 488nm. P.I. – proprietary information. N.C. – not calculable

Table 6.2 | NIST Bead Technical Specifications

Composition	Refractive Index (589nm)	Certified Mean Diameter (nm)	Microsphere Density (g/mL)	% Solids
Polystyrene	1.59	81	1.05	1
	1.59	100	1.05	1
	1.59	203	1.05	1
	1.59	400	1.05	1
	1.59	707	1.05	1
	1.59	1019	1.05	1
	1.59	1587	1.05	1
Silica	1.45	490	1.83	2
	1.45	730	1.98	2
	1.40	990	2.01	2
	1.46	1570	2.18	2

6.2.1.2 Output of EV Resolution Quantification Using FCM System Component Geometry Model

cFCMs modelled included the FACSCanto - Figure 6.2, Fortessa X-20 - Figure 6.3, LSR Fortessa - Figure 6.4, Attune NxT - Figure 6.5. Collated statistics for all cytometers can be found in Table 6.3. Figures show predicted scattering powers for a range of bead sizes and RIs, at the collection angle calculated for that FCM. Normalised to each of these figures is acquired NIST bead data. It can be seen that the acquired bead data fits well with both square and circular aperture collection models.

Determining how close the acquired data fitted with the predicted data can be seen in three ways. Firstly, the normalised acquired data points were divided by their predicted values and plots against the bead diameter. If a bead were to fit perfectly its normalised data over predicted data value would equal 1. Secondly, the gradient of a line of best fit on a normalised data vs. predicted data was obtained (forcing the intercept through 0). Thirdly, the sum of variation over all beads, where a value of 0 would equal the closest fitting, was calculated for each model. Each of these three observations is displayed to the right of each cytometers modelled resolution curve in Figure 6.2-Figure 6.5.

It can be seen in all modelled cFCMs that the 990nm silica bead population appears to be in the region of 1.45/1.46, rather than 1.40 (approximately equivalent to EV high RI) specified, Table 6.2. Despite being excluded from the calibration step, the 990nm population was assumed to have a RI of 1.46 so as to be include in the predicted vs. normalised results. The 990nm silica beads were therefore omitted from any further calibration factor normalisation, gradient, and variance calculations due to its RI appearing to diverge strongly from the RI supplied by the company. This was consistent across flow cytometers with varying collection angles as seen.

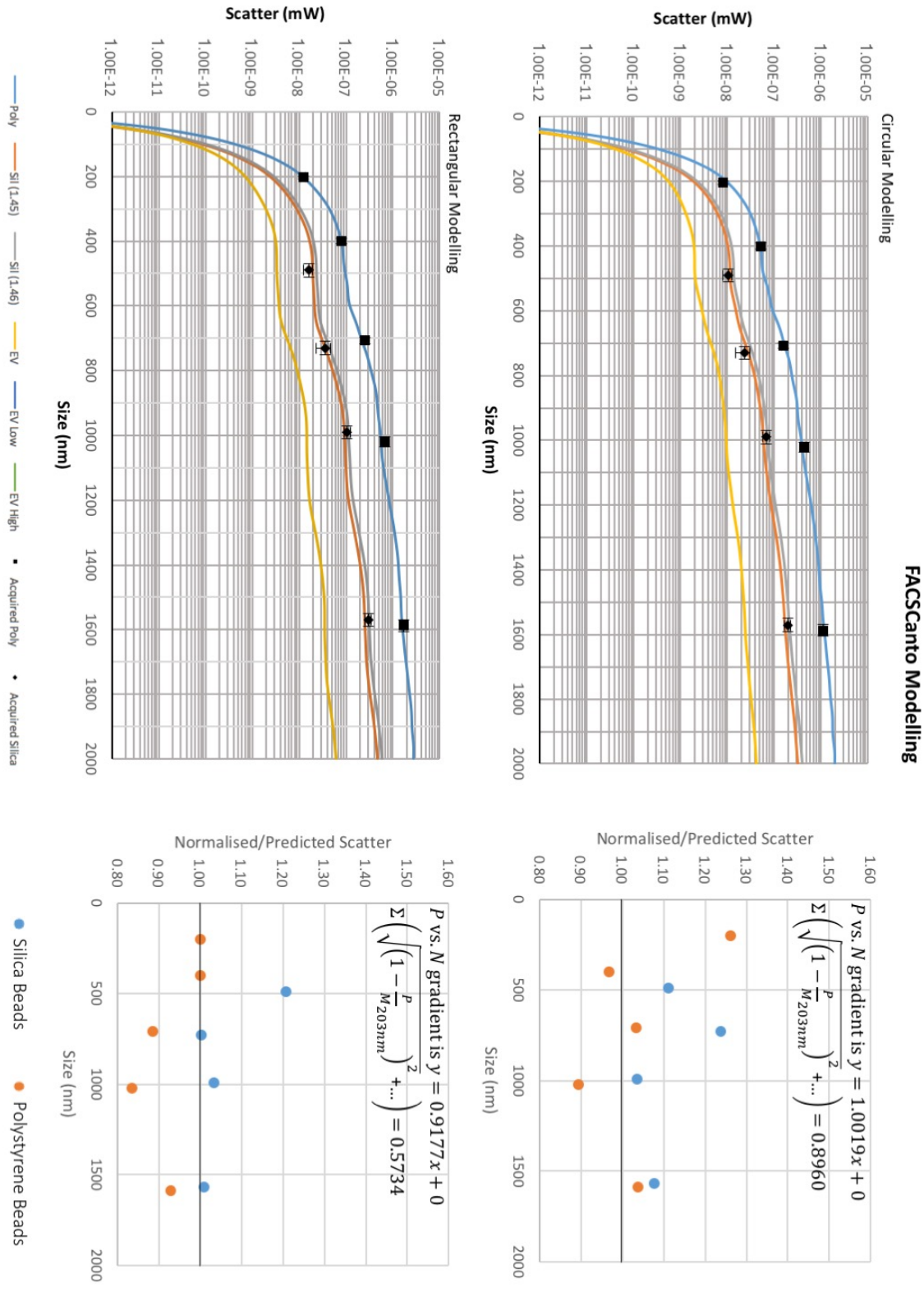

Figure 6.2 | Modelling of FACS Canto SSC Collection Optics (52.1° Collection Half-Angle)

Rectangular collection aperture modelling (bottom) was compared to that of circular collection aperture modelling (top). Graphs on the left show modelled predicted data (solid lines) for polystyrene, silica, and EV particles. Acquired data (points) is shown for polystyrene and silica bead populations. The goodness of fit is compared with graphs on the right, with solid line representing a perfect fit and points on top representing the acquired data for a given population.

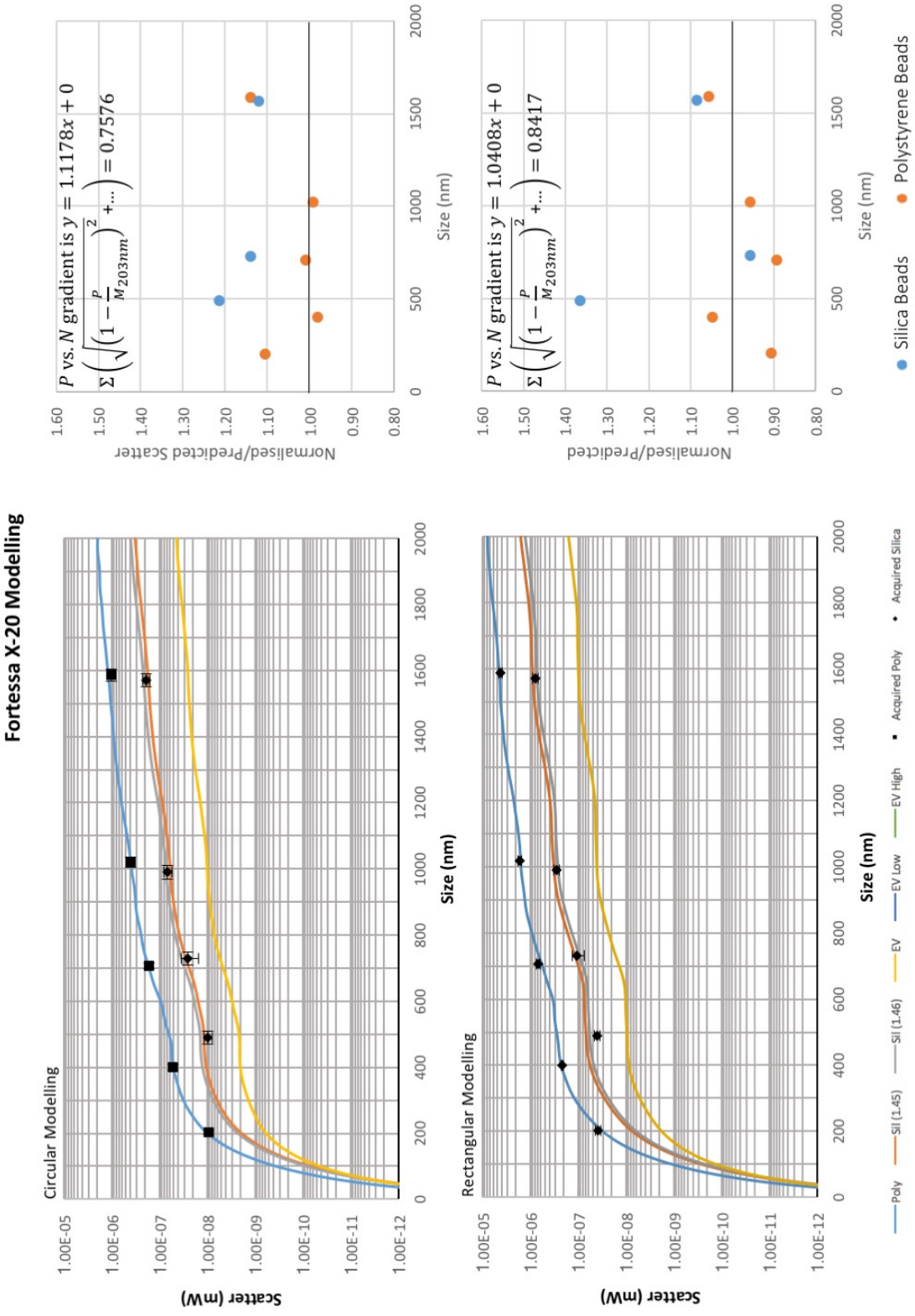

Figure 6.3 | Modelling of Fortessa X-20 SSC Collection Optics (52.1° Collection Half-Angle)

Rectangular collection aperture modelling (bottom) was compared to that of circular collection aperture modelling (top). Graphs on the left show modelled predicted data (solid lines) for polystyrene, silica, and EV particles. Acquired data (points) is shown for polystyrene and silica bead populations. The goodness of fit is compared with graphs on the right, with solid line representing a perfect fit and points on top representing the acquired data for a given population.

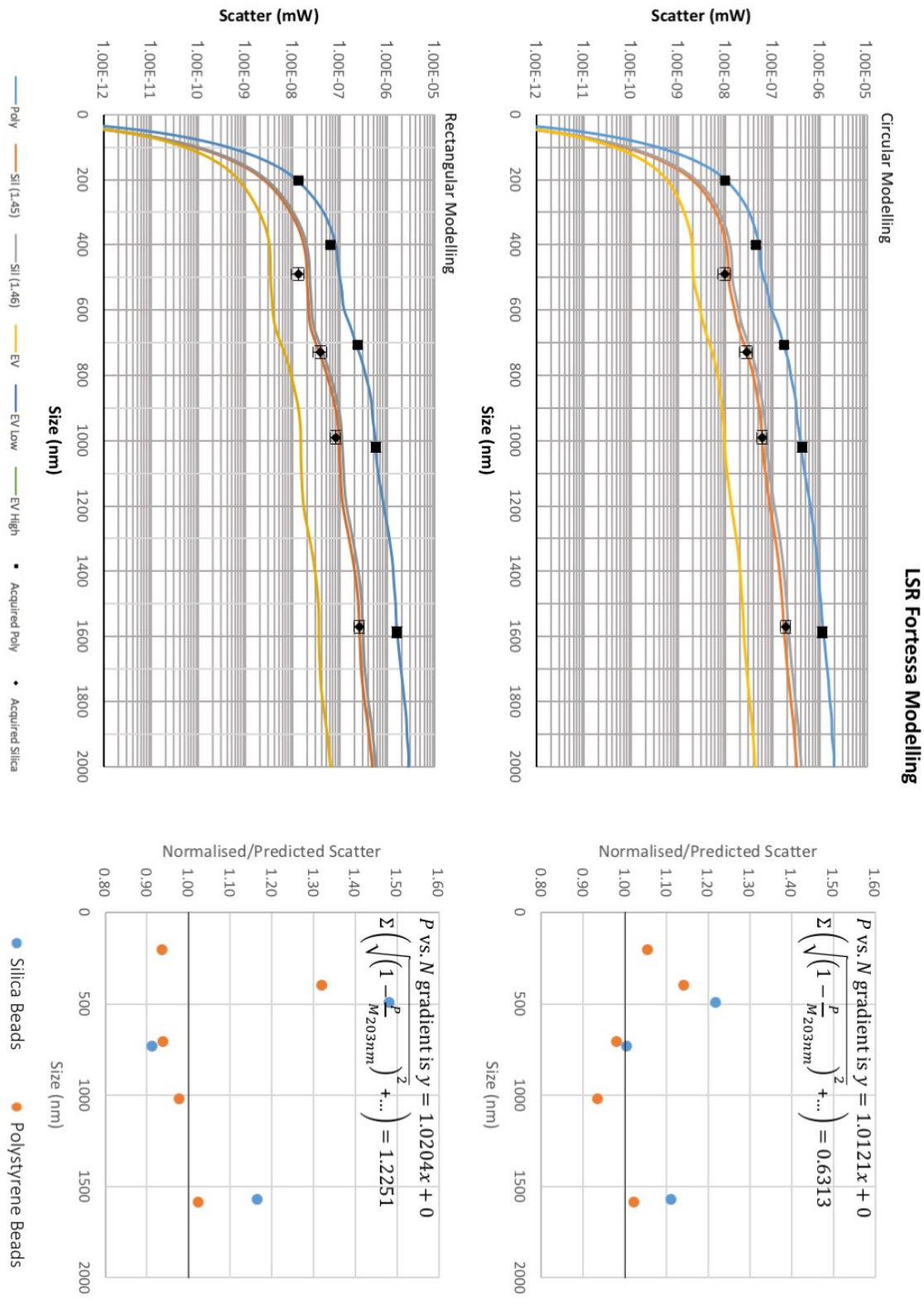

Figure 6.4 | Modelling of LSR Fortessa SSC Collection Optics (52.1° Collection Half-Angle)

Rectangular collection aperture modelling (bottom) was compared to that of circular collection aperture modelling (top). Graphs on the left show modelled predicted data (solid lines) for polystyrene, silica, and EV particles. Acquired data (points) is shown for polystyrene and silica bead populations. The goodness of fit is compared with graphs on the right, with solid line representing a perfect fit and points on top representing the acquired data for a given population.

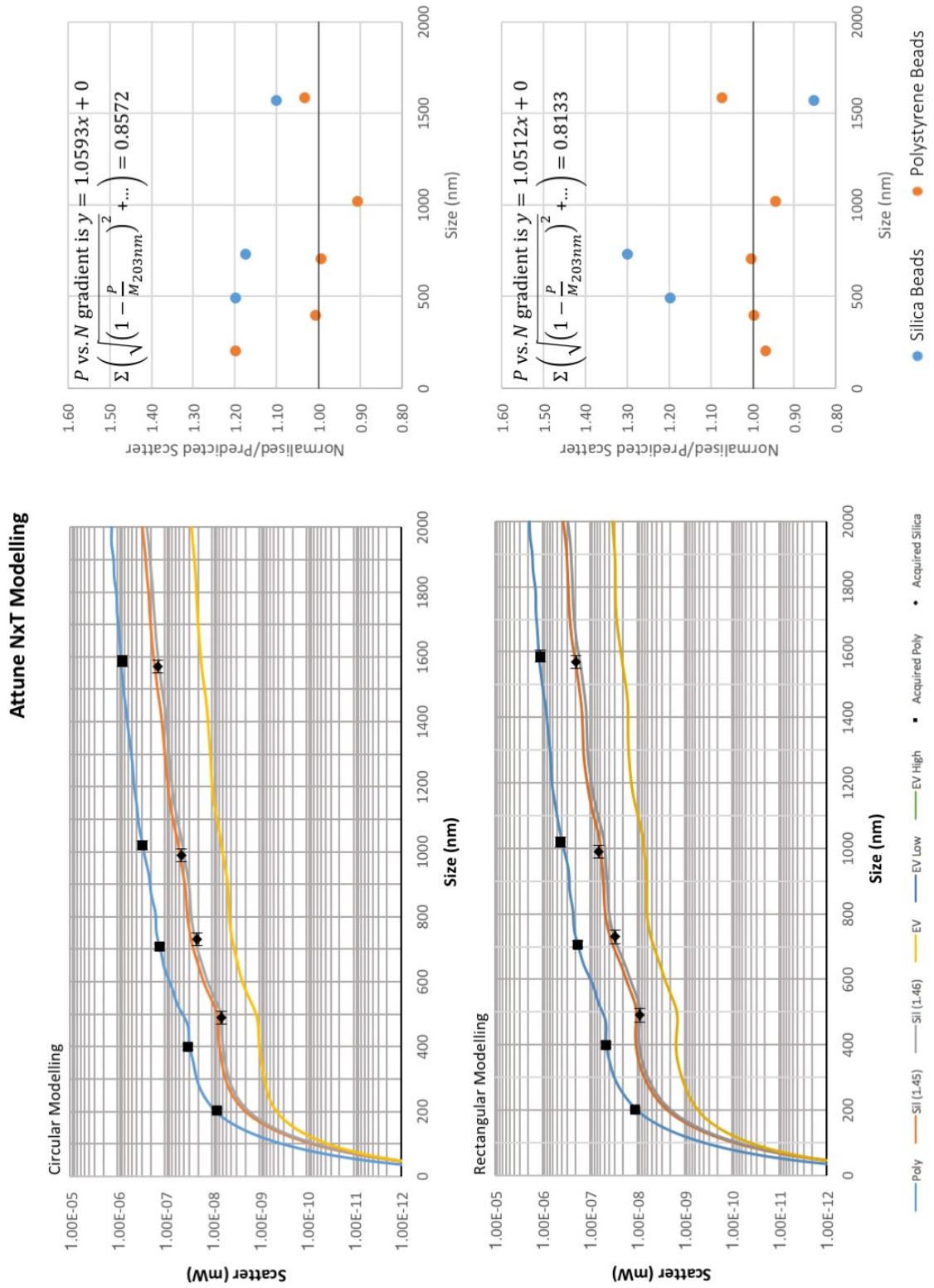

Figure 6.5 | Modelling of Attune NxT SSC Collection Optics (45° Collection Half-Angle)

Rectangular collection aperture modelling (bottom) was compared to that of circular collection aperture modelling (top). Graphs on the left show modelled predicted data (solid lines) for polystyrene, silica, and EV particles. Acquired data (points) is shown for polystyrene and silica bead populations. The goodness of fit is compared with graphs on the right, with solid line representing a perfect fit and points on top representing the acquired data for a given population.

Table 6.3 | Summary of Gradient and Variance of Acquired Bead Data for Geometric Models of Each Cytometer.

	Gradient		Variance	
	Circular	Rectangular	Circular	Rectangular
Fortessa X-20	1.1178	1.0408	0.7576	0.8417
LSR Fortessa	1.0121	1.0204	0.6313	1.2251
Canto	1.0019	0.9177	0.8960	0.5734
Attune NxT	1.0593	1.0512	0.8572	0.8133

Red text indicates gradient closest to y=1x+0, and lowest variance for each collection geometry.

The circular collection aperture appears to show the best fit for FACSCanto, Fortessa X-20, Figure 6.2, Figure 6.3. This indicates that the collection lens, or most likely collection fibre alignment affected the rectangular geometry of the cuvette limiting angle, or that pinhole apertures were the limiting angle. It can be seen that despite having the same flow cell and cuvette dimensions, the Fortessa X-20 fits the rectangular model more closely, and the circular model less closely than the FACSCanto, further suggesting that the models deviate due to aperture alignment.

It can be seen that gradient and variance fit the same geometry closest for half of the cytometers, Table 6.3. The discrepancy between these results is unclear. Deciding on the closest fitting model however is likely best done by assuming the gradient closest to y=1x+0 (predicted equals acquired) is best used as a predictive measure of fit. All gradients are however very close to y=1x+0, indicating the component geometries are a good measure of determining the SSC collection angle within the system.

Furthermore, Figure 6.6 shows how the collection half-angle from two of these cytometers can affect the relationship between the bead and biological data e.g. The Fortessa X-20, with a collection angle of 52.1°. shows 203nm polystyrene beads have approximately the same collected scatter as 490 silica beads. However, the Attune NxT, with a collection angle of 45°, shows the 203nm polystyrene beads to have a collected scatter over 10-fold higher than 490nm silica beads.

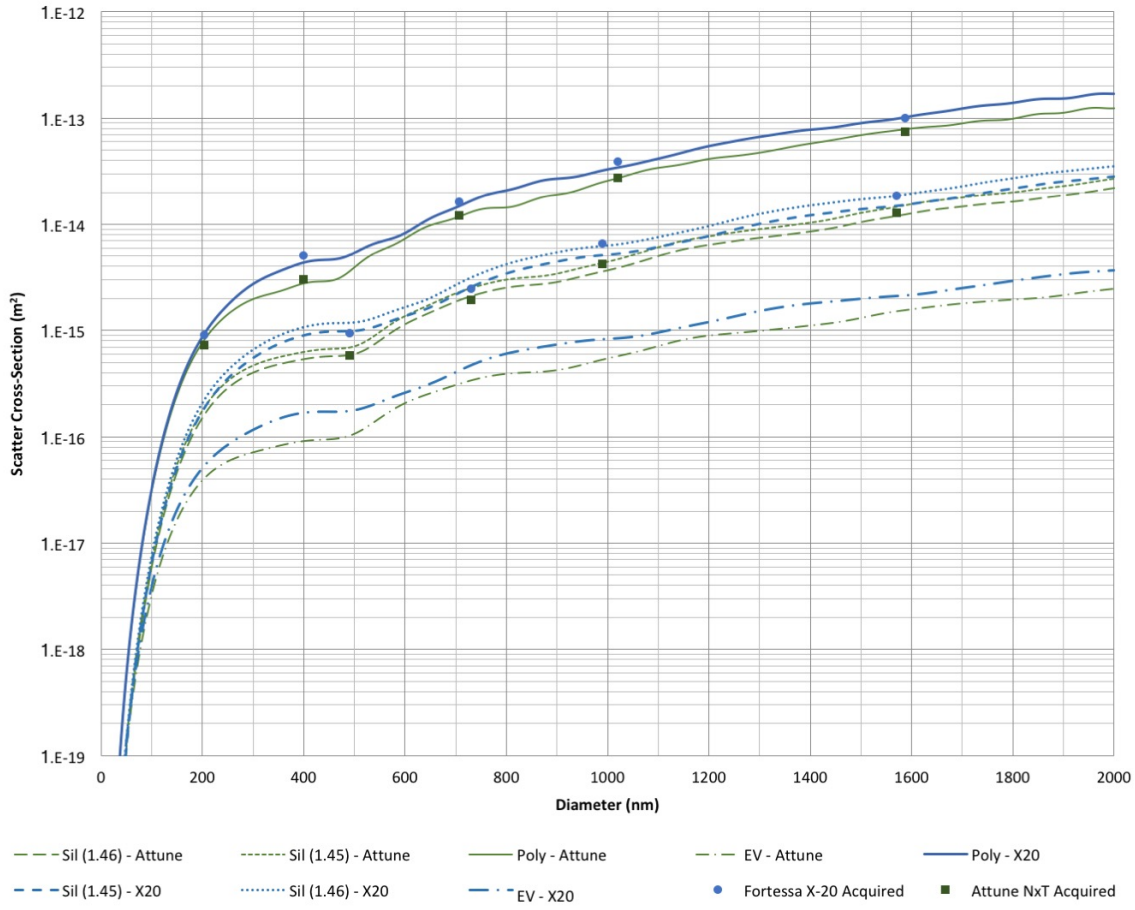

Figure 6.6 | Comparison of Scatter-Cross Sections from Cytometers with Different Collection Angles.

Shown are the circular aperture scatter-cross sections models of the Fortessa X-20 (half-angle = 52.1°) and Attune NxT (half-angle = 45°) to show the effect that collection half-angle can have on the relationship between bead and biological data.

This method clearly shows that it is possible to predict the relationship between size and collected scatter amplitude in a system with known component geometry, thereby being able to account for RI differences to determine the resolution of a system for particles of known RI. This type of modelling however relies on information that is viewed as proprietary to FCM manufacturers. The calculations involved are also not accessible to all biologists as it requires understanding of many principles that are common to physicists and engineers. A method of determining the collection angle, and geometry, without needing to determine collection angles using proprietary information, assumed component RI and optics principles is therefore desirable to make the implementation of this technique more accessible.

6.2.2 Validation of Mie Theory as a Standardisation Technique using Residual Platelet, Apoptotic Vesicle, and Microvesicle Differentiation Assay

So far in this chapter, modelling as a standardisation technique has been based on the acquisition of beads with a known size and refractive index and normalising their acquired arbitrary output unit data to predicted scatter power using modelling. This data has shown that modelled predicted data and acquired bead data show fit very well. Whilst this data suggests modelling angles of the machine are accurate, the predicted EV data must next be compared with acquired EV data in order to validate that modelled can be used for biological standardisation. In order to test this standardisation technique on biological samples a fluorescent assay was developed to differentiate between EV subsets with distinct size ranges e.g. apoptotic vesicles >1µm, platelets >1µm, MVs <1µm.

6.2.2.1 Sample Preparation & Acquisition

6mL of blood was drawn from 3 healthy individuals into citrated tubes. Tubes were centrifuged twice at 2000*g* for 10 minutes. Plasma was drawn off and stored at -80^{o}C. Supernatants were thawed at 37°C for 10 minutes. 50µL of plasma was added to 50µL 0.1µm double-filtered HEPES Buffered Saline (HBS). 2µL of Cell Light Mitochondria-GFP (3 hours), 2µL of 500µM BAPTA-1 (30 mins) or 1µL of 2mM CellEvent Caspase 3/7 (30 mins) and incubated at 37°C before pelleting at 18,000*g* for 30 mins. Supernatants were discarded and 50µL 0.1µm double-filtered HBS was used to resuspend the MV pellet. 20µL of 25µg/mL CD41a PerCP-Cy5.5 was added and incubated on ice for 15 mins. 1µL of 200µM VRD was added and incubated for 5 min before analysis. Unstained samples and single stained samples were run as controls. Multi-stained samples consisted of VRD, CD41a, with either CellEvent Caspase 3/7, Cell Light Mitochondrial-GFP, or BAPTA-1-AM. A Fortessa X-20 was used for analysis, with Megamix Plus FSC (Biocytex, France), polystyrene NIST and silica NIST beads (Thermofisher, UK) for calibration and Mie scatter modelling. Samples were diluted until an acquisition rate in the region 500 events per second was reached. Data analysis was carried out on imported FCS 3.0 files using FlowJo v10.0.8 (FlowJo LLC, Ashland, USA). Compensation matrices were first set, using CompBead data and single stained controls. Automated compensation matrix set up in FlowJo was first carried out, before being adjusted manually.

6.2.2.2 Results

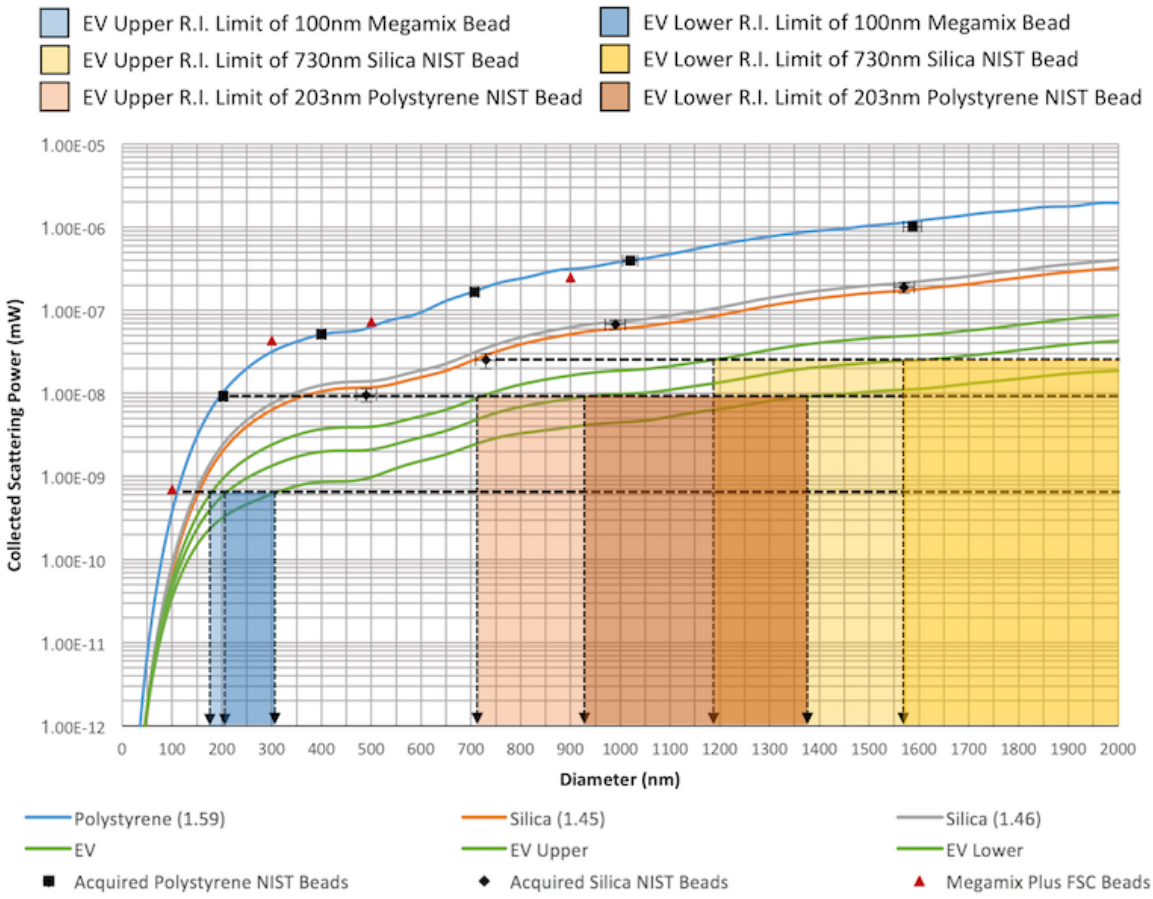

Figure 6.7 | Mie scatter Circular Aperture SSC modelling of Fortessa X-20 to demonstrate that modelling of sizes correlated well to actual bead sizes.

Solid coloured lines represent predicted data using modelling, points represent normalised acquired data. Black dashed lines show the intersection points of 100nm Megamix Bead, 203nm Polystyrene NIST beads, and 730nm silica beads with the predicted high-to-average, and average-to-low EV refractive index data (membrane RI 1.38±0.02 at 488nm). The light and dark blue shaded area represents the expected EV size range corresponding to the 100nm Megamix bead. This represents the minimum EV size detectable. The light and dark orange shaded area represents the size range of EVs corresponding to the 203nm polystyrene beads. The light and dark yellow shaded area represents the size range of EVs corresponding to the 730nm silica beads.

It can be seen that calibration with relatively high index beads would lead to a significant underestimation of the diameter of particles with lower refractive index, such as EVs, which are represented by three green curves in Figure 6.7 corresponding to their predicted scattered power with a membrane refractive index of 1.38±0.02. For example, 203nm polystyrene NIST beads equate to modelled EVs with an upper RI range being 820±100nm in diameter, or 1150±220nm with a lower RI range.

Identification of particle derivation was done using an assay that utilized: a membrane stain (VRD), a platelet marker (anti-CD41a), a calcium sensitive probe (BAPTA-1-AM), an apoptosis marker (Caspase 3/7), and a mitochondrial stain. Figure 6.8 shows flow cytometry data from nine phenotypes using multi-stained sample histogram overlays of SSC-H vs. Count. The description for each of these phenotypes, with their expected derivation using modelling are summarized in Table 6.4. Assays performed show a 203nm polystyrene NIST bead is shown on each graph for diameter reference, along with a 730nm silica NIST bead, which equates to modelled EVs with an upper RI range being 1375±200nm in diameter, or 1800±225nm with a lower RI range, Figure 6.8. Therefore, this modelling technique was then used to determine whether predicted diameters of EVs based on 203nm polystyrene, and 730nm silica beads correlate with acquired biological vesicle data.

VRD+, BAPTA-1-AM+, CD41a+ | Events have a membranous structure, platelet markers present, contain intracellular esterases, have a physiological $[Ca^{2+}]_i$. Most likely platelets and large PMVs. It can be seen in Figure 6.8, that there are 2 peaks for the phenotype; one at 200nm, and one above 700nm. These results would correlate well with large platelet MVs and platelets, respectively.

VRD+, BAPTA-1-AM+, CD41a- | Events have a membranous structure, non-platelet origin, contain intracellular esterases, have a physiological $[Ca^{2+}]_i$. Most likely apoptotic vesicles and large MVs. It can be seen in Figure 6.8, that there is one broad peak for this phenotype spreading over the 200nm and 700nm peaks. One sample appears to have a second peak well above 300nm also. These would correlate with apoptotic vesicles.

VRD+, BAPTA-1-AM-, CD41a+ | Events have a membranous structure, platelet origin, does not contain intracellular esterases or does not have a physiological $[Ca^{2+}]_i$. Most likely platelet MVs. It can be seen in Figure 6.8, that there is 1 peak for the phenotype, <200nm. This would be strongly indicative of platelet MVs.

VRD+, Caspase 3/7+, CD41a+ | Events have a membranous structure, platelet markers present, apoptotic markers present. Most likely apoptotic platelets. It can be seen in Figure 6.8, that there is 1 peak for the phenotype >300nm, with some sample events broadening out to low event counts below 200nm. These would correlate with platelets and large platelet MV.

VRD+, Caspase 3/7+, CD41a- | Events have a membranous structure, non-platelet origin, apoptotic markers present. Most likely apoptotic vesicles. It can be seen in Figure 6.8, that there is 1 peak for the phenotype at 700nm, with a some sample events broadening out to <200nm and >700nm. These would correlate with a discrete population of apoptotic vesicles.

VRD+, Caspase 3/7-, CD41a+ | Events have a membranous structure, platelet markers present, no apoptotic markers present. Most likely non-apoptotic platelets and platelet MVs. It can be seen in

Figure 6.8, that there are 2 peaks for the phenotype; one at 200nm, and one above 700nm. These results would correlate well with large platelet MVs and platelets, respectively.

VRD+, CellEvent Mito+, CD41a+ | Events have a membranous structure, platelet markers present, mitochondrial markers present. Most likely platelets, and possibly very large MVs. It can be seen in Figure 6.8, that there is 1 peak for the phenotype >700nm, with some sample events broadening out to low event counts below 200nm. These would correlate with platelets and large platelet MV.

VRD+, CellEvent Mito+, CD41a- | Events have a membranous structure, non-platelet origin, mitochondrial markers present. Most likely apoptotic bodies, and very large MVs, possibly large single mitochondrion. It can be seen in Figure 6.8, that there is 1 peak for the phenotype at 700nm, with a some sample events broadening out to <200nm and >700nm. These would correlate with a discrete population of apoptotic vesicles.

VRD+, CellEvent Mito-, CD41a+ | Events have a membranous structure, platelet markers present, mitochondrial markers not present. Most likely platelet MVs. It can be seen in Figure 6.8, that there are 2 peaks for the phenotype; one at 200nm, and one above 700nm. These results would correlate well with large platelet MVs and platelets, respectively. Due to this population still showing platelets, it is indicative of the sensitivity of the mitochondrial staining not being high enough, or the assay not staining all mitochondria.

Platelets can therefore be identified by being positive for the membrane stained (VRD+), mitochondrial stain (CellEvent Mito+), Caspase 3/7 positive, and CD41 positive. These phenotypes can be seen in Figure 6.8D & G. The majority of these particles are above the 730nm silica bead SSC power and are therefore at least above 1200nm if the highest predicted EV refractive index is assumed. This platelet population overlaps with one of the two populations in Figure 6.8F & I. There is a trough between the platelet population above the 730nm bead mark and the second population which is just below 730nm silica bead mark, Figure 6.8F & I. This second population which is therefore a platelet MV population. MVs have been defined as having an upper limit of 1000nm. If it is assumed that the trough at the upper end of the PMV population and lower end of the platelet population is equivalent to ~1000nm vesicle, Figure 6.8. The predicted 1000nm SSC power for EVs fits well with the acquired data and shows the biological vesicles fit closely with the higher EV predicted refractive index data for EVs.

Apoptotic vesicles in this assay will have the same features as platelets, however they will be negative for the CD41a platelet marker. These phenotypes can be seen in Figure 6.8E & H. Apoptotic vesicles are reported to be 1-5µm in diameter. The majority of positively stained apoptotic bodies sit on the 730nm silica bead mark. This indicates their size is a minimum of

1200nm, if a high refractive index is assumed. This again is in keeping with previously reported sizes for apoptotic vesicles.

Table 6.4 | Summary of Results from Multi-Stained Samples, Relating Fluorophore to Phenotype.

Phenotype	Membrane structure	Platelet Marker CD41a+	Physiological Ca^{2+} & Intracellular Esterases	Caspase 3/7	Mitochondrial Marker	Peak sizes	Interpreted outcome
(Fig 6.8A) VRD+ BAPTA-1-AM+ CD41a+	+	+	+	-	-	203nm & >730nm	Platelets and large PMVs
(Fig 6.8B) VRD+ BAPTA-1-AM+ CD41a	+	-	+	-	-	203-730 nm spread	Apoptotic vesicles and MVs
(Fig 6.8C) VRD+ BAPTA-1-AM- CD41a+	+	+	-	-	-	<203nm	PMVs
(Fig 6.8D) VRD+ Caspase 3/7+ CD41a+	+	+	-	+	-	>730nm	Platelets
(Fig 6.8E) VRD+ Caspase 3/7+ CD41a-	+	-	-	+	-	>730nm	Apoptotic Bodies
(Fig 6.8F) VRD+ Caspase 3/7- CD41a+	+	+	-	-	-	<203nm & >730nm	Platelets and PMVs
(Fig 6.8G) VRD+ CellEvent Mito+ CD41a+	+	+	-	-	+	>730nm	Platelets and large PMVs
(Fig 6.8H) VRD+ CellEvent Mito+ CD41a-	+	-	-	-	+	730nm	Apoptotic Bodies
(Fig 6.8I) VRD+ CellEvent Mito- CD41a+	+	+	-	-	-	<203nm & >730nm	Platelets and large PMVs

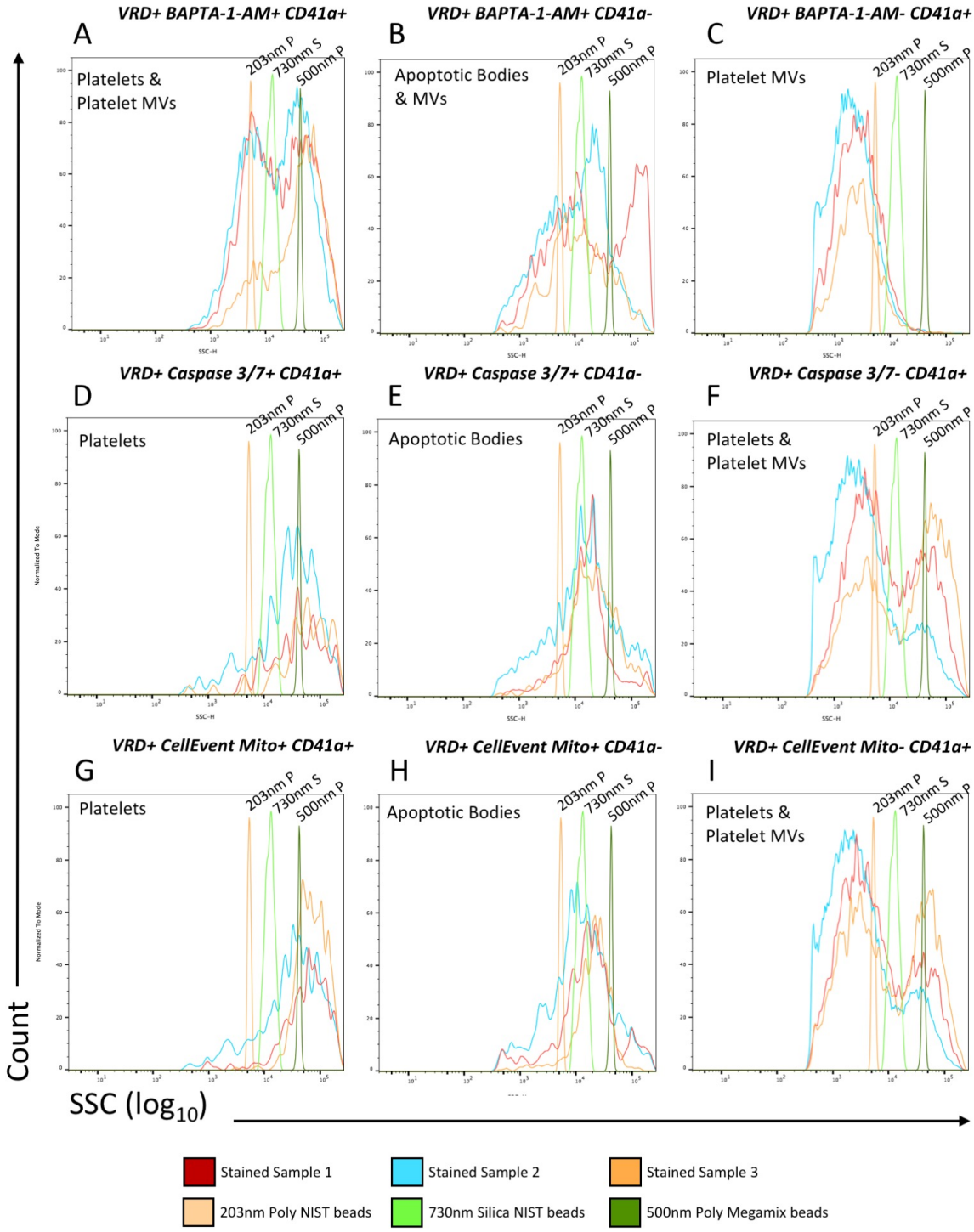

Figure 6.8 | Multi-Stained Plasma Assay for Mie Theory Standardisation Technique Validation.

Figure shows multi-stained plasma samples (n=3) overlaid with one another, in combinations of positive or negative for BAPTA-1-AM, Caspase 3/7, Mitochondrial Stain, and CD41a, with all plots being positive for VRD. 203nm polystyrene NIST beads, 730nm silica NIST beads, AND 500nm fluorescent Megamix beads are indicated in each graph.

In summary, modelling in this particular machine has ~1000nm vesicle cut-off represented by 200nm polystyrene beads, assuming the predicted RI. The phenotypes above describing platelets, platelet MVs, and apoptotic bodies correlate well with these theoretical cut-offs, and therefore validate modelling as a standardisation procedure. This staining assay shows that it is likely that the RI of biological vesicles appears to be slightly higher than the predicted, or that vesicles have a higher size cut off. In either case 700nm silica NIST beads on this cFCM platform appears to be an ideal cut-off to separate residual platelets and apoptotic bodies from MVs.

6.2.3 Determining cFCM SSC Collection Angle using Bead Acquisition

As seen in this Chapter, modelling of a cFCM based on its component geometry to account for refractive index differences between particles of the same size correlates well with acquired biological data. This technique's use as a standardisation technique is therefore very promising. Many of the variables that played into creating this model however was either proprietary (cuvette geometries, component refractive indices) or unknown (aperture geometry) and therefore obtained through contacts, or deduced. Using this method of standardisation is therefore not easily implementable for many in the EV field of research. A method of deducing a cFCM SSC collection angle for standardisation purposes is therefore required, this shall be investigated here.

cFCMs contain a number of components in the optical path following particle scatter, before reaching the SSC photodetector, Figure 6.9A. Understanding which range of angles is being collected is pivotal in implementing modelling as a standardisation technique. Companies manufacturing FCM equipment generally share their flow cell dimensions; they do not however share their cuvette dimensions, which in many cases are the limiting SSC collection angle (FACSCanto I, FACSCanto II, LSR Fortessa, Fortessa X-20, Gallios W2 etc). Determining the resolution of FCMs may therefore not be possible with the flow cell dimensions alone.

However, even knowing the component dimensions may not be enough, since an exact RIs need to be known in order to determine the exact collection angle. Fused silica (SiO_2) and quartz is advertised by different manufacturers to have varying RIs ranging from 1.46 to 1.54 (at 589nm). Changing the cuvette RI by this range can change the collection angle significantly. It is likely flow cells differ slightly in RI across machines as the FCMs tested here span several decades in their production, and components have likely changed in the way they have been manufactured, with materials differing slightly to offer better transmission efficiency, particularly at lower wavelengths.

Another area where predicting the collection geometry will be useful is for differing alignments between machines of the same type. The component most concerned in this case is the alignment

of the fibre optic cable carrying photons to the detectors, Figure 6.9B. When light is focussed from the cuvette onto the flow cell, chromatic aberration occurs, separating different wavelengths of light in space. When FCMs are aligned the fibre, optic cable is moved forwards or backwards until an optimal position for the users work is reached, Figure 6.9A. In changing this alignment, it is possible to cut a rectangular collection geometry into a circular collection geometry entirely, or somewhere in between.

A method to determine the machine resolution without knowing the dimensions of the components, or RI differences between mediums and alignment would therefore be beneficial to those using flow cytometers without known component measurements by simply acquiring beads, and shall be attempted here.

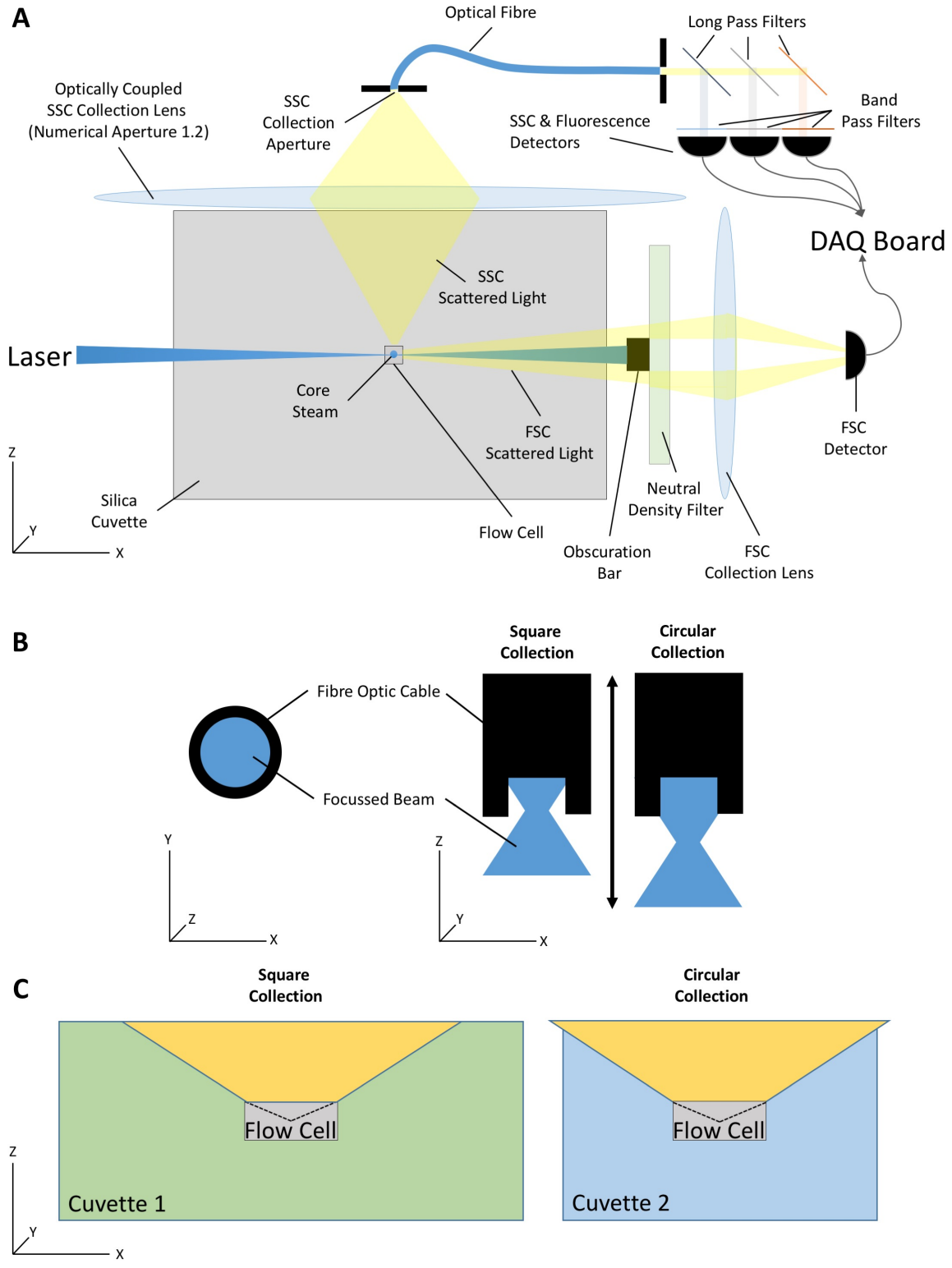

Figure 6.9 | Overview of Rectangular and Circular Light Collection with FCM System.

A) shows the top-down cross-section schematic of a flow cytometry interrogation zone with an illuminated particles light path on the way to FSC and SSC detectors. B) shows the optical fibre acting as the SSC collection aperture, with its movement forwards and backwards showing how square and circular collection geometries can be changed due to focal point of the SSC collection lens light (blue). C) shows two cuvettes with the same flow cell dimensions, with a cuvette of different dimensions. The light path of the flow cell on the left is not impeded by the cuvette having a flow cell limited collection angle, however the flow cell on the right has its light path from the flow cell impeded and therefore, has a cuvette limited collection angle.

6.2.3.1 Experiment & Model Design to Predict FCM SSC Collection Angle

NIST beads, Table 6.2, were acquired one size population at a time on each flow cytometer at their lowest flow rate, with an event rate of ~500E/sec, until a minimum of 5000 events were acquired. 990nm silica beads were omitted due to their disagreement with manufacturers details described in the previous section. The analysed bead population then had their SSC-H median value recorded. A database of each given NIST bead diameter and RI was computed with collection half-angles of 0° to 90° in increments of 0.1°, alongside the data acquired on the FCM. The database was computed for rectangular and circular SSC collection angles.

The obtained SSC-H median value for each bead was then divided by the predicted scatter for angles 0.1° to 90° sequentially. This data shows the calibration factor required for the obtained data to overlap with the modelled data across all of these angles. The coefficient of variation (standard deviation divided by the mean) was then calculated across all bead calibration factors for each particular angle. The angle at which the coefficient of variation was lowest, including both rectangular and circular collection apertures, was deduced to be the collection angle of the flow cytometer. A visual overview of this method can also be seen in Figure 6.11. These scripts were collated into an independent piece of software, with the graphical user interface shown in Figure 6.10.

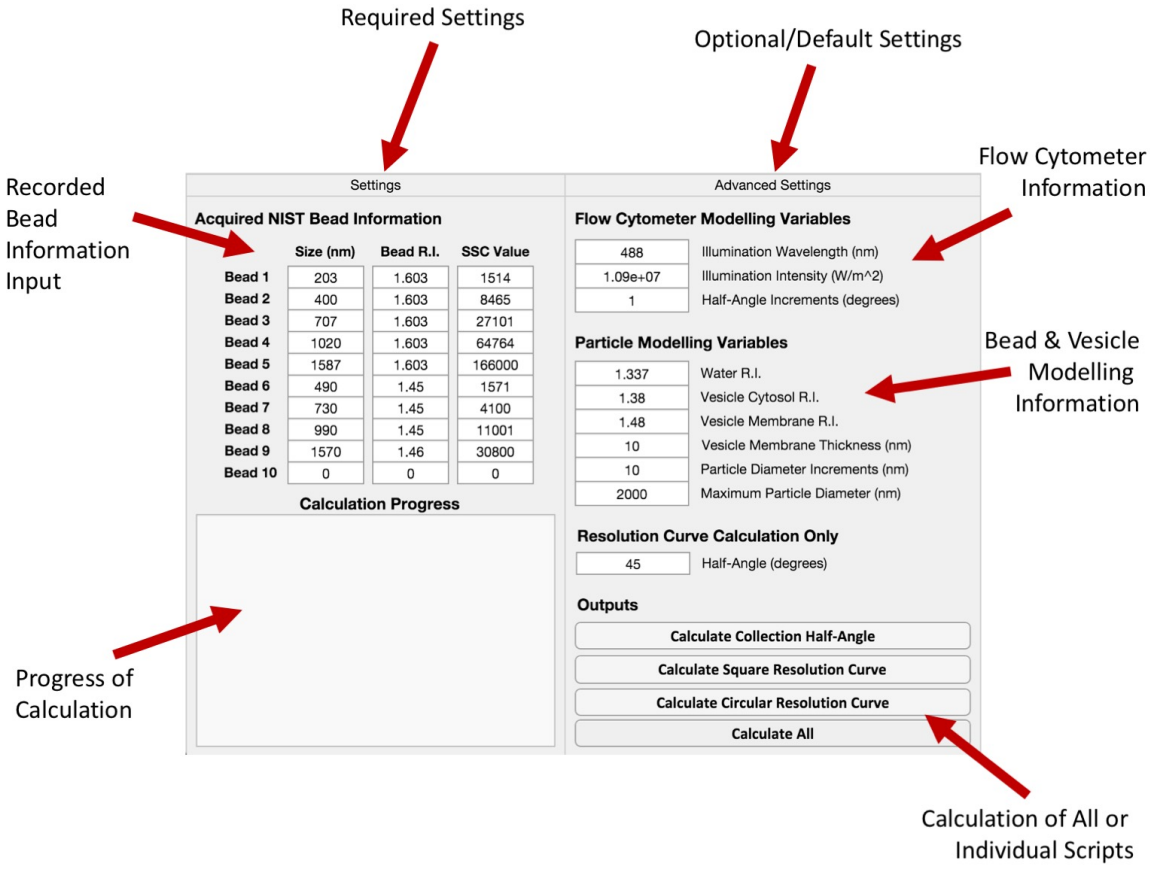

Figure 6.10 | SSC Collection Angle Determination Software Graphical User Interface.

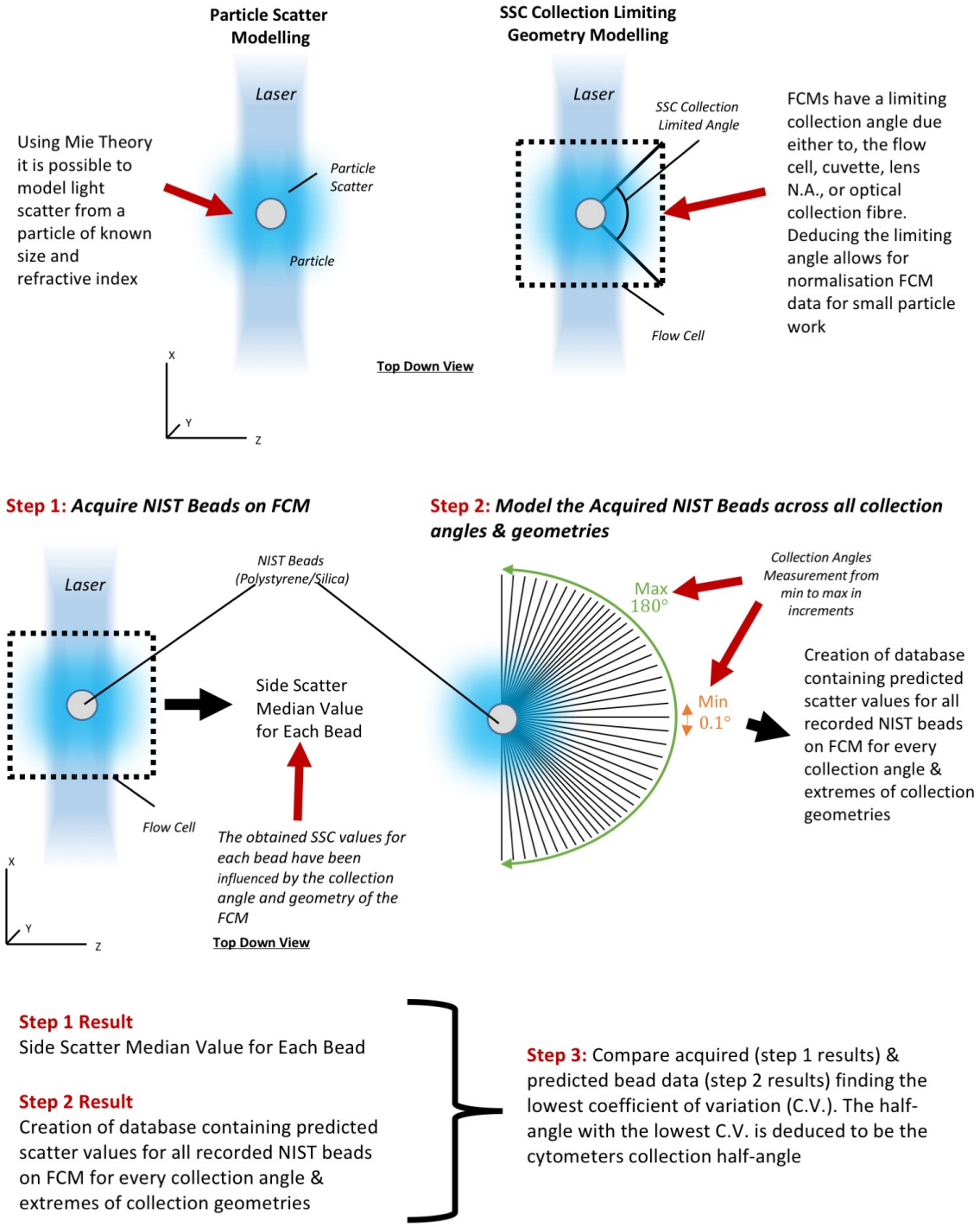

Figure 6.11 | Overview of cFCM Collection Angle Determination Method.

Top – shows model overviews previously used in Chapter 5 to determine total particle scatter, and then used to determine collected particle scatter when limited by a flow cell/cuvette geometry. Middle – shows that the collected particle scatter determined by the its geometry will influence the collected scatter power or a bead of known size and RI, and therefore the geometry can be deduced by matching it to a database of all possible collection angles and extremes of collection geometry (rectangular/circular). Bottom – shows that if the middle two steps are compared, the collection angle and geometry can be deduced by finding the angle and geometry with the lowest coefficient of variation between the collected and predicted data.

6.2.3.2 Output of FCM SSC Collection Angle Model

Acquired NIST bead data was then inputted into the model to deduce the collection limited angle of the Attune NxT(1) - Figure 6.12, Canto I - Figure 6.13, Fortessa X-20 - Figure 6.14, LSR Fortessa - Figure 6.15. The closest fitting angles (the angle with a coefficient of variation closest to 0%) are summarised in Table 6.5.

Figure 6.12 | Determined SSC Collection Angle and Geometry Curves for Attune NxT(1), and Acquired vs. Modelled Data for the Determined Collection Angle.

Top - Coefficient of Variation (%) represents the deviation from how well acquired NIST bead data fits with different collection half-angles for rectangular and circular model from 0-90°, in 0.05° increments. A coefficient of variation value closer to 0 represents less variation between the acquired and predicted data for that angle, and therefore a better fit. Bottom – shows modelled data of the acquired bead refractive indices from diameters of 0-2000nm, in increments of 10nm. Acquired bead data normalised the predicted data with a median calibration factor (see methods) is overlaid with predicted data to show goodness of fit at the closest fitting collection aperture geometry and collection angle.

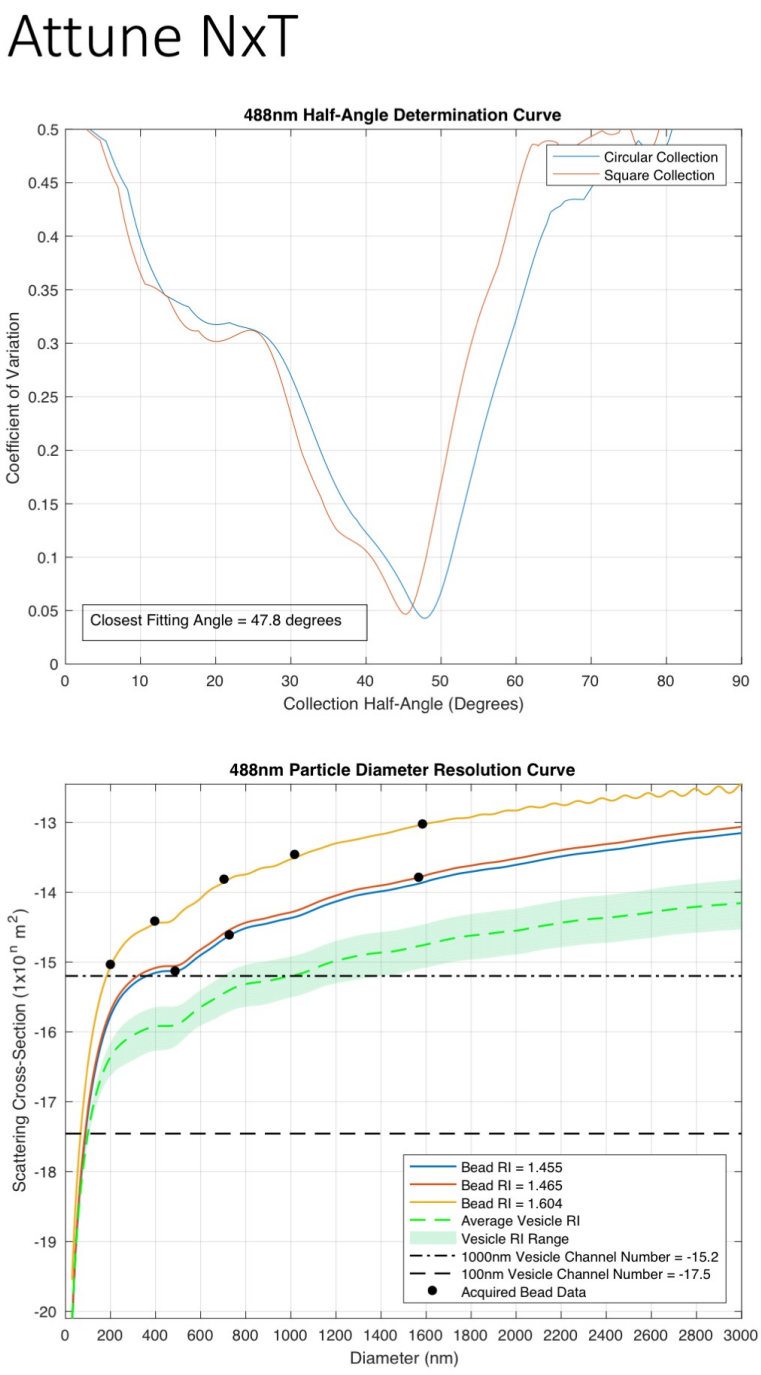

Figure 6.13 | Determined SSC Collection Angle and Geometry Curves for FACS Canto I, and Acquired vs. Modelled Data for the Determined Collection Angle.

Top - Coefficient of Variation (%) represents the deviation from how well acquired NIST bead data fits with different collection half-angles for rectangular and circular model from 0-90°, in 0.05° increments. A coefficient of variation value closer to 0 represents less variation between the acquired and predicted data for that angle, and therefore a better fit. Bottom – shows modelled data of the acquired bead refractive indices from diameters of 0-2000nm, in increments of 10nm. Acquired bead data normalised the predicted data with a median calibration factor (see methods) is overlaid with predicted data to show goodness of fit at the closest fitting collection aperture geometry and collection angle.

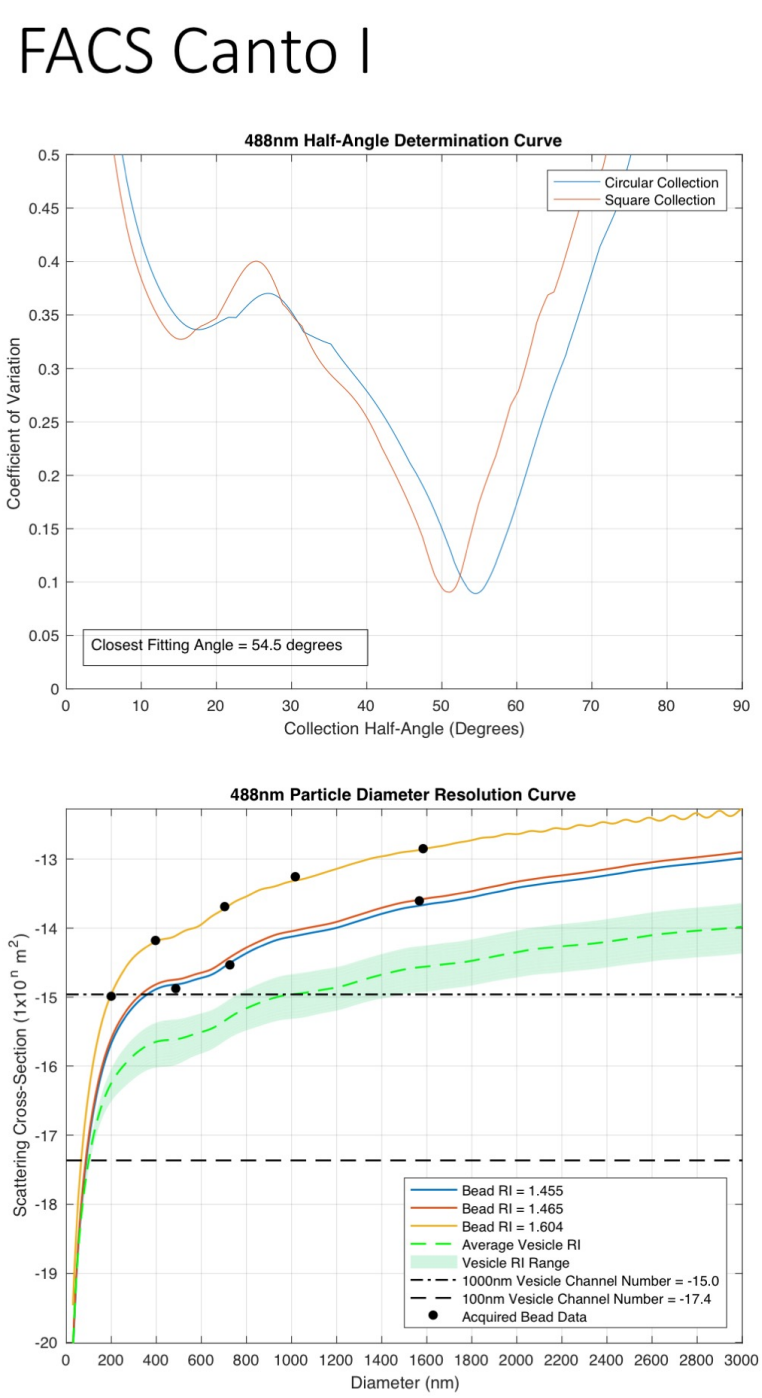

Figure 6.14 | Determined SSC Collection Angle and Geometry Curves for Fortessa X-20, and Acquired vs. Modelled Data for the Determined Collection Angle.

Top - Coefficient of Variation (%) represents the deviation from how well acquired NIST bead data fits with different collection half-angles for rectangular and circular model from 0-90°, in 0.05° increments. A coefficient of variation value closer to 0 represents less variation between the acquired and predicted data for that angle, and therefore a better fit. Bottom – shows modelled data of the acquired bead refractive indices from diameters of 0-2000nm, in increments of 10nm. Acquired bead data normalised the predicted data with a median calibration factor (see methods) is overlaid with predicted data to show goodness of fit at the closest fitting collection aperture geometry and collection angle.

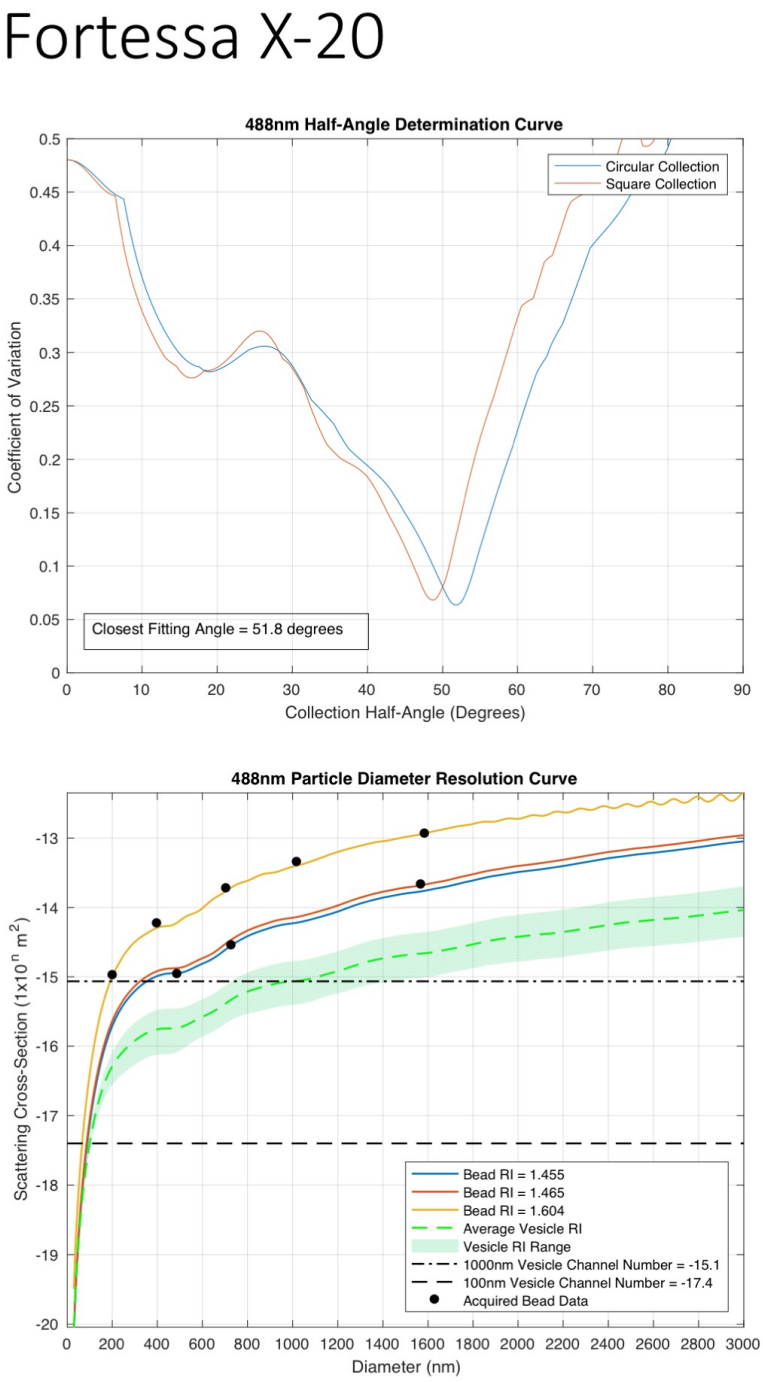

Figure 6.15 | Determined SSC Collection Angle and Geometry Curves for LSR Fortessa and Acquired vs. Modelled Data for the Determined Collection Angle.

Top - Coefficient of Variation (%) represents the deviation from how well acquired NIST bead data fits with different collection half-angles for rectangular and circular model from 0-90°, in 0.05° increments. A coefficient of variation value closer to 0 represents less variation between the acquired and predicted data for that angle, and therefore a better fit. Bottom – shows modelled data of the acquired bead refractive indices from diameters of 0-2000nm, in increments of 10nm. Acquired bead data normalised the predicted data with a median calibration factor (see methods) is overlaid with predicted data to show goodness of fit at the closest fitting collection aperture geometry and collection angle.

+

LSR Fortessa

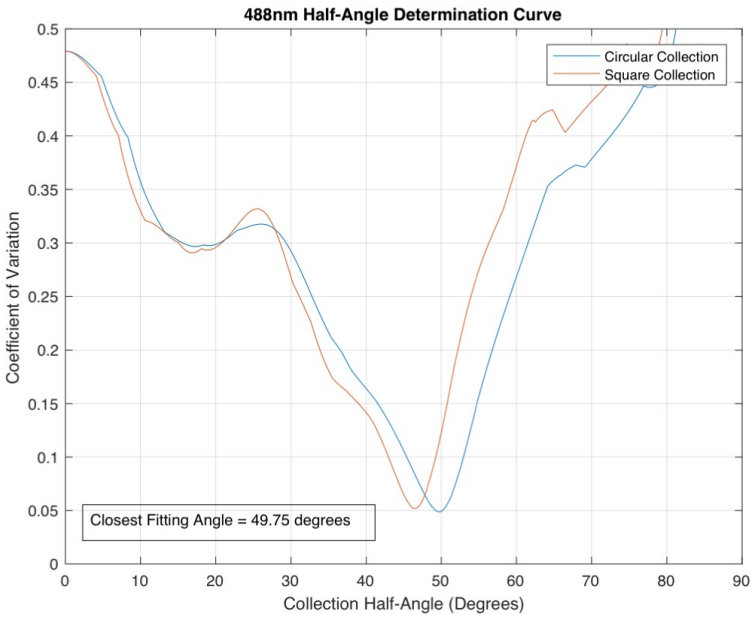

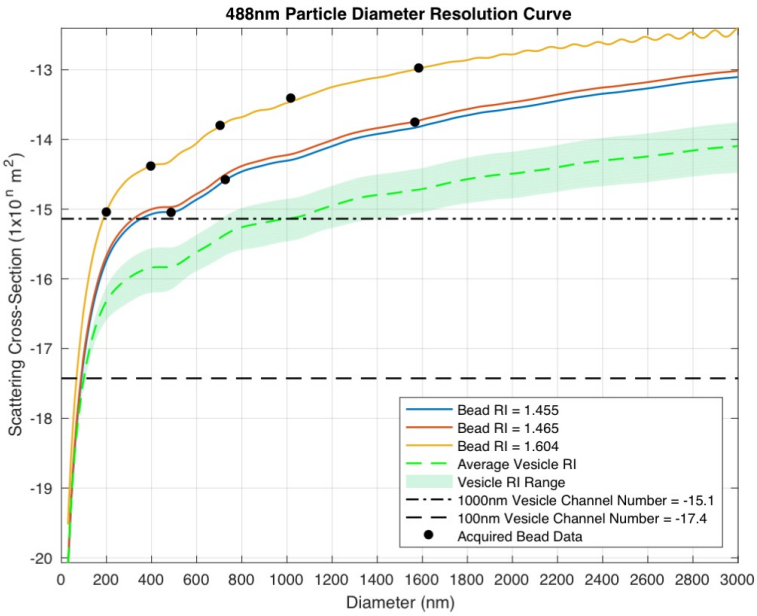

Table 6.5 | Summary of Best Fitting Determined Collection Scatter Angles using Modelling Compared with Collection Angles Determined by Optical Component Geometry.

	Geometric Limiting Angle (°)	Closest Fitting Angle (°)	Difference (%)
Fortessa X-20	52	51.8	0.4
LSR Fortessa	52	49.75	4.5
FACS Canto	52	54.5	4.6
Attune NxT (1)	45 (49.6*)	47.8	5.9 (3.8)

**Attune NxT SSC flow cell limiting angle is 45°, however it is possible for FSC spill over into SSC due to cuvette shape thereby increasing the angle to 49.6°. This is dependent on alignment.*

It can be seen in Table 6.5, that the determined collection angle differ from those calculated using the optical component geometry by a small margin. Determining whether the determined angle fits more closely than those of calculated with the component geometry is tricky. Due to the system implemented here, the determined angle will fit more closely with the acquired bead data due to being selected with the lowest coefficient of variation. This method however relies on the accuracy of the bead RI being reliable. Ideally the bead RI would be known to three decimal places rather than two, and measured independently to verify the manufacturer specifications. The margin by which the collection angles differ is however small enough to use as a standardisation technique to determine the diameter of vesicles account for the RI differences. This technique will also increase in reliability with a larger number of beads being acquired.

This method ideally would be validated on a machine with geometries and refractive indices being meticulously measured, altering the collection angles or geometries with use of slits or apertures would then allow testing and further validation of the modelling protocol.

Using beads alone without determining cFCM SSC collection geometries, to utilise as a standardisation technique is therefore viable and extremely useful. This enables researchers to use modelling as standardisation techniques without companies disclosing proprietary geometries or component refractive indices. This method also only requires users to input their bead data and acquired data readings, without the need for advanced physics.

6.3 Conclusion

As seen in the previous chapter separation index alone, using beads such as Megamix as cut-off values for standardisation, gives no bearing on a flow cytometer's resolution. Modelling is therefore required to determine system resolution, while separation index can be used to monitor the maintenance of a system's resolution over time, and efforts to increase resolution, whereby the collection angles and geometry remain consistent.

When applied to determining the resolution of flow cytometers, modelling appears to be accurate showing good correlation between acquired and predicted data. Rectangular and circular collection geometry profiles can also be seen as a useful distinction in fitting acquired with predicted data.

While there is good correlation between predicted and acquired data, the method currently has limitations. The technique requires the RI of beads to be accurate to at least 3 decimal places. This restriction likely accounts for the variation seen in the results, and accounts for some of the variation seen between the measured optical collection angles and the angles derived from prediction alone. This inaccuracy makes it hard to determine whether the normalisation of acquired data to predicted shows imperfections due to different collection angles within the system, or whether the discrepancies are due to variations in collection geometry either due to tolerances of building or assumed refractive indices.

The development of a fluorescence assay to separate EV subsets from one another, along with residual platelets, which all have distinctive size ranges, correlates well to theoretical data predicted through modelling of flow cytometry equipment. The close fit of acquired bead data, along with the strong correlation of biological data to modelling validates its use as standardisation method for the EV field. This data also shows that the accuracy of bead RI and collection angle calculation may not be perfectly accurate, but it is accurate to infer biological populations, and is therefore accurate enough in its current form to be used a standardisation technique.

Having shown that modelling using the optical component geometry information to determine the collection angle, and validating this method is accurate as a standardisation for biological data, a further alteration was made in order to determine collection angle without the need for proprietary, or unobtainable information required for modelling. This method determined the collection angle of machinery through bead acquisition alone. This method showed little deviation in collection angle compared to the method using optical component geometry, and makes Mie theory as a standardisation technique much more accessible to the community, due to only requiring the acquisition of beads that can be input into a piece of software, instead of obtaining proprietary component information, calculating collection angles, and performing modelling requiring advanced knowledge in scatter physics.

Chapter 7: Conventional Flow Cytometer Optimisation for EV Analysis

7.1 Introduction

Commercial cFCM to date have been developed primarily with the analysis of cells in mind. There are however many different FCM available, with some offering a larger degree of variability in set up than others. In these systems it is possible to make adjustments that will benefit the analysis of EVs.

In this chapter, the aim is to determine if it is possible to adjust variables, predominantly fluidics, to optimise FCMs for EV analysis. The effects on optical resolution and count accuracy will be investigated. The objective is to explore optimisations that will be suitable for users in a communal core facility with limited resources, and no prior engineering knowledge.

7.2 Methods & Results

7.2.1 Flow Rate Optimisation

Flow rate adjusts the size of the core stream a particle is suspended in. When a suspended particle enter the region of core stream the laser intersects, wider core streams will allow for more than one particle to be present, and in different positions relative to the lasers intensity profile.

In order to determine the effect of flow rate, fluorescent polystyrene beads of 100, 160, 200, 240, 300, 500, 900nm diameter (Biocytex, France) were analysed on a FACSAria using low, medium and high flow rates with sheath pressures of 20, 35 and 70 psi, along with 100 and 70µm nozzles. The results were then plotted using separation index units to determine the highest resolution.

It can be seen that the flow rate has a big influence on the resolution of the cytometer for submicron particles in the SSC parameter, Figure 7.1. At each pressure and nozzle, it can consistently be seen the highest resolution is at the lowest flow rate. There is also a trend that higher pressures results in higher resolutions. The same effect of flow rate on increased S.I. units on the FSC detector however is not seen, Figure 7.2.

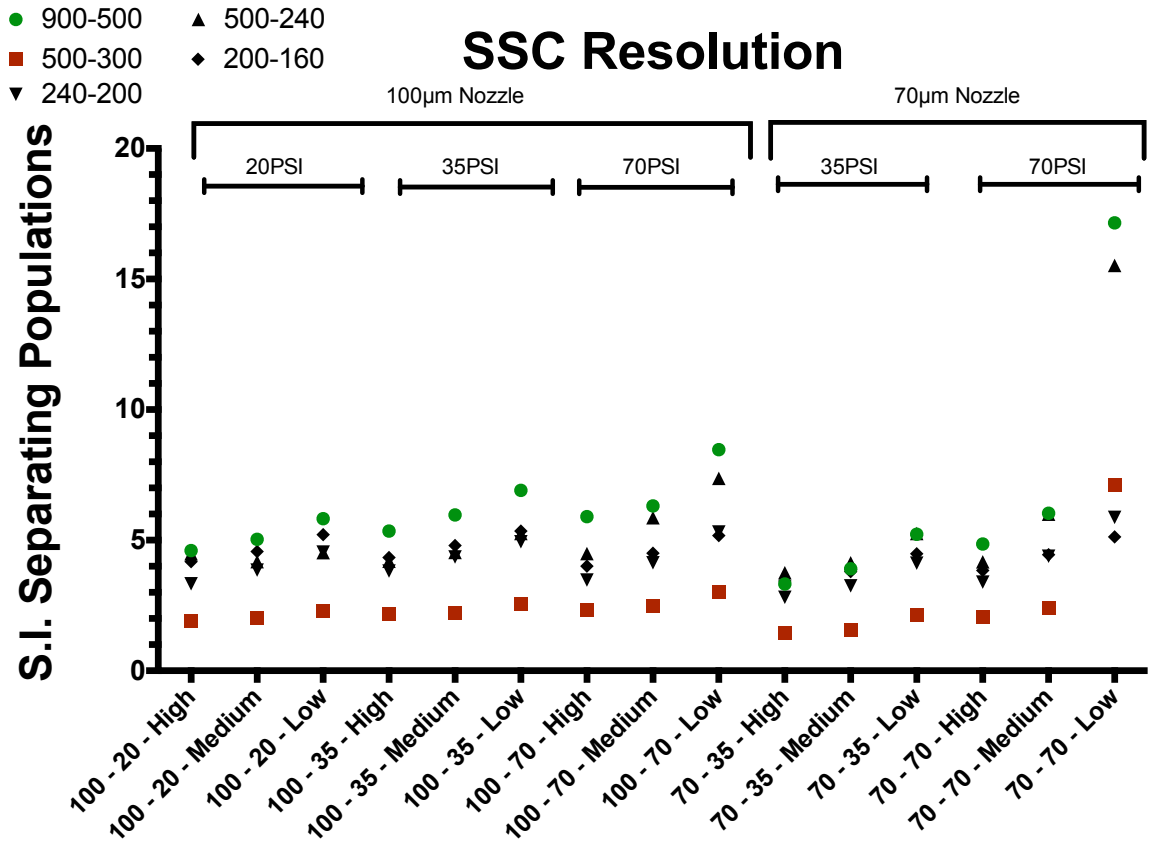

Figure 7.1 | The Effect of Flow Rate, Sheath Pressure, and Nozzle Diameter on FACSAria Bead Resolution.

Fluorescent polystyrene beads (100, 200, 240, 300, 500, 900nm diameter) were acquired at high, medium, and low flow rates. Nozzle diameters (70, 100µm) and sheath pressure (20, 35, 70psi) were tested for their effect on bead resolution. Bead resolution was calculated using separation index units. It can be seen that lower flow rates, and high sheath pressures results in high separation indexes between bead populations.

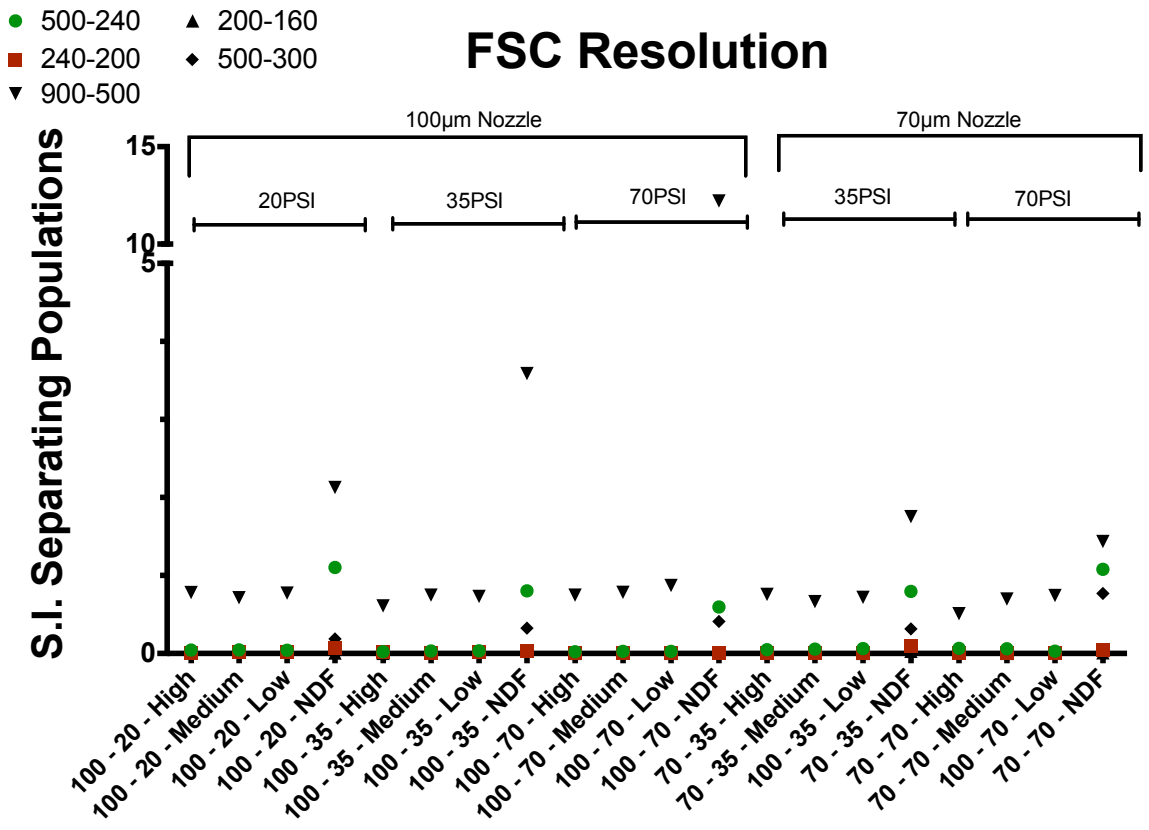

Figure 7.2 | The Effect of Flow Rate, Sheath Pressure, and Nozzle Diameter on FACSAria Bead Resolution.

Fluorescent polystyrene beads (100, 200, 240, 300, 500, 900nm diameter) were acquired at high, medium, and low flow rates. Nozzle diameters (70, 100µm) and sheath pressure (20, 35, 70psi) were tested for their effect on bead resolution. Bead resolution was calculated using separation index units. It can be seen that flow rate does not have large effects on the FSC separation index. Removal of the neutral density filter (NDF) resulted in large separation index between bead populations.

7.2.2 FSC Optimisation

In order to determine the effect of flow rate and the neutral density filter (NDF) on FSC resolution, fluorescent polystyrene beads of 100, 160, 200, 240, 300, 500, 900nm (Biocytex, France) were analysed on a FACSAria using low, medium and high flow rates with sheath pressures of 20, 35 and 70 psi, along with 100 and 70µm nozzles, with and without a NDF. All of these conditions were done with and without a neutral density filter. The results were then plotted using separation index units to determine the highest resolution.

The removal of the NDF causes an increase in signal from all 3 bead populations. Differentiation of 300nm and 500nm populations is possible when the NDF is removed, but not before, Figure 7.3. It can also be seen that flow rate also has an effect on resolution, with lower flow rate increasing the FSC signal at 20psi. It is unclear why there was decreased signal at 70psi, though it is likely to be due to movement of the core stream, and therefore misalignment with the obscuration bar.

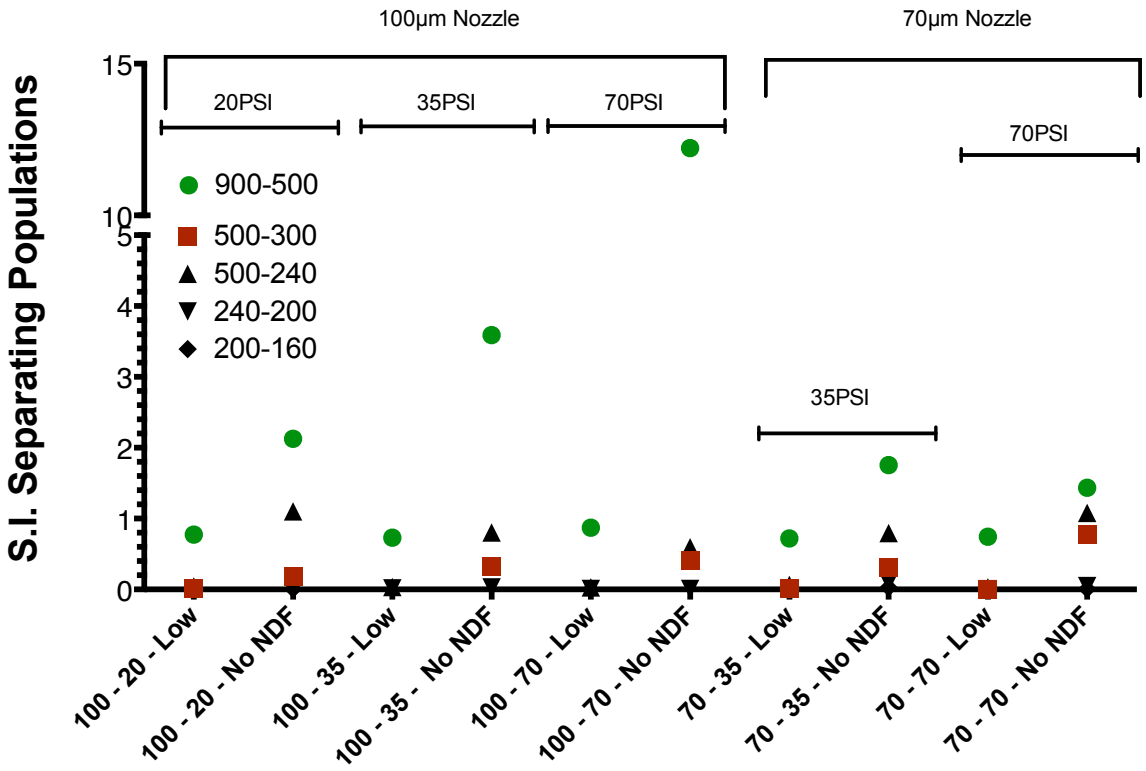

Figure 7.3 | Neutral Density Filter Testing on the FACSAria FSC Resolution

It can be seen that obscuration bar sizes generally had little effect on the FSC resolution, it is clear however that the 2mm blocker bar offered the highest resolution for both 900-500nm and 500-300nm bead differentiation. Wider obscuration bars in this case likely did not increase resolution due to the narrow FSC collection angle in the FACSAria.

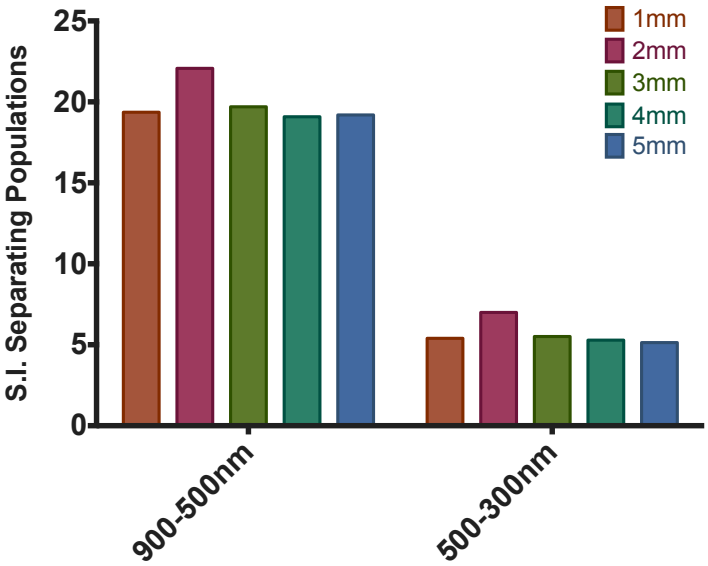

Figure 7.4 | Obscuration Bar Testing on FACSAria

7.2.3 Swarm Detection & Electronic Aborts

'Swarm detection' has become a common term in the EV field, used to describe tens, to hundreds, of small particles in the illuminated region of the core stream simultaneously. These particles alone would not have a high enough signal to trigger an event alone, but cumulatively they are capable of scatter enough light to surpass the threshold and trigger an event, merging their signals and therefore appear as one particle. This has become a common term due to much of the previous literature 'swarm detecting' data. The generally accepted method of determining single particle detection has been to perform serial dilutions. If the curve produces a linear total count with serial dilution it is assumed to be singlets.

Flow cytometry systems however have been developed to detect when multiple particles are present in the interrogation zone simultaneously. This is based on the number of peaks appearing within a certain time frame. Upon this being detected the event is 'aborted' and the count is not recorded. Most cFCMs record the rate at which events are aborted in this manner, and show a current and cumulative figure for the number of events aborted, known as the 'electronic abort rate'. This method of aborting events was developed with large particles; such as cells in mind. Its efficacy for detecting multiple small particles that are above or below the detection limits of the cFCM is relatively unexplored.

The aim of these experiments is to investigate whether even with linear reduction in total counts, events are being swarm detected, and to what degree.

7.2.3.1 Protocol

Polystyrene NIST beads of 203nm and 1587nm (ThermoFisher Scientific, Paisley, UK) were analysed on a Fortessa X-20 at the same voltage, with a SSC threshold for one minute at high, medium, and low flow rates for one minute. Beads were initially recorded at high concentration and serially diluted until the event rate for low flow rates was <500 events/sec. Upon completion of events being recorded, the total electronic abort rate was recorded. Bead concentrations were approximated using their supplied % concentration, and vary up to 10% in concentration.

7.2.3.2 Analysis

Firstly the effect of flow rate, and electronic aborts when compared to analysed bead concentrations was investigated, Figure 7.5. Plotted on the graph are the total number of electronic aborts recorded, along with the total number of unaborted particles recorded.

It can be seen that when serial dilution begins at high concentrations the total unaborted count is lower than the total electronic abort count, signifying the majority of events are being swarm

detected. As the serial dilution continues a peak is reached for the total unaborted count. The unaborted peak is reached at higher concentrations for both 1600 and 200nm beads at the low flow rate, followed by the medium and then high flow rate. Once reaching a peak total unaborted count, the total unaborted count then decreases relatively linearly for all flow rates. The electronic abort count however, is still high despite a linear event rate decrease at higher concentrations, signifying swarm detection, or at least coincidence detection is occurring despite a linear reduction in total event unaborted counts.

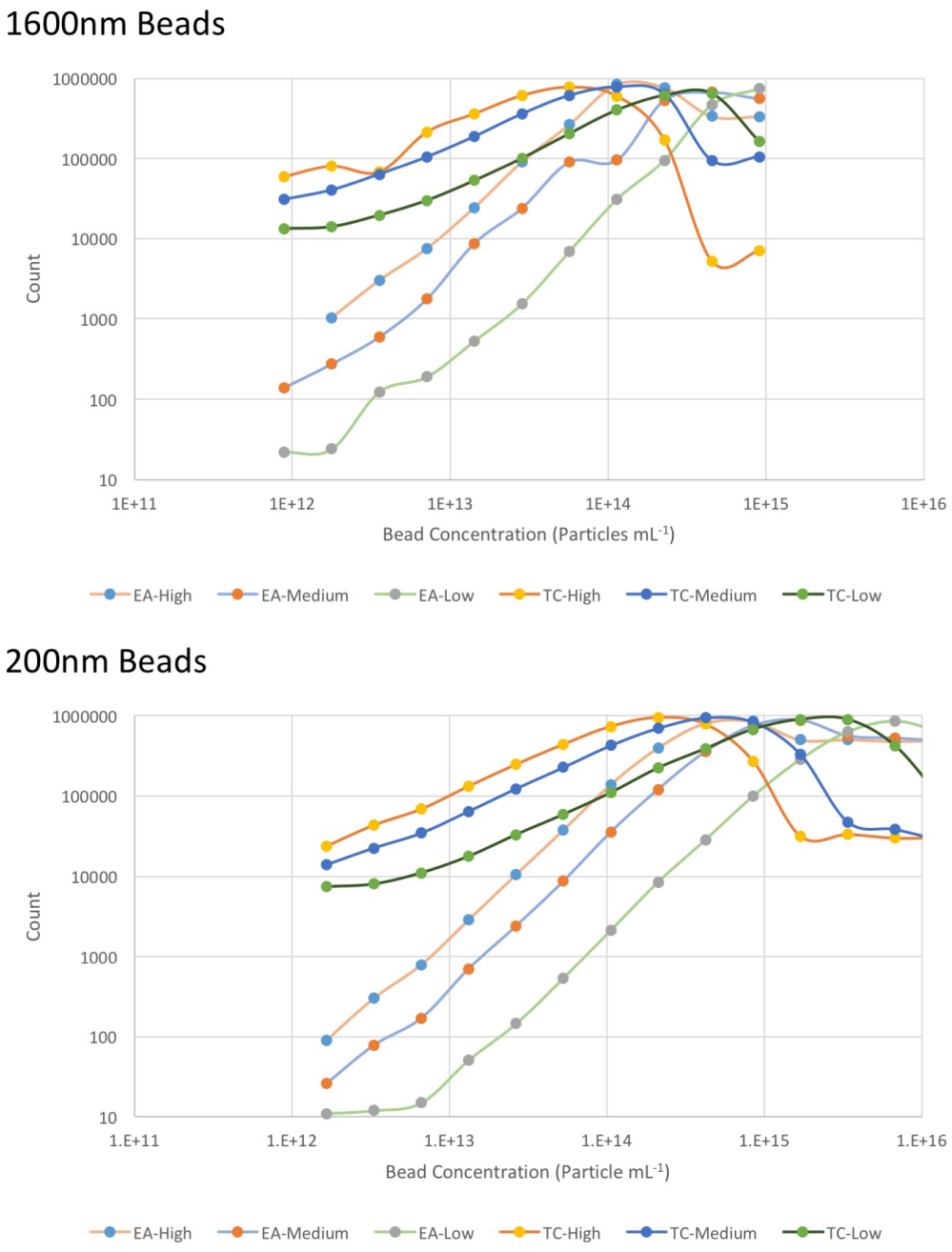

Figure 7.5 | Comparison of Bead Concentration and the Flow Rate on the Amount of Electronic Aborts.

Plotted are the total recorded count (TC) and total electronic aborts (EA) after one minute of analysis of 1600nm beads (top) and 200nm beads (bottom). Total counts and total electronic aborts are shown at high, medium, and low flow rates.

Further analysis of the electronic aborts compared to flow rate were therefore investigated, Figure 7.6.

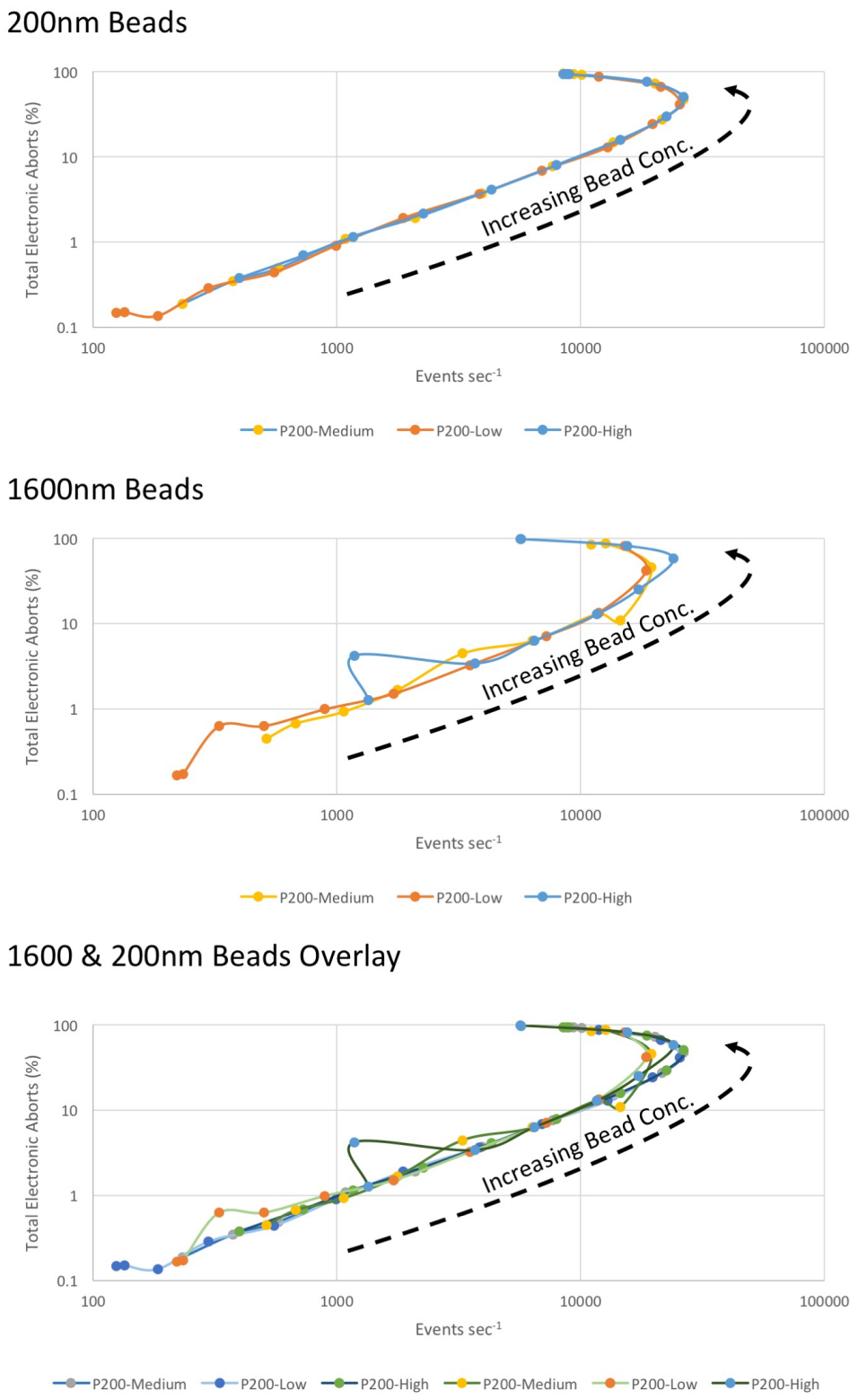

Figure 7.6 | Comparison of Total Electronic Aborts vs. Event Rate.

Plotted are the event rate per second of serially diluted samples, and the percentage of total events that were electronically aborted for 200nm beads (top), 1600nm beads (middle) and an overlay of 200nm and 1600nm data (bottom). Bead concentration increases from bottom to top, with values corresponding to concentrations shown in Figure 7.5.

It can be seen from these results that the percentage of electronic aborts is directly correlated with event rate, regardless of bead size, with 1600nm and 200nm bead data overlapping when data is overlaid. The area of true swarm detection with non-linear event rate compared with total electronic aborts can be seen when electronic aborts is above 50%.

It is not until the event rate is below 1000 events per second, that the total electronic abort rate account for 1% of the sample analysed. Despite linearity in serial dilutions, electronic aborts can account for anything up to 50% of the total sample passing through the interrogation point. Quantifying the portion of electronic aborts in % to event rate should therefore be done in order to obtain accurate counts, not just serially diluting until a linear trend occurs.

7.2.4 Sorter Core Stream Enumeration

Whilst cell sorters offer dexterity in their optimisation, their ability to produce reliable absolute counts is limited due to extended tubing between the sample uptake and the flow cell. The aim of this section is to produce a method of quantifying the core stream volume reliably in order to produce a method of calculating absolute counts by quantifying the core stream volume analysed over time.

A sample of concentrated dye was analysed for a set period of time (1-10mins), with the sample stream collected from between the FACSAria sorting plates. The collected sample was weighed, and using a spectrophotometer the dilution of the original sample was measured, then plotted against a standard curve. The standard curve was then used to determine the amount of original sample analysed within the set period of time, thus calculating the flow rate. An overview of this novel enumeration method can be seen in Figure 7.7.

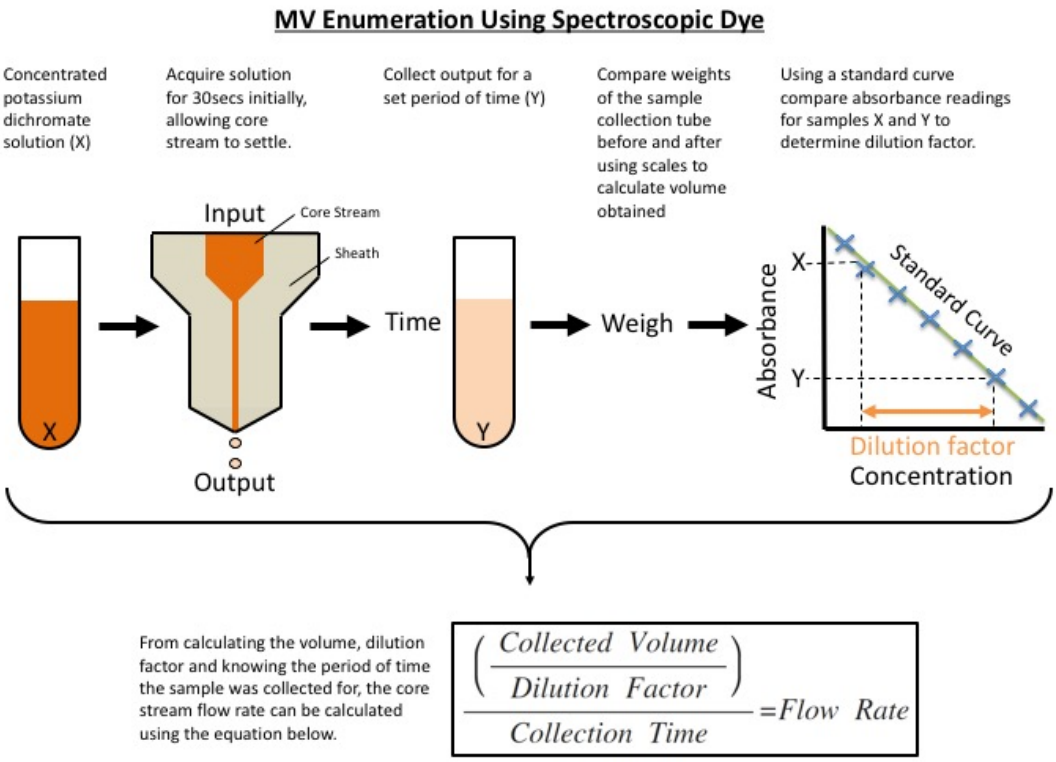

Figure 7.7 | Overview of Novel Flow Rate Quantification Method.

A number of steps were considered in order to reduce the significance of errors caused by the weight or spectroscopic measurements. The standard dilutions were made meticulously in 50mL falcon tubes with measurements in taken in ng. The region of highest spectroscopic accuracy was determined on a spectrophotometer. The sample dye run on the FACSAria was made to be approximately the concentration that would fit within the optimal spectroscopic analysis region upon being further diluted by the FACSAria. The diluted collected sample was analysed on a spectrophotometer, from here the dilution that had occurred could be calculated. This allows calculation of the amount of core stream collected, total sheath collected, and the core stream diameter. Samples were all repeated 3 times and had a mean taken. Spectrophotometer readings were all read twice with the average being used.

In order to reduce errors in core stream quantification, every step had to be as accurate as possible. Arguably the most crucial step was the accuracy of the spectrophotometry reading. It was therefore important that the concentration of dye being analysed was in the area of highest accuracy for the spectrophotometer. The reading given by a spectrophotometer corresponds to the transmission of a particular solution. These readings inherently have a sensitivity range as with all meteorology equipment. At the outer limits of this range the accuracy of the results are more variable.

This sensitivity range was deduced by using the following. If c_0 is the actual concentration and T_0 is the corresponding transmittance of the solution, the errors of each are c and T, respectively. Therefore the transmission measured is $T_0 + T$, which corresponds to $c_0 + c$. This can be summed up as $c_0 + c = c(T_0 + T)$. As can be seen by Figure 7.8, illustrating the –(TlnT)-1 against the optical transmission. A 'U' shape appears. By using this curve, we know that the optical transmission range with the highest accuracy is from ~0.20 to ~0.70.

The preliminary data obtained using this technique is promising and proves the concept. The standard curve can be seen in Figure 7.8. However, the methods needs improvement at the lower concentrations plotted as samples are diluted by 40 to 400 times when analysed. A more accurate spectrophotometer is required or higher concentrations of dye being analysed are required to compensate for the large dilution resulting from the flow cytometer analysis.

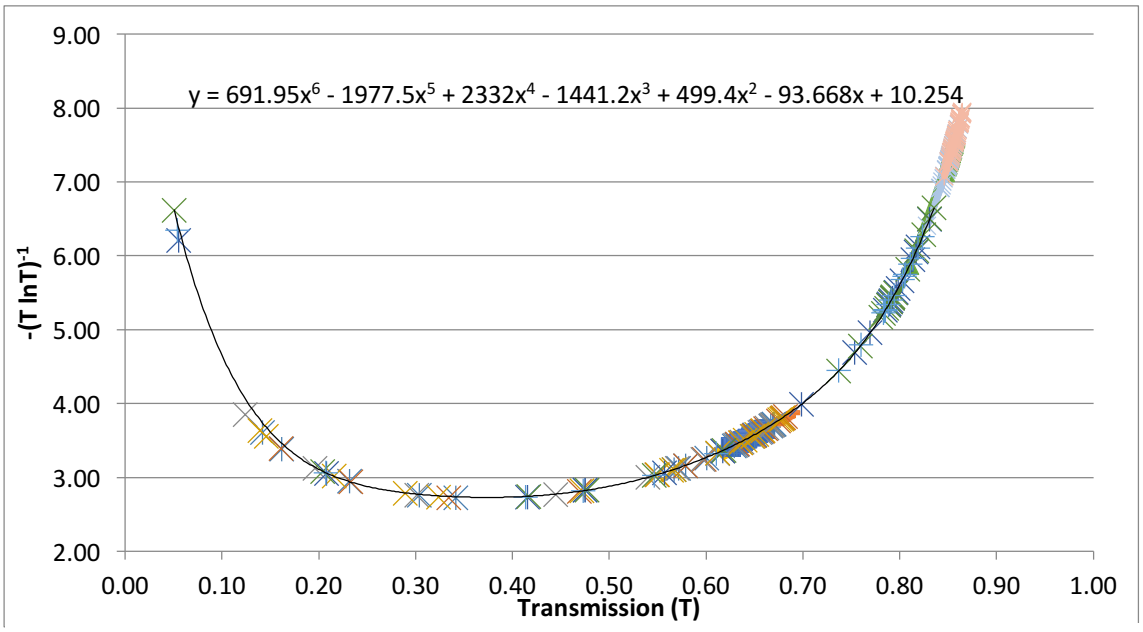

Figure 7.8 | Spectrophotometer Transmission Accuracy Curve.

Plotted using acquired data from spectroscopic analysis of standard dilutions as well as diluted dyes from flow cytometry analysis.

The overall collected streams remains consistent at low and high flow rates, Figure 7.9.

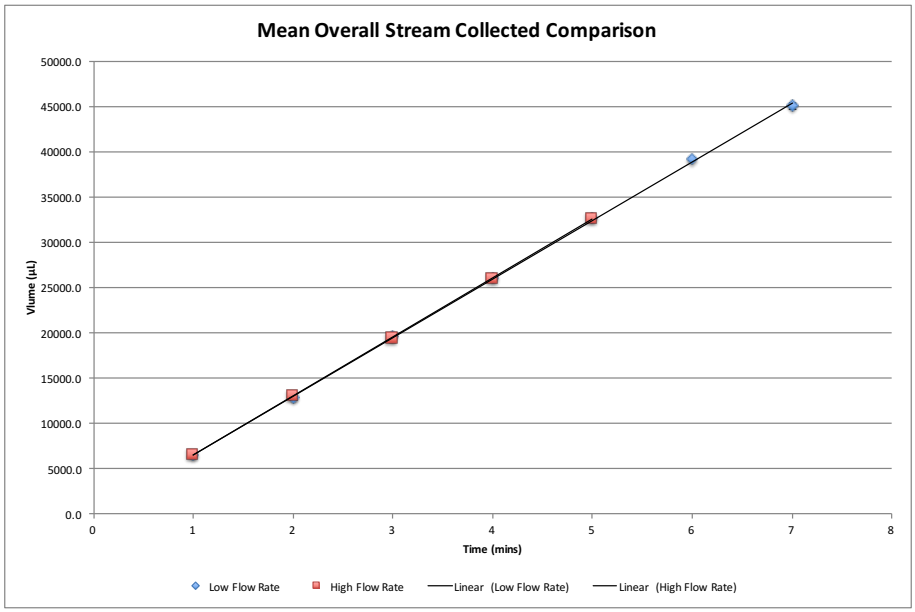

Figure 7.9 | Scatter Graph Showing the Mean Collected Overall Stream After a Set Amount of Time at High and Low Flow Rates.

Error bars indicate one standard deviation.

The overall collect core stream however is more variable at a higher flow rate than a lower flow rate, with larger deviations, Figure 7.10. It appears particularly stable at a low flow rate beyond a 2 minute recording time.

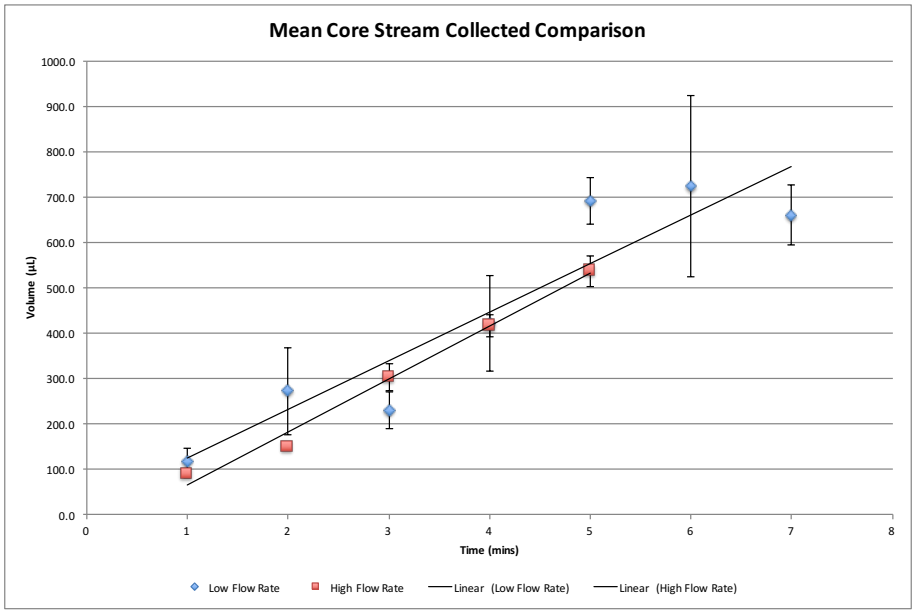

Figure 7.10 | Scatter Graph Showing the Mean Collected Overall Core Stream After a Set Amount of Time at a High and Low Flow Rate.

Error bars indicate one standard deviation.

The overall flow rate at a high and low rates can be seen to be fairly stable at both high and low flow rates, with there being slightly less deviation in the lower flow rate, Figure 7.11.

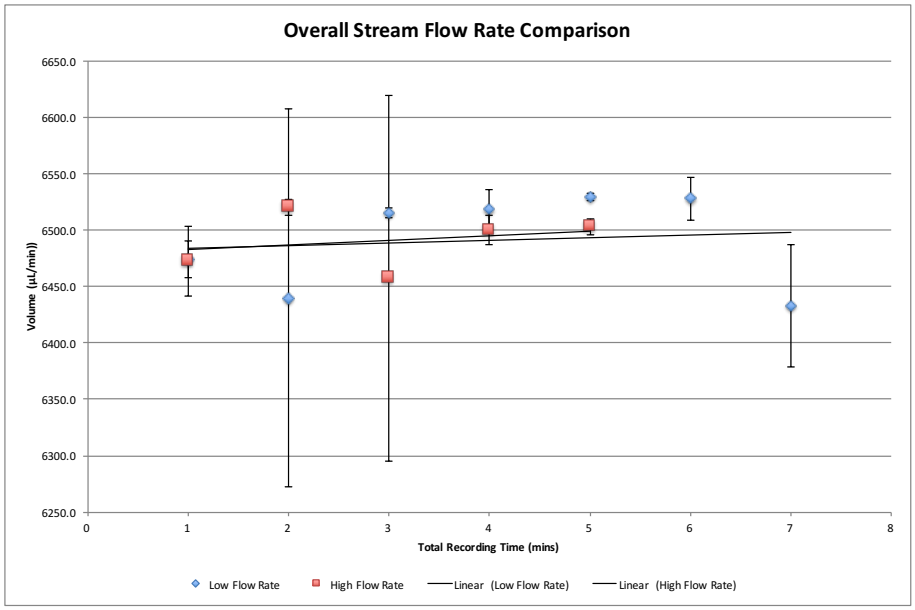

Figure 7.11 | Scatter Graph Showing the Mean Overall Collected Flow Rate at High and Low Settings.

Error bars indicate one standard deviation.

The core stream flow rate can be seen to be more stable at a lower flow rate, than at a higher flow rate, particularly after 2 minutes, where there is only ~10µL difference in the means and standard deviations spanning <20µL, Figure 7.12.

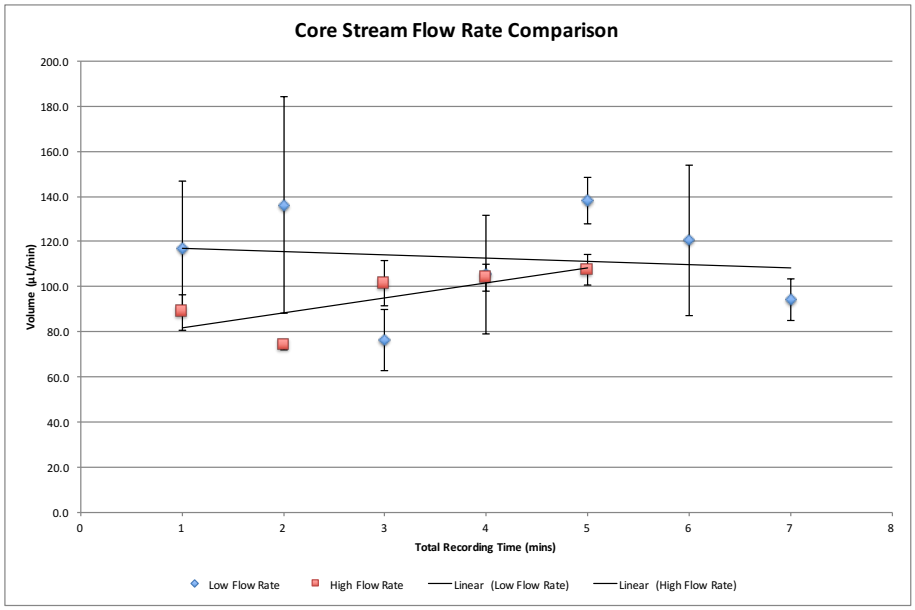

Figure 7.12 | Scatter Graph Showing the Mean Collected Core Stream Flow Rate at High and Low Settings.

Error bars indicated one standard deviation

7.3 Conclusion

It can be seen that large differences in the ability and accuracy of cFCM to resolve EVs is related to how the fluidics of a particular machine are utilised. It can be seen that low flow rates correlate with increased accuracy in resolving smaller particles both in FSC and SSC . This ensures a more consistent stream diameter for small particles to travel through. The result is a more consistent collection angle, along with particles consistently hitting the peak intensity of the Gaussian profile laser beam. Not only was flow rate linked to be important for resolution, but quantifying the event rate per sec to determine what portion of sample is likely going to be electronically aborted is an important finding in ensuring reliable counts.

Fluidic optimisation that was conducted in this chapter had large effects in small particle resolution. These methods are not however implementable to the same extent on cFCMs analysers when comparted to cFCM cell sorters.

Although we have shown the benefits of optimising cell sorters for small particle analysis, this instrumentation has the caveat of not currently being able to determine absolute concentrations of cells using methods such as counting beads. We have therefore also demonstrated a novel technique of quantifying the core stream volume over a period of time in order to calculate the absolute count of particles by quantifying the core stream volume analysed over time.

These novel methods highlight the limits of current cFCMs that have been optimised. These machines are constrained by their optical, fluidic, and electronic design for cells. In order to move on further from here for small particle analysis, a dFCM would need to be designed.

Chapter 8: Effect of Conventional Flow Cytometer Optimisation on Clinical EV Sample Acquisition

8.1 Introduction

In the previous chapters, it has been demonstrated that modelling can be used as a resolution standardisation technique and that various steps can be taken to modify cFCM for EV sample analysis. The benefits of these optimisation steps was investigated on a translation study investigating EVs from clinical samples. The aim of this study was to deduce whether an optimised protocol, based on findings from the previous chapters, affected the outcome of EV counts in clinical samples, when compared to a non-optimised protocol from samples. These samples were well suited to this investigation due to patients' blood volume being diluted by varying amounts upon cardiopulmonary bypass. By using the haemoglobin concentration measurements over the course of the surgery, the extent of dilution could be accounted for and normalised. If the counting method of each protocol was accurate a haemoglobin normalisation factor could account for the reduction in EV concentration.

8.2 Methods

8.2.1 Study Design

The absolute count of extracellular vesicles over the time course of cardiac bypass surgery was investigated using non-optimal and optimised extracellular vesicle flow cytometry procedures. Acquisition protocols, antibody panel design, and acquisition for un-optimised samples were conducted by J. Schofield *et al**. Acquisition protocol, antibody panel design and titration, analysis protocol, and cytometer modelling were conducted by J. Welsh. Sample acquisition was performed by M. Duffield. Statistical analysis was carried out by J. Welsh and M. Duffield. Some of this data has previously been presented as part of J. Schofield and M. Duffield's MMedSc theses.

8.2.2 Ethics

Ethics approval was given by the South Central NRES committee (Ref: 11/SC/0214) and the University of Southampton ERGO committee (Submission ID:14646). All participants provided written informed consent. All sample and participant data were link anonymised, with the master key kept under secure storage.

**This work was conducted as part of an MMedSci project title: "The effect of Cardiac Bypass Surgery on Platelet Microparticles' in April 2013*

8.2.3 Sample Isolation & Storage

19 individuals each donated 9 venous samples (6mL each) throughout the cardiac bypass surgery procedure, ranging from pre-anaesthesia, to 5-days post-operative, Table 8.1. Pre- and peri-operative samples were taken from the sampling port of the central venous and arterial lines. During cardiopulmonary bypass, samples were taken from the cardiopulmonary bypass machine. The 5-day post-bypass sample was taken from a venous cannula. The first 3mL of blood was discarded before collecting the 6mL sample into lithium heparin-coated Vacutainer tubes (BD Biosciences, Oxford, UK). Shear-stress was minimized by breaking the Vacutainer seal prior to sample collection. Samples were centrifuged within one hour twice at 2000*g* for 10 minutes at room temperature, isolating platelet poor plasma (PPP). Samples were initially stored at -20°C until transportation to -80°C freezers.

8.2.4 Sample Preparation

A comparison of key differences between protocols for sample preparation can be found in Figure 8.1.

8.2.4.1 Non-Optimised Sample Preparation

Non-optimised samples were thawed at 4°C for 10mins. 7.5µL of 6.25µg/mL anti-CD41a FITC (BD Bioscience, Oxford, UK), 7.5µL of 6.25µg/mL anti-CD42b PerCP (BioLegend, London, UK), 7.5µL of 6.25µg/mL anti-CD61 Pacific Blue (eBioscience, High Wycombe, UK), and 7.5µL of anti-CD62P PE (BD Bioscience, Oxford, UK) were added to a TruCount tube, before 30µL of PPP was added. After incubation, samples were diluted with 2.5mL of 0.22µm double-filtered phosphate buffered-saline. One set of unstained and isotype matched controls were prepared for total analysis.

8.2.4.2 Optimised Sample Preparation

Optimized samples being thawed at 37°C for 10 minutes. 30µL of PPP was added to 50µL 0.1µm double-filtered HEPES buffered saline (dfHBS) with 3µL of 200µg/mL anti-CD41a BV421 (BD Bioscience, Oxford, UK), 5µL of 400µg/mL anti-CD42b PerCP (Biolegend, London, UK), 5µL of 50µg/mL anti-CD61 APC (BD Bioscience, Oxford, UK), and 20.8µL of 6µg/mL anti-CD62P PE (BD Bioscience, Oxford, UK). Samples were incubated for 5mins before 10µL of 83µg/mL anti-MFGE8 FITC (Cambridge Bioscience, Cambridge, UK) was added and incubated on ice in the dark for a further 10 mins before acquisition. Following incubation, 1mL of 0.1µm dfHBS was added to incubated sample. An appropriate volume of this dilution was transferred to 1mL 1µm dfHBS in a tube with a known number of fluorescent beads for enumeration of the sample volume (TruCount Tubes, BD Bioscience, Oxford, UK), so as to obtained an acquisition rate of 500 events/sec. If the

volume required to obtain below 500 events/sec was below 10µL a mid-dilute tube was used. Isotype matched controls for were used for all colours, were analysed for each sample and diluted to the same extent as their matched antibody.

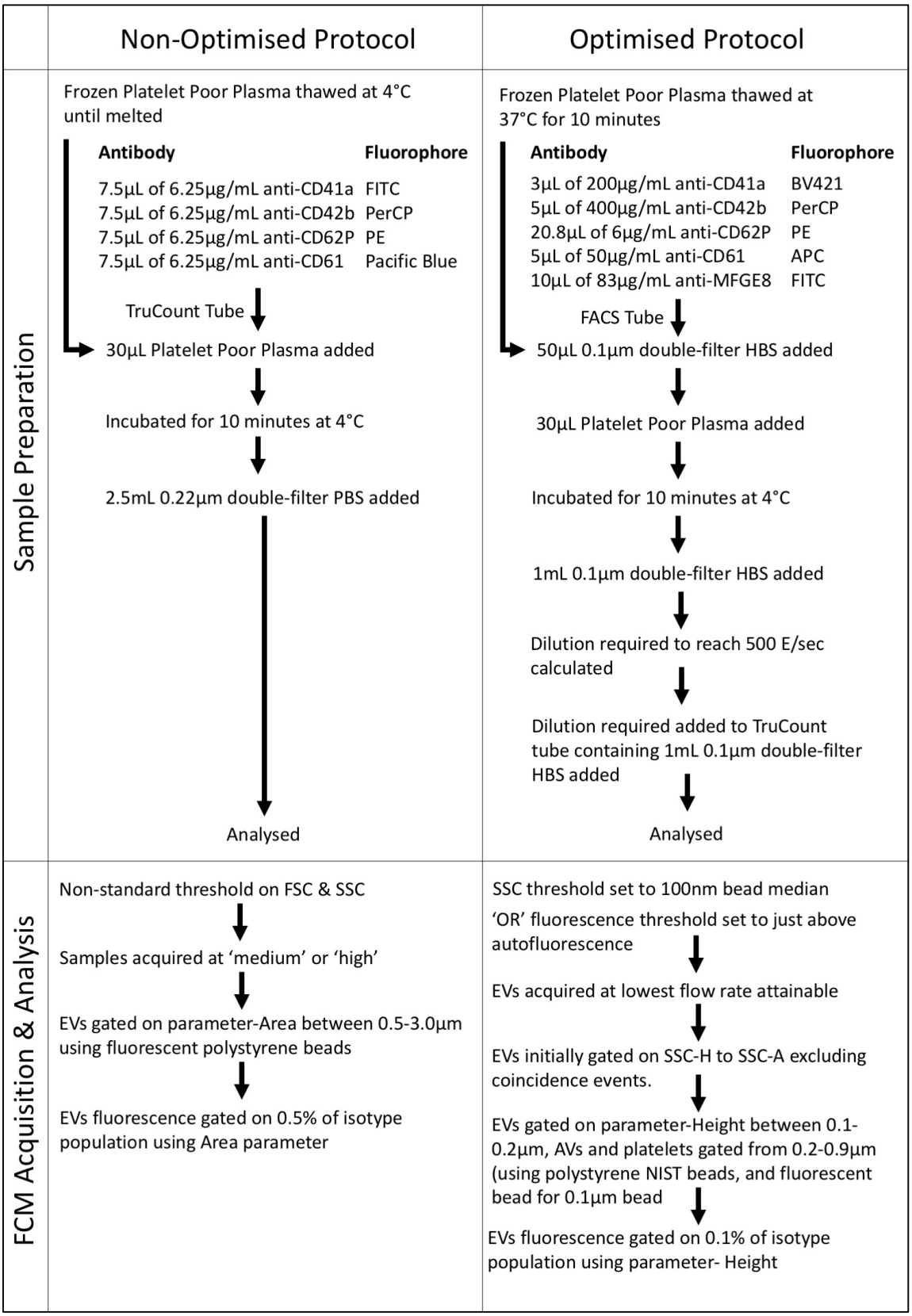

Figure 8.1 | Overview of key difference between the optimised and non-optimised protocols.

8.2.5 Sample Acquisition

Both cytometers picked have identical collection geometries, within the restraints of component manufacturing tolerance. This therefore means resolution standardisation curves using Mie theory will have the same size cut-offs for EV populations. A comparison of key differences between protocols for sample acquisition can be found in Figure 8.1.

8.2.5.1 Non-Optimised Sample Acquisition

Samples were analysed using a FACSCanto II (BD Biosciences, Oxford, UK) with FACSDiva software. Voltages were set to allow fluorescent polystyrene beads (Megamix, Biocytex, France) ranging in diameter from 0.5 to 3 µm, and TruCount beads within the FSC -A vs. SSC -A window. Compensation settings were calculated manually using fluorescently labelled platelet microvesicle populations (CD41a Pacific Blue, Annexin V FITC, Annexin V PerCP and Annexin V PE). Samples were analysed at medium or high flow rates until approximately 15,000 to 30,0000 TruCount beads had been obtained (gated on FSC-A vs. SSC-A).

8.2.5.2 Optimised Sample Acquisition

A BD Special Order LSRFortessa X-20 using FACSDiva 8.0 software (BD Biosciences, Oxford, UK) was used for EV sample acquisition and analysis. 100, 300, 500, 900nm fluorescent polystyrene beads (Megamix Plus FSC , Biocytex, France) were analysed on FSC-H, SSC -H. SSC and FSC voltages were increased until the 900nm population appeared in the upper right corner of a plot without detector saturation. A SSC threshold was set using the median SSC-H parameter of 100nm polystyrene fluorescent beads. 100, 200, 400, 700, 1000nm Polystyrene and 500, 700, 1000nm silica NIST beads (Thermofisher Scientific, Loughborough, UK) were then recorded a set thresholds and voltages for Mie scatter reference. Beads coated with anti-immunoglobin molecules (CompBeads) (BD Bioscience, Oxford, UK) independently stained with each fluorophore at the same concentration as samples, stained for 20 mins before acquisition, were analysed for each fluorophore, increasing the voltage for each until at the top of fluorescence-H log plot. An unstained sample was then analysed at the set fluorescence and scatter voltages. Appropriate thresholds were then set on 'OR' for each fluorescent channel, just above autofluorescence. All samples were analysed for initially for 30 seconds at the lowest flow rate attainable, allowing the core stream to stabilise, before being recorded for 6 minutes. Samples were diluted until an event rate of $\leq$500 events/sec was stable, with limited electronic aborts.

8.2.6 Data Analysis

8.2.6.1 Non-Optimised Data Analysis

Data analysis was carried out on FACSDiva software. Microvesicles were defined using polystyrene fluorescent beads of 0.5-3.0µm, with manually drawn gates of FSC-A vs. SSC-A dot plots. Data was reanalysed so as to have more representative results, with singlet gating being used on SSC-H vs. SSC-A plot. Fluorescence gating was re-done using the Height parameter with isotype controls for background fluorescence reference. The gating strategy resulted in 14 discrete subpopulations of platelet microvesicles.

8.2.6.2 Optimised Data Analysis

Data analysis was carried out on imported FCS 3.0 files using FlowJo v10.0.8 (FlowJo LLC, Ashland, USA). Compensation matrices were first set, using CompBead data with the automated compensation matrix set up in FlowJo.

Gating of MVs populations, based on Mie theory studies shown in previous chapters, was done between the bottom of the 100nm fluorescent polystyrene population (threshold set to median 100nm) and modal 200nm polystyrene NIST population. The AV population was set from the modal 200nm population to the 900 fluorescent polystyrene population. The total population (MA) was gated from lower 100nm fluorescent bead population up to the modal 900nm population. Fluorescent gating of negative events was done using isotype-matched controls for every patient. A bisector tool was used to set the left-hand gate at 99.9% of the population for each fluorophore-H measurement. Events appearing above this gate were assumed positively stained. These gates were then layered in order to identify specific EV subsets. MFGE8-FITC stained populations, as an exception, used a negatively stained population in order to determine positive events.

The gating strategy employed resulted in a total of 69 unique phenotypes. A subset of which were chosen for the analysis in the subsequent chapter, in order to have a manageable number of parameters to analyse.

8.2.7 EV Count Normalisation

Absolute EV counts were calculated by analysing stained samples in TruCount tubes (BD Bioscience, Oxford, UK). TruCount beads were gated on APC-Cy7-H vs. BV510-H. Absolute counts were then calculated using the following equations. Note, sample volume allows for dilution of

the sample with antibody mastermix, and further dilutions that allowed for events rates ≤500 events/sec.

$$Absolute\ MV\ count = \frac{Total\ TruCount\ bead\ no.}{Recorded\ TruCount\ beads} \times \frac{Recorded\ Parameter\ count}{Sample\ Volume\ in\ TruCount\ Tube}$$

8.2.8 Statistical Analysis

Data was analysed using Statistical Package for the Social Sciences (SPSS) Version 23.0 (IBM, New York, USA), and GraphPad Prism 6 (GraphPad Software Inc., La Jolia, USA). Time-points were compared using Wilcoxon matched pairs signed rank tests. The un-optimised samples here are likely swarm detecting EVs and predominantly measuring residual platelets due to gating from 500-3000nm on polystyrene beads. Therefore, the optimised sample were compared using the residual platelet and apoptotic vesicle gate (200-900nm polystyrene beads), rather than the true MV gate (100-200nm polystyrene beads).

8.3 Results

Due to the small sample size analysed only all CD41a+, all CD61+, all CD62P+, all CD42b+, phenotypes were compared and summarised in Figure 8.2 and Table 8.1.

The majority of counts across all CD markers for sampling (T0 to T8) are significantly different, with the optimised protocol consistently being showing higher counts than that of the non-optimised protocol. The standard error in the optimised protocol counts is also consistently lower than that of the non-optimised protocol counts.

Furthermore, the haemodilution correction, which attempts to account for the dilution of MVs due to cardiopulmonary bypass, can account for the drop in MV count with the optimised protocol. Haemodilution alone however does not account for the drop in MV concentration in the non-optimised protocol, indicating there is a mismatch between the amount of dilution and drop in MV count.

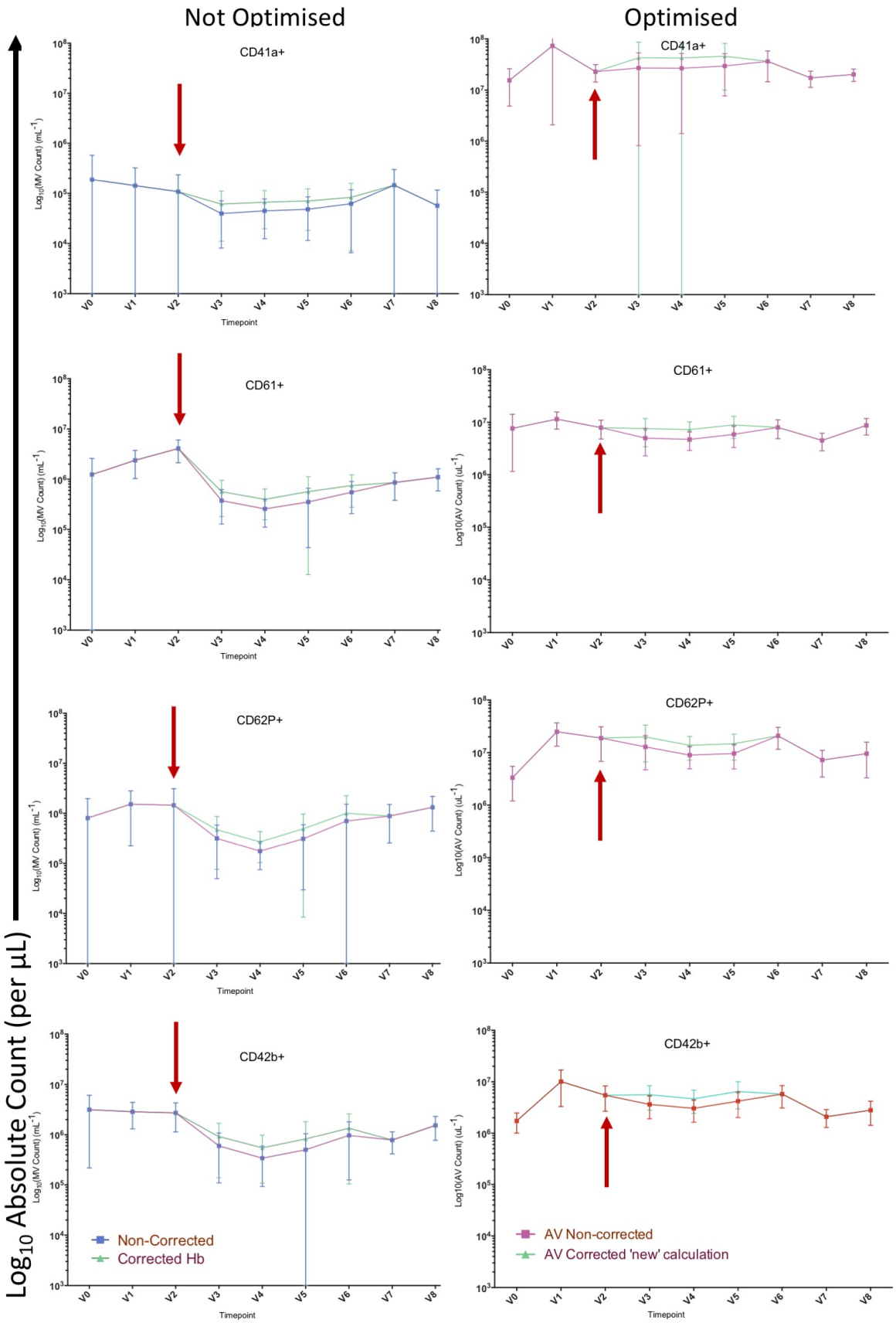

Figure 8.2 | Summary Graphs of Results of CD41, CD61, CD62P, CD42b Only Phenotypes from Optimised and Non-Optimised Sample Preparation and Analysis Protocols.

Non-haemocorrected PMV count (blue symbols/lines) and haemocorrected PMV count (green symbols/lines) (mL^{-1}) (logarithmic scale from $1x10^3$ to $1x10^8$) vs venous sampling point. A) CD41a+ B) CD42b+ C) CD61+ D) CD62P+. Data displayed is mean values with 95% confidence intervals.

Time-point descriptions are shown on Table 8.1. Red arrows indicate individuals being placed on cardiopulmonary bypass.

Table 8.1 | Summary Data from Wilcoxon-Matched Pairs Signed Rank Test Comparing Optimised and Non-Optimised Protocols for Counting Platelet MVs.

Sample Point	Stage of Surgery	CD41a	CD61	CD62P	CD42b
T0	Pre-operative, Post anaesthetic induction,	0.0431	0.8927	0.0431	0.0796
T1	Intra-operative, Pre-heparin administration	0.0001	0.0141	0.0002	0.0001
T2	Intra-operative, Post-heparin administration	0.0001	0.2122	0.0486	0.0001
T3	On cardiopulmonary bypass, Pre-aortic cross clamping	0.0002	0.0065	0.0002	0.0002
T4	On cardiopulmonary bypass, 10mins post-aortic cross clamping	0.0001	0.0005	0.0001	0.0001
T5	On cardiopulmonary bypass, 10mins post-aortic cross clamp removal	0.0002	0.0021	0.0002	0.0002
T6	Post-cardiopulmonary bypass, Post-protamine administration	0.0001	0.0055	0.0002	0.0002
T7	24-hours post-operative	0.0002	0.0021	0.0002	0.0021
T8	5-days post-operative	0.0010	0.0355	0.0010	0.0052

Highlighted (red) results represent $p<0.05$ and therefore a statistically significant difference between the optimised and non-optimised values.

8.4 Conclusion

These results have shown that the optimisation protocol steps produced more reliable, higher EV counts, with the ability to account for dilution occurring *in vivo*, during cardiac bypass surgery, using haemodilution normalisation. The non-optimal protocol analysis was unable to normalise the dilution factor using haemodilution normalisation, as well as producing lower, more varied EV counts. These results therefore nicely show the benefit to clinical sample analysis of modelling as a resolution standardisation technique, over previous attempts of bead calibration, as well as conventional flow cytometer optimisation discussed in Chapter 7:. Whilst the comparison of protocols is not perfect due to many varying aspects of the protocols differing, the results do show a representative effect of the summation of non-optimal procedures in the final results when comparing the methods. Future work may wish to pick individual areas of the protocol to alter, in order to accurately pinpoint what steps the largest differences in count accuracy can be attributed to. It is however most likely that the medium and high flow rates are the biggest factor in variability between results in the non-optimal protocol. This combined with a single dilution for all samples likely meant swarm detection frequently occurred, and would account for the significant decrease in counts seen. Now reliable standardisation techniques, and optimal settings

of the cFCMs for EV analysis have been discovered, clinical sample analysis can now be conducted.

Chapter 9: Clinical EV Sample Analysis: Non-Alcoholic Fatty Liver Disease

9.1 Introduction

Non-alcoholic fatty liver disease (NAFLD) is estimated to affect 10-40% of adults worldwide, and in developed countries is the most common liver disease in adolescents and children. There currently exist no effective medical treatments that are capable of completely reversing the disease other than dietary alterations, lifestyle changes and bariatric surgery. NAFLD is a progressive condition (Figure 9.1) characterised by the excess accumulation of fat in hepatocytes; steatosis. Steatosis often leads to hepatocyte injury with portal and lobular inflammation, non-alcoholic steatohepatitis (NASH). From here cirrhosis can occur, with some individuals then developing hepatocellular carcinoma (HCC). HCC has also been shown to occur in the absence of cirrhosis. NAFLD can be diagnosed or detected with imaging, but lesions of NASH can only currently be observed definitively with liver biopsies. A non-invasive diagnosis of NASH is therefore required for diagnosis purposes as well as follow-up monitoring of patients.

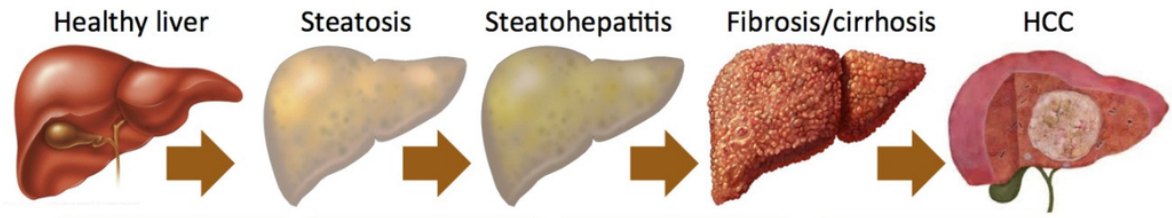

Figure 9.1 | Stages of NAFLD Progression from Healthy Liver, to Hepatocellular Carcinoma (HCC).

Edited image[167].

NAFLD is frequently associated with diabetes[168]. Both NALFD and diabetes are associated with increased cardiovascular risk factors and mortality. Type 2 diabetes mellitus (T2DM), NAFLD and obesity are insulin-resistant states that have all been associated with variation in EV subsets, when compared to those of healthy controls, Table 9.1. Individuals with central obesity are at an increased risk of insulin resistance, therefore increasing the risk of developing T2DM or NAFLD. Individuals with T2DM are also thought to be more susceptible to developing a more severe form of NAFLD. Currently only one publication has investigated EV subsets as potential biomarkers for NALFD[169]. EVs from several derivations are likely involved in NAFLD due to increased cardiovascular risk, and inflammation associated with the disease, and also correlated with increased EV concentrations, Table 9.1.

Table 9.1 | Studies Conducted to Date using MVs as Biomarkers in T2DM, NAFLD and Obesity.

Disease	Procoagulant Marker	Microvesicle markers (⋀ increase, ⋁ decrease, Ξ maintained)	Author
T2DM	Annexin V	⋀CD31+/CD42-, CD31+/CD42+, CD51, CD45, ΞCD62e	Feng et al., 2010 [170]
	Annexin V	⋀ total microvesicles CD142, CD66e, CD61	Diamant et al., 2002 [171]
	N/A	⋀ CD62P, CD63	Shouzu et al., 2004[183,]
	N/A	⋀ CD62P, CD63, CD14	Ogata et al., 2005, 2006 [172, 173]
	N/A	⋀ CD31, CD105, CD106	Tramontano et al., 2010 [174]
	N/A	⋀ CD42	Nomura et al., 1995 [175]
	Annexin V	⋀ CD62P, GPIX, CD63, PAC-1, CD14,	Nomura et al., 2004[176]
	N/A	⋀ CD144, Ξ CD41	Bernard et al., 2009 [177]
	N/A	⋀ CD42a/CD42b	Nomura et al., 2011[178]
	N/A	⋀ CD42b	Koga et al., 2006 [179]
	Annexin V	⋀ CD45, CD66b, CD14	Sabatier et al., 2002[180]
	N/A	⋀ CD62P, CD40	Tan et al., 2005 [181]
	Annexin V	⋀ CD31+/CD42b-, CD31+/AnV+	Jung et al., 2011 [182]
	Annexin V	⋀ CD42a/42b	Nomura, 2009[183]
	Annexin V	⋀ CD144, CD41, CD62P	Tsimerman et al., 2011[184]
	Annexin V	⋀ CD142	Sommeijer et al, 2005[185]
NAFLD	Annexin V	⋀ CD14, ⋁ CD41, CD15	Kornek et al. 2012[169]
Obesity	Annexin V	⋀ Total microvesicles	Goichot et al., 2006[186]
	Annexin V	⋀ CD31, CD42b	Esposito et al., 2006[187]
	N/A	⋀ CD144	Gunduz et al., 2012[188]
	Annexin V	⋀ Total microvesicles, ⋀ CD41+, CD31+/CD41-	Stepanian et al, 2013[189]
	N/A	⋀ CD41+	Murakami et al, 2007[190]
Platelets Markers – CD41, CD42, CD31, CD61, CD62P **Endothelial Markers – CD144, CD105, CD106, CD31, CD61, CD62P** **Leukocyte Markers – CD14, CD15** **Macrophage/Monocyte Markers – CD14, CD15, CD105** **Universal Markers – Annexin V, CD63**			

9.2 Study Aims

The aim of this study is to investigate EV modulation within NAFLD with regard to several aspects of the disease, Figure 9.2. Questions to be answered include:

1. Which MV and AV phenotype concentrations are highest in NAFLD?
2. How do PMV, EMV, and LMV concentrations differ in NAFLD with regard to treatment group at baseline, obesity, sex, and metabolic syndrome?
3. What is the relationship between EV concentration and liver fibrosis in NAFLD?
4. What is the relationship between EV concentration and liver & systemic inflammation?
5. What is the relationship between EV concentration and steatosis?

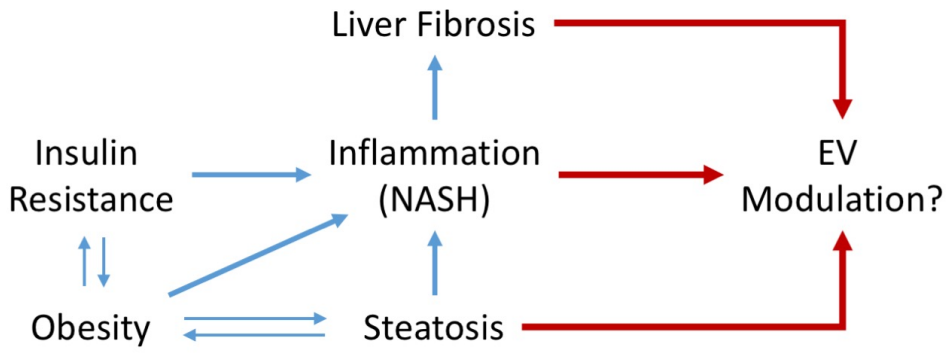

Figure 9.2 | Investigation of EV Modulation in NAFLD .

Shown are the interacting factors in the progression and development of NAFLD to liver fibrosis (blue) with the effects that could lead to EV modulation (red).

9.3 Methods

9.3.1 Study Design

Here EMV and LMVs were analysed implementing overlapping markers, allowing a detailed phenotypic analysis of subpopulations within NAFLD. The modulation of platelet, endothelial, and leukocyte EVs in individuals with NAFLD was investigated, in a subset of samples from a larger study. The design and rationale for the WELCOME (Wessex Evaluation of fatty Liver and Cardiovascular markers in NAFLD with OMacor Therapy) study have previously been reported[191]. Briefly 103 participants were randomized to either Omacor (docosahexaenoic acid (DHA) + eicosapentaenoic acid (EPA)) 4 g per day (n = 51) or 4 g per day of placebo (olive oil; n = 52). DHA+EPA and placebo capsules were gelatine coated and of similar appearance and taste. Erythrocyte EPA and DHA enrichment were (between baseline and end of study) to test adherence to the intervention in the DHA+EPA group and for contamination monitoring with DHA and EPA in the placebo group. Allocated medication compliance was also monitored by recording

returned unused capsules[192]. 44 patient samples were selected from the WELCOME Trial cohort, to determine the use of EVs as biomarkers for NAFLD. The subgroup was selected to represent the characteristics of the full study population based on (age, sex, treatment groups, body mass index (BMI), and fibrosis severity). Here only baseline data, and not post-treatment data is presented. Overall study design, recruitment, sample collection and all non-EV measurements were performed by Prof C. Byrne's research team. EV acquisition protocol, antibody panel design and titration, analysis protocol and cytometer modelling were conducted by J. Welsh. Sample acquisition was performed by H. McMillan, M. Duffield and J. Welsh. Sample analysis and statistical analysis was carried out by J. Welsh.

9.3.2 Ethics

The WELCOME study was approved by the Southampton and South West Hampshire local research ethics committee (08/H0502/165). All participants gave informed written consent. Omacor (DHA+EPA as ethyl esters), also known as Lovaza, was provided free of charge by Pronova BioPharma/Abbott (Pronova BioPharma ASA, Lysaker, Norway; Abbott Laboratories, Southampton, UK). The conduct of the trial, data analyses, and manuscript writing are all undertaken by the authors and are completely independent from Pronova BioPharma/Abbott.

9.3.3 Quantifying and Predicting Liver Fibrosis

Many ways of scoring liver fibrosis, and predicting liver fibrosis have been proposed. Methods used within the WELCOME trial are as follows.

9.3.3.1 Scheuer Fibrosis Score, 1991

The Scheuer Fibrosis Score is a histological scoring system of liver fibrosis, with grades 0-4. 0 = no fibrosis, 1 = enlarged, fibrotic portal tracts, 2=periportal or portal-portal septa but intact architecture, 3=fibrosis with architectural distortion but no obvious cirrhosis, 4=probable or definite cirrhosis[193].

9.3.3.2 Kleiner Score, 2005

The Kleiner Score, is a histological feature scoring system developed for use in clinical trials as a NAFLD stage score. The Kleiner score is composed of 14 histological features including steatosis (0-4), lobular inflammation (0-2), hepatocellular ballooning (0-2), and fibrosis (0-4)[194].

9.3.3.3 Fibrosis score, 2007

The Fibrosis Score, is a result of regression modelling using a variety of variables and is aimed at distinguishing fibrosis severity of 0-2 from 3-4. The resulting formula is as follows:

$$-1.675 + 0.037\times Age(years) + 0.094\times BMI\left(\frac{kg}{m^2}\right) + 1.13\times IFG/Diabetes(yes-1, no=0) + 0.99\times\frac{AST}{ALTratio} - 0.013\times platelet\ count\ (\times 10^9/L) - \ 0.66\times albumin(g/dL).$$

IFG = Impaired fasting glucose, AST=aspartate transaminase, ALT=alanine transaminase. The cut-offs values for the categories are: >0.676, High likelihood of advanced fibrosis, –1.455-0.676, intermediate likelihood of advanced fibrosis, <–1.455 low likelihood of advanced fibrosis[195].

9.3.3.4 Enhanced Liver Fibrosis (ELF) score, 2008

The ELF score, distinguishes fibrosis severity of 0-2 from 3-4. Using the formula:

$$LN(HA)\times 0.681 + LN(PIIINP)\times 0.775 + LN(TIMP1)\times 0.494 - 7.412$$[196].

LN=Natural Log, HA=Hyaluronic Acid, PIIINP=Type III Procollagen Peptide, TIMP1= TIMP Metallopeptidase Inhibitor 1.

9.3.4 Quantifying Fat Accumulation

9.3.4.1 Hepatic Fat Fractionation

This method involves calculating the hepatic fat fraction (HFF) as a percentage using the difference between in phase and out of phase measurements using proton spectroscopic imaging, a technique based on detecting the magnitude of chemical shifts [197].

9.3.4.2 Magnetic Resonance Spectroscopy

This method involves quantification of hepatic fat compared to water by using magnetic resonance signal intensities from images[198].

9.3.4.3 Dual-Emission X-ray Absorptiometry

This method involves calculating density using two x-ray beams of varying energy levels. The absorption of these beams can be then converted into a measure of specific soft tissues through signal attenuation[199].

9.3.5 Circulating Inflammatory Factor Measurement

Tissue inhibitor of matrix metalloproteinase-1 (TIMP-1) and hyaluronic acid (HA) were analysed using an ELISA kit Dynex DS2 platform. The Procollagen-III N-terminal Propeptide (PIIINP) assay was performed with a UniQ radioimmunoassay kit supplied by Orion Diagnostica (Product no.68570). IL-10, IL-8, MMP-9, MCP-1, IL-6, TNFα were measured on the Meso Scale Discovery (MSD) assays (Meso Scale Diagnostics LLC, Maryland, USA).

9.3.6 Sample Isolation & Storage

Blood samples (n=206) were drawn into citrated tubes using a 21G needle. Blood was centrifuged twice at 2000x*g* for 10 mins. The plasma was collected and aliquoted into 1mL tubes and stored at -80°C.

9.3.7 Sample Preparation

Antibody master mixes were made by adding antibodies and isotypes to 4 x 1.5mL labelled Eppendorfs. Volumes can be found in Table 9.4. Antibodies were used to distinguish between different EV derivations, Table 9.3. Procoagulant positive and negative were based on the presence of MFGE8, which binds to phosphatidylserine. Antibodies were vortexed briefly before pipetting. Master mixes were stored on ice, in the dark.

Table 9.2 | Cell types showing prominent expression of antibodies used.

CD Marker	Alternative Name	Prominent Expression
CD14	LPS Receptor	Mon./Mac., Gran.
CD16	FCRIIIA	Mon./Mac, Gran, T Cell, NK Cell, DC
CD284	TLR4	Mon./Mac.
CD41a	GPIIb	Platelets
CD42b	GPIX	Platelets
CD31	PECAM-1	Endothelial, Platelets
CD105	Endoglin	Endothelial
N/A	Lactadherin/MFGE8	Apoptotic Vesicles, Microvesicles

Mon./Mac. – Monocyte/Macrophage, Gran. – Granulocyte, NK Cell – Natural Killer Cell.

Selected EV cohort samples (n=88) were removed from the -80°C freezer, and stored on dry ice before being incubated at 37°C for 10 mins. 30µL of sample were added to FACS tubes containing 50µl 0.1µm double-filtered HEPES buffered saline (dfHBS). These also contained IgG master mixes,

antibodies, or just HBS depending on whether the sample was going to be isotype controls, antibody stained, or unstained samples, respectively.

Samples were then incubated on ice in the dark for 20 mins before being diluted further in 1mL of 0.1µm dfHBS. An appropriate volume of the sample was then transfer to a FACS tube (TruCount tube for antibody samples) containing 1mL of 0.1µm dfHBS that resulted in an event rate of <500E/s.

9.3.8 Sample Acquisition

A BD Special Order LSRFortessa X-20 using FACSDiva 8.0 software (BD Biosciences, Oxford, UK) was used for EV sample acquisition and analysis. 100, 300, 500, 900nm fluorescent polystyrene beads (Megamix Plus FSC , Biocytex, France) were analysed on FSC-H, SSC -H. SSC and FSC voltages were increased until the 900nm population appeared in the upper right corner of a plot without detector saturation. A SSC threshold was set using the median SSC-H parameter of 100nm polystyrene fluorescent beads. 100, 200, 400, 700, 1000nm Polystyrene and 500, 700, 1000nm silica NIST beads (Thermofisher Scientific, Loughborough, UK) were then recorded at set thresholds and voltages for Mie scatter reference. CompBeads (BD Bioscience, Oxford, UK) independently stained with each fluorophore at the same concentration as samples, stained for 20mins before acquisition, were analysed for each fluorophore, increasing the voltage for each until at the top of fluorescence-H log plot. An unstained sample was then analysed at the set fluorescence and scatter voltages. Appropriate thresholds were then set on 'OR' for each fluorescent channel, just above autofluorscence. All samples were analysed for initially for 30 seconds at the lowest flow rate attainable, allowing the core stream to stabilise before events, before being recorded for 6minutes. Samples were diluted until an event rate of ≤500 events/sec was stable, with limited electronic aborts.

9.3.9 Data Analysis

Data analysis was carried out on imported FCS 3.0 files using FlowJo v10.0.8 (FlowJo LLC, Ashland, USA). Compensation matrices were first set, using CompBead data with the automated compensation matrix set up in FlowJo.

Gating of MVs populations was based on Mie theory modelling of the Fortessa X-20 shown in previous chapters. Cut-offs for the MV gate were chosen to be from the 100nm fluorescent polystyrene population (threshold set to median 100nm) and modal 200nm polystyrene NIST population (Figure 6.7). The AV population was set from the modal 200nm population to the 900 fluorescent polystyrene population. The total population (MA) was gated from lower 100nm fluorescent bead population up to the modal 900nm population. Fluorescent gating of negative

events was done using isotype-matched controls for every patient. A bisector tool was used to set the left-hand gate at 99.9% of the population for each fluorophore-H measurement. Events appearing above this gate were assumed positively stained. These gates were then layered in order to identify specific EV subsets. MFGE8-FITC stained populations (MFG+), as an exception, used a negatively stained population in order to determine positive events.

The gating strategy employed resulted in a total of 78 unique phenotypes. Further populations were created using sums of populations, and ratios. This conclusive list exceeded 600 variables. A subset of which were chosen for the analysis in the subsequent chapter, in order to have a manageable amount. Cell derivation was determined based on high expression cell types and were categorised using Table 9.3.

Leukocyte Panel	MFG	CD284	CD16	NCD14	CD284 MON
			CD16	CD14	CD284 MON
			CD14	NCD16	CD284 MON
			NCD14	NCD16	CD284 MON
		NCD284	CD14	NCD16	NCD284 MON
			CD14	CD16	NCD284 MON
			CD16	NCD14	OTHER
	NMFG	CD284	CD16	NCD14	CD284 MON
			CD16	CD14	CD284 MON
			CD14	NCD16	CD284 MON
			NCD14	NCD16	CD284 MON
		NCD284	CD14	NCD16	NCD284 MON
			CD14	CD16	NCD284 MON
			CD16	NCD14	OTHER
	CD284		CD16	NCD14	CD284 MON
			CD16	CD14	CD284 MON
			CD14	NCD16	CD284 MON
	NCD284		CD14	NCD16	NCD284 MON
			CD14	CD16	NCD284 MON
			CD16	NCD14	OTHER

Endothelial Panel	MFG	CD105	NCD31	NCD41/42	EMV
			CD31	NCD41/42	EMV
		NCD105	CD41/42	NCD31	PMV
			CD41/42	CD31	PMV
			CD31	NCD41/42	EMV
	NMFG	CD105	NCD31	NCD41/42	EMV
			CD31	NCD41/42	EMV
		NCD105	CD41/42	NCD31	PMV
			CD41/42	CD31	PMV
			CD31	NCD41/42	EMV
	CD105		NCD31	NCD41/42	EMV
			CD31	NCD41/42	EMV
	NCD105		CD41/42	NCD31	PMV
			CD41/42	CD31	PMV
			CD31	NCD41/42	EMV

Table 9.3 | Categorical Phenotyping Method Used for EV Cell Derivation Grouping, Based on Prominent CD Marker Expression.

NCDx- Negatively stained for CD Marker 'x', CDx – Positively stained for CD Marker 'x, MFG-Positively Stained for MFGE8, NMFG-Negatively Stained with MFGE8, CD284 MON – Monocyte/Macrophage Derivation with a CD284 positive phenotype, NCD284 MON – Monocyte/Macrophage Derivation with a CD284 negative phenotype, PMV- Platelet Derivation, EMV-Endothelial Derivation, OTHER- T-cell, Dendritic Cell, or Natural Killer Cell Derivation.

9.3.10 EV Count Normalisation

Absolute EV counts were calculated by analysing stained samples in TruCount tubes (BD Bioscience, Oxford, UK). TruCount beads were gated on APC-Cy7-H vs. BV510-H. Absolute counts were then calculated using the following equations. Note, sample volume allows for dilution of

the sample with antibody mastermix, and further dilutions that allowed for events rates ≤500 events/sec.

$$Absolute\ MV\ count = \frac{Total\ TruCount\ bead\ no.}{Recorded\ TruCount\ beads} \times \frac{Recorded\ Parameter\ count}{Sample\ Volume\ in\ TruCount\ Tube}$$

9.3.11 Statistical Analysis

Data was analysed using Statistical Package for the Social Sciences (SPSS) Version 23.0 (IBM, New York, USA), and GraphPad Prism 6 (GraphPad Software Inc., La Jolia, USA). EV data was added to a pre-existing SPSS database including metabolic, fibrosis and inflammatory markers courtesy of Professor C. D. Byrne. Samples were tested for normality using Shapiro-Wilk tests with a $p< 0.05$ marking significance. Variables were duplicated and then converted to Log10 values and re-run using a Shapiro-Wilk tests, with a $p<0.05$ marking significance. All variables were auto-transformed with variables above 3.0 standard deviations replaced with cut-off values, these variables were then re-run through the Shapiro-Wilk tests, with a $p<0.05$ marking significance.

Non-parametric data was compared using a Kruskal-Wallis test, if nominal comparison variables were above 2. A Mann-Whitney U-test was used if non-parametric data was being compared to a nominal data set of 2. A one-way analysis of variance was used to compare parametric variables against nominal variables with more than 2 categories. Unpaired sample t-tests were used to compare EV variables between nominal variables between 2 groups. Multiple comparisons tests used for nominal variables were subjective depending on the variable and were done as stated in the results.

Table 9.4 | NAFLD Study Antibody and Isotype Information.

Listed are the antibody and isotype panels implemented in the NAFLD investigation.

		Antibody	Fluorochrome	Isotype	Conc. (µg/mL)	Test Vol (µL)	µg per test	Supplier
Endothelial	Antibodies	MFGE8	FITC	NA	83	10	0.83	Cambridge Bioscience
		CD42b	PerCP	Mouse IgG1, κ	400	5	2	BD Bioscience
		CD41a	PerCPCy5.5	Mouse IgG1, κ	25	20	0.5	BD Bioscience
		CD105	BV421	Mouse IgG1, κ	50	5	0.25	BD Bioscience
		CD31	PE	Mouse IgG1, κ	6.25	20	0.125	BD Bioscience
	Isotype	NA	PerCP	Mouse IgG1, κ	100	20	2	BD Bioscience
		NA	PerCPCy5.5	Mouse IgG1, κ	200	2.5	0.5	BD Bioscience
		NA	BV421	Mouse IgG1, κ	200	1.25	0.25	BD Bioscience
		NA	PE	Mouse IgG1, κ	50	2.5	0.125	BD Bioscience
Leukocyte	Antibodies	MFGE8	FITC	NA	83	10	0.83	Cambridge Bioscience
		CD14	PerCPCy5.5	Mouse IgG2b, κ	100	5	0.5	BD Bioscience
		CD16	BV421	Mouse IgG1, κ	50	5	0.25	BD Bioscience
		CD284	PE	Mouse IgG1, κ	50	5	0.25	BD Bioscience
	Isotype	NA	PerCPCy5.5	IgG2b, Mouse	12.5	40	0.5	BD Bioscience
		NA	BV421	IgG1, Mouse	200	1.25	0.25	BD Bioscience
		NA	PE	IgG1, Mouse	50	5	0.25	BD Bioscience

9.4 Results

9.4.1 Cohort Characteristics

Cohort characteristics are given in

Table 9.5. Samples were selected to match gender, metformin and diabetes as closely as possible.

Table 9.5 | Cohort Selection Summary.

	Selected Cohort Overview
Gender	Male=22 Female=22
Age (years)	49.89 SD±11.41
Diabetes	T2DM = 22 T1DM = 1 No DM = 21
Metformin	Yes = 20 No = 24
BMI (kg m^{-2})	32.62 SD±6.10
Fibrosis	1.86 SD±1.35 n=28

Summarised are the variables that were aimed to be matched from the full cohort, to the selected cohort. These parameters include, gender, age, diabetes (type 1=T1DM, type 2=T2DM), metformin use, BMI, and fibrosis.

9.4.1.1 EV Overview

Absolute count comparisons of microvesicle (MV) and apoptotic vesicle (AV) cell derivations are shown in Figure 9.3a, c, respectively. Absolute comparisons of MV and AV expressed CD marker expression are shown in Figure 9.3b, d, respectively. Groupings of phenotypes can be seen in Table 9.3. CD284 positive monocyte/macrophages (CD284 MON) MVs and AVs counts are the most abundant cell derivation, Figure 9.3a, c. This group is however primarily composed of CD14. The 'other' leukocyte grouping is the least abundant EV phenotype. CD14 positive MVs and AVs are the most prevalent with CD16 positive least prevalent in MVs, and CD284 positive being the least prevalent marker in AVs.

9.4.1.2 Diabetes

Diabetes has commonly been associated with EV increases[170-185]. The effect diabetes on individuals with NAFLD was therefore investigated in the selected cohort. A comparison of individuals diagnosed with T2DM compared to individuals who did not have DM was carried out using a Kruskal Wallis Test. No difference was observed for any of the EV testing variables (data not shown).

9.4.1.3 Obesity

The severity of obesity and its correlation to EV modulation was investigated. It was not possible to compare obese to lean individuals, due to lack of lean individuals in the cohort. Individuals were grouped based on their BMI in groups overweight (BMI 25-29.9), obese (BMI 30-39.9) and extremely obese (BMI >40), and compared using a Kruskal Wallis Test for differences in EV phenotypes. No differences were observed in the tested MV and AV phenotypes (data not shown).

Absolute Counts

a) Median Breakdown of MV Derivations

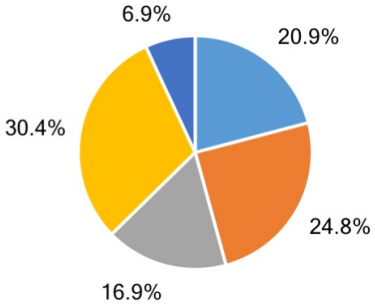

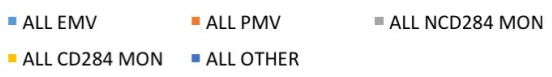

	ALL EMV	ALL PMV	NCD284 MON	CD284 MON	ALL OTHER
Min.	4.04E+06	3.40E+06	1.62E+06	5.29E+06	3.82E+05
25%	3.47E+07	4.02E+07	2.16E+07	5.67E+07	8.85E+06
Median	6.56E+07	7.79E+07	5.31E+07	9.54E+07	2.17E+07
75%	1.41E+08	1.30E+08	9.78E+07	1.63E+08	5.86E+07
Max.	9.99E+08	2.72E+08	2.30E+08	9.24E+08	2.02E+08

b) Median Breakdown of MV CD Markers

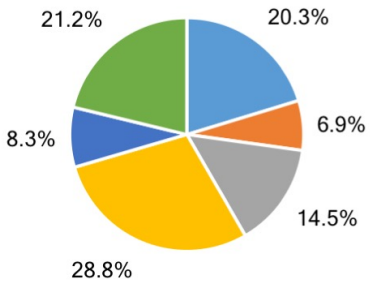

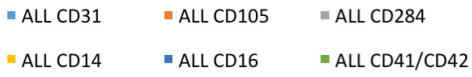

	ALL CD31	ALL CD105	ALL CD284	ALL CD14	ALL CD16	ALL CD41/42
Min.	2.26E+06	1.31E+06	1.62E+06	5.35E+06	3.82E+05	3.40E+06
25%	3.53E+07	8.08E+06	2.16E+07	6.03E+07	1.11E+07	4.02E+07
Median	7.46E+07	2.53E+07	5.31E+07	1.06E+08	3.05E+07	7.79E+07
75%	1.19E+08	6.35E+07	9.78E+07	1.67E+08	7.85E+07	1.30E+08
Max.	3.87E+08	7.15E+08	2.30E+08	9.28E+08	2.16E+08	2.72E+08

c) Median Breakdown of AV Derivations

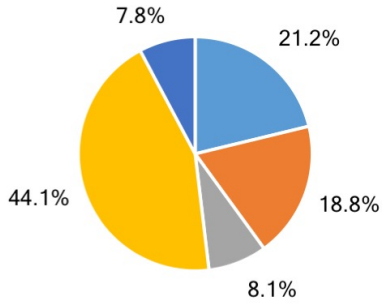

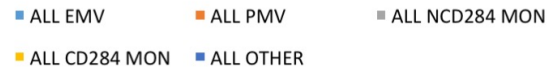

	ALL EMV	ALL PMV	NCD284 MON	CD284 MON	ALL OTHER
Min.	3.82E+05	5.01E+05	6.76E+05	1.81E+06	0.00E+00
25%	8.85E+06	7.75E+06	3.18E+06	2.19E+07	3.10E+06
Median	2.17E+07	1.92E+07	8.32E+06	4.52E+07	7.97E+06
75%	5.86E+07	4.49E+07	2.05E+07	5.46E+07	1.52E+07
Max.	2.02E+08	1.52E+08	6.91E+07	4.59E+08	9.79E+07

d) Median Breakdown of AV CD Markers

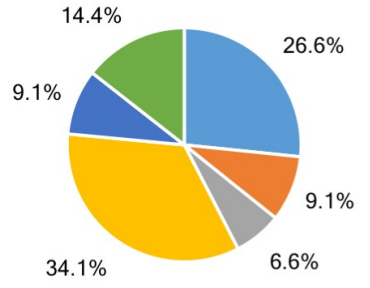

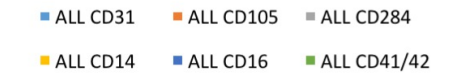

	ALL CD31	ALL CD105	ALL CD284	ALL CD14	ALL CD16	ALL CD41/42
Min.	1.46E+06	2.11E+05	6.76E+05	1.81E+06	1.32E+05	5.01E+05
25%	1.88E+07	3.09E+06	3.33E+06	2.46E+07	4.83E+06	7.75E+06
Median	3.55E+07	1.21E+07	8.85E+06	4.54E+07	1.21E+07	1.92E+07
75%	6.74E+07	3.45E+07	2.14E+07	5.84E+07	2.70E+07	4.49E+07
Max.	1.49E+08	2.46E+08	6.91E+07	4.61E+08	1.10E+08	1.52E+08

Statistical Significance Between Cell Derivations & Phenotypes

Comparison	ALL CD31 vs. ALL CD105	ALL CD31 vs. ALL CD284	ALL CD31 vs. ALL CD14	ALL CD31 vs. ALL CD16	ALL CD105 vs. ALL CD284	ALL CD105 vs. ALL CD14	ALL CD105 vs. ALL CD16	ALL CD284 vs. ALL CD14	ALL CD284 vs. ALL CD16	ALL CD14 vs. ALL CD16	ALL EMV vs. ALL PMV	ALL EMV vs. ALL GRAN	ALL EMV vs. ALL MON	ALL EMV vs. ALL OTHER	ALL PMV vs. ALL GRAN	ALL PMV vs. ALL MON	ALL PMV vs. ALL OTHER	ALL GRAN vs. ALL MON	ALL GRAN vs. ALL OTHER	ALL MON vs. ALL OTHER
MV	*	ns	ns	*	ns	****	ns	**	ns	****	ns	ns	ns	***	ns	ns	***	*	ns	****
AV	**	****	ns	*	ns	***	ns	****	ns	**	ns	*	ns	**	ns	ns	*	****	ns	****

Figure 9.3 \| Overview of Microvesicle (MV) and Apoptotic Vesicle (AV) Median Absolute Counts from Endothelial, Platelet and Leukocyte Origin in Individuals with NAFLD.

Shown are the breakdown of MV absolute count cell derivation (a), MV CD marker prominence (b), AV absolute count cell derivation (c), AV CD marker prominence (d), and summarised in the bottom table are the statistical significances between cell derivations and prominent CD markers.

9.4.1.4 Sex

Sex has been suggested to affect EV concentrations[78]. The effect of sex was therefore investigated. EV phenotypes and phenotypic ratios were compared between men and women. Differences were observed predominantly for endothelial cell derived AV phenotypes,

Figure 9.4. The differences between endothelial derived AV phenotypes (AB_ALL_CD105_NCD31_NCD41|42, AB_ALL_EMV) are due to an outlier, Figure 9.4a,b. The ratio of endothelial to platelet derived AVs (p=0.037) and number of procoagulant residual platelets to non-procoagulant residual platelets (p=0.025) are significantly different between the sexes,

Figure 9.4c, d. In summary there is a higher number of procoagulant to non-procoagulant platelet concentration in females than males (

Figure 9.4d), and a higher number of total endothelial apoptotic bodies to platelets in males when compared to females (

Figure 9.4c).

Table 9.6 | Summary of Significant Difference between Genders and EV Concentrations.

	AB_ALL_CD105_NCD31_NCD41_42	AB_ALL_EMV	AB_EMV_O_PMV	AB_MFG_PMV_O_NMFG_PMV
Total N	44	44	44	40
Mann-Whitney U	156	154	153	283
Wilcoxon W	409	407	406	493
Test Statistic	156	154	153	283
Standard Error	42.603	42.603	42.603	36.967
Standardized Test Statistic	-2.019	-2.066	-2.089	2.245
Asymptotic Sig. (2-sided test)	0.044	0.039	0.037	0.025
Exact Sig. (1-sided test)	NA	NA	NA	0.024

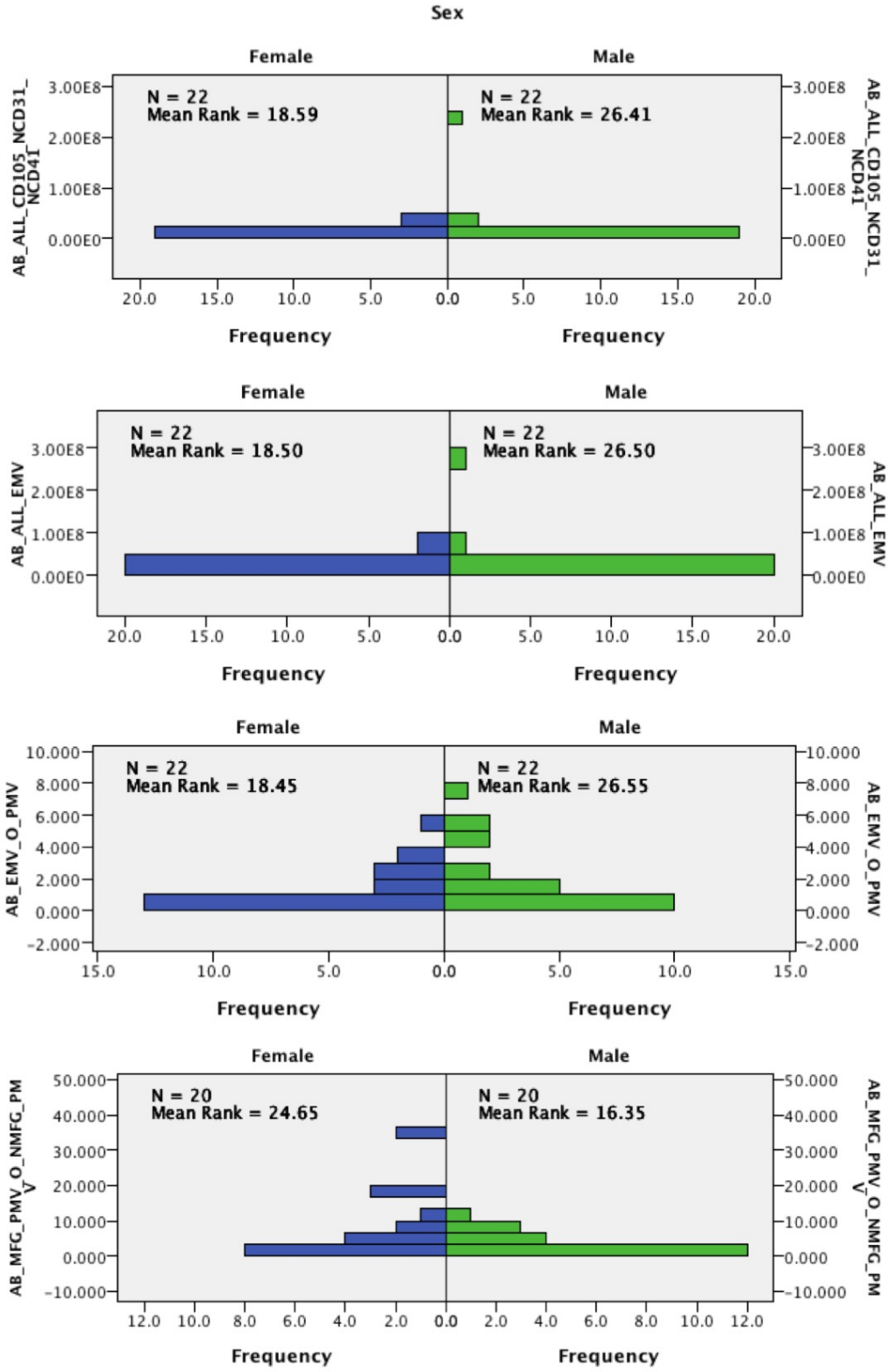

Figure 9.4 | Summary of Significant Difference between Genders and EV Concentrations.

Figure shows comparison histograms of phenotypes showing significance between sexes.

9.4.1.5 Metabolic Syndrome

Due to nearly all individuals being diagnosed with the IDF classification of metabolic syndrome, a comparison of individuals with and without metabolic syndrome could not be done. The features of metabolic syndrome are: high fasting blood glucose concentration ($\geq$ 100mmol/dL), low concentration of high-density lipoprotein (HDL) concentration ($<$ 40mg/dL), hypertension (systolic blood pressure $\geq$ 130 mm Hg, or diastolic $\geq$ 85 mm Hg), and hypertriglyceridemia ($\geq$ 150mg/dL), were therefore compared using EV counts for each phenotype using a Mann-Whitney U test. Due to all patients enrolled in the trial exceeding the IDF central obesity cut off value, comparisons could not be made. Significant results can be found summarised in Table 9.7. It can be seen that there are clear differences in the EV phenotypes modulated by the conditions leading to the metabolic syndrome classification.

Increased fasting blood glucose is associated with increased numbers of CD284 MVs, as well as an increased ratio of platelet MVs to monocyte MVs. Increased fasting blood glucose is associated with decreased procoagulant endothelial AVs, and decreased CD16+ CD14+ monocytes AVs, Table 9.7.

Decreased HDL is associated with increased ratio of monocyte MVs and endothelial MVs to CD16 only leukocyte MVs, Table 9.7.

Increased triglycerides are associated with increases in endothelial and platelet MVs, and CD16 only leukocyte AVs. A lower ratio procoagulant endothelial MVs and AVs is also associated with triglycerides, Table 9.7.

Hypertension is associated with increased endothelial MV to platelet MV, and endothelial MV to leukocyte MV ratios, Table 9.7.

In summary, leukocyte MVs and AVs are associated predominantly with high blood glucose, while decreased leukocyte MVs and AVs and increased endothelial MVs and AVs are associated with high triglycerides, low HDL, and hypertension.

Table 9.7 | Summary of Significant EV Phenotype Concentration Differences in Metabolic Syndrome Criteria.

	Phenotype	Hyperglycaemia	HDL	Hypertriglyceridemia	Hypertension
MV	MFG EMV over NMFG EMV	0.032		0.028	0.024
	CD284 MON over NCD284 MON	0.027			
	CD284 over CD14	0.028			
	PMV over MON	0.043			
	NMFG EMV			0.033	
	NMFG PMV			0.048	
	ALL EMV			0.028	
	ALL CD31			0.028	
	EMV over MON			0.018	0.000
	EMV over CD14			0.010	0.000
	CD31 over CD14			0.038	0.003
	NMFG EMV over NMFG PMV				0.019
	EMV over PMV				0.046
	EMV over NCD284 MON				0.000
	EMV over ALL CD284				0.000
	CD105 over CD284				0.003
	CD105 over CD14				0.007
	Mon over Other LMVs		0.039		
	EMV over OTHER LMVs		0.035		
	ALL CD31 ONLY			0.022	
AV	ALL CD16 ONLY			0.037	
	MFG EMV over NMFG EMV	0.046		0.027	
	CD16 CD14 ONLY	0.040			
	CD284 over CD16	0.025			
MV + AV	MFG EMV over NMFG EMV	0.025			
	CD284 MON over NCD284 MON	0.025			
	CD284 over CD14	0.024			
	EMV over MON	0.034			
	EMV over CD14	0.025			
	Mon over Other		0.035		
	EMV over OTHER		0.029		
	NMFG EMV			0.033	
	ALL EMV			0.038	
	ALL CD31			0.035	
	MFG EMV over NMFG EMV			0.017	
	EMV over CD14			0.045	0.000
	MA_EMV over NCD284 MON				0.000
	MA_EMV over MON				0.006
	EMV over CD284				0.017
	CD105 over CD284				0.016
	CD105 over CD14				0.049

Cut-offs: Triglycerides >150mg/dL, HDL cholesterol <40mg/dL (males) <50mg/dL (females), Blood pressure >130 mm Hg systolic, >85 mm Hg diastolic, Fasting blood glucose >100mmol/dL. Peach-coloured cells indicate group above cut-off having increased mean rank (i.e. significantly increased with feature), green-coloured cell indicate group above cut-off having a lower mean rank (i.e. significantly decreased with feature).

9.4.2 Relationship between EVs and Liver Fibrosis

Currently the gold-standard diagnosis of fibrosis severity is a liver biopsy, with fibrosis being one of the final stages in the progression of NAFLD, Figure 9.5. This raises practical issues due to biopsies being invasive and costly, as well as making it hard to test therapeutic interventions over a period of time. It would therefore be useful if a simple blood based biomarker test was available. We have investigated the relative behaviour of EVs and liver fibrosis to test if EVs are a suitable biomarker.

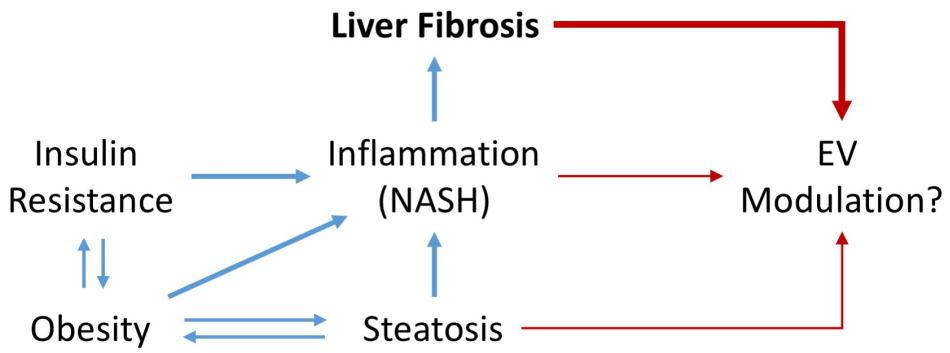

Figure 9.5 | Investigation of EV Modulation Due to Liver Fibrosis

Here comparisons of fibrosis scoring methods, within the trial, were compared using Spearmen correlation to confirm their relationship with fibrosis biopsy scoring (Scheuer fibrosis score) in this cohort, Table 9.8.

Table 9.8 | Spearmen Correlation Analysis of Fibrosis Scoring Methods.

	ELF Score			Fibrosis Score			Scheuer Fibrosis Score		
	C.C.	Sig.	N	C.C.	Sig.	N	C.C.	Sig.	N
ELF Score				.325*	0.034	43	.770**	<0.001	28
Fibrosis Score	.325*	0.034	43				.475*	0.011	28
Scheuer Fibrosis Score	.770**	<0.001	28	.475*	0.011	28			

C.C. – correlation coefficient, Sig – Significance.

Linearity of the scoring systems can be confirmed, with the results from Spearmen correlation analysis, Table 9.8. It can be seen that the ELF score has a higher correlation coefficient and significance than Fibrosis score, when compared with the Scheuer Fibrosis score.

Spearmen correlation was then conducted between the fibrosis regression scores, and endothelial EV variables, to determine whether EV phenotype absolute counts linearly correlate with fibrosis severity, Table 9.9. Due to both fibrosis scoring methods showing significant correlations with Scheuer Fibrosis scores, EV phenotypes were compared to all three scoring methods.

Table 9.9 | Spearmen Correlation Analysis of Fibrosis Scoring Systems with Endothelial EV Phenotypes

		ELF Score			Fibrosis Score			Scheuer Fibrosis Score		
	Phenotypes	C.C.	Sig.	N	C.C.	Sig.	N	C.C.	Sig.	N
MV	ALL_CD105_NCD31_NCD41	-0.154	0.318	44	-0.033	0.833	43	-.489**	0.008	28
	ALL_NCD105_CD31_NCD41	-0.077	0.619	44	-0.122	0.436	43	-.401*	0.034	28
	NMFG_EMV	-0.074	0.633	44	-0.039	0.803	43	-.428*	0.023	28
	ALL_EMV	-0.065	0.677	44	-0.058	0.711	43	-.425*	0.024	28
	ALL_CD105	-0.164	0.288	44	-0.005	0.975	43	-.441*	0.019	28
	MFG_PMV_O_NMFG_PMV	.313*	0.041	43	-0.167	0.292	42	.486*	0.01	27
	NMFG_EMV_O_NMFG_PMV	-0.132	0.393	44	0.162	0.299	43	-.388*	0.042	28
	EMV_O_PMV	-0.266	0.081	44	0.113	0.47	43	-.476*	0.01	28
AV	AV_MFG_EMV_O_MFG_PMV	0.023	0.888	40	.333*	0.038	39	-0.11	0.601	25
MV+AV	MA_ALL_CD105_NCD31_NCD41	-0.149	0.336	44	-0.017	0.913	43	-.490**	0.008	28
	MA_NMFG_EMV	-0.064	0.679	44	-0.016	0.919	43	-.383*	0.044	28
	MA_ALL_EMV	-0.056	0.719	44	-0.034	0.829	43	-.410*	0.03	28
	MA_MFG_PMV_O_NMFG_PMV	0.248	0.105	44	-0.177	0.257	43	.384*	0.044	28
	MA_EMV_O_PMV	-0.253	0.098	44	0.15	0.338	43	-.418*	0.027	28

C.C. – correlation coefficient, Sig – Significance.

It can be seen that all EV phenotypes correlating to fibrosis scores are inverse correlations, meaning that EV counts decrease as severity of fibrosis decreases. Procoagulant positive to negative ratios all appear to be positive correlations, meaning there is a higher concentration of phosphatidylserine positive EVs compared to phosphatidylserine negative EVs. Endothelial over platelet ratios being inverse also, meaning there are increased numbers of residual platelets and platelet MVs when compared to endothelial AVs and MVs, respectively. It can also be seen that ELF and fibrosis score do not correlate with any endothelial or platelet EV phenotypes, but instead with the ratio of procoagulant to non-procoagulant EV phenotypes. Testing of linearity between endothelial and platelet phenotypes with fibrosis scoring highlighted potential phenotypes worth considering under a more appropriate statistical test, such as an ANOVA or Kruskal-Wallis multiple comparisons post-hoc test.

Spearmen correlation was then conducted between the fibrosis regression scores and leukocyte EV variables to determine whether EV phenotype counts linearly correlate with fibrosis severity, Table 9.10.

Table 9.10 | Spearmen Correlation Analysis of Fibrosis Scoring and Leukocyte EV Phenotypes

		ELF Score			Fibrosis Score			Scheuer Fibrosis Score		
	Phenotypes	C.C.	Sig.	N	C.C.	Sig.	N	C.C.	Sig.	N
MV	MFG_MV2	0.002	0.991	44	-.328*	0.032	43	-0.347	0.07	28
	ALL_NCD284_CD16_NCD14	-0.107	0.488	44	-0.172	0.27	43	-.397*	0.036	28
	ALL_NCD284_NCD16_CD14	-0.016	0.92	44	-.314*	0.04	43	-0.298	0.123	28
	NMFG_MON	-0.195	0.205	44	-.303*	0.048	43	-.479**	0.01	28
	ALL_MON	-0.154	0.318	44	-0.297	0.053	43	-.440*	0.019	28
	ALL_CD16	-0.155	0.314	44	-0.142	0.363	43	-.391*	0.039	28
	ALL_CD14	-0.15	0.33	44	-.310*	0.043	43	-.448*	0.017	28
	MV_PMV_OTHER	0.248	0.104	44	0.038	0.809	43	.377*	0.048	28
AV	AV_MFG_MV2	0.017	0.914	44	-.343*	0.024	43	-0.332	0.084	28
	AV_ALL_CD284_NCD16_NCD14	-0.01	0.951	44	-0.078	0.621	43	-.387*	0.042	28
	AV_ALL_NCD284 MON	-0.057	0.714	44	-0.068	0.666	43	-.392*	0.039	28
	AV_ALL_CD284	-0.057	0.714	44	-0.068	0.666	43	-.392*	0.039	28
	AV_EMV_OTHER	-0.041	0.792	43	.316*	0.042	42	0.241	0.217	28
MV+AV	MA_MFG_MV2	0.002	0.988	44	-.358*	0.018	43	-0.344	0.073	28
	MA_ALL_NCD284_CD16_NCD14	-0.074	0.634	44	-0.229	0.139	43	-.401*	0.034	28
	MA_ALL_NCD284_NCD16_CD14	0.013	0.932	44	-.303*	0.048	43	-0.218	0.265	28
	MA_NMFG_MON	-0.222	0.147	44	-0.297	0.053	43	-.460*	0.014	28
	MA_ALL_ NCD284 MON	-0.048	0.757	44	-0.165	0.289	43	-.390*	0.04	28
	MA_ALL_MON	-0.17	0.27	44	-0.295	0.055	43	-.436*	0.02	28
	MA_ALL_CD284	-0.048	0.757	44	-0.165	0.289	43	-.390*	0.04	28
	MA_ALL_CD16	-0.148	0.336	44	-0.168	0.281	43	-.401*	0.035	28
	MA_ALL_CD14	-0.183	0.236	44	-.302*	0.049	43	-.430*	0.022	28

C.C. – correlation coefficient, Sig – Significance.

Unlike endothelial and platelet EV phenotypes, many leukocyte phenotypes correlate with fibrosis score, though none correlated with ELF score, Table 9.10. LMV phenotypes are particularly correlated with fibrosis appear to be of monocyte origin, Table 9.10. It can be seen that all EV phenotypes correlating to fibrosis scores are all inverse correlations. The ratios of endothelial, and platelet EVs, to other CD16 leukocyte EVs is positive. Further investigation into monocyte MV concentration correlation with fibrosis severity is therefore warranted.

The 'ALL MON' (Sum of CD14+ and CD14+CD16+) population was normalised using Log_{10} function and further investigated using a Gabriel post-hoc multiple comparisons test, Figure 9.6.

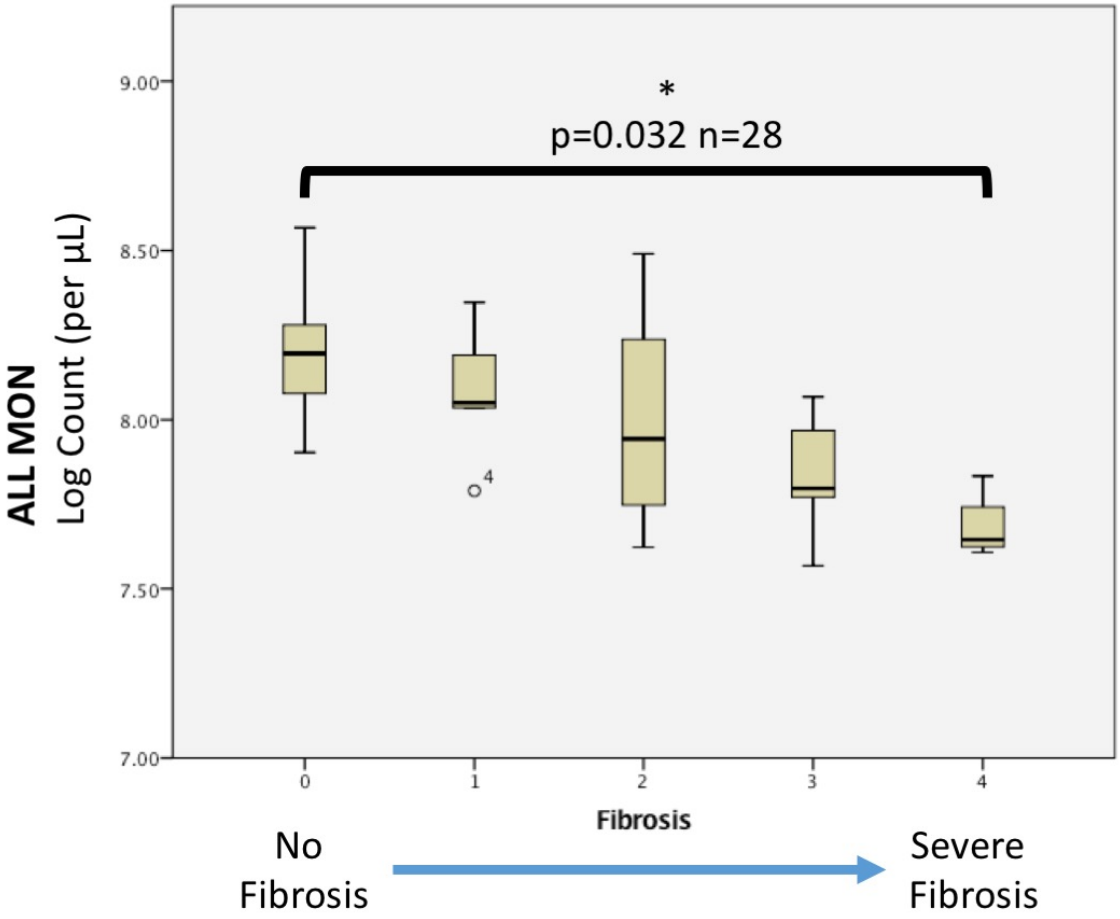

ANOVA

	Sum of Squares	df	Mean Square	F	Sig.
Between Groups	0.765	4	0.191	3.46	0.026
Within Groups	1.105	20	0.055		
Total	1.869	24			

Multiple Comparisons

(I) Fibrosis	(J) Fibrosis	Mean Difference (I-J)	Std. Error	Sig.	95% Confidence Interval	
					Lower Bound	Upper Bound
0	1	0.12211	0.14865	0.992	-0.3408	0.585
	2	0.20742	0.14232	0.779	-0.2353	0.6501
	3	0.37032	0.14865	0.179	-0.0926	0.8332
	4	0.52177	0.15767	*0.032	0.0316	1.012

* The mean difference is significant at the 0.05 level.

Figure 9.6 | Fibrosis Severity Multiple Comparisons with Monocyte Subset Concentration

Shown are the concentration of Monocyte derived MVs stratified by patient liver fibrosis biopsy score. Tables below show significance of the data with an ANOVA and post-hoc multiple comparisons test.

Multiple comparisons testing of the 'ALL MON' concentration with fibrosis severity reveals an inverse correlation with monocyte MV count decreasing as fibrosis severity increases. This relationship was further tested by using a linear regression model. The ELF regression score is currently widely used to diagnose the severity of fibrosis, and consists of 3 parameters (TIMP-1, Hyaluronic acid (HA), and P3NP). It was not possible to test the 'ALL MON' variable in the ELF regression model due to the lack of samples tested. Its predict power as a fibrosis marker in a regression model was instead investigated compared to the other ELF score variables using a receiver operator curve (ROC), Figure 9.7.

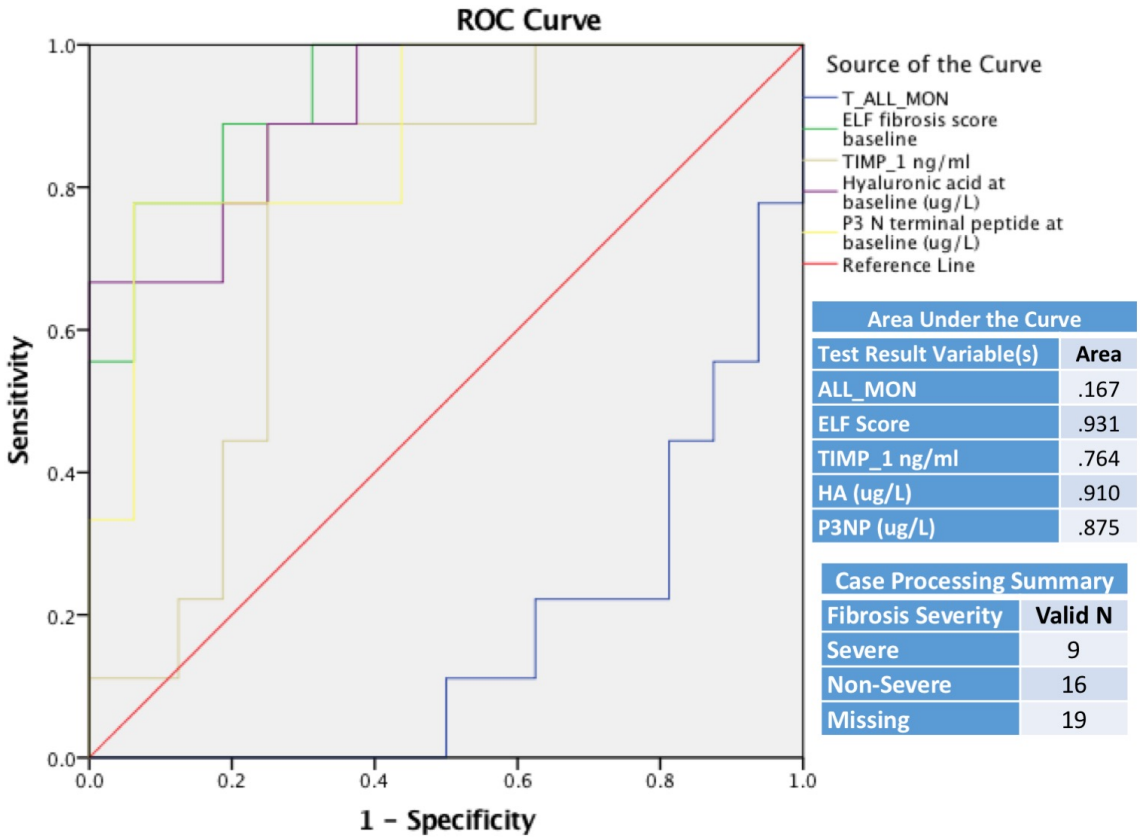

Area Under the Curve	
Test Result Variable(s)	Area
ALL_MON	.167
ELF Score	.931
TIMP_1 ng/ml	.764
HA (ug/L)	.910
P3NP (ug/L)	.875

Case Processing Summary	
Fibrosis Severity	Valid N
Severe	9
Non-Severe	16
Missing	19

Figure 9.7 | Fibrosis Severity ROC

The sensitivity and specificity of ALL_MONs to predict severe from non-severe fibrosis was compared to the ELF score, and its individual constituents – TIMP1, HA, P3NP.

A ROC curve shows the true positive rate (sensitivity) against the false positive rate (1-specificity). It can be seen using the area under the curve ROC comparison of the ELF score and its constituents that the ALL_MON parameter shows higher relative area under the curve, than TIMP-1. It may therefore be beneficial as a parameter within the ELF score. The n value of this tested cohort is however too small to definitively show its benefit of using the ALL_MON variable within the ELF score.

Further testing of LMVs, and in particular CD14+ & CD14+CD16+ is therefore merited in ordered to further elucidate their potential as diagnostic biomarkers, with regard to fibrosis severity in NAFLD.

9.4.3 Relationship between EVs and Liver Inflammation and Circulating Inflammation Modulatory Factors

NAFLD is a chronic inflammatory condition, with changes seen in the liver as well as in a number circulating inflammatory factors. Here the correlation of EVs with liver inflammation and circulating inflammatory modulators were investigated, Figure 9.8.

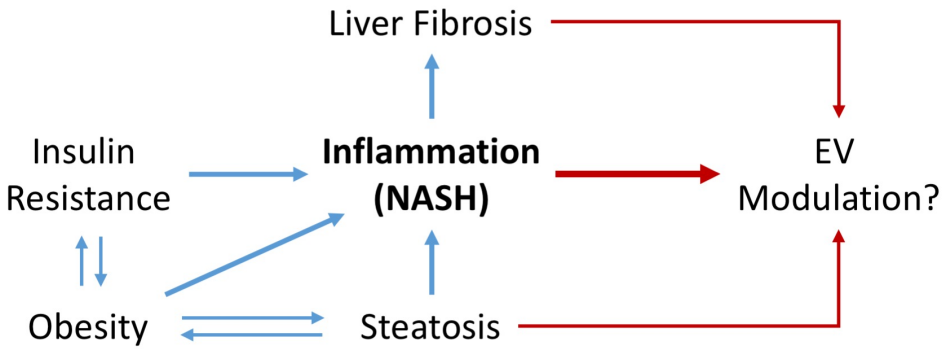

Figure 9.8 | Investigation into the Association Between Inflammation and EV Modulation.

Looking first of all at liver inflammation, it was seen that no individual MV or AV concentration corresponded directly with the level of lobular inflammation on a scale of 0-3 (**0** = no inflammatory foci, **1** = <2 inflammatory foci per 200 x field, **2** = 2-4 inflammatory foci per 200 x field, **3** = >4 inflammatory foci per 200 x field) (Data not shown).

Spearmen analysis of EVs with circulating inflammatory factors: interleukin-10 (IL-10), interleukin-8 (IL-8), interleukin-6 (IL-6), monocyte chemoattractant protein-1 (MCP-1), matrix metallopeptidase-9 (MMP-9), tissue inhibitor of metallopeptidases-1 (TIMP-1), tumour necrosis factor-α (TNFα) was carried out.

IL-8 was associated with increased numbers of a number of platelet MV phenotypes, ALL PMV shown in Figure 9.9a. MMP-9 was associated with a decrease in a specific subset of platelet MVs, ALL NCD105 CD31 CD41|42 shown in Figure 9.9b. IL-6 was correlated with CD14 only MVs, Figure 9.9c. TNFα was associated with increases in NCD284 and CD284 monocytes, Figure 9.10a, b. TIMP-1 was associated with both PS positive platelet and endothelial derived MV increases (Figure 9.11a,b), as well as procoagulant CD284 positive and negative (NCD284) monocytes (Figure 9.11c, d). IL-10 and MCP-1 did not show a correlation with any EV concentration increases.

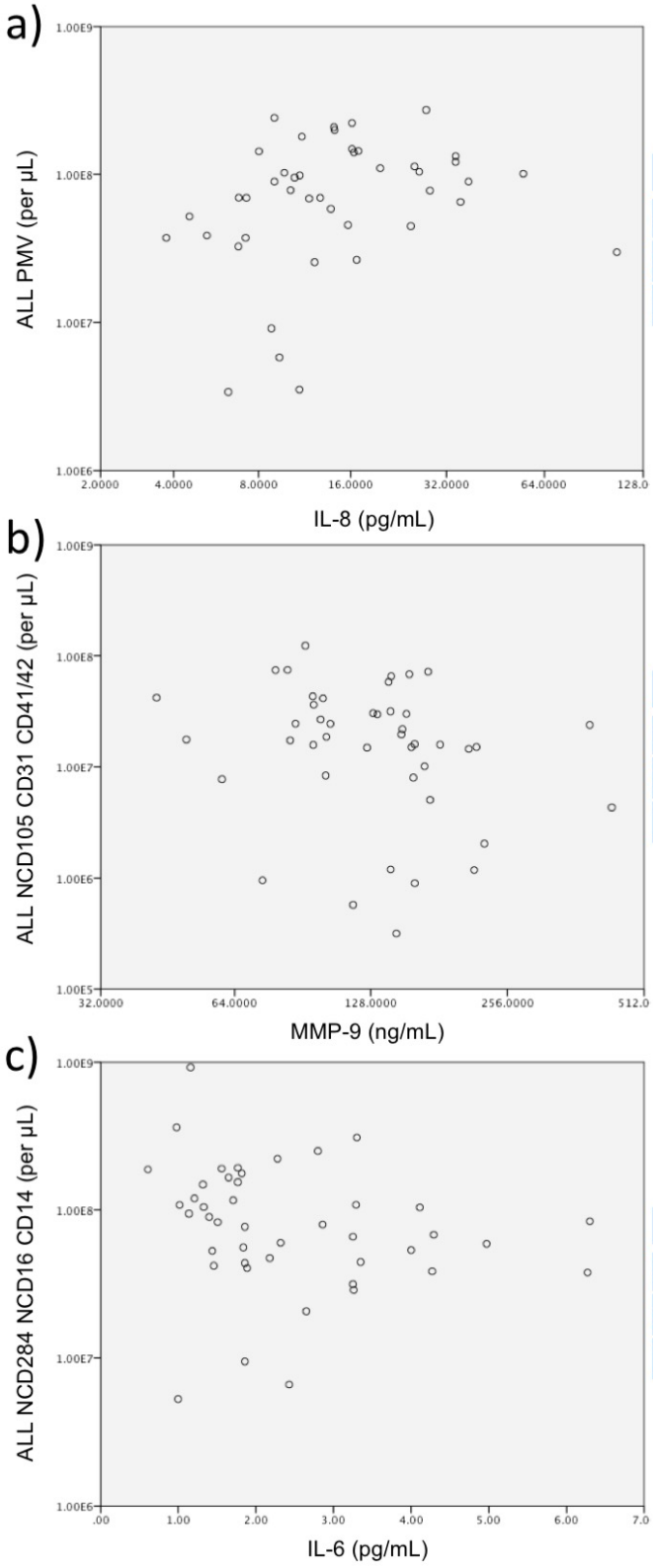

	IL-8 pg/ml
Correlation Coefficient	.322
Sig. (2-tailed)	0.033
N	44

	MMP-9 ng/ml
Correlation Coefficient	-0.350
Sig. (2-tailed)	0.02
N	44

	IL-6 pg/ml
Correlation Coefficient	-0.352
Sig. (2-tailed)	0.019
N	44

Figure 9.9 | IL-8, MMP-9, & IL-6 Correlation Scatterplots with Platelet and Leukocyte EV phenotypes

Shown are EV phenotypes that show significant correlation with IL-6 concentration.

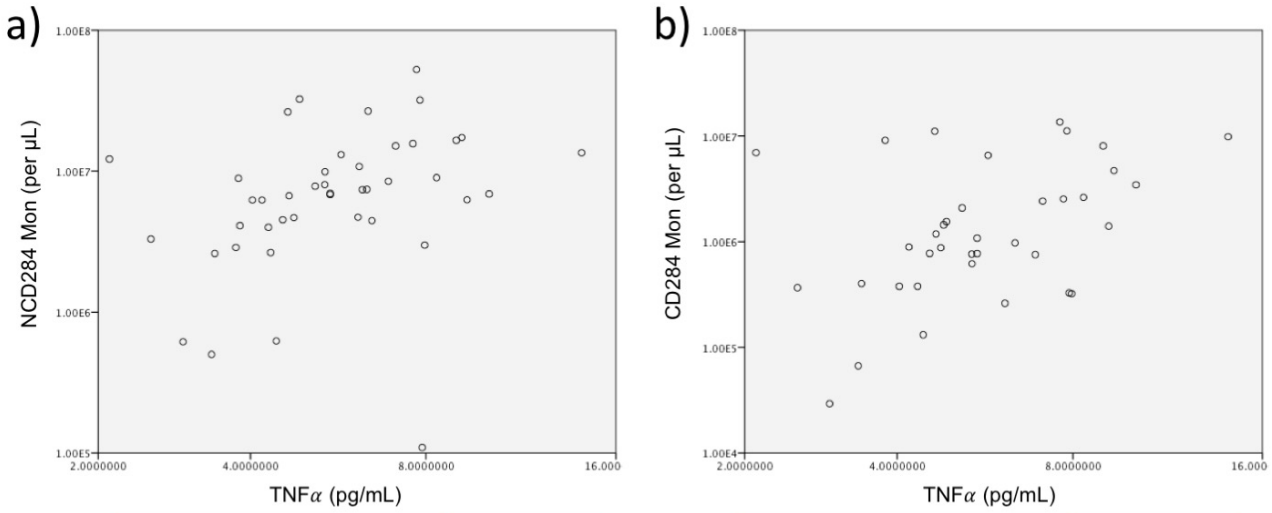

	TNFa pg/ml
Correlation Coefficient	.467
Sig. (2-tailed)	0.002
N	44

	TNFa pg/ml
Correlation Coefficient	.403
Sig. (2-tailed)	0.013
N	44

Figure 9.10 | TNFα Correlation Scatterplots with Leukocyte EV phenotypes

Shown are EV phenotypes that show significant correlation with TNFα concentration.

a)

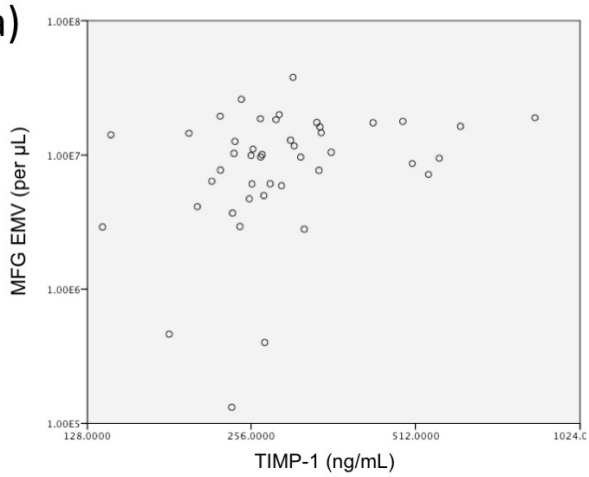

	TIMP 1 ng/ml
Correlation Coefficient	.322
Sig. (2-tailed)	0.033
N	44

b)

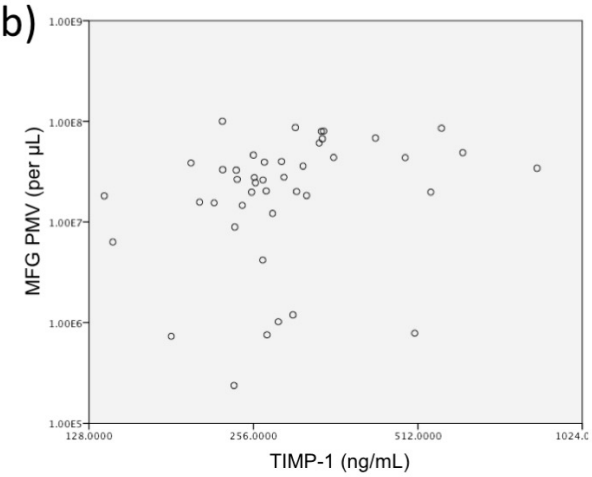

	TIMP 1 ng/ml
Correlation Coefficient	.418
Sig. (2-tailed)	0.005
N	43

c)

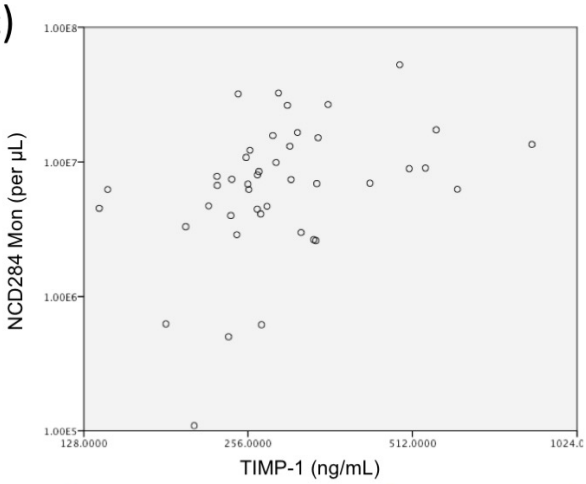

	TIMP 1 ng/ml
Correlation Coefficient	.458
Sig. (2-tailed)	0.002
N	43

d)

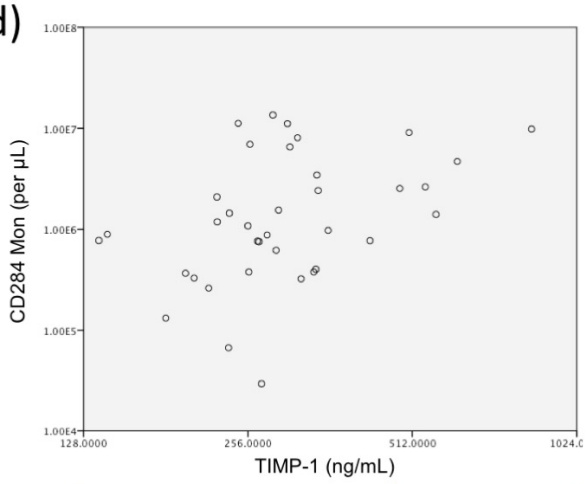

	TIMP 1 ng/ml
Correlation Coefficient	.431
Sig. (2-tailed)	0.008
N	37

Figure 9.11 | TIMP-1 Correlation Scatterplots with Platelet, Endothelial, and Leukocyte EV phenotypes

Shown are EV phenotypes that show significant correlation with TIMP-1 concentration.

In summary, TIMP-1 is associated with increases in leukocyte MV release, and PS positive endothelial and platelet release. TNFα and IL-6 only correlate with leukocyte MV release, while MMP-9 and IL-8 are associated with platelet MV release, Figure 9.12.

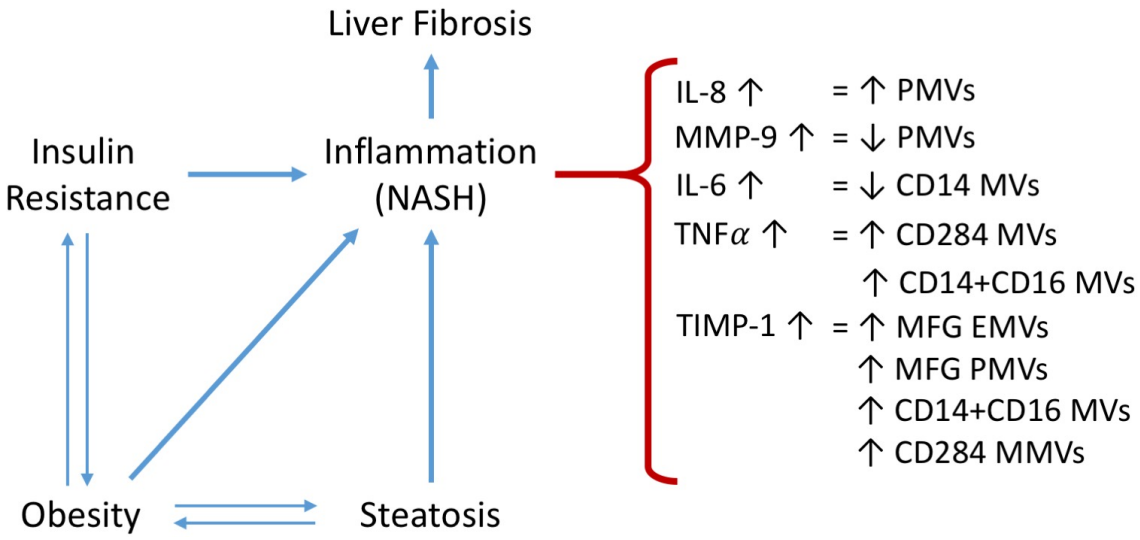

Figure 9.12 | Relationship Between Inflammation and EV Modulation.

Summarised are the EV phenotypes that show significant correlations with inflammatory factors in NAFLD.

9.4.4 Relationship between EVs and Steatosis

The accumulation of fat in the liver (steatosis) is a hallmark of NAFLD. The severity of steatosis alone however does not act as a predictor of the stage of NAFLD. Here the predictive potential of EVs to determine the severity of steatosis is investigated. In addition, this study examines whether the relationship between EVs and other hallmark features of NAFLD such as inflammation and liver fibrosis are independent or related to steatosis, Figure 9.13.

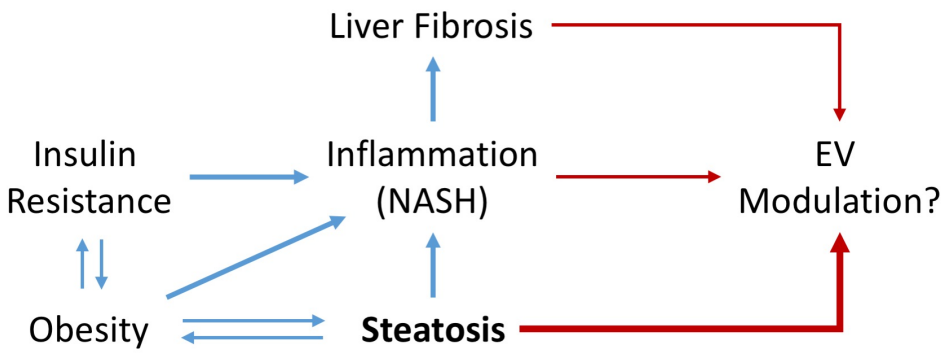

Figure 9.13 | Investigation into the Association between Steatosis and EV Modulation.

Firstly, steatosis scores obtained from surgery, using qualitative analysis with steatosis grading from 0-3, with <5%, 5-33%, 33-66%, and >66% fat coverage, respectively were compared to other

techniques of determining fat concentration. Methods include: Dual-energy x-ray absorptiometry measurement of free fat, fat mass, and bone mineral density, expressed in Kg and %, Hepatic fat fractionation using magnetic resonance spectroscopy. It can be seen that qualitative steatosis scoring only correlates positively with hepatic fat fractions (correlation coefficient 0.420, p=0.026, n=28), and weakly with DEXA Trunk/Limb Fat Mass Ratio (correlation coefficient 0.379, p=0.047, n=28). This was done to investigate if a continuous variable had a very strong correlation with steatosis, in which case it would be a useful measure to statistical compare with absolute counts.

The association between steatosis and different EV phenotype concentrations was then compared across groups using a Kruskal-Wallis test, Table 9.11. Other methods of measuring fat accumulations were omitted due to not correlating with steatosis scoring (data not shown). It can be seen that CD31 phenotypes (ALL_NCD105_CD31_NCD41, ALL CD31, MA_ALL_CD31), PS-negative PMVs (NMFG_MPV), and the AV-leukocyte ratio (AV_Mon_Other, MA_Mon_Other) show differences between absolute counts across steatosis severity. CD31-only MVs show the most significant relationship with steatosis severity, p=0.016. More numerical power however would be required to determine whether CD31 only is higher in the most severe steatosis group, Figure 9.14.

Table 9.11 | Association between Steatosis and EV Phenotypes

	ALL_NCD105_CD31_NCD41	NMFG_PMV	ALL_CD31	MA_ALL_CD31	AV_Mon_Other	MA_Mon_Other
Chi-Square	8.244	6.961	8.091	6.375	6.251	6.605
df	2	2	2	2	2	2
Asymp. Sig.	0.016	0.031	0.018	0.041	0.044	0.037

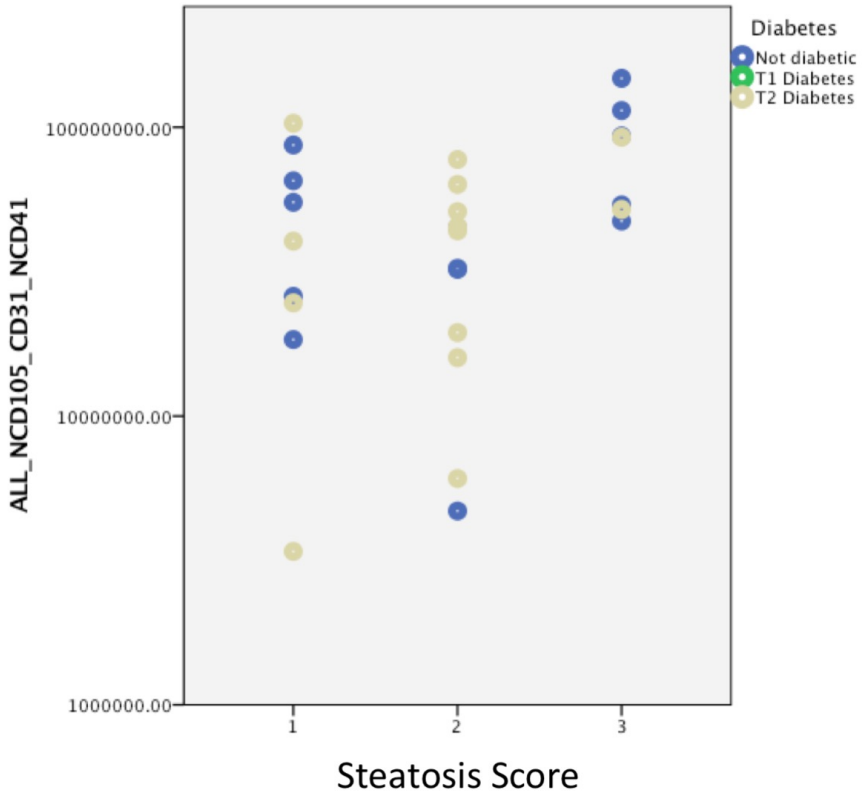

Figure 9.14 | Association between Steatosis and CD31 MVs

Steatosis severity is on a scale from non-severe (1) to severe (3)

9.5 Conclusion

The findings in this chapter particularly highlight the complexity and heterogeneity of NAFLD as a disease. It can be seen that the simplified progression of NAFLD from steatosis to liver fibrosis, does have associations with distinct EV subsets, particularly with those that have been identified as MVs, as summarised in Figure 9.15.

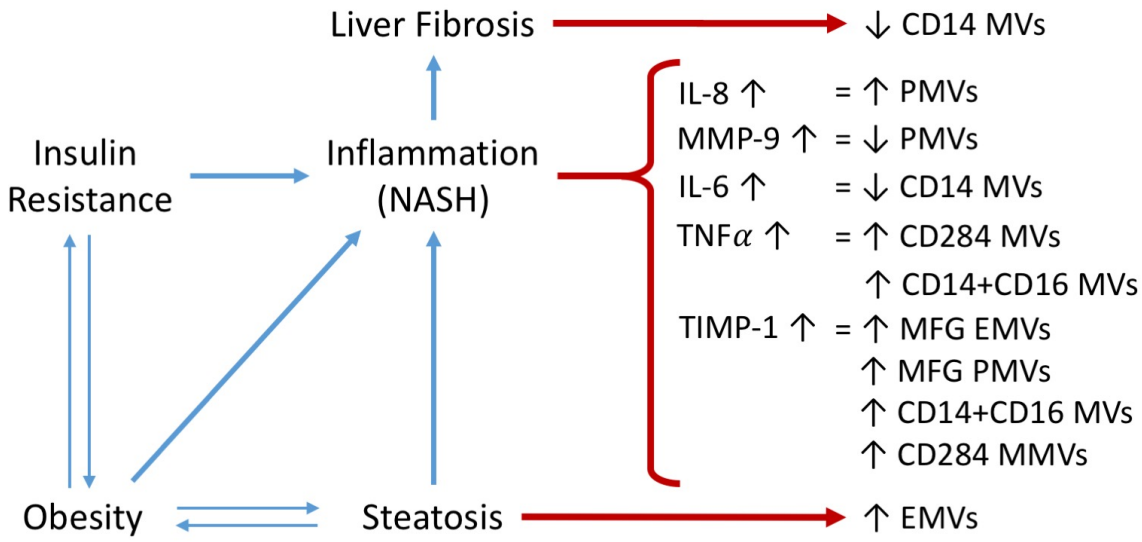

Figure 9.15 | Overview of NAFLD Progression and Association with Particular EV Subsets at Different Stages.

Summarised are the EV phenotypes that show significant correlations with liver fibrosis, inflammatory factors and steatosis in NAFLD.

This study set out to answer the following questions:

- ***Which MV and AV phenotype concentrations are highest in NAFLD?***

CD14 LMVs is highest in concentration, with EMV and PMVs next most abundant. CD16 and CD284 LMVs are lowest in concentration. This was also true for AVs.

- ***How do PMV, EMV and LMV concentrations differ in NAFLD with regard to diabetes, obesity, sex, and metabolic syndrome?***

Sex appeared to influence EMV and PMV phenotypes, with metabolic syndrome criteria modulating EMVs, PMVs, and LMVs. Diabetes and obesity severity showed no difference in EV phenotypes tested.

- ***What is the relationship between EV concentration and liver fibrosis in NAFLD ?***

CD14 MVs showed a strong inverse correlation with the severity of fibrosis.

- ***What is the relationship between EV concentration and liver & systemic inflammation?***

Circulating inflammatory factors showed correlations with EMVs, PMVs, and LMVs. TIMP-1 and TNFα showed the strongest correlations with EV subsets. No relationship was observed between lobular inflammation severity and EVs.

- ***What is the relationship between EV concentration and steatosis?***

Severe steatosis is associated with increased CD31-postive EMV concentration.

Due to the limited statistical power of the small sample size, it is not possible to further depict associations between EV subsets and hypothesize a more comprehensive mechanistic reasoning for the modulation EV subsets in NAFLD. It is however clear from this pilot study that MVs from a broad range of cellular origins are being highly modulated in response to their environment. The most distinct result is the association of fibrosis severity with a decreased concentration of CD14 MVs.

The development of resolution determination techniques, along with cFCM optimisation techniques for EV analysis has enabled differentiation between MVs and AVs more comprehensively than has previously reported in the literature. This study therefore provides novel insights into the progression of NAFLD and its association with EVs.

Chapter 10: General Discussion

In order to analyse EVs in clinical samples, novel methods had to be developed, validated and tested. The six experimental chapters in this thesis describe novel advances in the EV field.

1. Chapter 4 investigates how flow cytometer resolution should be quantified for small particles, and the variation seen between commercial cFCMs.
2. Chapter 5 of this thesis introduces key concepts in understanding how small particles scatter light, and the relationship between size, the amplitude of light scattered, and spatial distribution of scattered light. The effect of limiting the collection of light being collected at different angles and geometries was then investigated, simulating the effect of flow cytometry scatter collection, and its effects on small particle resolution.
3. Chapter 6 investigates Mie theory as a standardisation technique in flow cytometry. This modelling was extended to allow prediction of flow cytometer collection geometries from bead acquisition alone. An assay was also developed to differentiate and enumerate EVs, apoptotic vesicles, and residual platelets. This assay also acted to validate the modelling standardisation in Chapter 6.
4. Chapter 7 of this thesis introduced the problems faced with cFCM detection limits. Methods of optimisation for cFCM were demonstrated, along with presenting a novel method of core stream enumeration.
5. Chapter 8 of this thesis compared a non-optimised analysis protocol, to an optimised protocol developed in Chapter 5, on clinical samples. The results showed that the optimised protocol produced reliable counts, higher in number and lower in variation.
6. Chapter 9 of this thesis focussed on EVs in individuals with NAFLD. This chapter again utilised the novel techniques developed in Chapters 4-7 to allow differentiation of EV subsets, to a higher resolution and using phenotypes that have previously been investigated to date. This study also provides novel insights in to the modulation of PMV, EMV, and LMV with regard to liver fibrosis severity, inflammation and steatosis in NAFLD.

10.1 General Limitations

Across all experiments implementing biological samples, the number of samples analysed was a limiting factor. This was due to funds available, not having a functioning cFCM, or time constraints. The cFCMs implemented in data analysis within this thesis are not dedicated FCMs, the full population of EVs was therefore not detectable, and possibly not the population majority, due to the detection limit of the Fortessa X-20 being ~170-200nm for EVs, based on Mie theory.

Stronger significance in results may therefore be gained from detection of EVs with an increased resolution, particularly in the NAFLD study. Whilst Mie theory as a standardisation technique has been demonstrated in this thesis particularly with regard to platelet MVs, RI of EVs from different cell derivations must be demonstrated to fully validate this standardisation technique. Having clear cut cell derivations, particularly for leukocytes, is a difficult task. Here this was done by researching the cell types with the most abundant expression of the particular CD marker. It is however possible for phenotypes such as CD14 and CD284 to be derived from monocyte/macrophages and granulocytes. Once an EV is outside of its cell of derivation it may be unlikely that its derivation can ever be deduced from a plasma sample if a unique marker to that cell is not expressed.

10.2 EV Detection & Resolution Standardisation

The first steps in the standardisation field resulted in the development of polystyrene beads, without fully accounting for their RI or differing collection geometries in cFCMs, in 2010[85]. Using Mie theory to account for RI was first proposed as a standardisation technique 2 years later[148]. While this technique accounted for RI of polystyrene and silica beads, and other verification studies have attempted to measure the RI of very select sizes of EVs, a biological assay to date has not validated Mie theory as a standardisation technique. Here, this has been done for the first time, and confirmed that the predicted and measured RI of EVs are a good approximation. Mie theory as a standardisation technique partly has not caught on due to the complexity in physics calculations for biologists, as well as gaining access to proprietary information. The work illustrated in the thesis has provided a method that would allow biologists to use Mie theory as a standardisation technique, with only needing access to a library of reference values, and acquiring beads of known size and RI on a particular flow cytometer (publication in preparation). This potentially opens up doors for many in the field that were previously unable to use this technique as a standardisation procedure.

Alternative methods for determining diameter have also been demonstrated, one of which uses intercalating dyes and has been demonstrated to resolve vesicles of 30nm diameter[48]. By determining the molecules of equivalent soluble fluorophore (MESF) units of a particular dye and running the correct controls, it is possible to infer surface area based on the fluorescence intensity of the intercalating dye [48]. By calculating surface area, one is able to further deduce diameter. Though attractive as a measurement technique for cFCM due to fluorescence triggering having a higher signal to noise ratio than scatter, it requires a large amount of work per sample, and is unlikely practical for large cohort studies. If implementable however this technique can be further developed so as to determine RI using Mie theory, due to diameter being

determined irrespective of EV RI This method may be useful for comparison of sizing EV samples for their overlap with the methods evaluated here. Vesicles such as lipoproteins may however be the limiting factor in methods utilised for this protocols such as this where staining of membrane lipids solely is required.

It is becoming increasingly clear from the development of standardisation techniques that the resolution, both of fluorescence and scatter, is currently too low in cFCMs to accommodate the phenotyping of the full range of EVs. The development of dFCMs (dedicated-FCMs) is required for the progression of this field as a whole. Utilising the findings from cFCM optimisation into a dFCM would therefore be a future area of development of this work, which has already begun with preliminary data in Chapter 5. Developments in EV detection and resolution made in this thesis now allow accurate and sensitive analysis of EVs in clinical samples.

10.3 EVs in Non-Alcoholic Fatty Liver Disease

Multi-organ inflammation is a common phenomenon in obesity, diabetes and NAFLD, and is likely to alter MV production due to stimulation of the vasculature, leukocytes and platelets. The phenotype of the resulting MV is also likely to differ to those of healthy controls due to the inflammatory phenotype of the cells shedding MVs. Studies to date have shown this, particularly in T2DM which has had the most clinical research conducted of the three conditions, where MVs are concerned. The majority of studies conducted to date show an increase in platelet, endothelial and leukocyte MVs.

Only one study has been conducted on NAFLD MVs to date, Table 9.1, and showed a decrease in platelet MVs and CD15 leukocyte MVs, with an increase in CD14 MVs, Table 9.1. Therefore, the data in the conducted pilot study of this thesis contributes to the field in a significant and novel way.

As seen in many of the previously published studies on metabolic diseases, Table 9.1, few true phenotypic analyses have been done, due to using only a single marker for the identification of each MV cell type derivation. In none of the published studies, Table 9.1, has RI been taken into account, or high-resolution flow cytometry been conducted. In many of these publications it is therefore likely that swarm detection, or larger EVs such as AVs, along with residual platelets have been analysed. This would make sense since many publications to date have referenced PMVs accounting for 90% of the MV population[200-202]. If cytometers were not measuring below the 200nm polystyrene bead mark on SSC, Table 9.1, it would only be possible to analyse residual platelets and swarm detected MVs. The implications of the standardisation techniques developed in 2012 and further developed here and validated therefore have heavy implications on the

current published literature. Many EVs detected in early literature likely are swarm detected events or AVs. The true potential of MVs as biomarkers in metabolic disease is therefore yet to be elucidated.

The standardisation techniques utilised in this thesis have therefore provided a novel perspective into the use of MV and AVs as biomarkers in metabolic disease. Despite offering novel insights into NAFLD, Table 9.1 particularly with regard to the fibrosis severity, the studies here were limited by sample size and lack of healthy controls, which were a limitation of funds and study design. Future work would therefore aim to have a comparison point to healthy controls, along with analysing a larger number of samples to allow subset analysis in this complicated disease.

Appendices

Appendix A FSC Obscuration Bar Optimisation

A.1 Introduction

It can be seen from modelling particle scatter that the majority of light scattered by submicron particles of all sizes, has the highest intensity of light directed in the first ~60degrees, figure 7. It can also be seen that submicron particle scatter and size decrease in a relatively linear fashion unlike SSC light, figure 8.

For these reasons FSC optimisation could have large benefits in terms of sizing EVs. Here I try to determine the ideal obscuration bar size for dedicated flow cytometer FSC optics, which has a laser beam spot size of 25x5µm and a total power of 50mW. I will also try to determine the maximum amount of noise generated by the focussing sheath to determine the maximum amount of noise possibly derived from it.

A.2 Methods

A basic Rayleigh scatter model was created to simulate the noise derived from sheath into the FSC collection optics. This model was based on the work done by Morel who described the Rayleigh scatter of pure water in expression[203]:

$$b(\lambda, \theta) = b_{90}(1 + \cos^2 \theta)\left(\frac{550}{\lambda[nm]}\right)^{4.34}$$

This model has been altered to take into account the FSC optics of a flow cytometry system, a diagram of which can be seen in Figure 21. This model assumes:

- The laser beam is an infinitely thin line and its power is constant throughout the cell.
- Radial symmetry of the laser, beam block and collection lens.
- All light scattered into the lens (r_l), but outside the beam block (r_b), is collected.
- Light scattering from the beam happens at any point $x = 0\ to\ L$.

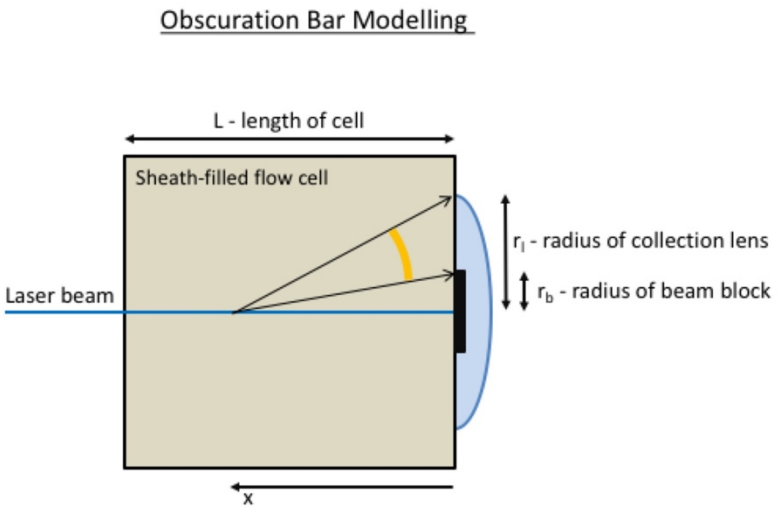

Figure 21 - Shows an overview of the Rayleigh scatter model created

The total fraction of laser light scattered into the lens by Rayleigh scatter can be described as:

$$q = 2\pi \int_0^L dx \int_{\theta_b(x)}^{\theta_l(x)} b(\lambda,\theta)\sin\theta d\theta \qquad \text{with} \qquad \theta_{b,l}(x) = \tan^{-1}\frac{r_{b,l}}{x}$$

The result of integration is as follows:

$$q = 2\pi b_{90}\left(\frac{550}{\lambda[nm]}\right)^{4.34}\frac{1}{3}\left[\frac{4L^2}{\sqrt{L^2+r_b^2}} - \frac{4L^2}{\sqrt{L^2+r_l^2}} - 5r_b + 5r_l + \frac{4r_b^2}{\sqrt{L^2+r_b^2}} - \frac{4r_l^2}{\sqrt{L^2+r_l^2}}\right]$$

where:

$$P_{Rayleigh} = qP_0$$

The amount of light scatter from a particle can then be compared to that of the sheath by using the following equation:

$$P_{Part} = I_0 r_p^2 \pi Q_{sca} = P_0 \frac{r_p^2}{r_0^2} Q_{sca}$$

Where r_p is the particle radius and $I_0 = \frac{P_0}{(r_0^2\pi)}$, r_0 is the laser spot size assuming a circular beam, Q_{sca} is the Mie coefficient using circular or rectangular collection aperture scripts mentioned previously.

In order to accurately implement Mie theory, the scattered light path from the illuminated particle to the detector is required. This includes refractive indices of mediums and collection angles. Typically, an illuminated particle will be suspended in a saline solution with a matched refractive index to the solution it is being hydrodynamically focussed with. Here I have assumed refractive index of ~1.337. The light then propagates to the flow cell with an approximate

refractive index of ~1.463. In the forward scatter direction, the scattered light will then hit air, with a refractive index of ~1.00, before being focused with a lens.

The ideal obscuration bar size can be calculated by using the laser beam waist at the point of where the obscuration bar would be, then using the predicted scatter of particles using Mie theory. By subtracting the laser spill over at different blocking angles from the predicted scatter of particles at the same angles, the optimum signal to noise ratio and therefore obscuration bar size can be deduced. This is heavily dependent upon the laser's beam profile, intensity and spot size and the overall collection angle of scattered light.

In order to simulate the signal to noise ratio for the FSC optics, the contributing factor of sheath was determined using Rayleigh scatter. This was done assuming a collection lens with a N.A. of 0.43 found as standard on the commercial Attune NxT, limiting the collection half angle to $33.69°$ and of 0.80 which would allow a collection half angle of $45°$, taking full advantage of the square flow cell.

A.3 Results

Using the Rayleigh scatter model previously discussed, it is possible to determine the contribution of sheath to signal noise, and the effect of different obscuration bar sizes, as seen in Figures 22-23.

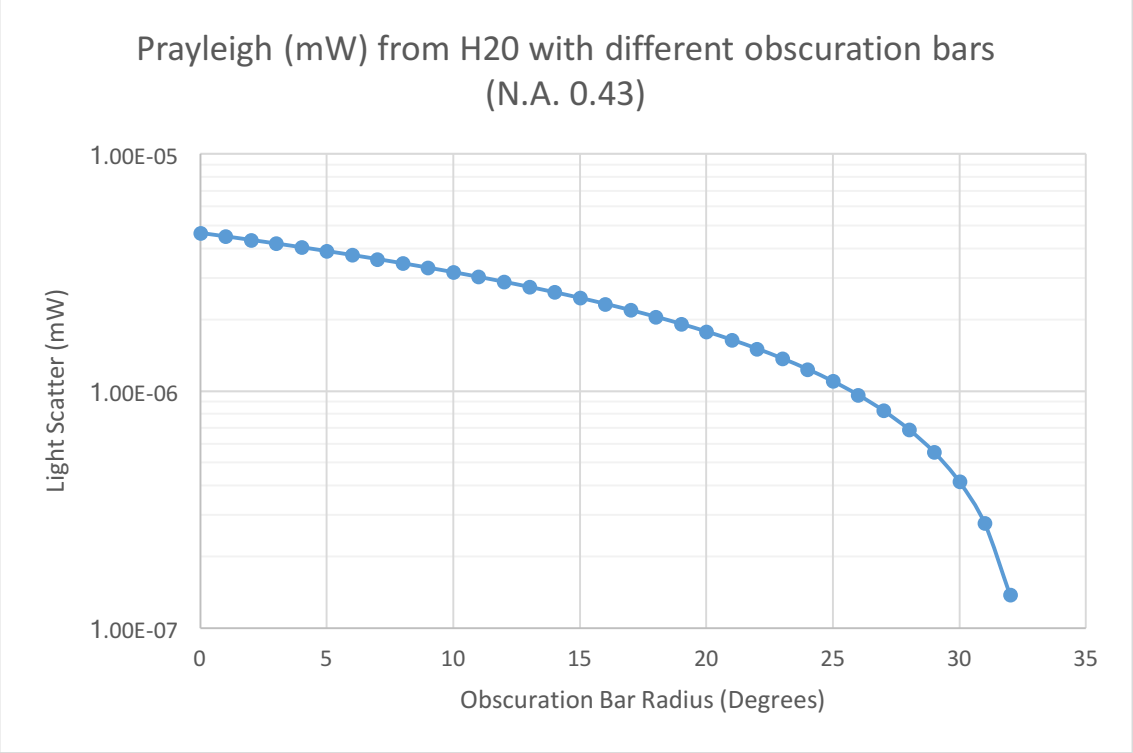

Figure 22 - Shows the estimated noise derived from sheath in the flow cell and the effect of increasing the obscuration bar with a collection lens with a numerical aperture of 0.43

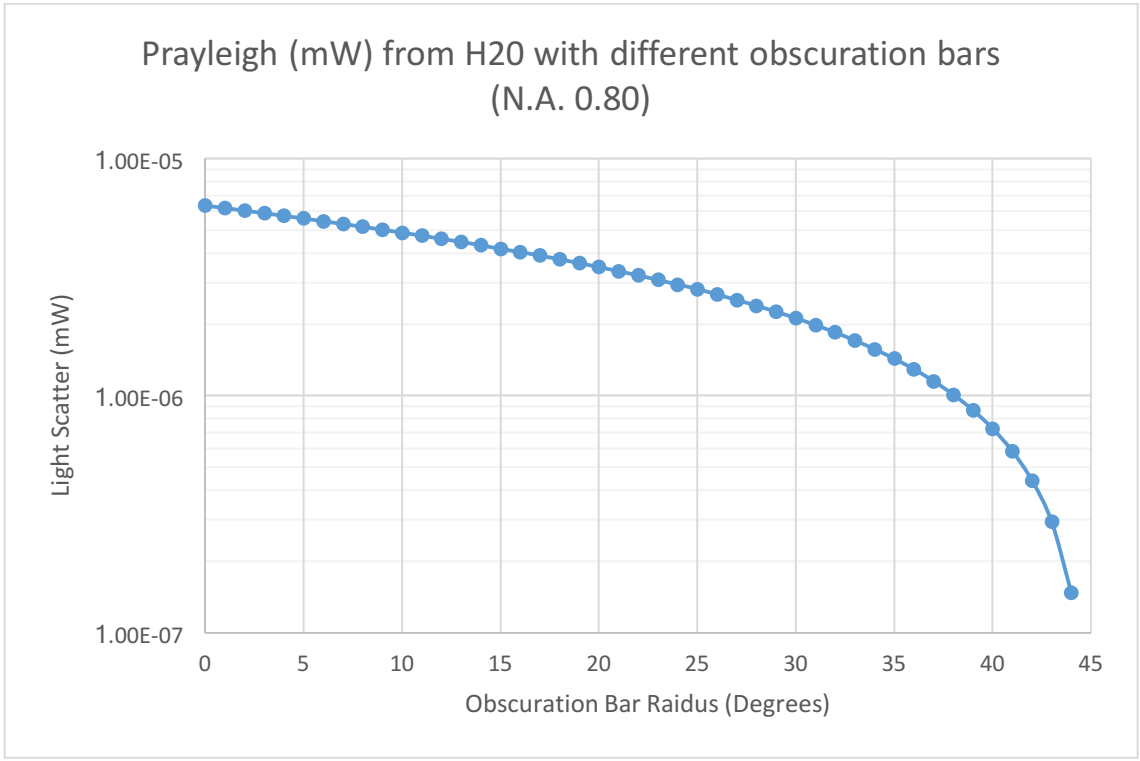

Figure 23 - Shows the estimated noise derived from sheath in the flow cell and the effect of increasing the obscuration bar with a collection lens with a numerical aperture of 0.80.

It can be seen applying this data to the predicted light scatter of particles to create an optimal signal to noise ratio, gives an optimum signal at ~20-22° for both 0.43 and 0.80 numerical apertures, Figure 24&25. It can also be seen that the signal to noise ratio decreases at a slower rate with a collection lens with a 0.80 N.A. than that of the 0.43 N.A. lens.

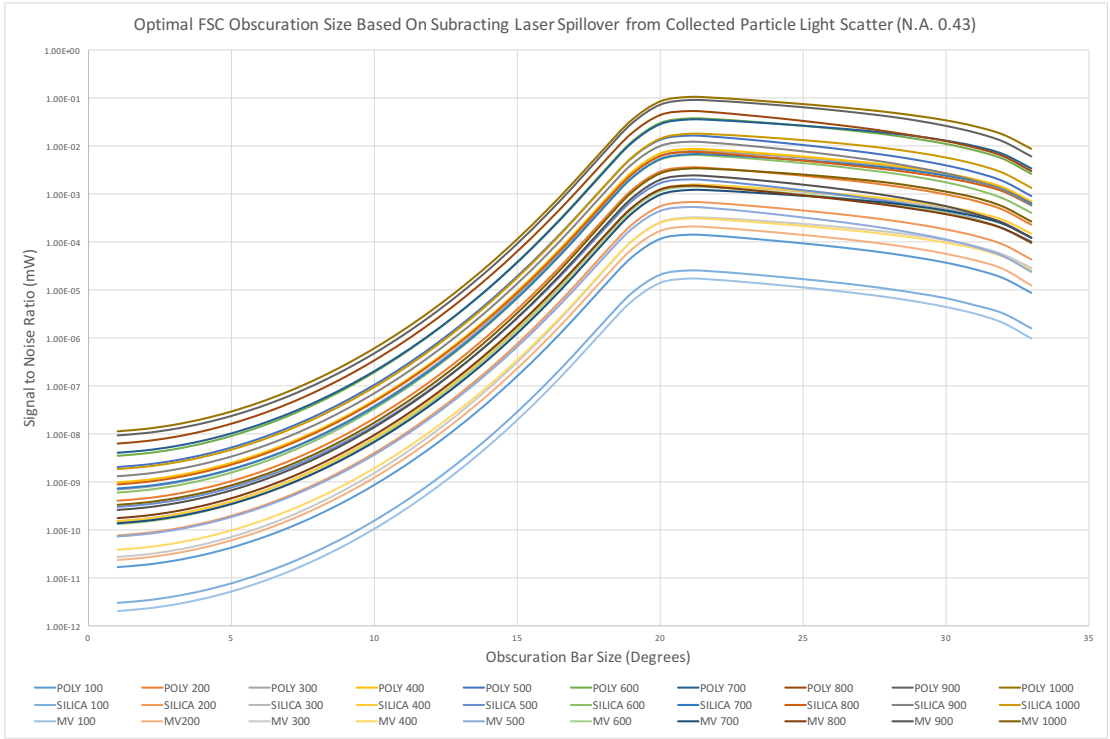

Figure 24 - Shows the optimal obscuration bar size with regards to signal to laser noise for a collection lens with a numerical aperture of 0.43

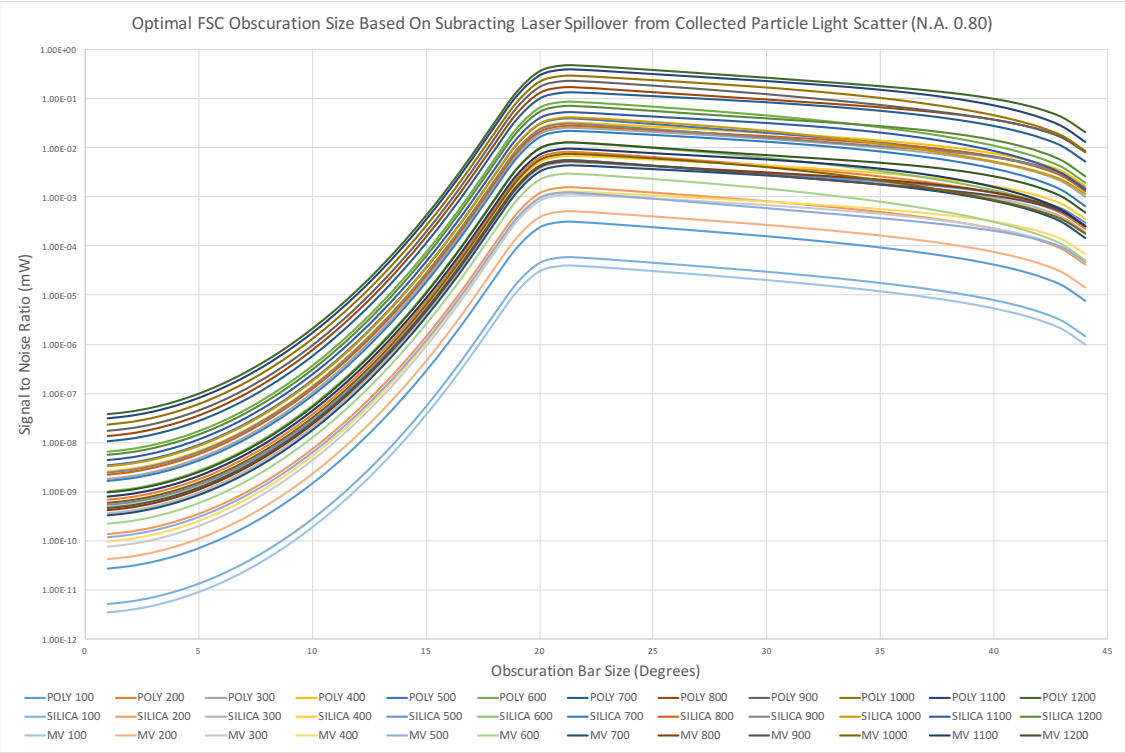

Figure 25 - Shows the optimal obscuration bar size with regards to signal to laser noise for a collection lens with a numerical aperture of 0.80

A.4 Discussion

This work shows that the 0.80 N.A. FSC collection angle has more tolerance in implementation that the 0.43N.A. and gives a starting point for both lenses to develop optimal FSC obscuration bars for a laser beam with a spot size of 5x5µm.

Future work will involve developing obscuration bars that create the predicted collection angles to determine if the theoretical optimum signal to noise ratio is the optimal size in practice.

Appendix B NAFLD Testing Variables

B.1 EV Phenotypes Output Variables

1. MFG_MV1
2. MFG_CD105_CD31_NCD41
3. MFG_CD105_NCD31_NCD41
4. MFG_NCD105_CD31_CD41
5. MFG_NCD105_CD31_NCD41
6. MFG_NCD105_NCD31_CD41
7. NMFG_CD105_CD31_NCD41
8. NMFG_CD105_NCD31_NCD41
9. NMFG_NCD105_CD31_CD41
10. NMFG_NCD105_CD31_NCD41
11. NMFG_NCD105_NCD31_CD41
12. ALL_CD105_CD31_NCD41
13. ALL_CD105_NCD31_NCD41
14. ALL_NCD105_CD31_CD41
15. ALL_NCD105_CD31_NCD41
16. ALL_NCD105_NCD31_CD41
17. MFG_EMV
18. MFG_PMV
19. NMFG_EMV
20. NMFG_PMV
21. ALL_EMV
22. ALL_PMV
23. ALL_CD105
24. ALL_CD31
25. MFG_EMV_O_NMFG_EMV
26. MFG_PMV_O_NMFG_PMV
27. MFG_EMV_O_MFG_PMV
28. NMFG_EMV_O_NMFG_PMV
29. EMV_O_PMV
30. CD31_O_CD105
31. AB_MFG_MV1
32. AB_MFG_CD105_CD31_NCD41
33. AB_MFG_CD105_NCD31_NCD41
34. AB_MFG_NCD105_CD31_CD41
35. AB_MFG_NCD105_CD31_NCD41
36. AB_MFG_NCD105_NCD31_CD41
37. AB_NMFG_CD105_CD31_NCD41
38. AB_NMFG_CD105_NCD31_NCD41
39. AB_NMFG_NCD105_CD31_CD41
40. AB_NMFG_NCD105_CD31_NCD41
41. AB_NMFG_NCD105_NCD31_CD41
42. AB_ALL_CD105_CD31_NCD41
43. AB_ALL_CD105_NCD31_NCD41
44. AB_ALL_NCD105_CD31_CD41
45. AB_ALL_NCD105_CD31_NCD41
46. AB_ALL_NCD105_NCD31_CD41
47. AB_MFG_EMV
48. AB_MFG_PMV
49. AB_NMFG_EMV
50. AB_NMFG_PMV
51. AB_ALL_EMV
52. AB_ALL_PMV
53. AB_ALL_CD105
54. AB_ALL_CD31
55. AB_MFG_EMV_O_NMFG_EMV
56. AB_MFG_PMV_O_NMFG_PMV
57. AB_MFG_EMV_O_MFG_PMV
58. AB_NMFG_EMV_O_NMFG_PMV
59. AB_EMV_O_PMV
60. AB_CD31_O_CD105
61. MA_MFG_MV1
62. MA_MFG_CD105_CD31_NCD41
63. MA_MFG_CD105_NCD31_NCD41
64. MA_MFG_NCD105_CD31_CD41
65. MA_MFG_NCD105_CD31_NCD41
66. MA_MFG_NCD105_NCD31_CD41
67. MA_NMFG_CD105_CD31_NCD41
68. MA_NMFG_CD105_NCD31_NCD41
69. MA_NMFG_NCD105_CD31_CD41
70. MA_NMFG_NCD105_CD31_NCD41
71. MA_NMFG_NCD105_NCD31_CD41
72. MA_ALL_CD105_CD31_NCD41
73. MA_ALL_CD105_NCD31_NCD41
74. MA_ALL_NCD105_CD31_CD41
75. MA_ALL_NCD105_CD31_NCD41
76. MA_ALL_NCD105_NCD31_CD41
77. MA_MFG_EMV
78. MA_MFG_PMV
79. MA_NMFG_EMV
80. MA_NMFG_PMV
81. MA_ALL_EMV
82. MA_ALL_PMV
83. MA_ALL_CD105
84. MA_ALL_CD31
85. MA_MFG_EMV_O_NMFG_EMV
86. MA_MFG_PMV_O_NMFG_PMV
87. MA_MFG_EMV_O_MFG_PMV
88. MA_NMFG_EMV_O_NMFG_PMV
89. MA_EMV_O_PMV
90. MA_CD31_O_CD105
91. MFG_MV2
92. MFG_CD284_CD16_CD14
93. MFG_CD284_CD16_NCD14
94. MFG_CD284_NCD16_CD14
95. MFG_CD284_NCD16_NCD14
96. MFG_NCD284_CD16_CD14
97. MFG_NCD284_CD16_NCD14
98. MFG_NCD284_NCD16_CD14
99. NMFG_CD284_CD16_CD14
100. NMFG_CD284_CD16_NCD14
101. NMFG_CD284_NCD16_CD14
102. NMFG_CD284_NCD16_NCD14
103. NMFG_NCD284_CD16_CD14
104. NMFG_NCD284_CD16_NCD14
105. NMFG_NCD284_NCD16_CD14
106. ALL_CD284_CD16_CD14
107. ALL_CD284_CD16_NCD14
108. ALL_CD284_NCD16_CD14
109. ALL_CD284_NCD16_NCD14
110. ALL_NCD284_CD16_CD14
111. ALL_NCD284_CD16_NCD14
112. ALL_NCD284_NCD16_CD14
113. MFG_GRAN
114. MFG_MON
115. NMFG_GRAN
116. NMFG_MON
117. ALL_GRAN
118. ALL_MON
119. ALL_CD284
120. ALL_CD16
121. ALL_CD14
122. MV_Gran_Mon
123. MV_Mon_Other
124. MV_Gran_Other
125. MV_CD284_CD14
126. MV_CD14_CD16

127. MV_CD284_CD16
128. MV_EMV_GRAN
129. MV_EMV_MON
130. MV_EMV_OTHER
131. MV_PMV_GRAN
132. MV_PMV_MON
133. MV_PMV_OTHER
134. MV_EMV_CD284
135. MV_EMV_CD14
136. MV_EMV_CD16
137. MV_PMV_CD284
138. MV_PMV_CD14
139. MV_PMV_CD16
140. MV_CD105_CD284
141. MV_CD105_CD14
142. MV_CD105_CD16
143. MV_CD31_CD284
144. MV_CD31_CD14
145. MV_CD31_CD16
146. AB_MFG_MV2
147. AB_MFG_CD284_CD16_CD14
148. AB_MFG_CD284_CD16_NCD14
149. AB_MFG_CD284_NCD16_CD14
150. AB_MFG_CD284_NCD16_NCD14
151. AB_MFG_NCD284_CD16_CD14
152. AB_MFG_NCD284_CD16_NCD14
153. AB_MFG_NCD284_NCD16_CD14
154. AB_NMFG_CD284_CD16_CD14
155. AB_NMFG_CD284_CD16_NCD14
156. AB_NMFG_CD284_NCD16_CD14
157. AB_NMFG_CD284_NCD16_NCD14
158. AB_NMFG_NCD284_CD16_CD14
159. AB_NMFG_NCD284_CD16_NCD14
160. AB_NMFG_NCD284_NCD16_CD14
161. AB_ALL_CD284_CD16_CD14
162. AB_ALL_CD284_CD16_NCD14
163. AB_ALL_CD284_NCD16_CD14
164. AB_ALL_CD284_NCD16_NCD14
165. AB_ALL_NCD284_CD16_CD14
166. AB_ALL_NCD284_CD16_NCD14
167. AB_ALL_NCD284_NCD16_CD14
168. AB_MFG_GRAN
169. AB_MFG_MON
170. AB_NMFG_GRAN
171. AB_NMFG_MON
172. AB_ALL_GRAN
173. AB_ALL_MON
174. AB_ALL_CD284
175. AB_ALL_CD16
176. AB_ALL_CD14
177. AB_Gran_Mon
178. AB_Mon_Other
179. AB_Gran_Other
180. AB_CD284_CD14
181. AB_CD14_CD16
182. AB_CD284_CD16
183. AB_EMV_GRAN
184. AB_EMV_MON
185. AB_EMV_OTHER
186. AB_PMV_GRAN
187. AB_PMV_MON
188. AB_PMV_OTHER
189. AB_MV_CD284
190. AB_EMV_CD14
191. AB_EMV_CD16
192. AB_PMV_CD284
193. AB_PMV_CD14
194. AB_PMV_CD16
195. AB_CD105_CD284
196. AB_CD105_CD14
197. AB_CD105_CD16
198. AB_CD31_CD284
199. AB_CD31_CD14
200. AB_CD31_CD16
201. MA_MFG_MV2
202. MA_MFG_CD284_CD16_CD14
203. MA_MFG_CD284_CD16_NCD14
204. MA_MFG_CD284_NCD16_CD14
205. MA_MFG_CD284_NCD16_NCD14
206. MA_MFG_NCD284_CD16_CD14
207. MA_MFG_NCD284_CD16_NCD14
208. MA_MFG_NCD284_NCD16_CD14
209. MA_NMFG_CD284_CD16_CD14
210. MA_NMFG_CD284_CD16_NCD14
211. MA_NMFG_CD284_NCD16_CD14
212. MA_NMFG_CD284_NCD16_NCD14
213. MA_NMFG_NCD284_CD16_CD14
214. MA_NMFG_NCD284_CD16_NCD14
215. MA_NMFG_NCD284_NCD16_CD14
216. MA_ALL_CD284_CD16_CD14
217. MA_ALL_CD284_CD16_NCD14
218. MA_ALL_CD284_NCD16_CD14
219. MA_ALL_CD284_NCD16_NCD14
220. MA_ALL_NCD284_CD16_CD14
221. MA_ALL_NCD284_CD16_NCD14
222. MA_ALL_NCD284_NCD16_CD14
223. MA_MFG_GRAN
224. MA_MFG_MON
225. MA_NMFG_GRAN
226. MA_NMFG_MON
227. MA_ALL_GRAN
228. MA_ALL_MON
229. MA_ALL_CD284
230. MA_ALL_CD16
231. MA_ALL_CD14
232. MA_Gran_Mon
233. MA_Mon_Other
234. MA_Gran_Other
235. MA_CD284_CD14
236. MA_CD14_CD16
237. MA_CD284_CD16
238. MA_EMV_GRAN
239. MA_EMV_MON
240. MA_EMV_OTHER
241. MA_PMV_GRAN
242. MA_PMV_MON
243. MA_PMV_OTHER
244. MA_EMV_CD284
245. MA_EMV_CD14
246. MA_EMV_CD16
247. MA_PMV_CD284
248. MA_PMV_CD14
249. MA_PMV_CD16
250. MA_CD105_CD284
251. MA_CD105_CD14
252. MA_CD105_CD16
253. MA_CD31_CD284
254. MA_CD31_CD14
255. MA_CD31_CD16
256. DIFF_MFG_MV1
257. DIFF_MFG_CD105_CD31_NCD41
258. DIFF_MFG_CD105_NCD31_NCD41
259. DIFF_MFG_NCD105_CD31_CD41
260. DIFF_MFG_NCD105_CD31_NCD41
261. DIFF_MFG_NCD105_NCD31_CD41
262. DIFF_NMFG_CD105_CD31_NCD41
263. DIFF_NMFG_CD105_NCD31_NCD41
264. DIFF_NMFG_NCD105_CD31_CD41
265. DIFF_NMFG_NCD105_CD31_NCD41
266. DIFF_NMFG_NCD105_NCD31_CD41
267. DIFF_ALL_CD105_CD31_NCD41
268. DIFF_ALL_CD105_NCD31_NCD41
269. DIFF_ALL_NCD105_CD31_CD41
270. DIFF_ALL_NCD105_CD31_NCD41

271. DIFF_ALL_NCD105_NCD31_CD41
272. DIFF_MFG_EMV
273. DIFF_MFG_PMV
274. DIFF_NMFG_EMV
275. DIFF_NMFG_PMV
276. DIFF_ALL_EMV
277. DIFF_ALL_PMV
278. DIFF_ALL_CD105
279. DIFF_ALL_CD31
280. DIFF_MFG_EMV_O_NMFG_EMV
281. DIFF_MFG_PMV_O_NMFG_PMV
282. DIFF_MFG_EMV_O_MFG_PMV
283. DIFF_NMFG_EMV_O_NMFG_PMV
284. DIFF_EMV_O_PMV
285. DIFF_CD31_O_CD105
286. DIFF_AB_MFG_MV1
287. DIFF_AB_MFG_CD105_CD31_NCD41
288. DIFF_AB_MFG_CD105_NCD31_NCD41
289. DIFF_AB_MFG_NCD105_CD31_CD41
290. DIFF_AB_MFG_NCD105_CD31_NCD41
291. DIFF_AB_MFG_NCD105_NCD31_CD41
292. DIFF_AB_NMFG_CD105_CD31_NCD41
293. DIFF_AB_NMFG_CD105_NCD31_NCD41
294. DIFF_AB_NMFG_NCD105_CD31_CD41
295. DIFF_AB_NMFG_NCD105_CD31_NCD41
296. DIFF_AB_NMFG_NCD105_NCD31_CD41
297. DIFF_AB_ALL_CD105_CD31_NCD41
298. DIFF_AB_ALL_CD105_NCD31_NCD41
299. DIFF_AB_ALL_NCD105_CD31_CD41
300. DIFF_AB_ALL_NCD105_CD31_NCD41
301. DIFF_AB_ALL_NCD105_NCD31_CD41
302. DIFF_AB_MFG_EMV
303. DIFF_AB_MFG_PMV
304. DIFF_AB_NMFG_EMV
305. DIFF_AB_NMFG_PMV
306. DIFF_AB_ALL_EMV
307. DIFF_AB_ALL_PMV
308. DIFF_AB_ALL_CD105
309. DIFF_AB_ALL_CD31
310. DIFF_AB_MFG_EMV_O_NMFG_EMV
311. DIFF_AB_MFG_PMV_O_NMFG_PMV
312. DIFF_AB_MFG_EMV_O_MFG_PMV
313. DIFF_AB_NMFG_EMV_O_NMFG_PMV
314. DIFF_AB_EMV_O_PMV
315. DIFF_AB_CD31_O_CD105
316. DIFF_MA_MFG_MV1
317. DIFF_MA_MFG_CD105_CD31_NCD41
318. DIFF_MA_MFG_CD105_NCD31_NCD41
319. DIFF_MA_MFG_NCD105_CD31_CD41
320. DIFF_MA_MFG_NCD105_CD31_NCD41
321. DIFF_MA_MFG_NCD105_NCD31_CD41
322. DIFF_MA_NMFG_CD105_CD31_NCD41
323. DIFF_MA_NMFG_CD105_NCD31_NCD41
324. DIFF_MA_NMFG_NCD105_CD31_CD41
325. DIFF_MA_NMFG_NCD105_CD31_NCD41
326. DIFF_MA_NMFG_NCD105_NCD31_CD41
327. DIFF_MA_ALL_CD105_CD31_NCD41
328. DIFF_MA_ALL_CD105_NCD31_NCD41
329. DIFF_MA_ALL_NCD105_CD31_CD41
330. DIFF_MA_ALL_NCD105_CD31_NCD41
331. DIFF_MA_ALL_NCD105_NCD31_CD41
332. DIFF_MA_MFG_EMV
333. DIFF_MA_MFG_PMV
334. DIFF_MA_NMFG_EMV
335. DIFF_MA_NMFG_PMV
336. DIFF_MA_ALL_EMV
337. DIFF_MA_ALL_PMV
338. DIFF_MA_ALL_CD105
339. DIFF_MA_ALL_CD31
340. DIFF_MA_MFG_EMV_O_NMFG_EMV
341. DIFF_MA_MFG_PMV_O_NMFG_PMV
342. DIFF_MA_MFG_EMV_O_MFG_PMV
343. DIFF_MA_NMFG_EMV_O_NMFG_PMV
344. DIFF_MA_EMV_O_PMV
345. DIFF_MA_CD31_O_CD105
346. DIFF_MFG_MV2
347. DIFF_MFG_CD284_CD16_CD14
348. DIFF_MFG_CD284_CD16_NCD14
349. DIFF_MFG_CD284_NCD16_CD14
350. DIFF_MFG_CD284_NCD16_NCD14
351. DIFF_MFG_NCD284_CD16_CD14
352. DIFF_MFG_NCD284_CD16_NCD14
353. DIFF_MFG_NCD284_NCD16_CD14
354. DIFF_NMFG_CD284_CD16_CD14
355. DIFF_NMFG_CD284_CD16_NCD14
356. DIFF_NMFG_CD284_NCD16_CD14
357. DIFF_NMFG_CD284_NCD16_NCD14
358. DIFF_NMFG_NCD284_CD16_CD14
359. DIFF_NMFG_NCD284_CD16_NCD14
360. DIFF_NMFG_NCD284_NCD16_CD14
361. DIFF_ALL_CD284_CD16_CD14
362. DIFF_ALL_CD284_CD16_NCD14
363. DIFF_ALL_CD284_NCD16_CD14
364. DIFF_ALL_CD284_NCD16_NCD14
365. DIFF_ALL_NCD284_CD16_CD14
366. DIFF_ALL_NCD284_CD16_NCD14
367. DIFF_ALL_NCD284_NCD16_CD14
368. DIFF_MFG_GRAN
369. DIFF_MFG_MON
370. DIFF_NMFG_GRAN
371. DIFF_NMFG_MON
372. DIFF_ALL_GRAN
373. DIFF_ALL_MON
374. DIFF_ALL_CD284
375. DIFF_ALL_CD16
376. DIFF_ALL_CD14
377. DIFF_MV_Gran_Mon
378. DIFF_MV_Mon_Other
379. DIFF_MV_Gran_Other
380. DIFF_MV_CD284_CD14
381. DIFF_MV_CD14_CD16
382. DIFF_MV_CD284_CD16
383. DIFF_MV_EMV_GRAN
384. DIFF_MV_EMV_MON
385. DIFF_MV_EMV_OTHER
386. DIFF_MV_PMV_GRAN
387. DIFF_MV_PMV_MON
388. DIFF_MV_PMV_OTHER
389. DIFF_MV_EMV_CD284
390. DIFF_MV_EMV_CD14
391. DIFF_MV_EMV_CD16
392. DIFF_MV_PMV_CD284
393. DIFF_MV_PMV_CD14
394. DIFF_MV_PMV_CD16
395. DIFF_MV_CD105_CD284
396. DIFF_MV_CD105_CD14

397. DIFF_MV_CD105_CD16
398. DIFF_MV_CD31_CD284
399. DIFF_MV_CD31_CD14
400. DIFF_MV_CD31_CD16
401. DIFF_AB_MFG_MV2
402. DIFF_AB_MFG_CD284_CD16_CD14
403. DIFF_AB_MFG_CD284_CD16_NCD14
404. DIFF_AB_MFG_CD284_NCD16_CD14
405. DIFF_AB_MFG_CD284_NCD16_NCD14
406. DIFF_AB_MFG_NCD284_CD16_CD14
407. DIFF_AB_MFG_NCD284_CD16_NCD14
408. DIFF_AB_MFG_NCD284_NCD16_CD14
409. DIFF_AB_NMFG_CD284_CD16_CD14
410. DIFF_AB_NMFG_CD284_CD16_NCD14
411. DIFF_AB_NMFG_CD284_NCD16_CD14
412. DIFF_AB_NMFG_CD284_NCD16_NCD14
413. DIFF_AB_NMFG_NCD284_CD16_CD14
414. DIFF_AB_NMFG_NCD284_CD16_NCD14
415. DIFF_AB_NMFG_NCD284_NCD16_CD14
416. DIFF_AB_ALL_CD284_CD16_CD14
417. DIFF_AB_ALL_CD284_CD16_NCD14
418. DIFF_AB_ALL_CD284_NCD16_CD14
419. DIFF_AB_ALL_CD284_NCD16_NCD14
420. DIFF_AB_ALL_NCD284_CD16_CD14
421. DIFF_AB_ALL_NCD284_CD16_NCD14
422. DIFF_AB_ALL_NCD284_NCD16_CD14
423. DIFF_AB_MFG_GRAN
424. DIFF_AB_MFG_MON
425. DIFF_AB_NMFG_GRAN
426. DIFF_AB_NMFG_MON
427. DIFF_AB_ALL_GRAN
428. DIFF_AB_ALL_MON
429. DIFF_AB_ALL_CD284
430. DIFF_AB_ALL_CD16
431. DIFF_AB_ALL_CD14
432. DIFF_AB_Gran_Mon
433. DIFF_AB_Mon_Other
434. DIFF_AB_Gran_Other
435. DIFF_AB_CD284_CD14
436. DIFF_AB_CD14_CD16
437. DIFF_AB_CD284_CD16
438. DIFF_AB_EMV_GRAN
439. DIFF_AB_EMV_MON
440. DIFF_AB_EMV_OTHER
441. DIFF_AB_PMV_GRAN
442. DIFF_AB_PMV_MON
443. DIFF_AB_PMV_OTHER
444. DIFF_AB_MV_CD284
445. DIFF_AB_EMV_CD14
446. DIFF_AB_EMV_CD16
447. DIFF_AB_PMV_CD284
448. DIFF_AB_PMV_CD14
449. DIFF_AB_PMV_CD16
450. DIFF_AB_CD105_CD284
451. DIFF_AB_CD105_CD14
452. DIFF_AB_CD105_CD16
453. DIFF_AB_CD31_CD284
454. DIFF_AB_CD31_CD14
455. DIFF_AB_CD31_CD16
456. DIFF_MA_MFG_MV2
457. DIFF_MA_MFG_CD284_CD16_CD14
458. DIFF_MA_MFG_CD284_CD16_NCD14
459. DIFF_MA_MFG_CD284_NCD16_CD14
460. DIFF_MA_MFG_CD284_NCD16_NCD14
461. DIFF_MA_MFG_NCD284_CD16_CD14
462. DIFF_MA_MFG_NCD284_CD16_NCD14
463. DIFF_MA_MFG_NCD284_NCD16_CD14
464. DIFF_MA_NMFG_CD284_CD16_CD14
465. DIFF_MA_NMFG_CD284_CD16_NCD14
466. DIFF_MA_NMFG_CD284_NCD16_CD14
467. DIFF_MA_NMFG_CD284_NCD16_NCD14
468. DIFF_MA_NMFG_NCD284_CD16_CD14
469. DIFF_MA_NMFG_NCD284_CD16_NCD14
470. DIFF_MA_NMFG_NCD284_NCD16_CD14
471. DIFF_MA_ALL_CD284_CD16_CD14
472. DIFF_MA_ALL_CD284_CD16_NCD14
473. DIFF_MA_ALL_CD284_NCD16_CD14
474. DIFF_MA_ALL_CD284_NCD16_NCD14
475. DIFF_MA_ALL_NCD284_CD16_CD14
476. DIFF_MA_ALL_NCD284_CD16_NCD14
477. DIFF_MA_ALL_NCD284_NCD16_CD14
478. DIFF_MA_MFG_GRAN
479. DIFF_MA_MFG_MON
480. DIFF_MA_NMFG_GRAN
481. DIFF_MA_NMFG_MON
482. DIFF_MA_ALL_GRAN
483. DIFF_MA_ALL_MON
484. DIFF_MA_ALL_CD284
485. DIFF_MA_ALL_CD16
486. DIFF_MA_ALL_CD14
487. DIFF_MA_Gran_Mon
488. DIFF_MA_Mon_Other
489. DIFF_MA_Gran_Other
490. DIFF_MA_CD284_CD14
491. DIFF_MA_CD14_CD16
492. DIFF_MA_CD284_CD16
493. DIFF_MA_EMV_GRAN
494. DIFF_MA_EMV_MON
495. DIFF_MA_EMV_OTHER
496. DIFF_MA_PMV_GRAN
497. DIFF_MA_PMV_MON
498. DIFF_MA_PMV_OTHER
499. DIFF_MA_EMV_CD284
500. DIFF_MA_EMV_CD14
501. DIFF_MA_EMV_CD16
502. DIFF_MA_PMV_CD284
503. DIFF_MA_PMV_CD14
504. DIFF_MA_PMV_CD16
505. DIFF_MA_CD105_CD284
506. DIFF_MA_CD105_CD14
507. DIFF_MA_CD105_CD16
508. DIFF_MA_CD31_CD284
509. DIFF_MA_CD31_CD14
510. DIFF_MA_CD31_CD16
511. LOG_MFG_MV1
512. LOG_MFG_CD105_CD31_NCD41
513. LOG_MFG_CD105_NCD31_NCD41
514. LOG_MFG_NCD105_CD31_CD41
515. LOG_MFG_NCD105_CD31_NCD41
516. LOG_MFG_NCD105_NCD31_CD41
517. LOG_NMFG_CD105_CD31_NCD41
518. LOG_NMFG_CD105_NCD31_NCD41
519. LOG_NMFG_NCD105_CD31_CD41
520. LOG_NMFG_NCD105_CD31_NCD41
521. LOG_NMFG_NCD105_NCD31_CD41
522. LOG_ALL_CD105_CD31_NCD41
523. LOG_ALL_CD105_NCD31_NCD41
524. LOG_ALL_NCD105_CD31_CD41
525. LOG_ALL_NCD105_CD31_NCD41
526. LOG_ALL_NCD105_NCD31_CD41

527. LOG_MFG_EMV
528. LOG_MFG_PMV
529. LOG_NMFG_EMV
530. LOG_NMFG_PMV
531. LOG_ALL_EMV
532. LOG_ALL_PMV
533. LOG_ALL_CD105
534. LOG_ALL_CD31
535. LOG_MFG_EMV_O_NMFG_EMV
536. LOG_MFG_PMV_O_NMFG_PMV
537. LOG_MFG_EMV_O_MFG_PMV
538. LOG_NMFG_EMV_O_NMFG_PMV
539. LOG_EMV_O_PMV
540. LOG_CD31_O_CD105
541. LOG_AB_MFG_MV1
542. LOG_AB_MFG_CD105_CD31_NCD41
543. LOG_AB_MFG_CD105_NCD31_NCD41
544. LOG_AB_MFG_NCD105_CD31_CD41
545. LOG_AB_MFG_NCD105_CD31_NCD41
546. LOG_AB_MFG_NCD105_NCD31_CD41
547. LOG_AB_NMFG_CD105_CD31_NCD41
548. LOG_AB_NMFG_CD105_NCD31_NCD41
549. LOG_AB_NMFG_NCD105_CD31_CD41
550. LOG_AB_NMFG_NCD105_CD31_NCD41
551. LOG_AB_NMFG_NCD105_NCD31_CD41
552. LOG_AB_ALL_CD105_CD31_NCD41
553. LOG_AB_ALL_CD105_NCD31_NCD41
554. LOG_AB_ALL_NCD105_CD31_CD41
555. LOG_AB_ALL_NCD105_CD31_NCD41
556. LOG_AB_ALL_NCD105_NCD31_CD41
557. LOG_AB_MFG_EMV
558. LOG_AB_MFG_PMV
559. LOG_AB_NMFG_EMV
560. LOG_AB_NMFG_PMV
561. LOG_AB_ALL_EMV
562. LOG_AB_ALL_PMV
563. LOG_AB_ALL_CD105
564. LOG_AB_ALL_CD31
565. LOG_AB_MFG_EMV_O_NMFG_EMV
566. LOG_AB_MFG_PMV_O_NMFG_PMV
567. LOG_AB_MFG_EMV_O_MFG_PMV
568. LOG_AB_NMFG_EMV_O_NMFG_PMV
569. LOG_AB_EMV_O_PMV
570. LOG_AB_CD31_O_CD105
571. LOG_MA_MFG_MV1
572. LOG_MA_MFG_CD105_CD31_NCD41
573. LOG_MA_MFG_CD105_NCD31_NCD41
574. LOG_MA_MFG_NCD105_CD31_CD41
575. LOG_MA_MFG_NCD105_CD31_NCD41
576. LOG_MA_MFG_NCD105_NCD31_CD41
577. LOG_MA_NMFG_CD105_CD31_NCD41
578. LOG_MA_NMFG_CD105_NCD31_NCD41
579. LOG_MA_NMFG_NCD105_CD31_CD41
580. LOG_MA_NMFG_NCD105_CD31_NCD41
581. LOG_MA_NMFG_NCD105_NCD31_CD41
582. LOG_MA_ALL_CD105_CD31_NCD41
583. LOG_MA_ALL_CD105_NCD31_NCD41
584. LOG_MA_ALL_NCD105_CD31_CD41
585. LOG_MA_ALL_NCD105_CD31_NCD41
586. LOG_MA_ALL_NCD105_NCD31_CD41
587. LOG_MA_MFG_EMV
588. LOG_MA_MFG_PMV
589. LOG_MA_NMFG_EMV
590. LOG_MA_NMFG_PMV
591. LOG_MA_ALL_EMV
592. LOG_MA_ALL_PMV
593. LOG_MA_ALL_CD105
594. LOG_MA_ALL_CD31
595. LOG_MA_MFG_EMV_O_NMFG_EMV
596. LOG_MA_MFG_PMV_O_NMFG_PMV
597. LOG_MA_MFG_EMV_O_MFG_PMV
598. LOG_MA_NMFG_EMV_O_NMFG_PMV
599. LOG_MA_EMV_O_PMV
600. LOG_MA_CD31_O_CD105
601. LOG_MFG_MV2
602. LOG_MFG_CD284_CD16_CD14
603. LOG_MFG_CD284_CD16_NCD14
604. LOG_MFG_CD284_NCD16_CD14
605. LOG_MFG_CD284_NCD16_NCD14
606. LOG_MFG_NCD284_CD16_CD14
607. LOG_MFG_NCD284_CD16_NCD14
608. LOG_MFG_NCD284_NCD16_CD14
609. LOG_NMFG_CD284_CD16_CD14
610. LOG_NMFG_CD284_CD16_NCD14
611. LOG_NMFG_CD284_NCD16_CD14
612. LOG_NMFG_CD284_NCD16_NCD14
613. LOG_NMFG_NCD284_CD16_CD14
614. LOG_NMFG_NCD284_CD16_NCD14
615. LOG_NMFG_NCD284_NCD16_CD14
616. LOG_ALL_CD284_CD16_CD14
617. LOG_ALL_CD284_CD16_NCD14
618. LOG_ALL_CD284_NCD16_CD14
619. LOG_ALL_CD284_NCD16_NCD14
620. LOG_ALL_NCD284_CD16_CD14
621. LOG_ALL_NCD284_CD16_NCD14
622. LOG_ALL_NCD284_NCD16_CD14
623. LOG_MFG_GRAN
624. LOG_MFG_MON
625. LOG_NMFG_GRAN
626. LOG_NMFG_MON
627. LOG_ALL_GRAN
628. LOG_ALL_MON
629. LOG_ALL_CD284
630. LOG_ALL_CD16
631. LOG_ALL_CD14
632. LOG_MV_Gran_Mon
633. LOG_MV_Mon_Other
634. LOG_MV_Gran_Other
635. LOG_MV_CD284_CD14
636. LOG_MV_CD14_CD16
637. LOG_MV_CD284_CD16
638. LOG_MV_EMV_GRAN
639. LOG_MV_EMV_MON
640. LOG_MV_EMV_OTHER
641. LOG_MV_PMV_GRAN
642. LOG_MV_PMV_MON
643. LOG_MV_PMV_OTHER
644. LOG_MV_EMV_CD284
645. LOG_MV_EMV_CD14
646. LOG_MV_EMV_CD16
647. LOG_MV_PMV_CD284
648. LOG_MV_PMV_CD14
649. LOG_MV_PMV_CD16
650. LOG_MV_CD105_CD284
651. LOG_MV_CD105_CD14
652. LOG_MV_CD105_CD16

653. LOG_MV_CD31_CD284
654. LOG_MV_CD31_CD14
655. LOG_MV_CD31_CD16
656. LOG_AB_MFG_MV2
657. LOG_AB_MFG_CD284_CD16_CD14
658. LOG_AB_MFG_CD284_CD16_NCD14
659. LOG_AB_MFG_CD284_NCD16_CD14
660. LOG_AB_MFG_CD284_NCD16_NCD14
661. LOG_AB_MFG_NCD284_CD16_CD14
662. LOG_AB_MFG_NCD284_CD16_NCD14
663. LOG_AB_MFG_NCD284_NCD16_CD14
664. LOG_AB_NMFG_CD284_CD16_CD14
665. LOG_AB_NMFG_CD284_CD16_NCD14
666. LOG_AB_NMFG_CD284_NCD16_CD14
667. LOG_AB_NMFG_CD284_NCD16_NCD14
668. LOG_AB_NMFG_NCD284_CD16_CD14
669. LOG_AB_NMFG_NCD284_CD16_NCD14
670. LOG_AB_NMFG_NCD284_NCD16_CD14
671. LOG_AB_ALL_CD284_CD16_CD14
672. LOG_AB_ALL_CD284_CD16_NCD14
673. LOG_AB_ALL_CD284_NCD16_CD14
674. LOG_AB_ALL_CD284_NCD16_NCD14
675. LOG_AB_ALL_NCD284_CD16_CD14
676. LOG_AB_ALL_NCD284_CD16_NCD14
677. LOG_AB_ALL_NCD284_NCD16_CD14
678. LOG_AB_MFG_GRAN
679. LOG_AB_MFG_MON
680. LOG_AB_NMFG_GRAN
681. LOG_AB_NMFG_MON
682. LOG_AB_ALL_GRAN
683. LOG_AB_ALL_MON
684. LOG_AB_ALL_CD284
685. LOG_AB_ALL_CD16
686. LOG_AB_ALL_CD14
687. LOG_AB_Gran_Mon
688. LOG_AB_Mon_Other
689. LOG_AB_Gran_Other
690. LOG_AB_CD284_CD14
691. LOG_AB_CD14_CD16
692. LOG_AB_CD284_CD16
693. LOG_AB_EMV_GRAN
694. LOG_AB_EMV_MON
695. LOG_AB_EMV_OTHER
696. LOG_AB_PMV_GRAN
697. LOG_AB_PMV_MON
698. LOG_AB_PMV_OTHER
699. LOG_AB_MV_CD284
700. LOG_AB_EMV_CD14
701. LOG_AB_EMV_CD16
702. LOG_AB_PMV_CD284
703. LOG_AB_PMV_CD14
704. LOG_AB_PMV_CD16
705. LOG_AB_CD105_CD284
706. LOG_AB_CD105_CD14
707. LOG_AB_CD105_CD16
708. LOG_AB_CD31_CD284
709. LOG_AB_CD31_CD14
710. LOG_AB_CD31_CD16
711. LOG_MA_MFG_MV2
712. LOG_MA_MFG_CD284_CD16_CD14
713. LOG_MA_MFG_CD284_CD16_NCD14
714. LOG_MA_MFG_CD284_NCD16_CD14
715. LOG_MA_MFG_CD284_NCD16_NCD14
716. LOG_MA_MFG_NCD284_CD16_CD14
717. LOG_MA_MFG_NCD284_CD16_NCD14
718. LOG_MA_MFG_NCD284_NCD16_CD14
719. LOG_MA_NMFG_CD284_CD16_CD14
720. LOG_MA_NMFG_CD284_CD16_NCD14
721. LOG_MA_NMFG_CD284_NCD16_CD14
722. LOG_MA_NMFG_CD284_NCD16_NCD14
723. LOG_MA_NMFG_NCD284_CD16_CD14
724. LOG_MA_NMFG_NCD284_CD16_NCD14
725. LOG_MA_NMFG_NCD284_NCD16_CD14
726. LOG_MA_ALL_CD284_CD16_CD14
727. LOG_MA_ALL_CD284_CD16_NCD14
728. LOG_MA_ALL_CD284_NCD16_CD14
729. LOG_MA_ALL_CD284_NCD16_NCD14
730. LOG_MA_ALL_NCD284_CD16_CD14
731. LOG_MA_ALL_NCD284_CD16_NCD14
732. LOG_MA_ALL_NCD284_NCD16_CD14
733. LOG_MA_MFG_GRAN
734. LOG_MA_MFG_MON
735. LOG_MA_NMFG_GRAN
736. LOG_MA_NMFG_MON
737. LOG_MA_ALL_GRAN
738. LOG_MA_ALL_MON
739. LOG_MA_ALL_CD284
740. LOG_MA_ALL_CD16
741. LOG_MA_ALL_CD14
742. LOG_MA_Gran_Mon
743. LOG_MA_Mon_Other
744. LOG_MA_Gran_Other
745. LOG_MA_CD284_CD14
746. LOG_MA_CD14_CD16
747. LOG_MA_CD284_CD16
748. LOG_MA_EMV_GRAN
749. LOG_MA_EMV_MON
750. LOG_MA_EMV_OTHER
751. LOG_MA_PMV_GRAN
752. LOG_MA_PMV_MON
753. LOG_MA_PMV_OTHER
754. LOG_MA_EMV_CD284
755. LOG_MA_EMV_CD14
756. LOG_MA_EMV_CD16
757. LOG_MA_PMV_CD284
758. LOG_MA_PMV_CD14
759. LOG_MA_PMV_CD16
760. LOG_MA_CD105_CD284
761. LOG_MA_CD105_CD14
762. LOG_MA_CD105_CD16
763. LOG_MA_CD31_CD284
764. LOG_MA_CD31_CD14
765. LOG_MA_CD31_CD16
766. AV_O_MFG_MV1
767. AV_O_MFG_CD105_CD31_NCD41
768. AV_O_MFG_CD105_NCD31_NCD41
769. AV_O_MFG_NCD105_CD31_CD41
770. AV_O_MFG_NCD105_CD31_NCD41
771. AV_O_MFG_NCD105_NCD31_CD41
772. AV_O_NMFG_CD105_CD31_NCD41
773. AV_O_NMFG_CD105_NCD31_NCD41
774. AV_O_NMFG_NCD105_CD31_CD41
775. AV_O_NMFG_NCD105_CD31_NCD41
776. AV_O_NMFG_NCD105_NCD31_CD41
777. AV_O_ALL_CD105_CD31_NCD41
778. AV_O_ALL_CD105_NCD31_NCD41
779. AV_O_ALL_NCD105_CD31_CD41
780. AV_O_ALL_NCD105_CD31_NCD41
781. AV_O_ALL_NCD105_NCD31_CD41
782. AV_O_MFG_EMV
783. AV_O_MFG_PMV
784. AV_O_NMFG_EMV
785. AV_O_NMFG_PMV

786. AV_O_ALL_EMV
787. AV_O_ALL_PMV
788. AV_O_ALL_CD105
789. AV_O_ALL_CD31
790. AV_O_MFG_MV2
791. AV_O_MFG_CD284_CD16_CD14
792. AV_O_MFG_CD284_CD16_NCD14
793. AV_O_MFG_CD284_NCD16_CD14
794. AV_O_MFG_CD284_NCD16_NCD14
795. AV_O_MFG_NCD284_CD16_CD14
796. AV_O_MFG_NCD284_CD16_NCD14
797. AV_O_MFG_NCD284_NCD16_CD14
798. AV_O_NMFG_CD284_CD16_CD14
799. AV_O_NMFG_CD284_CD16_NCD14
800. AV_O_NMFG_CD284_NCD16_CD14
801. AV_O_NMFG_CD284_NCD16_NCD14
802. AV_O_NMFG_NCD284_CD16_CD14
803. AV_O_NMFG_NCD284_CD16_NCD14
804. AV_O_NMFG_NCD284_NCD16_CD14
805. AV_O_ALL_CD284_CD16_CD14
806. AV_O_ALL_CD284_CD16_NCD14
807. AV_O_ALL_CD284_NCD16_CD14
808. AV_O_ALL_CD284_NCD16_NCD14
809. AV_O_ALL_NCD284_CD16_CD14
810. AV_O_ALL_NCD284_CD16_NCD14
811. AV_O_ALL_NCD284_NCD16_CD14
812. AV_O_MFG_GRAN
813. AV_O_MFG_MON
814. AV_O_NMFG_GRAN
815. AV_O_NMFG_MON
816. AV_O_ALL_GRAN
817. AV_O_ALL_MON
818. AV_O_ALL_CD284
819. AV_O_ALL_CD16
820. AV_O_ALL_CD14
821. T_LOG_ALL_MON
822. T_LOG_ALL_CD14
823. MFG_MON_NMFG_MON
824. MFG_GRAN_NMFG_GRAN
825. MFG_OTHER_NMFG_OTHER
826. AV_MFG_MON_NMFG_MON
827. AV_MFG_GRAN_NMFG_GRAN
828. AV_MFG_OTHER_NMFG_OTHER
829. MA_MFG_MON_NMFG_MON
830. MA_MFG_GRAN_NMFG_GRAN
831. MA_MFG_OTHER_NMFG_OTHER

Index

Bibliography

1. Stryer JMBJLTL. Biochemistry. 7th Edition ed: Basingstoke : W.H. Freeman, 2012.; 2012.

2. Dashti M, Kulik W, Hoek F, Veerman EC, Peppelenbosch MP, Rezaee F. A Phospholipidomic Analysis of All Defined Human Plasma Lipoproteins. Sci Rep-Uk. 2011;1.

3. Laulagnier K, Motta C, Hamdi S, Roy S, Fauvelle F, Pageaux JF, et al. Mast cell- and dendritic cell-derived exosomes display a specific lipid composition and an unusual membrane organization. Biochem J. 2004;380(Pt 1):161-71.

4. Subra C, Laulagnier K, Perret B, Record M. Exosome lipidomics unravels lipid sorting at the level of multivesicular bodies. Biochimie. 2007;89(2):205-12.

5. Pienimaeki-Roemer A, Kuhlmann K, Bottcher A, Konovalova T, Black A, Orso E, et al. Lipidomic and proteomic characterization of platelet extracellular vesicle subfractions from senescent platelets. Transfusion. 2015;55(3):507-21.

6. Vidal M, Sainte-Marie J, Philippot JR. Asymmetric distribution of phospholipids in the membrane of vesicles released during in vitro maturation of guinea pig reticulocytes: evidence precluding a role for " …. Asymmetric distribution of phospholipids in the membrane of vesicles released during in vitro maturation of guinea pig reticulocytes: evidence precluding a role for " …. 1989.

7. Kerr JF, Wyllie AH, Currie AR. Apoptosis: a basic biological phenomenon with wide-ranging implications in tissue kinetics. Br J Cancer. 1972;26(4):239-57.

8. Hristov M, Erl W, Linder S, Weber PC. Apoptotic bodies from endothelial cells enhance the number and initiate the differentiation of human endothelial progenitor cells in vitro. Blood. 2004;104(9):2761-6.

9. Turiak L, Misjak P, Szabo TG, Aradi B, Paloczi K, Ozohanics O, et al. Proteomic characterization of thymocyte-derived microvesicles and apoptotic bodies in BALB/c mice. J Proteomics. 2011;74(10):2025-33.

10. Thery C, Boussac M, Veron P, Ricciardi-Castagnoli P, Raposo G, Garin J, et al. Proteomic analysis of dendritic cell-derived exosomes: a secreted subcellular compartment distinct from apoptotic vesicles. J Immunol. 2001;166(12):7309-18.

11. Wolf P. The nature and significance of platelet products in human plasma. Br J Haematol. 1967;13(3):269-88.

12. Chargaff E, West R. The biological significance of the thromboplastic protein of blood. J Biol Chem. 1946;166(1):189-97.

13. Pan BT, Teng K, Wu C, Adam M, Johnstone RM. Electron microscopic evidence for externalization of the transferrin receptor in vesicular form in sheep reticulocytes. J Cell Biol. 1985;101(3):942-8.

14. Johnstone RM, Adam M, Hammond JR, Orr L, Turbide C. Vesicle formation during reticulocyte maturation. Association of plasma membrane activities with released vesicles (exosomes). J Biol Chem. 1987;262(19):9412-20.

15. Belshaw R, Pereira V, Katzourakis A, Talbot G, Paces J, Burt A, et al. Long-term reinfection of the human genome by endogenous retroviruses. Proc Natl Acad Sci U S A. 2004;101(14):4894-9.

16. Kajima M, Pollard M. Detection of viruslike particles in germ-free mice. J Bacteriol. 1965;90(5):1448-54.

17. Bock M, Stoye JP. Endogenous retroviruses and the human germline. Curr Opin Genet Dev. 2000;10(6):651-5.

18. Barbulescu M, Turner G, Seaman MI, Deinard AS, Kidd KK, Lenz J. Many human endogenous retrovirus K (HERV-K) proviruses are unique to humans. Curr Biol. 1999;9(16):861-8.

19. Florl AR, Lower R, Schmitz-Drager BJ, Schulz WA. DNA methylation and expression of LINE-1 and HERV-K provirus sequences in urothelial and renal cell carcinomas. Br J Cancer. 1999;80(9):1312-21.

20. Gotzinger N, Sauter M, Roemer K, Mueller-Lantzsch N. Regulation of human endogenous retrovirus-K Gag expression in teratocarcinoma cell lines and human tumours. J Gen Virol. 1996;77 (Pt 12):2983-90.

21. Yoder JA, Walsh CP, Bestor TH. Cytosine methylation and the ecology of intragenomic parasites. Trends Genet. 1997;13(8):335-40.

22. Depil S, Roche C, Dussart P, Prin L. Expression of a human endogenous retrovirus, HERV-K, in the blood cells of leukemia patients. Leukemia. 2002;16(2):254-9.

23. Reiche J, Pauli G, Ellerbrok H. Differential expression of human endogenous retrovirus K transcripts in primary human melanocytes and melanoma cell lines after UV irradiation. Melanoma Res. 2010;20(5):435-40.

24. Golan M, Hizi A, Resau JH, Yaal-Hahoshen N, Reichman H, Keydar I, et al. Human endogenous retrovirus (HERV-K) reverse transcriptase as a breast cancer prognostic marker. Neoplasia. 2008;10(6):521-33.

25. Wang-Johanning F, Frost AR, Jian B, Epp L, Lu DW, Johanning GL. Quantitation of HERV-K env gene expression and splicing in human breast cancer. Oncogene. 2003;22(10):1528-35.

26. Taruscio D, Mantovani A. Factors regulating endogenous retroviral sequences in human and mouse. Cytogenet Genome Res. 2004;105(2-4):351-62.

27. Bieda K, Hoffmann A, Boller K. Phenotypic heterogeneity of human endogenous retrovirus particles produced by teratocarcinoma cell lines. J Gen Virol. 2001;82(Pt 3):591-6.

28. van Meer G, Voelker DR, Feigenson GW. Membrane lipids: where they are and how they behave. Nature reviews Molecular cell biology. 2008;9(2):112-24.

29. Marsh D. Lateral pressure profile, spontaneous curvature frustration, and the incorporation and conformation of proteins in membranes. Biophysical journal. 2007;93(11):3884-99.

30. Elmore S. Apoptosis: a review of programmed cell death. Toxicologic pathology. 2007;35(4):495-516.

31. Reed JC. Mechanisms of apoptosis. The American journal of pathology. 2000.

32. Fink SL, Cookson BT. Apoptosis, pyroptosis, and necrosis: mechanistic description of dead and dying eukaryotic cells. Infection and immunity. 2005;73(4):1907-16.

33. Taylor RC, Cullen SP, Martin SJ. Apoptosis: controlled demolition at the cellular level. Nat Rev Mol Cell Biol. 2008;9(3):231-41.

34. Vanden Berghe T, Linkermann A, Jouan-Lanhouet S, Walczak H, Vandenabeele P. Regulated necrosis: the expanding network of non-apoptotic cell death pathways. Nature reviews Molecular cell biology. 2014;15(2):135-47.

35. Kim D-KK, Kang B, Kim OY, Choi D-SS, Lee J, Kim SR, et al. EVpedia: an integrated database of high-throughput data for systemic analyses of extracellular vesicles. Journal of extracellular vesicles. 2013;2.

36. Kalra H, Simpson RJ, Ji H, Aikawa E, Altevogt P, Askenase P, et al. Vesiclepedia: a compendium for extracellular vesicles with continuous community annotation. PLoS biology. 2012;10(12).

37. Henne W, Stenmark H, Emr SD. Molecular mechanisms of the membrane sculpting ESCRT pathway. Cold Spring Harbor Perspectives in Biology. 2013;5(9).

38. Kowal J, Tkach M, Thery C. Biogenesis and secretion of exosomes. Curr Opin Cell Biol. 2014;29:116-25.

39. Akers JC, Gonda D, Kim R, Carter BS, Chen CC. Biogenesis of extracellular vesicles (EV): exosomes, microvesicles, retrovirus-like vesicles, and apoptotic bodies. J Neurooncol. 2013;113(1):1-11.

40. Colombo M, Moita C, van Niel G, Kowal J, Vigneron J, Benaroch P, et al. Analysis of ESCRT functions in exosome biogenesis, composition and secretion highlights the heterogeneity of extracellular vesicles. J Cell Sci. 2013;126(Pt 24):5553-65.

41. Colombo M, Raposo G, Thery C. Biogenesis, secretion, and intercellular interactions of exosomes and other extracellular vesicles. Annu Rev Cell Dev Biol. 2014;30:255-89.

42. Stuffers S, Wegner SC, Stenmark H, Brech A. Multivesicular endosome biogenesis in the absence of ESCRTs. Traffic. 2009.

43. Ostrowski M, Carmo NB, Krumeich S, Fanget I. Rab27a and Rab27b control different steps of the exosome secretion pathway. Nature cell …. 2010.

44. Baietti MF, Zhang Z, Mortier E, Melchior A. Syndecan-syntenin-ALIX regulates the biogenesis of exosomes. Nature cell …. 2012.

45. Savina A, Fader CM, Damiani MT, Colombo MI. Rab11 promotes docking and fusion of multivesicular bodies in a calcium-dependent manner. Traffic. 2005.

46. Abrami L, Brandi L, Moayeri M, Brown MJ, Krantz BA. Hijacking multivesicular bodies enables long-term and exosome-mediated long-distance action of anthrax toxin. Cell reports. 2013.

47. Hsu C, Morohashi Y, Yoshimura S. Regulation of exosome secretion by Rab35 and its GTPase-activating proteins TBC1D10A–C. The Journal of cell …. 2010.

48. Stoner SA, Duggan E, Condello D, Guerrero A, Turk JR, Narayanan PK, et al. High sensitivity flow cytometry of membrane vesicles. Cytometry Part A : the journal of the International Society for Analytical Cytology. 2016;89(2):196-206.

49. Satta N, Toti F, Fressinaud E, Meyer D, Freyssinet JM. Scott syndrome: an inherited defect of the procoagulant activity of platelets. Platelets. 1997;8(2-3):117-24.

50. Dachary-Prigent J, Pasquet JM, Fressinaud E, Toti F, Freyssinet JM, Nurden AT. Aminophospholipid exposure, microvesiculation and abnormal protein tyrosine phosphorylation in the platelets of a patient with Scott syndrome: a study using physiologic agonists and local anaesthetics. Br J Haematol. 1997;99(4):959-67.

51. Yang H, Kim A, David T, Palmer D, Jin T, Tien J, et al. TMEM16F forms a Ca2+-activated cation channel required for lipid scrambling in platelets during blood coagulation. Cell. 2012;151(1):111-22.

52. Williamson P, Christie A, Kohlin T, Schlegel RA, Comfurius P, Harmsma M, et al. Phospholipid scramblase activation pathways in lymphocytes. Biochemistry. 2001;40(27):8065-72.

53. Kmit A, van Kruchten R, Ousingsawat J, Mattheij NJ, Senden-Gijsbers B, Heemskerk JW, et al. Calcium-activated and apoptotic phospholipid scrambling induced by Ano6 can occur independently of Ano6 ion currents. Cell Death Dis. 2013;4:e611.

54. Sims PJ, Wiedmer T, Esmon CT, Weiss HJ, Shattil SJ. Assembly of the Platelet Prothrombinase Complex Is Linked to Vesiculation of the Platelet Plasma-Membrane - Studies in Scott Syndrome - an Isolated Defect in Platelet Procoagulant Activity. Journal of Biological Chemistry. 1989;264(29):17049-57.

55. Dasgupta SK, Abdel-Monem H, Guchhait P, Nagata S, Thiagarajan P. Role of lactadherin in the clearance of phosphatidylserine-expressing red blood cells. Transfusion. 2008;48(11):2370-6.

56. Connor DE, Exner T, Ma DD, Joseph JE. The majority of circulating platelet-derived microparticles fail to bind annexin V, lack phospholipid-dependent procoagulant activity and demonstrate greater expression of glycoprotein Ib. Thromb Haemost. 2010;103(5):1044-52.

57. Nguyen DB, Thuy Ly TB, Wesseling MC, Hittinger M, Torge A, Devitt A, et al. Characterization of Microvesicles Released from Human Red Blood Cells. Cellular physiology and biochemistry : international journal of experimental cellular physiology, biochemistry, and pharmacology. 2016;38(3):1085-99.

58. Ramakrishnan DP, Hajj-Ali RA, Chen Y, Silverstein RL. Extracellular Vesicles Activate a CD36-Dependent Signaling Pathway to Inhibit Microvascular Endothelial Cell Migration and Tube Formation. Arteriosclerosis, thrombosis, and vascular biology. 2016;36(3):534-44.

59. Campbell LE, Nelson J, Gibbons E, Judd AM, Bell JD. Membrane properties involved in calcium-stimulated microparticle release from the plasma membranes of S49 lymphoma cells. ScientificWorldJournal. 2014;2014:537192.

60. Maeno E, Ishizaki Y, Kanaseki T, Hazama A, Okada Y. Normotonic cell shrinkage because of disordered volume regulation is an early prerequisite to apoptosis. Proceedings of the National Academy of Sciences of the United States of America. 2000;97(17):9487-92.

61. Jimenez AJ, Maiuri P, Lafaurie-Janvore J, Divoux S, Piel M, Perez F. ESCRT machinery is required for plasma membrane repair. Science (New York, NY). 2014;343(6174):1247136.

62. Hurley JH. ESCRTs are everywhere. The EMBO Journal. 2015;34(19):2398-407.

63. Ward TH, Cummings J, Dean E, Greystoke A. Biomarkers of apoptosis. British journal of …. 2008.

64. Chakraborty JB, Oakley F. Mechanisms and biomarkers of apoptosis in liver disease and fibrosis. International journal of …. 2012.

65. Ariel A, Fredman G, Sun Y-PP, Kantarci A, Dyke TE, Luster AD, et al. Apoptotic neutrophils and T cells sequester chemokines during immune response resolution through modulation of CCR5 expression. Nature immunology. 2006;7(11):1209-16.

66. Smalley DM, Sheman NE, Nelson K, Theodorescu D. Isolation and identification of potential urinary microparticle biomarkers of bladder cancer. J Proteome Res. 2008;7(5):2088-96.

67. Berckmans RJ, Sturk A, van Tienen LM, Schaap MC, Nieuwland R. Cell-derived vesicles exposing coagulant tissue factor in saliva. Blood. 2011;117(11):3172-80.

68. Morel N, Morel O, Petit L, Hugel B, Cochard JF, Freyssinet JM, et al. Generation of procoagulant microparticles in cerebrospinal fluid and peripheral blood after traumatic brain injury. J Trauma. 2008;64(3):698-704.

69. Liu S, Wei L, Zhang Y, Xu M, Wang C, Zhou J. Procoagulant activity and cellular origin of microparticles in human amniotic fluid. Thromb Res. 2014;133(4):645-51.

70. Zonneveld MI, Brisson AR, van Herwijnen MJ, Tan S, van de Lest CH, Redegeld FA, et al. Recovery of extracellular vesicles from human breast milk is influenced by sample collection and vesicle isolation procedures. J Extracell Vesicles. 2014;3.

71. Kulp A, Kuehn MJ. Biological functions and biogenesis of secreted bacterial outer membrane vesicles. Annu Rev Microbiol. 2010;64:163-84.

72. Schooling SR, Beveridge TJ. Membrane vesicles: an overlooked component of the matrices of biofilms. J Bacteriol. 2006;188(16):5945-57.

73. Manning AJ, Kuehn MJ. Contribution of bacterial outer membrane vesicles to innate bacterial defense. BMC Microbiol. 2011;11:258.

74. Tashiro Y, Uchiyama H, Nomura N. Multifunctional membrane vesicles in Pseudomonas aeruginosa. Environ Microbiol. 2012;14(6):1349-62.

75. Gyorgy B, Szabo TG, Pasztoi M, Pal Z, Misjak P, Aradi B, et al. Membrane vesicles, current state-of-the-art: emerging role of extracellular vesicles. Cell Mol Life Sci. 2011;68(16):2667-88.

76. Raposo G, Stoorvogel W. Extracellular vesicles: exosomes, microvesicles, and friends. J Cell Biol. 2013;200(4):373-83.

77. Mashburn LM, Whiteley M. Membrane vesicles traffic signals and facilitate group activities in a prokaryote. Nature. 2005;437(7057):422-5.

78. Barteneva NS, Fasler-Kan E, Bernimoulin M, Stern JNH, Ponomarev ED, Duckett L, et al. Circulating microparticles: square the circle. Bmc Cell Biology. 2013;14.

79. Vajen T, Mause SF, Koenen RR. Microvesicles from platelets: novel drivers of vascular inflammation. Thromb Haemost. 2015;114(2):228-36.

80. Buzas EI, Gyorgy B, Nagy G, Falus A, Gay S. Emerging role of extracellular vesicles in inflammatory diseases. Nat Rev Rheumatol. 2014;10(6):356-64.

81. Dignat-George F, Boulanger CM. The many faces of endothelial microparticles. Arterioscler Thromb Vasc Biol. 2011;31(1):27-33.

82. Headland SE, Norling LV. The resolution of inflammation: Principles and challenges. Semin Immunol. 2015;27(3):149-60.

83. Ibrahim AGE, Cheng K, Marban E. Exosomes as Critical Agents of Cardiac Regeneration Triggered by Cell Therapy. Stem Cell Rep. 2014;2(5):606-19.

84. Sato YT, Umezaki K, Sawada S, Mukai S-AA, Sasaki Y, Harada N, et al. Engineering hybrid exosomes by membrane fusion with liposomes. Sci Rep-Uk. 2016;6:21933.

85. Lacroix R, Robert S, Poncelet P, Kasthuri RS, Key NS, Dignat-George F, et al. Standardization of platelet-derived microparticle enumeration by flow cytometry with calibrated beads: results of the International Society on Thrombosis and Haemostasis SSC Collaborative workshop. J Thromb Haemost. 2010;8(11):2571-4.

86. Lacroix R, Judicone C, Mooberry M, Boucekine M, Key NS, Dignat-George F, et al. Standardization of pre-analytical variables in plasma microparticle determination: results of the International Society on Thrombosis and Haemostasis SSC Collaborative workshop. J Thromb Haemost. 2013.

87. Boing AN, van der Pol E, Grootemaat AE, Coumans FA, Sturk A, Nieuwland R. Single-step isolation of extracellular vesicles by size-exclusion chromatography. J Extracell Vesicles. 2014;3.

88. Witwer KW, Buzas EI, Bemis LT, Bora A, Lasser C, Lotvall J, et al. Standardization of sample collection, isolation and analysis methods in extracellular vesicle research. J Extracell Vesicles. 2013;2.

89. Szatanek R, Ran J, Siedlar M, J-Krzyworzeka M. Isolation of extracellular vesicles: Determining the correct approach (Review). International Journal of Molecular Medicine. 2015;36(1):11-7.

90. Chandler WL. Microparticle counts in platelet-rich and platelet-free plasma, effect of centrifugation and sample-processing protocols. Blood Coagul Fibrinolysis. 2013;24(2):125-32.

91. Cvjetkovic A, Lötvall J, Lässer C. The influence of rotor type and centrifugation time on the yield and purity of extracellular vesicles. Journal of extracellular vesicles. 2014;3.

92. Thiagarajan P, Tait JF. Collagen-induced exposure of anionic phospholipid in platelets and platelet-derived microparticles. The Journal of biological chemistry. 1991;266(36):24302-7.

93. Pasquet JM, Dachary-Prigent J, Nurden AT. Microvesicle release is associated with extensive protein tyrosine dephosphorylation in platelets stimulated by A23187 or a mixture of thrombin and collagen. Biochem J. 1998;333 (Pt 3):591-9.

94. Pasquet JM, Dachary-Prigent J, Nurden AT. Comparison between the loss of platelet membrane asymmetry, microvesiculation and the tyrosine phosphorylation of proteins. Prostaglandins Leukot Essent Fatty Acids. 1997;57(4-5):451-3.

95. Pasquet JM, Dachary-Prigent J, Nurden AT. Calcium influx is a determining factor of calpain activation and microparticle formation in platelets. Eur J Biochem. 1996;239(3):647-54.

96. Pasquet JM, Toti F, Nurden AT, Dachary-Prigent J. Procoagulant activity and active calpain in platelet-derived microparticles. Thromb Res. 1996;82(6):509-22.

97. Balasubramanian K, Bevers EM, Willems GM, Schroit AJ. Binding of annexin V to membrane products of lipid peroxidation. Biochemistry. 2001;40(30):8672-6.

98. Ida M, Satoh A, Matsumoto I, Kojima-Aikawa K. Human annexin V binds to sulfatide: contribution to regulation of blood coagulation. J Biochem. 2004;135(5):583-8.

99. Langen R, Isas JM, Hubbell WL, Haigler HT. A transmembrane form of annexin XII detected by site-directed spin labeling. Proc Natl Acad Sci U S A. 1998;95(24):14060-5.

100. Dasgupta SK, Guchhait P, Thiagarajan P. Lactadherin binding and phosphatidylserine expression on cell surface-comparison with annexin A5. Transl Res. 2006;148(1):19-25.

101. Gyorgy B, Modos K, Pallinger E, Paloczi K, Pasztoi M, Misjak P, et al. Detection and isolation of cell-derived microparticles are compromised by protein complexes resulting from shared biophysical parameters. Blood. 2011;117(4):e39-48.

102. Gyorgy B, Paloczi K, Kovacs A, Barabas E, Beko G, Varnai K, et al. Improved circulating microparticle analysis in acid-citrate dextrose (ACD) anticoagulant tube. Thromb Res. 2014;133(2):285-92.

103. Abdel-Monem H, Dasgupta SK, Le A, Prakasam A, Thiagarajan P. Phagocytosis of platelet microvesicles and beta2- glycoprotein I. Thromb Haemost. 2010;104(2):335-41.

104. Tan X, Shi J, Fu Y, Gao C, Yang X, Li J, et al. Role of erythrocytes and platelets in the hypercoagulable status in polycythemia vera through phosphatidylserine exposure and microparticle generation. Thromb Haemost. 2013;109(6):1025-32.

105. Tian Y, Salsbery B, Wang M, Yuan H, Yang J, Zhao Z, et al. Brain-derived microparticles induce systemic coagulation in a murine model of traumatic brain injury. Blood. 2015;125(13):2151-9.

106. Dasgupta SK, Abdel-Monem H, Niravath P, Le A, Bellera RV, Langlois K, et al. Lactadherin and clearance of platelet-derived microvesicles. Blood. 2009;113(6):1332-9.

107. Shi J, Pipe SW, Rasmussen JT, Heegaard CW, Gilbert GE. Lactadherin blocks thrombosis and hemostasis in vivo: correlation with platelet phosphatidylserine exposure. J Thromb Haemost. 2008;6(7):1167-74.

108. Matsuda A, Jacob A, Wu R, Zhou M, Nicastro JM, Coppa GF, et al. Milk fat globule-EGF factor VIII in sepsis and ischemia-reperfusion injury. Mol Med. 2011;17(1-2):126-33.

109. Okazaki S, Kato R, Uchida Y, Taguchi T, Arai H, Wakatsuki S. Structural basis of the strict phospholipid binding specificity of the pleckstrin homology domain of human evectin-2. Acta Crystallogr D Biol Crystallogr. 2012;68(Pt 2):117-23.

110. Krappa R, Nguyen A, Burrola P, Deretic D, Lemke G. Evectins: Vesicular proteins that carry a pleckstrin homology domain and localize to post-Golgi membranes. Proceedings of the National Academy of Sciences of the United States of America. 1999;96(8):4633-8.

111. Uchida Y, Hasegawa J, Chinnapen D, Inoue T, Okazaki S, Kato R, et al. Intracellular phosphatidylserine is essential for retrograde membrane traffic through endosomes. Proceedings of the National Academy of Sciences of the United States of America. 2011;108(38):15846-51.

112. Hanshaw RG, Lakshmi C, Lambert TN, Johnson JR, Smith BD. Fluorescent detection of apoptotic cells by using zinc coordination complexes with a selective affinity for membrane surfaces enriched with phosphatidylserine. Chembiochem : a European journal of chemical biology. 2005;6(12):2214-20.

113. Nolte-'t Hoen EN, van der Vlist EJ, Aalberts M, Mertens HC, Bosch BJ, Bartelink W, et al. Quantitative and qualitative flow cytometric analysis of nanosized cell-derived membrane vesicles. Nanomedicine. 2012;8(5):712-20.

114. van der Vlist EJ, Nolte-'t Hoen EN, Stoorvogel W, Arkesteijn GJ, Wauben MH. Fluorescent labeling of nano-sized vesicles released by cells and subsequent quantitative and qualitative analysis by high-resolution flow cytometry. Nat Protoc. 2012;7(7):1311-26.

115. Nolan JP, Stoner SA. A trigger channel threshold artifact in nanoparticle analysis. Cytometry A. 2013;83(3):301-5.

116. Demchenko AP. Beyond annexin V: fluorescence response of cellular membranes to apoptosis. Cytotechnology. 2013;65(2):157-72.

117. Shynkar†‡ VV, Klymchenko*† AS, Kunzelmann§ C, Duportail† G, Muller† CD, Demchenko†‖ AP, et al. Fluorescent Biomembrane Probe for Ratiometric Detection of Apoptosis. Journal of the American Chemical Society. 2007;129(7):2187-93.

118. Zwicker JI, Lacroix R Fau - Dignat-George F, Dignat-George F Fau - Furie BC, Furie Bc Fau - Furie B, Furie B. Measurement of platelet microparticles. (1940-6029 (Electronic)).

119. Perfetto SP, Chattopadhyay PK, Roederer M. Seventeen-colour flow cytometry: unravelling the immune system. Nat Rev Immunol. 2004;4(8):648-55.

120. Chattopadhyay PK, Hogerkorp C-M, Roederer M. A chromatic explosion: the development and future of multiparameter flow cytometry. Immunology. 2008;125(4):441-9.

121. Nolan JP. Flow Cytometry of Extracellular Vesicles: Potential, Pitfalls, and Prospects. Curr Protoc Cytom. 2015;73:13 4 1-6.

122. Erni R, Rossell MD, Kisielowski C, Dahmen U. Atomic-resolution imaging with a sub-50-pm electron probe. Phys Rev Lett. 2009;102(9):096101.

123. Arraud N, Linares R, Tan S, Gounou C, Pasquet JM, Mornet S, et al. Extracellular vesicles from blood plasma: determination of their morphology, size, phenotype and concentration. J Thromb Haemost. 2014;12(5):614-27.

124. Binnig G, Quate CF, Gerber C. Atomic force microscope. Phys Rev Lett. 1986;56(9):930-3.

125. Holscher H, Allers W, Schwarz UD, Schwarz A, Wiesendanger R. Interpretation of "true atomic resolution" images of graphite (0001) in noncontact atomic force microscopy. Phys Rev B. 2000;62(11):6967-70.

126. Pecora d. Doppler shifts in light scattering from pure liquids and polymer solutions. The Journal of Chemical Physics. 1964;40(6):1604-14.

127. Clark NA, Lunacek JH, Benedek GB. A Study of Brownian Motion Using Light Scattering. American Journal of Physics. 1970;38(5):575-&.

128. van der Pol E, Coumans F, Varga Z, Krumrey M, Nieuwland R. Innovation in detection of microparticles and exosomes. J Thromb Haemost. 2013;11 Suppl 1:36-45.

129. Shao HL, Yoon TJ, Liong M, Weissleder R, Lee H. Magnetic nanoparticles for biomedical NMR-based diagnostics. Beilstein J Nanotech. 2010;1:142-54.

130. Issadore D, Min C, Liong M, Chung J, Weissleder R, Lee H. Miniature magnetic resonance system for point-of-care diagnostics. Lab on a Chip. 2011;11(13):2282-7.

131. Gleber G, Cibik L, Haas S, Hoell A, Muller P, Krumrey M. Traceable size determination of PMMA nanoparticles based on Small Angle X-ray Scattering (SAXS). J Phys Conf Ser. 2010;247.

132. Ito T, Sun L, Bevan MA, Crooks RM. Comparison of nanoparticle size and electrophoretic mobility measurements using a carbon-nanotube-based coulter counter, dynamic light scattering, transmission electron microscopy, and phase analysis light scattering. Langmuir. 2004;20(16):6940-5.

133. Ito T, Sun L, Henriquez RR, Crooks RM. A carbon nanotube-based coulter nanoparticle counter. Acc Chem Res. 2004;37(12):937-45.

134. Vogel R, Willmott G, Kozak D, Roberts GS, Anderson W, Groenewegen L, et al. Quantitative sizing of nano/microparticles with a tunable elastomeric pore sensor. Anal Chem. 2011;83(9):3499-506.

135. Roberts GS, Yu S, Zeng Q, Chan LC, Anderson W, Colby AH, et al. Tunable pores for measuring concentrations of synthetic and biological nanoparticle dispersions. Biosens Bioelectron. 2012;31(1):17-25.

136. Puppels GJ, Demul FFM, Otto C, Greve J, Robertnicoud M, Arndtjovin DJ, et al. Studying Single Living Cells and Chromosomes by Confocal Raman Microspectroscopy. Nature. 1990;347(6290):301-3.

137. Sebba DS, Watson DA, Nolan JP. High Throughput Single Nanoparticle Spectroscopy. Acs Nano. 2009;3(6):1477-84.

138. Chen KH, Hobley J, Foo YL, Su XD. Wide-field single metal nanoparticle spectroscopy for high throughput localized surface plasmon resonance sensing. Lab on a Chip. 2011;11(11):1895-901.

139. Zhu S, Ma L, Wang S, Chen C, Zhang W, Yang L, et al. Light-scattering detection below the level of single fluorescent molecules for high-resolution characterization of functional nanoparticles. Acs Nano. 2014;8(10):10998-1006.

140. Chandler WL, Yeung W, Tait JF. A new microparticle size calibration standard for use in measuring smaller microparticles using a new flow cytometer. J Thromb Haemost. 2011;9(6):1216-24.

141. Montoro-Garcia S, Shantsila E, Orenes-Pinero E, Lozano ML, Lip GY. An innovative flow cytometric approach for small-size platelet microparticles: influence of calcium. Thromb Haemost. 2012;108(2):373-83.

142. Caspersson TO. Cell growth and cell function, a cytochemical study. 1st ed. New York,: Norton; 1950. 185 p. p.

143. Crosland-Taylor PJ. A device for counting small particles suspended in a fluid through a tube. Nature. 1953;171(4340):37-8.

144. Mellors RC, Silver R. A micro-fluorometric scanner for the differential detection of cells; application of exfoliative cytology. Science. 1951;114(2962):356-60.

145. Mellors RC, Keane JF, Jr., Papanicolaou GN. Nucleic acid content of the squamous cancer cell. Science. 1952;116(3011):265-9.

146. Hercher M, Mueller W, Shapiro HM. Detection and discrimination of individual viruses by flow cytometry. Journal of Histochemistry & Cytochemistry. 1979;27(1):350-2.

147. van der Pol E, Coumans FA, Grootemaat AE, Gardiner C, Sargent IL, Harrison P, et al. Particle size distribution of exosomes and microvesicles determined by transmission electron microscopy, flow cytometry, nanoparticle tracking analysis, and resistive pulse sensing. J Thromb Haemost. 2014;12(7):1182-92.

148. van der Pol E, van Gemert MJ, Sturk A, Nieuwland R, van Leeuwen TG. Single vs. swarm detection of microparticles and exosomes by flow cytometry. J Thromb Haemost. 2012;10(5):919-30.

149. Kantor AB, Moore WA, Meehan S, Parks DR. Current Protocols in Cytometry. wiley. 2016.

150. Chase ES, Hoffman RA. Resolution of dimly fluorescent particles: A practical measure of fluorescence sensitivity. Cytometry. 1998.

151. Schwartz A, Gaigalas AK, Wang L, Marti GE, Vogt RF, Fernandez-Repollet E. Formalization of the MESF unit of fluorescence intensity. Cytometry B Clin Cytom. 2004;57(1):1-6.

152. Schwartz A, Wang L, Early E, Gaigalas A, Zhang YZ, Marti GE, et al. Quantitating fluorescence intensity from fluorophore: The definition of MESF assignment. Journal of Research of the National Institute of Standards and Technology. 2002;107(1):83.

153. Wood J. Fundamental flow cytometer properties governing sensitivity and resolution. Cytometry. 1998.

154. Wood J, Hoffman RA. Evaluating fluorescence sensitivity on flow cytometers: an overview. Cytometry. 1998.

155. Steen HB. Noise, Sensitivity, and Resolution of Flow Cytometers. Cytometry. 1992;13(8):822-30.

156. Lacroix R, Robert S, Poncelet P, Dignat-George F. Overcoming limitations of microparticle measurement by flow cytometry. Semin Thromb Hemost. 2010;36(8):807-18.

157. Mullier F, Illy N, Chatelain C, DognÉ JM, Chatelain B. More on: calibration for the measurement of microparticles: needs, interests, and limitations of calibrated polystyrene beads for flow cytometry-based quantification of biological microparticles. Journal of Thrombosis and Haemostasis. 2011;9(8):1679.

158. Mullier F, Bailly N, Chatelain C, Dogne JM, Chatelain B. More on: calibration for the measurement of microparticles: needs, interests, and limitations of calibrated polystyrene beads for flow cytometry-based quantification of biological microparticles. J Thromb Haemost. 2011;9(8):1679-81; author reply 81-2.

159. Robert S, Poncelet P, Lacroix R, Raoult D, Dignat-George F. More on: calibration for the measurement of microparticles: value of calibrated polystyrene beads for flow cytometry-based sizing of biological microparticles. J Thromb Haemost. 2011;9(8):1676-8; author reply 81-2.

160. Mie G. Beiträge zur Optik trüber Medien, speziell kolloidaler Metallösungen. Annalen der physik. 1908;330(3):377-445.

161. C. M. MATLAB functions for Mie scattering and absorption. 2002-11.

162. van Manen HJ, Verkuijlen P, Wittendorp P, Subramaniam V, van den Berg TK, Roos D, et al. Refractive index sensing of green fluorescent proteins in living cells using fluorescence lifetime imaging microscopy. Biophys J. 2008;94(8):L67-9.

163. Beuthan J, Minet O, Helfmann J, Herrig M, Muller G. The spatial variation of the refractive index in biological cells. Phys Med Biol. 1996;41(3):369-82.

164. Foladori P, Quaranta A, Ziglio G. Use of silica microspheres having refractive index similar to bacteria for conversion of flow cytometric forward light scatter into biovolume. Water Res. 2008;42(14):3757-66.

165. van der Pol E, Coumans FA, Sturk A, Nieuwland R, van Leeuwen TG. Refractive index determination of nanoparticles in suspension using nanoparticle tracking analysis. Nano Lett. 2014;14(11):6195-201.

166. Gardiner C, Shaw M, Hole P, Smith J, Tannetta D, Redman CW, et al. Measurement of refractive index by nanoparticle tracking analysis reveals heterogeneity in extracellular vesicles. J Extracell Vesicles. 2014;3:25361.

167. Baffy G. MicroRNAs in Nonalcoholic Fatty Liver Disease. Journal of clinical medicine. 2015;4(12):1977-88.

168. Byrne CD, Targher G. NAFLD: a multisystem disease. J Hepatol. 2015;62(1 Suppl):S47-64.

169. Kornek M, Lynch M, Mehta SH, Lai M, Exley M, Afdhal NH, et al. Circulating microparticles as disease-specific biomarkers of severity of inflammation in patients with hepatitis C or nonalcoholic steatohepatitis. Gastroenterology. 2012;143(2):448-58.

170. Feng B, Chen Y, Luo Y, Chen M, Li X, Ni Y. Circulating level of microparticles and their correlation with arterial elasticity and endothelium-dependent dilation in patients with type 2 diabetes mellitus. Atherosclerosis. 2010;208(1):264-9.

171. Diamant M. Elevated Numbers of Tissue-Factor Exposing Microparticles Correlate With Components of the Metabolic Syndrome in Uncomplicated Type 2 Diabetes Mellitus. Circulation. 2002;106(19):2442-7.

172. Ogata N, Nomura S, Shouzu A, Imaizumi M, Arichi M, Matsumura M. Elevation of monocyte-derived microparticles in patients with diabetic retinopathy. Diabetes Res Clin Pract. 2006;73(3):241-8.

173. Ogata N, Imaizumi M, Nomura S, Shozu A, Arichi M, Matsuoka M, et al. Increased levels of platelet-derived microparticles in patients with diabetic retinopathy. Diabetes Res Clin Pract. 2005;68(3):193-201.

174. Tramontano AF, Lyubarova R, Tsiakos J, Palaia T, Deleon JR, Ragolia L. Circulating endothelial microparticles in diabetes mellitus. Mediators Inflamm. 2010;2010:250476.

175. <Atherosclerosis 1995 Nomura S.pdf>.

176. <Journal of thrombosis and thrombolysis 2004 Nomura S.pdf>.

177. Bernard S, Loffroy R, Serusclat A, Boussel L, Bonnefoy E, Thevenon C, et al. Increased levels of endothelial microparticles CD144 (VE-Cadherin) positives in type 2 diabetic patients with coronary noncalcified plaques evaluated by multidetector computed tomography (MDCT). Atherosclerosis. 2009;203(2):429-35.

178. Nomura S, Omoto S, Yokoi T, Fujita S, Ozasa R, Eguchi N, et al. Effects of miglitol in platelet-derived microparticle, adiponectin, and selectin level in patients with type 2 diabetes mellitus. Int J Gen Med. 2011;4:539-45.

179. Koga H, Sugiyama S, Kugiyama K, Fukushima H, Watanabe K, Sakamoto T, et al. Elevated levels of remnant lipoproteins are associated with plasma platelet microparticles in patients with type-2 diabetes mellitus without obstructive coronary artery disease. Eur Heart J. 2006;27(7):817-23.

180. <Diabetes 2002 Sabatier F.pdf>.

181. Tan KT, Tayebjee MH, Lim HS, Lip GY. Clinically apparent atherosclerotic disease in diabetes is associated with an increase in platelet microparticle levels. Diabet Med. 2005;22(12):1657-62.

182. Jung KH, Chu K, Lee ST, Bahn JJ, Kim JH, Kim M, et al. Risk of macrovascular complications in type 2 diabetes mellitus: endothelial microparticle profiles. Cerebrovasc Dis. 2011;31(5):485-93.

183. Nomura S, Inami N, Shouzu A, Omoto S, Kimura Y, Takahashi N, et al. The effects of pitavastatin, eicosapentaenoic acid and combined therapy on platelet-derived microparticles and adiponectin in hyperlipidemic, diabetic patients. Platelets. 2009;20(1):16-22.

184. Tsimerman G, Roguin A, Bachar A, Melamed E, Brenner B, Aharon A. Involvement of microparticles in diabetic vascular complications. Thromb Haemost. 2011;106(2):310-21.

185. <2005 Sommeijer DW.pdf>.

186. Goichot B, Grunebaum L, Desprez D, Vinzio S, Meyer L, Schlienger JL, et al. Circulating procoagulant microparticles in obesity. Diabetes & Metabolism. 2006;32(1):82-5.

187. Esposito K, Ciotola M, Schisano B, Gualdiero R, Sardelli L, Misso L, et al. Endothelial microparticles correlate with endothelial dysfunction in obese women. J Clin Endocrinol Metab. 2006;91(9):3676-9.

188. Gunduz Z, Dursun I, Tulpar S, Bastug F, Baykan A, Yikilmaz A, et al. Increased endothelial microparticles in obese and overweight children. J Pediatr Endocrinol Metab. 2012;25(11-12):1111-7.

189. Stepanian A, Bourguignat L, Hennou S, Coupaye M, Hajage D, Salomon L, et al. Microparticle increase in severe obesity: not related to metabolic syndrome and unchanged after massive weight loss. Obesity (Silver Spring). 2013;21(11):2236-43.

190. Murakami T, Horigome H, Tanaka K, Nakata Y, Ohkawara K, Katayama Y, et al. Impact of weight reduction on production of platelet-derived microparticles and fibrinolytic parameters in obesity. Thromb Res. 2007;119(1):45-53.

191. Scorletti E, Bhatia L, McCormick KG, Clough GF, Nash K, Calder PC, et al. Design and rationale of the WELCOME trial: A randomised, placebo controlled study to test the efficacy of purified long chainomega-3 fatty acid treatment in non-alcoholic fatty liver disease [corrected]. Contemporary clinical trials. 2014;37(2):301-11.

192. Scorletti E, Bhatia L, McCormick KG, Clough GF, Nash K, Hodson L, et al. Effects of purified eicosapentaenoic and docosahexaenoic acids in nonalcoholic fatty liver disease: results from the Welcome* study. Hepatology. 2014;60(4):1211-21.

193. Scheuer PJ. Classification of chronic viral hepatitis: a need for reassessment. Journal of hepatology. 1991;13(3):372-4.

194. Kleiner DE, Brunt EM, Van Natta M, Behling C, Contos MJ, Cummings OW, et al. Design and validation of a histological scoring system for nonalcoholic fatty liver disease. Hepatology. 2005;41(6):1313-21.

195. Angulo P, Hui JM, Marchesini G, Bugianesi E, George J, Farrell GC, et al. The NAFLD fibrosis score: a noninvasive system that identifies liver fibrosis in patients with NAFLD. Hepatology. 2007;45(4):846-54.

196. Guha IN, Parkes J, Roderick P, Chattopadhyay D, Cross R, Harris S, et al. Noninvasive markers of fibrosis in nonalcoholic fatty liver disease: Validating the European Liver Fibrosis Panel and exploring simple markers. Hepatology. 2008;47(2):455-60.

197. Dixon WT. Simple proton spectroscopic imaging. Radiology. 1984;153(1):189-94.

198. Bannas P, Kramer H, Hernando D, Agni R, Cunningham AM, Mandal R, et al. Quantitative magnetic resonance imaging of hepatic steatosis: Validation in ex vivo human livers. Hepatology (Baltimore, Md). 2015;62(5):1444-55.

199. Carlson-Newberry SJ, Costello RB. Dual-Energy X-Ray Absorptiometry: Research Issues and Equipment. Dual-Energy X-Ray Absorptiometry: Research Issues and Equipment. 1997.

200. Italiano JE, Jr., Mairuhu AT, Flaumenhaft R. Clinical relevance of microparticles from platelets and megakaryocytes. Curr Opin Hematol. 2010;17(6):578-84.

201. Flaumenhaft R, Dilks JR, Richardson J, Alden E, Patel-Hett SR, Battinelli E, et al. Megakaryocyte-derived microparticles: direct visualization and distinction from platelet-derived microparticles. Blood. 2009;113(5):1112-21.

202. Mause SF, Weber C. Microparticles: protagonists of a novel communication network for intercellular information exchange. Circ Res. 2010;107(9):1047-57.

203. Morel A. Etude experimentale de la diffusion de la lumiere par l'eau, les solutions de chlorure de sodium, et l'eau de mer optiquement pures. J Chim Phys. 1966;10:1359–66.